TU Delft

Delft University of Technology

Concrete in dynamic tension

The fracture process

Vegt, Ilse

DOI
10.4233/uuid:c351e276-e7e2-4153-98e6-bea6882cfb30

Publication date
2016

Document Version
Final published version

Citation (APA)
Vegt, I. (2016). *Concrete in dynamic tension: The fracture process*. [Dissertation (TU Delft), Delft University of Technology]. https://doi.org/10.4233/uuid:c351e276-e7e2-4153-98e6-bea6882cfb30

Important note
To cite this publication, please use the final published version (if applicable).
Please check the document version above.

Copyright
Other than for strictly personal use, it is not permitted to download, forward or distribute the text or part of it, without the consent of the author(s) and/or copyright holder(s), unless the work is under an open content license such as Creative Commons.

Takedown policy
Please contact us and provide details if you believe this document breaches copyrights.
We will remove access to the work immediately and investigate your claim.

This work is downloaded from Delft University of Technology.
For technical reasons the number of authors shown on this cover page is limited to a maximum of 10.

Concrete in dynamic tension: The fracture process

Proefschrift

ter verkrijging van de graad van doctor
aan de Technische Universiteit Delft,
op gezag van de Rector Magnificus prof.ir. K.Ch.A.M. Luyben;
voorzitter van het College voor Promoties,
in het openbaar te verdedigen op
dinsdag 6 december 2016 om 10:00 uur
door

Ilse VEGT

Civiel Ingenieur, geboren te Den Helder, Nederland

Dit proefschrift is goedgekeurd door de

promotor: Prof.Dr.Ir. K. Van Breugel, TU Delft en

copromotor: Dr.Ir. J. Weerheijm, TU Delft en TNO Defence, Safety & Security

Samenstelling promotiecommissie bestaat uit:

Rector magnificus	voorzitter
Prof.Dr.Ir. K. Van Breugel	promotor
Dr.Ir. J. Weerheijm	copromotor

onafhankelijke leden:

Prof.Dr. P.A. Forquin	Laboratoire 3SR, Grenoble, Frankrijk
Prof.Dr.Ir. D.A. Hordijk	Faculteit Civiele Techniek, TU Delft
Prof.Dr.-Ing. habil. J. Ozbolt	Institute of Construction Materials, University of Stuttgart
Prof.Dr.Ir. H.E.J.G. Schlangen	Faculteit Civiele Techniek, TU Delft
Prof.Dr.Ir. L.J. Sluijs	Faculteit Civiele Techniek, TU Delft

ISBN 978-94-6186-747-6
Printed by Rodi Media, The Netherlands.
Cover: Rodi Media, lay-out J. Krug (Rodi Media).

@ 2016 I. Vegt. All rights reserved. No part of the material protected by this copyright notice may be reproduced or utilized in any form or by any means, electronic or mechanical, including photocopying, recording or by any information storage and retrieval system, without permission from the author.

ACKNOWLEDGEMENT

The research reported in this thesis is carried out at the Stevin Laboratory at the Delft University of Technology and at the TNO Prins Maurits Laboratory in Rijswijk.
The financial support provided by the Netherlands Technology Foundation (STW) and the financial and technical support given by the research organisation TNO are gratefully acknowledged.

First of all, I would like to express my sincere gratitude to Professor Klaas van Breugel for his encouragement, positive feedback, support and guidance.

I especially want to thank my supervisor and copromotor Jaap Weerheijm, for his continuous support, the productive discussions, the feedback and encouragement. Jaap, without you I would have never finished this thesis. Thank you for not letting me give up.

Thanks to Gerard Timmers, Arjan Thijssen and Reinoud van de Kasteele for their contribution to the experimental part of this study.

I want to express my thankfulness to Dr.ir. Leo Pel from the University of Eindhoven for providing me with the opportunity to use the NMR equipment to determine the moisture in the pores. I also want to thank Gijs van der Heijden for his assistance with the NMR experiments.

I want to thank my colleagues from the TUDelft, who, during my time at the TUDelft working om my PhD, have supported me and have made my time at the TUDelft pleasant and filled with humour. I want to specially mention Ronnie Pedersen, with whom I worked together in a joint STW program, and my roommate Peter Moonen. Ronnie and Peter, thanks for the fruitful discussions and the pleasant conversations. I also want to mention my good friend and fellow PhD-student Sonja Fennis, who made my lunch- and coffee breaks very pleasant and was always there to listen, talk and lift my spirits.

Furthermore, I want to thank Martijn Schroor and my direct colleagues from the local government of Bergen for their patience, support and for the time they have given me to finish my PhD. Martijn, thank you for the encouragement to finish my PhD and for believing in me, even when I wasn't believing in myself.

Acknowledgement

Finally, I want to thank my family and especially my parents and husband Patrick for their ongoing support, love and believe in me. Their support and love has given me the courage to carry on and finally finish my thesis. Patrick, you are my rock. Thank you for always being there for me.

Voor mijn meiden Sanne en Tessa;
‘Als je valt, weer opstaat en doorgaat,
kom je uiteindelijk altijd daar waar je wil zijn.’

SUMMARY

Concrete is commonly used in protective and civil structures, like tunnels and storage buildings. For the design and reliable safety assessment of such structures it is very important to know the behaviour of concrete under static loading conditions as well as under impulsive loading. To understand the behaviour of concrete under impulsive loading and to be able to predict the failure behaviour, it is important to know the influence of the loading rate on concrete strength and failure parameters and to quantify how they change with increasing loading rate. The fact that material parameters depend on the applied loading rate is called *rate dependency*.

Objectives

The mechanical response of concrete structures is often predicted with numerical material models in a finite element context. To properly predict the response of structures under impulsive loading, the rate dependency should be included explicitly in the material model. To validate a physically realistic concrete material model for high loading rates, experimental data on the rate dependency of concrete tensile strength and fracture properties is needed. Data which shows the influence of the loading rate on the mechanical parameters like strength and stiffness can be found in literature for low as well as high loading rates (> 1000 GPa/s). However, data on the rate dependency of the fracture energy, and especially the fracture behaviour, is scarce. Therefore, the objective of this study is to quantify the rate effect on the tensile strength and stiffness at medium and high loading rates, as well as to determine the stress-displacement relation that reflects the fracture process and determines the fracture energy.

Besides experimental data on the rate dependency of concrete properties, it is also important to understand the physical mechanisms behind the rate effects. The physical mechanisms will explain the change in concrete behaviour under dynamic loading conditions. A detailed analysis of the causes behind the rate dependency of concrete is missing in literature. There is no common explanation of the underlying mechanisms of the rate dependency of concrete tensile properties. Therefore, one of the objectives of this study is to identify the different mechanisms behind the rate effects on tensile properties and to quantify the influence of the different mechanisms. To gain detailed information on the mechanisms behind the rate dependency and to be able to quantify the influence of the different mechanisms, information on the rate effects on fracture characteristics (width of the fracture zone, crack distribution and crack /fracture lengths) is needed. The experimental research (at macro level) is, therefore, combined with microscopic research.

Experimental program

A research program has been developed to study the rate dependency of concrete tensile fracture properties. To study the rate effect on the tensile properties of concrete, uniaxial tensile test are conducted at three different loading rates:

– Static loading rate as a reference; loading rate 10^{-4} GPa/s;
– Moderate loading rate with the gravity driven Split Hopkinson Bar set-up (SHB) at the Delft University of Technology; loading rate 50 GPa/s;
– High loading rate with a newly developed Modified Split Hopkinson Bar set-up (MSHB) at the laboratory of TNO in Rijswijk; loading rate > 1000 GPa/s.

From literature it was concluded that the moisture in the pores plays an important role in the rate dependency of concrete properties, especially in the moderate loading rate regime (up to 50 GPa/s). Therefore, it was decided to study the influence of moisture on the rate dependency of the tensile fracture properties by varying the loading rate, moisture content and microstructure. To study the influence of the microstructure, two types of concretes are used; Portland cement concrete and Blast Furnace Slag (BFS) cement concrete. BFS cement concrete has a denser microstructure with less capillary pores.

To study the influence of moisture in the pore system on the rate effects on concrete tensile properties, the concrete specimens have been subjected to four different moisture

conditions for approximately 21 days (after being drilled out of the cubes at an age of 28 days).
The four different moisture conditions are:

– "Normal" condition: specimens are stored under controlled conditions of 20°C and 50% RH;
– "Wet" condition: specimens are immersed in water;
– "Dry-50" condition: specimens are dried in an oven of 50°C and 15% RH;
– "Dry-105" condition: specimens are dried in an oven of 105°C and 2% RH.

After the uniaxial tensile tests are finished, the fracture patterns have been studied by impregnating the cracks with epoxy and studying them by microscope. The influence of the rate dependency on the fracture parameters has been determined by quantifying the rate effects on the lengths of the different cracks and on the width of the fracture zone.

Test set-ups

For the static tests (loading rate 10^{-4} GPa/s), deformation controlled uniaxial tensile tests have been performed on cylindrical concrete specimens (Ø 74 mm, length 100 mm).
The gravity driven Split Hopkinson Bar is used to conduct the uniaxial tensile tests at moderate loading rate (50 GPa/s). This SHB set-up consists of two cylindrical aluminium bars between which the concrete specimen (Ø 74 mm, length 100 mm) is glued. The tensile stress wave is generated with a drop weight, which slides along the lower bar and hits an anvil at the bottom end. The tensile wave travels upwards through the aluminium bar and through the specimen, fracturing the specimen when the tensile strength of the concrete is reached.
For the very high loading rates (> 1000 GPa/s) a new Modified Split Hopkinson Bar (MSHB) set-up is used. The Modified Split Hopkinson Bar is based on a different principle than the Split Hopkinson Bar, i.e. the principle of spalling. A shock wave is introduced into a horizontal steel bar by detonating an explosive charge at one end of the bar. At the other end, the concrete specimen is attached which is first loaded in compression and will fail in tension due to the reflected tensile wave (spalling).

In the Modified Split Hopkinson Bar set-up a new innovative measurement technique was used, enabling direct measurement of strains and deformations of the loaded specimens. The direct measurement method used in the Split Hopkinson Bar and Modified Split

Hopkinson Bar set-ups generates information on real-time strains and deformations. This makes it possible to reconstruct failure behaviour and has given insight in the different causes of the observed rate effects.

Experimental results

For the moderate loading rates (50 GPa/s) an increase of the tensile strength of approximately 2 MPa is found for dry and normally cured concrete compared to the static tests. For wet concrete, the increase in tensile strength was found to be more pronounced, approximately 4 MPa for Portland cement concrete and 3 MPa for Blast Furnace Slag cement concrete.

At high loading rates (1700 – 2450 GPa/s), the tensile strength results have shown an increase of approximately 5-7 MPa for normal and dry concrete and 12-15 MPa for wet concrete.

The fracture characteristics, i.e. fracture lengths and widths of the fracture zone, and the failure behaviour have been quantified by measuring the individual and summarized crack lengths and determining the stress-deformation curves. From the results it was concluded that the width and length of the macro fracture are not influenced by the loading rate. For normally cured and dry concrete and loading rates up to 50 GPa/s, the fracture energy, shape of the stress-deformation curve, width of the fracture zone and the number of micro cracks are hardly affected by the loading rate. Wet concrete shows enhanced resistance in the post-peak phase of the stress-deformation curve. For the high loading rate regime (> 50 GPa/s) the total summarized length of the micro cracks and the width of the fracture zone increase considerably, as well as the resistance in the post-peak phase of the stress-deformation curve and the fracture energy.

Mechanisms

With the available experimental data on tensile strength, fracture characteristics and post-peak failure behaviour, the failure mechanisms have been reconstructed and the main causes for rate dependency of the tensile strength and fracture resistance have been identified. The most important possible causes are (1) structural inertia of the fracture zone, (2) influence of inertia at micro level which can delay crack initiation and propagation, (3) additional micro cracking and (4) enhanced fracture resistance caused by moisture in the pores (Stefan effect).

By using basic principles of fracture mechanics and a simple model based on the Stefan effect, the different mechanisms and the loading rates at which these mechanisms have significant effect have been determined. Nuclear Magnetic Resonance and Mercury Intrusion Porosimetry results provide necessary data on moisture distribution in the pore system.

Structural inertia effects

For the experimental data from the presented research and the method used to measure and analyse the data (1D approach), it was shown that structural inertia of the fracture zone (axial direction) does not contribute to the obtained enhanced tensile strength for the moderate as well as the high loading rate regime. Also, structural inertia of the fracture zone hardly affects the post peak behaviour of concrete. This holds for all concrete types and moisture contents studied.

Effect of micro inertia, Stefan effect and additional cracking

The mechanism which causes the strength increase due to moisture in the pores is the so called Stefan effect. The Stefan effect is explained as the reaction force, which is induced when two plates with moisture in between are separated.

The equation to calculate the Stefan effect is modified to fit concrete pore structure properties. To incorporate the concrete structure, it is assumed that the Stefan effect is valid for cylindrical pores.

From the NMR data combined with the experimental data on strength and fracture energy and the Stefan effect model, it was concluded that only the moisture in the *capillary* pores contributes to the enhanced tensile strength and post-peak resistance.

The dominant mechanism in the *moderate loading rate* regime (< 50 GPa/s) causing the *tensile strength* increase due to moisture in the pores is the Stefan effect. In the *high loading rate* regime, both the Stefan effect and the micro inertia effects on crack propagation due to the limitation on crack velocity contribute to the increase in tensile strength.

The enhanced *fracture resistance* in the post peak behavior for wet concrete and *moderate loading rates* up to 50 GPa/s has been ascribed to the viscous effects of moisture in the concrete pores (Stefan effect). For the *high loading rate* regime, loading rates exceeding 50 GPa/s, the enhanced resistance in the post-peak behaviour is partly caused by the

formation of additional (micro) cracks. However, the increase in (micro) crack length is insufficient to explain the observed high fracture energy increase for the high loading rate regime. Therefore, the increased fracture toughness in the post-peak behaviour in the high loading rate regime has been explained by the formation of additional (micro) cracks as well as the viscous behaviour of concrete (wet concrete) and by the micro inertia effects due to material inherent limitation of the crack velocity.

Future application

The acquired knowledge on the mechanisms behind the rate dependency of concrete fracture properties can be used to improve numerical models. One of the most commonly used approaches to model concrete fracture is the application of continuum models. The properties and behaviour of the elements in a continuum model are defined by a constitutive law, which also determines the change in properties when fracture takes place. For modelling failure under dynamic loading conditions, the mechanisms behind the rate effects on concrete tensile properties, i.e. moisture in the capillary pores, additional micro cracking and micro inertia effects due to limitations on crack velocity, should be incorporated into the constitutive material model. Which mechanisms should be incorporated into the material model depends on the scale at which modelling takes place.

The presented research has also shown that for modelling dynamic experiments the internal material length scale, an important parameter to model fracture processes, should be based on the width of the macro fracture zone and connected micro cracks. This zone contains the macro crack, which physically separates the specimen in two halves, as well as the micro cracks that are attached/connected to the macro crack. The width of the macro fracture zone with connected micro cracks does not significantly change with increasing loading rate. Subsequently, the internal length scale as defined for a specific model also does not significantly change with increasing loading rate.

The dominant mechanisms found in the presented research can be implemented in dynamic models and the acquired data set[1] can be used to validate the developed models.

[1] *Available at the TUDelft, for information contact dr.ir. J. Weerheijm*

With the suggested dominant mechanisms and knowledge on the rate dependency of the concrete tensile strength and fracture behaviour, the response of concrete materials under dynamic loading can now be better understood and predicted more accurately.

SAMENVATTING

Het materiaal beton wordt veel toegepast voor betonnen beschermingsconstructies en civiel technische constructies, zoals tunnels en opslag gebouwen. Om dergelijke constructies te kunnen ontwerpen en betrouwbare risicoanalyses te kunnen uitvoeren is het belangrijk om het gedrag van beton te kennen onder zowel statische als dynamische belastingen. Voor het begrijpen van het gedrag van beton onder dynamische belasting en om het breukgedrag van beton te kunnen voorspellen is het belangrijk om te weten wat de invloed van de belastingsnelheid is op de betonsterkte en de breukparameters en om te kwantificeren hoe deze betonparameters veranderen bij hoge belastingsnelheden. Als materiaalparameters afhankelijk zijn van de belastingsnelheid noemen we dat *'snelheidsafhankelijkheid'*.

Doelstellingen

De mechanische respons van betonconstructies wordt vaak voorspeld met behulp van numerieke modellen. Om de respons van constructies die dynamisch worden belast juist te kunnen voorspellen, zou de snelheidsafhankelijkheid van de betonparameters expliciet moeten worden opgenomen in het gebruikte materiaalmodel. Experimentele data over de snelheidsafhankelijkheid van de betontreksterkte en de breukparameters is nodig voor het valideren van een realistisch betonmodel dat het breukgedrag onder dynamische belastingen kan voorspellen op basis van de onderliggende mechanismen.

Data over de invloed van de belastingsnelheid op mechanische materiaaleigenschappen als de treksterkte of stijfheid van beton kan in de literatuur worden gevonden voor lage zowel als hoge belastingsnelheden (> 1000 GPa/s). Data over de snelheidsafhankelijkheid van de *breukenergie* en het *breukgedrag* van beton is echter schaars. In dit onderzoek gaat het dan ook niet alleen om het kwantificeren van de snelheidsafhankelijkheid van de

treksterkte en stijfheid, maar ook om het bepalen van de spanning-vervormings-relatie. Deze spannings-vervormings-relatie beschrijft het breukgedrag van beton en kwantificeert de breukenergie.

Naast experimentele data over de snelheidsafhankelijkheid van betonparameters is het ook belangrijk om de fysische mechanismen achter de snelheidsafhankelijkheid te kennen en begrijpen. De fysische mechanismen verklaren de veranderingen in het gedrag van beton dat dynamisch wordt belast. In de literatuur is geen gedetailleerde analyse te vinden van de mechanismen achter de snelheidsafhankelijkheid van de betonparameters onder trekbelasting. Daarom is een tweede doelstelling van dit onderzoek het *bepalen en benoemen* van de verschillende mechanismen achter de snelheidseffecten op betonparameters en het *kwantificeren* van de invloed van deze verschillende mechanismen op de snelheidsafhankelijkheid. Om de mechanismen te kunnen identificeren en de invloed te kwantificeren is gedetailleerde informatie nodig over de snelheidsafhankelijkheid van de breukkenmerken (breedte van de breukzone, scheurverdeling en scheur/breuk lengtes). Daarom is ervoor gekozen om het experimentele onderzoek naar de snelheidsafhankelijkheid van betonparameters, dat uitgevoerd wordt op macro niveau, te combineren met microscopisch onderzoek naar deze breukkenmerken.

Experimenteel programma

Een onderzoeksprogramma is opgesteld om de snelheidsafhankelijkheid van betonparameters onder trekbelasting te bestuderen. Om de snelheidseffecten op de trekparameters van beton te onderzoeken zijn eenassige trekproeven uitgevoerd met drie verschillende belastingsnelheden:

- Statische trekproef als referentie; belastingsnelheid 10^{-4} GPa/s;
- Middelhoge belastingsnelheid met een door zwaartekracht aangedreven Split Hopkinson Bar testopstelling (SHB) gesitueerd op de Technische Universiteit Delft; belastingsnelheid 50 GPa/s;
- Hoge belastingsnelheid met een nieuw ontwikkelde Modified Split Hopkinson Bar testopstelling (MSHB) in het laboratorium van TNO in Rijswijk; belasting-snelheid > 1000 GPa/s.

Uit literatuur blijkt dat het vocht in de poriën een belangrijke rol speelt in de snelheidsafhankelijkheid van betonparameters, vooral in het middelhoge snelheidsregime (tot 50 GPa/s). Daarom is besloten om de invloed van het vocht op de snelheidsafhankelijkheid van breukparameters onder trek te bestuderen door zowel de belastingsnelheid te variëren als de vochthoeveelheid en de microstructuur van het beton. Om de invloed van de microstructuur te bepalen zijn er twee verschillende soorten beton toegepast, Portlandcement beton en Hoogovencement beton. Hoogovencement beton heeft een dichtere microstructuur dan Portlandcement beton en heeft minder capillaire poriën.

Om de invloed van de hoeveelheid vocht dat aanwezig is in de poriën op de snelheidseffecten in beton te bestuderen, zijn de betonnen proefstukken aan vier verschillende omgevingen blootgesteld voor de duur van ongeveer 21 dagen (nadat de proefstukken op een leeftijd van 28 dagen uit betonnen kubussen geboord zijn)
De vier verschillende omgevingscondities zijn:

– "Normale" conditie: de proefstukken worden opgeslagen in een gecontroleerde omgeving met een temperatuur van 20°C en een relatieve vochtigheid (RV) van 50%;
– "Natte" conditie: proefstukken worden ondergedompeld in water;
– "Droog-50" conditie: proefstukken worden gedroogd in een oven met een temperatuur van 50°C en een RV van 15%;
– "Droog-105" conditie: proefstukken worden gedroogd in een oven met een temperatuur van 105°C en een RV van 2%.

Nadat de eenassige trekproeven zijn afgerond worden de breukpatronen bekeken door de proefstukken te impregneren met epoxy en ze vervolgens te bestuderen met een microscoop. De invloed van de belastingsnelheid op de breukparameters is bepaald door de scheurlengtes en breedte van de scheurzone te kwantificeren bij de verschillende belastingsnelheden.

Testopstellingen

Voor de statische proeven (belastingsnelheid 10^{-4} GPa/s) worden vervorming gestuurde trekproeven uitgevoerd op cilindrische betonnen proefstukken (Ø 74 mm, lengte 100 mm). De door zwaartekracht aangedreven Split Hopkinson Bar testopstelling is gebruikt om

eenassige trekproeven uit te voeren bij middelhoge belastingsnelheden (50 GPa/s). Deze testopstelling bestaat uit twee verticale cilindrische aluminium staven waartussen een betonnen proefstuk wordt gelijmd (Ø 74 mm, lengte 100 mm). De trekbelasting wordt gegenereerd door een valgewicht, dat langs de onderste staaf glijdt en aan het einde op een aambeeld valt. Vervolgens beweegt een trekgolf door de onderste aluminium staaf omhoog en belast het betonnen proefstuk, waarna het breekt als de treksterkte bereikt is.

Voor eenassige trekproeven met de hoge belastingsnelheden (> 1000 GPa/s) is een nieuw ontwikkelde Modified Split Hopkinson Bar testopstelling (MSHB) gebruikt. De methode van de MSHB is gebaseerd op een ander principe dan de SHB, namelijk de splijttechniek. Een schokgolf wordt opgewekt door explosieven en doorgegeven aan één zijde van een horizontale stalen staaf. Aan de andere kant van de staaf is een betonnen proefstuk aangebracht. Dit proefstuk wordt eerst belast door de drukgolf en breekt vervolgens doordat de terugkerende trekgolf de treksterkte overschrijdt (splijttechniek).

Een nieuwe meetmethode is ontwikkeld voor het meten van de vervormingen in de MSHB opstelling. Door deze meetmethode kunnen de spanningen en de vervormingen direct worden gemeten, net als bij de SHB opstelling. Door de directe meetmethode kunnen spanningen en vervormingen in de tijd worden gemeten en dit geeft extra informatie om uiteindelijk het breukgedrag van beton te kunnen reconstrueren. Ook kan door de gemeten spanningen en vervormingen in de tijd meer inzicht worden verkregen in de oorzaken van de gemeten snelheidseffecten in beton.

Experimentele resultaten

Bij middelhoge belastingsnelheid (50 GPa/s) wordt een verhoging van de treksterkte waargenomen van ongeveer 2 MPa ten opzichte van de statische treksterkte voor droog en normaal geconditioneerd beton. Voor nat beton is de verhoging van de treksterkte hoger; ongeveer 4 MPa voor nat Portlandcement beton en 3 MPa voor nat Hoogovencement beton.

De resultaten voor de treksterkte bij hoge belastingsnelheden (1700 – 2450 GPa/s) tonen aan dat deze hoge snelheden leiden tot een verhoging van de treksterkte van ongeveer 5 – 7 MPa voor normaal geconditioneerd en droog beton en ongeveer 12 – 15 MPa voor nat beton.

De breukkenmerken, namelijk de breuklengtes en breedtes van de breukzones, en het breukgedrag zijn gekwantificeerd door de individuele scheuren te meten en vervolgens de lengtes op te tellen en door het bepalen van de spannings-vervormingscurves. De resultaten laten zien dat de breedte van de macroscheurzone en de macroscheurlengte niet worden beïnvloed door de belastingsnelheid. Voor normaal geconditioneerd en droog beton en belastingsnelheden tot 50 GPa/s veranderen de breukenergie, de vorm van de spannings-vervormingscurve, de breedte van de scheurzone en de hoeveelheid microscheuren nauwelijks. In de spannings-vervormingscurve van nat beton is extra weerstand in de post-piek fase te zien.
In het hoge belastingsnelheidregime (> 50 GPa/s) nemen de totale opgetelde microscheurlengtes en de breedte van de scheurzone aanmerkelijk toe. Dit geldt ook voor de weerstand in de post-piek fase van de spannings-vervormingscurve en voor de breukenergie.

Mechanismen

Met de experimentele resultaten voor de treksterkte, breukkenmerken en post-piek breukgedrag zijn de breukmechanismen gereconstrueerd en zijn de belangrijkste oorzaken van de snelheidsafhankelijkheid van de treksterkte en breukweerstand bepaald. De belangrijkste oorzaken zijn (1) constructieve traagheidseffecten in de breukzone, (2) invloed van micro traagheidseffecten die het ontstaan en het groeien van de scheuren tegen kunnen gaan, (3) extra microscheurvorming en (4) vergrootte breukweerstand veroorzaakt door het vocht in de poriën van het beton (Stefan effect).
Door de basis principes van breukmechanica toe te passen en een simpel model gebaseerd op het Stefan effect, zijn de verschillende mechanismen onderzocht en de belastingsnelheden vastgesteld waarop deze mechanismen een rol gaan spelen. Nuclear Magnetic Resonance resultaten en kwikporositeitsmetingen geven de benodigde informatie over de vochtverdeling in het porie systeem van het beton.

Constructieve traagheidseffecten

Voor de experimentele data van dit onderzoek en de methode die is toegepast om de data te meten en analyseren (1D analyse), is vastgesteld dat constructieve traagheidseffecten in de breukzone geen bijdrage leveren aan de toegenomen sterkte bij middelhoge en hoge belastingsnelheden. Ook is aangetoond dat traagheidseffecten in de breukzone (axiale

richting) nauwelijks effect hebben op het breukgedrag van beton. Dit geldt voor alle betonsoorten en vochtigheden van beton die in dit onderzoek zijn toegepast.

Effect van micro traagheidseffecten, het Stefan effect en extra microscheurvorming

Het zogenaamde Stefan effect is het mechanisme dat zorgt voor een sterktetoename door het vocht in de poriën. Het Stefan effect wordt uitgelegd als de reactiekracht die ontstaat wanneer twee vlakke platen met vocht ertussen uit elkaar worden getrokken.

De vergelijking waarmee het Stefan effect kan worden berekend is aangepast zodat hij toepasbaar is voor de porie structuur van beton. Om de vergelijking te kunnen toepassen op de microstructuur van beton is aangenomen dat het Stefan effect ook geldt voor cilindervormige poriën.

Uit de NMR data, gecombineerd met de experimentele resultaten voor de treksterkte en de breukenergie en uit het Stefan effect model, is geconcludeerd dat alleen het vocht in de *capillaire* poriën bijdraagt aan de toegenomen sterkte en breukweerstand onder dynamische belastingen.

Het dominante mechanisme in het *middelhoge belastingsnelheidregime* (< 50 GPa/s) dat een toename van de *treksterkte* veroorzaakt is het Stefan effect van het vocht in de poriën. In het *hoge belastingsnelheidregime* dragen zowel het Stefan effect als de micro traagheidseffecten die het groeien van de scheuren vertragen door de materiaaleigen gelimiteerde scheursnelheid bij aan de toename in treksterkte onder dynamische belastingen.

De toegenomen *breukweerstand* in het post-piek gedrag van nat beton en bij *middelhoge belastingsnelheden* tot 50 GPa/s wordt toegeschreven aan de viskeuze effecten van het vocht in de betonporiën (Stefan effect). In het *hoge belastingsnelheidregime*, met belastingsnelheden hoger dan 50 GPa/s, wordt de toegenomen weerstand in post-piek breukgedrag gedeeltelijk veroorzaakt door toegenomen microscheurvorming. De toename in microscheurlengte is echter niet voldoende om de hoge toename in breukenergie in het hoge belastingsnelheidregime te verklaren. Daarom wordt toegenomen taaiheid in het post-piek breukgedrag toegeschreven aan zowel de toename in microscheurvorming als ook het viskeuze gedrag van beton (nat beton, Stefan effect) en aan de micro traagheidseffecten door de materiaaleigen gelimiteerde scheursnelheid.

Toekomstige toepassingen van de data

De opgedane kennis over de mechanismen achter de snelheidsafhankelijkheid van de beton breukparameters kan gebruikt worden om numerieke modellen te verbeteren. Een van de meeste gebruikte methoden om het breukgedrag van beton te modelleren is het toepassen van continuüm modellen. De eigenschappen en het gedrag van de elementen in een continuüm model worden beschreven in een constitutieve relatie. Deze constitutieve relatie bepaalt ook hoe de eigenschappen van beton veranderen als de sterkte is overschreden en breuk is ingetreden. Om het breukgedrag van beton onder dynamische belastingen te kunnen modelleren moeten de mechanismen achter de snelheidsafhankelijkheid van de betonparameters, namelijk het Stefan effect door het vocht in de capillaire poriën, extra microscheurvorming en micro traagheidseffecten door de gelimiteerde scheursnelheid, worden meegenomen in het constitutieve materiaalmodel. Welke mechanismen moeten worden meegenomen in het materiaalmodel is afhankelijk van de schaal waarop het beton wordt gemodelleerd.

Het in dit proefschrift gepresenteerde onderzoek heeft ook aangetoond dat voor het modelleren van dynamische experimenten de interne lengteschaal, wat een belangrijke parameter is voor het modelleren van breukprocessen, gebaseerd zou moeten zijn op de breedte van de zone die zowel de macroscheur als de daaraan gekoppelde microscheuren bevat. Deze zone bevat de macroscheur, die de proefstukken fysisch in twee helften verdeelt en de microscheuren die aan de macroscheur grenzen/zijn gekoppeld. De breedte van de zone die de macroscheur en de daaraan gekoppelde microscheuren bevat verandert niet significant als de belastingsnelheid toeneemt. Derhalve zal ook de interne lengteschaal, gedefinieerd voor een specifiek model, niet significant veranderen bij toenemende belastingsnelheid.

Het onderzoek gepresenteerd in dit proefschrift heeft de dominante mechanismen aan het licht gebracht die de snelheidsafhankelijkheid van betonparameters onder trek veroorzaken. Deze mechanismen kunnen worden geïmplementeerd in dynamische modellen en de verworven data set[1] kan worden gebruikt om de nieuw ontwikkelde modellen te valideren.

[1] *Beschikbaar aan de TUDelft, voor informatie kan contact worden opgenomen met dr.ir. J. Weerheijm*

Met de voorgestelde dominante mechanismen en de kennis die is opgedaan over de snelheidsafhankelijkheid van de treksterkte en het breukgedrag van beton, kan de respons van dynamisch belaste betonnen constructies beter worden begrepen en nauwkeuriger worden voorspeld.

TABLE OF CONTENTS

Summary vii

Samenvatting xv

1 Introduction 1
- 1.1 Background 1
- 1.2 Research objective 2
- 1.3 Research strategy 3
- 1.4 Outline of the thesis 4

2 Concrete properties, fracture characteristics and rate dependency 7
- 2.1 Introduction 7
- 2.2 Concrete 8
  - 2.2.1 Hydration of concrete 8
  - 2.2.2 Pore structure 9
  - 2.2.3 Cement type and influence on pore structure 11
  - 2.2.4 Conditions and the influence on pore structure 12
  - 2.2.5 Drying damage 14
  - 2.2.6 Drying at what temperature? 15
- 2.3 Fracture of concrete in tension 19
  - 2.3.1 Meso and micro level 19
  - 2.3.2 Failure process in tension 20
  - 2.3.3 Stress-displacement and stress-deformation curves 22
  - 2.3.4 Parameters that influence failure of concrete in tension 25
- 2.4 Rate dependency of concrete 27
  - 2.4.1 Failure process at high loading rates 28
  - 2.4.2 Tensile strength 29
  - 2.4.3 Fracture energy at high loading rates 31
  - 2.4.4 Moisture and rate dependency 32
  - 2.4.5 Modelling fracture of concrete and the rate effects on tensile fracture properties 34
- 2.5 Conclusions and missing links 35

3 Experimental program to study the rate dependency of concrete tensile properties 37
3.1 Scope of the experimental program 37
3.2 Experimental program 38
3.3 Concrete and specimens 40
3.3.1 Concrete 40
3.3.2 Specimens 41
3.3.3 Conditioning the specimens 42
3.4 Nuclear Magnetic Resonance (NMR) 45
3.4.1 NMR set-up 45
3.4.2 NMR samples and tests 48
3.5 Static test set-up 49
3.5.1 The static set-up at the TUDelft 49
3.5.2 Measuring system 51
3.5.3 Non symmetric failure of specimen in static tests due to set-up 54
3.6 Split Hopkinson Bar 55
3.6.1 Description of set-up 55
3.6.2 Measuring system 56
3.6.3 Acoustic impedance 61
3.6.4 Dispersion of signals 62
3.7 Modified Split Hopkinson Bar 64
3.7.1 Description of set-up 64
3.7.2 Measuring system 68
3.7.3 Determination of stress-deformation curve 71
3.7.4 Dispersion of signals 77
3.7.5 Comparison with Metz set-up and measuring method 80
3.8 Microscopic research 81
3.8.1 Fabrication of samples 81
3.8.2 Analysis of thin- and thick-sections 84
3.9 Conclusions 85

4 Rate effects on tensile properties of normally cured concrete 87
4.1 Introduction 87
4.2 Dynamic experiments: critical review and reliability of dynamic data 87

4.2.1 Split Hopkinson Bar correction on synchronization 88
4.2.2 Linear elastic behaviour in MSHB tests 90
4.2.3 Compressive damping in Modified Split Hopkinson Bar tests 92
4.2.4 Tensile damping in Modified Split Hopkinson Bar tests 93
4.2.5 1D analysis 97
4.2.6 Summary of reliability of experimental data 98
4.3 Young's modulus 99
4.3.1 Experimental results 100
4.3.2 Results from literature and standards 101
4.4 Tensile strength 101
4.4.1 Experimental results 101
4.4.2 Results on tensile strength from literature 103
4.5 Failure behaviour 105
4.5.1 Stress-displacement and stress-deformation curves 105
4.5.2 Bumps in the Modified Split Hopkinson Bar tests 108
4.5.3 Fracture energy 109
4.5.4 Results from literature on fracture energy 110
4.5.5 Fracture characteristics 112
4.6 Analysis of loading rate effects on tensile strength: apparent and true dynamic strength 119
4.6.1 Structural inertia in the fracture zone 121
4.6.2 Crack initiation 126
4.6.3 Crack propagation 128
4.6.4 Moisture content 131
4.7 Analysis of loading rate effects on failure behaviour 131
4.7.1 Additional micro cracking 132
4.7.2 Structural inertia of fracture zone 134
4.7.3 Stress-deformation curve and bumps 143
4.8 Conclusions 149

5 Influence of moisture on rate effects on concrete tensile properties 153
5.1 Introduction 153
5.2 Experimental test program on moisture 154
5.3 Microstructure of concrete 155

5.3.1 Influence of conditioning on pore structure 155
5.3.2 Pore structure with MIP 158
5.3.3 Pore structure with NMR 161
5.4 Moisture in the specimens 163
5.4.1 Saturation level, standard method 164
5.4.2 Moisture in pores with NMR 165
5.5 Dynamic experiments: critical review and reliability of experimental data 169
5.5.1 Damping in compression and tension for the MSHB tests 170
5.5.2 Summary of reliability of experimental data 171
5.6 Young's modulus and moisture 171
5.6.1 Experimental results 171
5.6.2 Results from literature on Young's modulus and moisture 175
5.7 Tensile strength and moisture 177
5.7.1 Experimental results 177
5.7.2 Results from literature on tensile strength and moisture 180
5.8 Failure behaviour and moisture 182
5.8.1 Stress-displacement and stress-deformation curves 182
5.8.2 Fracture energy 188
5.8.3 Results from literature on fracture energy and moisture 190
5.8.4 Fracture characteristics 191
5.8.5 Corrected fracture characteristics 204
5.9 Tensile strength: influence of moisture 206
5.9.1 Inertia at micro level 207
5.9.2 Moisture in pores 208
5.9.3 Influence loading rate on strength results, high loading rate regime 224
5.10 Post peak failure behaviour: influence of moisture 225
5.10.1 Structural inertia in post peak phase; stress-deformation curves 226
5.10.2 Additional micro cracking 229
5.10.3 Micro inertia 231
5.10.4 Influence of moisture on post peak 232
5.11 Conclusions 234

6 Conclusions and recommendations 237
6.1 Objective 237
6.2 Conclusions 237
6.3 Recommendations 242

References 245

Appendix A 253

Appendix B 256

Curriculum Vitae 259

CHAPTER 1: INTRODUCTION

1.1 Background

The fires and explosions in tunnels like the Mont Blanc Tunnel (1999), the Tauerntunnel (1999) and the Yanling tunnel in China (2012), the explosion of the firework storage in Enschede (2000), the terrorist attacks on the World Trade Centre (2001), in London (2005) and in Boston (2013), and in 2015 the explosion in a chemical factory in Tianjin in China; all those catastrophes have raised questions on how to prevent the occurrence of similar incidents in the future, but also on how to limit the terrible consequences in case of such a catastrophe. Tunnels that can withstand an explosion, safe storage of high energetic materials and protection against terrorist attack have become important safety issues. To limit the consequences of disasters it is important to design future protective structures to withstand impact loading, but also to determine the failure risk of existing structures. For the design of structures, risk-assessment and the determination of safety measures to be taken in case of a disaster, knowledge on the response of materials and structures under explosive loading is necessary.

Concrete is commonly used in protective and civil structures, like tunnels and storage buildings. For the design and reliable safety assessment of such structures it is very important to know the behaviour of concrete under static loading conditions as well as under impulsive loading. To understand the behaviour of concrete under impulsive loading and to be able to predict the failure behaviour, it is important to know the influence of the loading rate on concrete strength and failure parameters and to quantify how they change with increasing loading rate. The fact that material parameters depend on the applied loading rate is called *rate dependency*.

The dynamic material properties of concrete under *tensile* loading are important parameters for the response of concrete structures under impact and explosive loading. The tensile strength and fracture energy of concrete strongly influence the failure mode and loadbearing capacity of the structure. The tensile properties influence not only the overall response, but also the local failure modes. Also, the strength and fracture energy under tensile loading are more rate dependent than in compression. Therefore, the presented experimental research is focused on the rate dependency of concrete properties in tension and not in compression.

1.2 Research objective

The mechanical response of concrete structures is often predicted with numerical material models in a finite element context. With the current computational capacity and the knowledge on numerical modelling, force and stress distributions can be calculated in concrete structures under complex dynamic loading conditions. However, most computational models use material models that are based on static loading conditions with dynamic modification factors to account for the rate dependency of concrete properties. To properly predict the response of structures under impulsive loading, the rate dependency should be included explicitly in the material model.

The reliability of rate dependent material models developed in the past depends on correct analysis of the major physical phenomena behind the rate dependency of concrete properties and the validation of the model.

To validate a physically realistic concrete material model for high loading rates, experimental data on the rate dependency of concrete tensile strength and fracture properties is needed. Data which shows the influence of the loading rate on the mechanical parameters like strength and stiffness can be found in literature for low as well as high loading rates (> 1000 GPa/s). However, data on the rate dependency of the fracture energy, and especially the fracture behaviour, is scarce. Therefore, an experimental program is defined to quantify the rate effect on the strength and stiffness at medium and high loading rates, as well as to determine the stress-displacement relation that reflects the fracture process and determines the fracture energy.

Key issue in the experimental program is the influence of the loading rate on the fracture behaviour of concrete. Besides experimental data on the rate dependency of concrete properties, it is also important to understand the physical mechanisms behind the rate effects.

The physical mechanisms will explain the change in concrete behaviour under dynamic loading conditions. An important issue in the dynamic material response is the energy dissipation during the fracture process at micro- and meso level and the influence of the loading rate on the fracture process. The level at which fracturing and, therefore, the energy absorption takes place influences the scale at which the concrete has to be modelled. The material length scale, which is an important parameter in numerical modelling is, therefore, also related to the material response and failure mechanisms.

The experimental program is part of a combined computational and experimental research project at the Delft University of Technology (TUDelft), dealing with the response of concrete under impulsive loading. The research project is defined within the collaboration program of TNO and the TUDelft on Impact Dynamics of Structures and Materials. Aim of the combined project is a physically realistic material model that includes rate effects on concrete fracture properties. The experimental findings presented in this thesis have been used by R.R. Pedersen to develop and validate a new phenomenological rate dependent material model [Pedersen 2009]. In retrospect, the developed numerical model could be used to generate output where direct measurements would be too time consuming or impossible.

1.3 Research strategy

Hitherto, the experimental research on dynamic behaviour of concrete was mainly focussed on the determination of the uniaxial tensile strength at medium loading rates (< 50 GPa/s) and high loading rates (> 1000 GPa/s). The fracture energy has not been studied extensively yet and experimental data at high loading rates (> 1000 GPa/s) is scarce. Therefore, in this experimental research not only the tensile strength, but also the fracture energy is determined at 'static' (10^{-4} GPa/s), moderate (± 50 GPa/s) and high loading rates (> 1000 GPa/s). To determine the fracture energy for the high loading rates, a new measurement method has been developed that can capture the stress-

displacement relation and, therefore, quantify the energy dissipated in the fracture process.

In addition to tensile strength and fracture energy, fracture parameters like crack lengths and width of the fracture zone are important parameters for the characterization of the dynamic material response. Without knowledge of the failure mechanisms at meso scale and the influence of the loading rate on crack patterns and damage development, a proper prediction of failure processes in concrete under impulsive loading conditions is not possible. The mechanisms causing the rate effects are not completely understood yet. One of the possible causes mentioned by other researchers [Cadoni 2001a, Ross 1996, Rossi 1992, Toutlemonde 1995a and Toutlemonde 1995b] is the moisture in the pore structure of concrete. To be able to understand the mechanisms and create new data, experiments have been carried out at different loading rates and with different moisture contents.

To summarize, the main objectives are:

- Quantify rate effect on:
  - Tensile strength
  - Stiffness
  - Fracture energy
- Study influence of loading rate on fracture behaviour by determining stress-displacement curves and softening at different loading rates and by quantifying rate effect on fracture parameters at meso level.
- Reconstruct the failure processes and understand the physical mechanisms behind the rate effect on concrete tensile properties for two different loading rate regimes, using experimental data, different moisture content and simplified analytical methods.

1.4 Outline of the thesis

The thesis consists of 6 chapters. The thesis starts with the introduction of the research objective and strategy in chapter 1. Chapter 2 will discuss the fracture process of concrete and the rate dependency of concrete fracture properties in more detail and gives an overview of the results obtained on rate dependency by other researchers. The relevant

parameters to study the rate effects are determined. Also, existing models on rate dependency of concrete properties are shortly discussed.

The experimental program is described in chapter 3 and the different test set-ups are explained. In chapter 4 the results of experiments to quantify the rate effects on tensile properties for standard conditioned concrete are presented and discussed. Also, the main causes of the rate dependency of concrete fracture properties are identified. The experimental results are compared with experimental results presented in literature. The influence of moisture on the rate dependency of concrete fracture properties is discussed in chapter 5. Experimental results of concrete with different moisture content, loaded at the previously mentioned three static and dynamic loading rates, are presented. With a simplified model based on the Stefan effect, the enhanced resistance due to the influence of moisture is quantified and the important parameters are determined.

The thesis is concluded with chapter 6. In that chapter the main results and conclusions are summarized. Also, recommendations for further research are given.

CHAPTER 2: CONCRETE PROPERTIES, FRACTURE CHARACTERISTICS AND RATE DEPENDENCY

2.1 Introduction

To understand the behaviour of concrete under impulsive loading and to be able to predict the failure behaviour, it is important to quantify the influence of the loading rate on the fracture process. Important properties to describe the fracture process are tensile strength, Young's modulus, fracture energy and characteristics of the fracture zone.

In this chapter not only theory on concrete properties, fracture characteristics and rate dependency from literature will be given, but also the results of some additional experiments are presented. These experiments were performed to apply the knowledge found in literature to the specific type of concrete or curing conditions used in the current research, or to determine the right set of boundary conditions for the experimental research.

First, in paragraph 2.2, the hydration process and microstructure formation of concrete is described. Also, the influence of curing conditions on the microstructure of concrete is discussed. This information is necessary for a proper analysis and interpretation of the results on the effects of moisture on the rate dependency of the fracture properties. The results of experimental research conducted by the author on drying damage is also presented in this paragraph, to be able to determine the appropriate drying temperature that should be used when drying specimens and to quantify the initial damage due to this drying. Theory on the fracture process is described in detail in paragraph 2.3. The fracture process of concrete is usually described by a stress deformation relation. In the research presented in this thesis two different testing techniques are used (load controlled- and

deformation controlled tests), resulting in two different types of 'stress deformation relations'; the stress-displacement curve and the stress-deformation curve. The difference is explained in paragraph 2.3.3. Also, the subsequent phases during fracture are identified and coupled to the softening curve. The relevant parameters to study the rate effects on fracture properties are given.

In paragraph 2.4 existing data on the rate dependency of concrete fracture properties are presented and the theories behind the rate dependency are described. Also, some existing models on rate dependency found in literature are shortly discussed. In this paragraph, some conclusions are drawn from the data found in literature, the 'missing links' are identified and a strategy is determined for the experimental research of this thesis.

2.2 Concrete

2.2.1 Hydration of cement

Concrete is composed of aggregates, water and cement. The cement reacts with water and forms cement paste, which is the binding agent in concrete; Cement paste binds the aggregates together to form a solid material. The choice of cement type influences the mechanical properties of the concrete. In the Netherlands, the most common cement types are Blast Furnace Slag cement and Portland cement. Portland cement consists of grinded Portland cement clinker. Blast Furnace Slag cement also consists of Portland cement clinker, but the hydraulic material blast furnace slag is added. The raw material for the production of Portland clinker mainly consists of limestone ($CaCO_3$), silica (SiO_2), alumina (Al_2O_3) and iron oxide (Fe_2O_3). The hydraulic clinker minerals are formed through mixing and heating of the raw materials (up to approximately 1450°C). The main clinker minerals are tricalcium silicate (C_3S), dicalcium silicate (C_2S), tricalcium aluminate (C_3A) and tetracalcium aluminoferrite (C_4AF).

The hydration process is described by many researchers [Reinhardt 1985, Souwerbren 1998, Van Breugel 1997]. First, the C_3A will go into solution and reacts with the added gypsum to form tricalcium sulphate, also called ettringite. After this first rapid reaction a stage of low reactivity follows, the dormant stage. When the hydration continuous, the C_3S minerals hydrate to form calcium silicate hydrates (CSH). With the formation of this long

fibred CSH, the cement grains are connected with each other and the hardening of the cement paste starts. C_2S also forms calcium silicate hydrates, but a little later. During hydration, calcium hydroxide (CH) is also formed in the water rich pores of the concrete, but the contribution to the strength is less than the other hydration products. Calcium Silicate Hydrates (CSH) are mainly responsible for the strength of the cement paste. Both the hydrates from C_3S and C_2S are essential for the formation of a strong material. The reaction products of the other two clinker minerals, C_3A and C_4AF, have a considerably lower strength than that of C_3S and C_2S.

Table 2.1 Clinker minerals and chemical composition [Reinhardt 1985, Souwerbren 1998].

Name	Chemical composition	Abbreviation
Tricalcium silicate	$3CaO \cdot SiO_2$	C_3S
Dicalcium silicate	$2CaO \cdot SiO_2$	C_2S
Tricalcium aluminate	$3CaO \cdot Al_2O_3$	C_3A
Tetracalcium aluminoferrite	$4CaO \cdot Al_2O_3 \cdot Fe_2O_3$	C_4AF

A certain amount of water is necessary for the start and progress of the hydration process. The amount of water is usually expressed as the water/cement ratio (w/c-ratio). Full hydration of the cement is obtained when 40% of the weight of cement is added as water; 25% of this water will be chemically bound and 15% physically bound. Theoretically, a w/c-ratio of 0.4 should lead to full hydration of the cement. In reality, a w/c-ratio of more than 0.4 does not guarantee a full hydration, because the water might not reach the core of all the cement particles. A higher value for the w/c-ratio is often used for better workability. The w/c-ratio affects the porosity of the cement paste and has a direct influence on the mechanical properties of concrete.

The porosity of concrete is an important factor. Both strength and durability are directly influenced by the porosity.

2.2.2 Pore structure

The pore structure depends on the degree of hydration and the w/c-ratio. As stated in the previous paragraph, a w/c-ratio of 0.4 will theoretically lead to full hydration of the cement.

If the w/c-ratio is larger than 0.4, the excess water remains as free water in the cement structure in capillary pores. In Figure 2.1 the effect of the w/c-ratio on the pore size distribution is shown. The pore size distribution of Figure 2.1 is determined using a so called solvent replacement technique. Solvent replacement techniques are effective specimen preparation techniques to determine the pore structure [Aligizaki 2006].

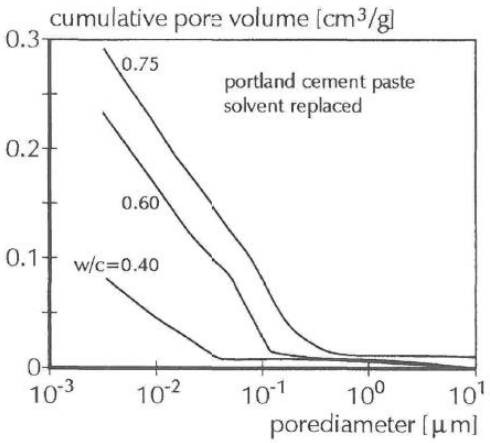

Figure 2.1 Effect of w/c-ratio on the pore size distribution and pore volume of hardened cement paste [Van Mier 1997] according to [Hansen 1986].

During hydration the pore structure changes. First, a lot of water is available and a large number of capillary pores are present. During hydration the capillary pores are filled with hydration products and decrease in size until they eventually disappear. Due to the decreasing amount of capillary pores, the porosity will decrease during hydration. The hydration will stop when all the cement particles are hydrated or when water is no longer available for hydration. When water is added in a later stadium, the hydration can start up again.

The pores in the hardened cement paste have different sizes. Very small pores (nanometre range) are present in the cement gel itself, the so called gel pores. Capillary pores (micrometre range) are developed between the CSH particles. Even larger pores (millimetre range) may develop when air is entrapped during mixing of the concrete. Especially the larger pores (air voids and capillary pores) have a substantial effect on the mechanical properties. Also, it is believed by several researchers that the water in the

pores is the main cause of the rate dependency of fracture properties for loading rates smaller than 50 GPa/ [Ross 1996, Rossi 1990a, Toutlemonde 1998]. The pore structure and moisture content are, therefore, very important for the explanation of the rate effects on the fracture properties of concrete.

The pores can be subdivided into different size categories. There is general agreement about the size of the different pores, although the boundaries of the categories differ for several researchers [Mindess et al. 2002, Aligizaki 2006, Van Breugel 1997, Bazant et al. 1982, Aligizaki 2006], see Table 2.2. The boundaries of the different categories are not strict and dependent on the shape of the pores.

Table 2.2 Size and categories of pores in concrete by different researchers and the author [Mindess et al. 2002, Bazant et al. 1982, Metha 1986].

Concrete	Gel pores [nm]	Capillary pores [µm]	Air voids [mm]
Mindess et al.	< 10	0.0025 - 10	0.1 – 1
Wittmann/Bazant	0.4 – 2.4	0.0024 - 50	0.05 – 1
Metha	1 – 3	0.01 - 5	0.05 – 1
Author	1 – 50	0.05 - 10	> 0.01

Several researchers have investigated the pore size distribution and the different methods to determine the distribution [Ye 2003, Aligizaki 2006, Van Breugel 1997]. It has been concluded that the different methods all have some disadvantages and that caution is needed for the interpretation of the results. According to Aligizaki [Aligizaki 2006] there are two methods that can be used for the determination of the pore size distribution of gel- and capillary pores, sizes ranging from 1 nm to 10 µm. These methods are the Nuclear Magnetic Resonance method (NMR) and Mercury Intrusion Porosimetry (MIP). Both methods will be used by the author to determine the pore size distribution of the different concretes used in the presented research.

2.2.3 Cement type and influence on pore structure

Curing conditions and cement composition influence the porosity and pore size distribution. In this paragraph the influence of the cement composition on the pore

structure is described. The next paragraph deals with the influence of curing conditions, like wetting, elevated temperatures and drying.

For the presented research, the two most common types of cement are chosen to investigate the influence of the pore structure on the rate dependency of the concrete fracture properties: Blast Furnace Slag (BFS) cement concrete and Portland cement concrete. Blast Furnace Slag cement consists of Portland cement clinkers, but the hydraulic material blast furnace slag is added. Due to this blast furnace slag, the hydration process of BFS cement is slower than Portland cement. The hydration also continues longer and the composition of the hydration products are somewhat different, i.e. a denser microstructure is formed. According to Van Mier [Van Mier 1997] and Souwerbren [Souwerbren 1998] the microstructure of Blast Furnace Slag cement concrete is denser than that of Portland cement concrete, although the total porosity is higher.

The total porosity is not evenly distributed in the hardened cement paste [Van Mier 1997]. Due to the presence of aggregate particles, zones with different porosity are created at the interface of the cement matrix and these aggregates. The aggregate particles often have a very low porosity and no exchange of water will occur between the aggregate particle and the cement paste during hydration. Generally, a layer of CH crystals is formed at the surface of the aggregate particles. The interface zone is very porous and is called the Interfacial Transition Zone (ITZ). The (bond) strength of this ITZ is normally regarded as the weakest link in concrete and, therefore, influences the total strength of the material considerably.

2.2.4 Conditions and the influence on pore structure

Besides the cement composition, the pore structure of concrete is also influenced by the curing conditions used to store, dry or wet the specimens. With a water-cement ratio (w/c-ratio) of 0.5 (as has been used for the experiments presented by the author) theoretically all cement particles should be hydrated and capillary pores are formed which hold the additional water. In practice, however, it is possible that unhydrated cement particles are still present in the cement paste, when curing with water is started. The water that is added when mixing concrete is not always able to reach the core of the (partly) unhydrated cement particles. These unhydrated particles can be activated when rewetted. Therefore,

the conditions in which the specimen are kept before the day of testing (at approximately seven weeks) considerably influence the final pore structure. For the interpretation of the experimental results, it is important to determine what the effect of the different curing conditions is on the final pore structure of the concrete samples.

In the presented research, the influence of moisture on the rate dependency of concrete fracture properties is studied. For this study, specimens are cured under different conditions. Concrete specimens have been submersed in water, kept under controlled conditions of 20˚C and 50% RH ('Normal' condition) or dried in an oven. To check whether the wet curing condition influences the microstructure of concrete used in the presented research, the pore structures of the concrete specimens cured under different conditions are studied and visualized with an Environmental Scanning Electron Microscope (ESEM).

The wet concrete specimens have been submersed in water at an age of 28 days until the day of testing. The ESEM results for Portland cement concrete show that due to the presence of water the un-hydrated cement particles start to hydrate again, filling the pores and creating a denser structure. Figure 2.3 shows this denser cement structure of wet concrete compared to the specimens kept under controlled conditions of 20˚C and 50% RH (see Figure 2.3 compared to Figure 2.2). The black areas are the pores, the dark gray areas are the aggregate particles and the lighter gray area with white spots is the cement paste with unhydrated cement particles (white spots). The higher density of the re-wetted concrete is especially clear around the aggregate particles.

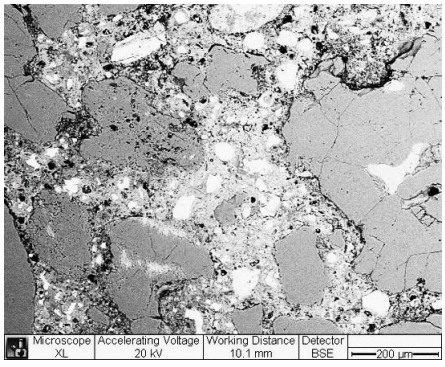

Figure 2.2 Microstructure of Portland cement concrete kept at 50% RH and 20°C, determined by ESEM.

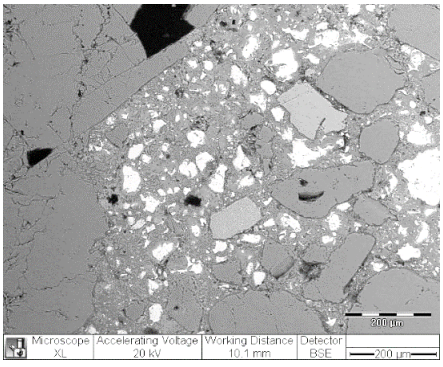

Figure 2.3 Microstructure of wetted Portland cement concrete, determined by ESEM.

The denser and more homogeneous structure of re-wetted concrete can theoretically lead to a higher tensile strength. Experimental results on static tensile strength of wet concrete, however, do not support this conclusion. The data from several authors [Cadoni 2001b, Ross 1996, Hordijk 1990, Hordijk 1991] show that the static tensile strength decreases for wet concretes. One of the possible explanations suggested by Wittmann [Wittmann 1972] is based on the Munich Model from Wittmann [Wittmann 1977]. The Munich model describes the pore structure of concrete as CSH particles with primary and secondary bound water (see Figure 2.4). The primary bound water is physically bound to the surface of the CSH particles, whereas the secondary bound water is bound by VanderWaals forces. Wittmann proposes [Wittmann 1972] that the presence of water in the gel pores increases the distances between the CSH-molecules of the concrete and, therefore, decreases the internal VanderWaals forces that hold the structure together. This means that lower force is needed to fracture the structure and, therefore, the static strength is lower.

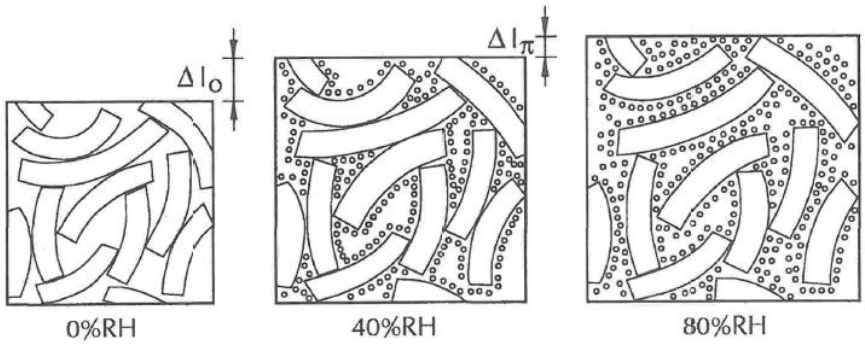

Figure 2.4 Munich Model from Wittmann [Wittmann 1977], Figure according to [Van Mier 1997].

2.2.5 Drying damage

To study the influence of moisture on the rate dependency of concrete fracture properties, samples are needed without moisture. This means that the samples have to be dried in an oven. In literature, a drying temperature of more than 100°C is often chosen to remove the moisture from concrete specimens [for instance Hordijk 1991, Aligizaki 2006, Toutlemonde 1998, Ross 1996, Rossi 1990a, Zheng 2004a]. However, drying at high temperatures can create damage in the specimen [Bisschop 2002].

The elevated temperature in a drying oven can lead to a better hydration degree, provided that enough water is available. This could result in a denser structure of the cement paste. However, when the temperature is very high and the environment in the oven is very dry (very low relative humidity) damage can occur. There are two different causes for damage at high temperatures and low humidity's:

(1) damage due to the difference between the thermal expansion coefficients of aggregate particles and cement paste.
(2) damage due to drying shrinkage of the cement paste.

The drying shrinkage is caused by two different mechanisms [Bisschop 2002]:

- Damage due to self-restraint.
  When specimens are dried a moisture gradient develops: the outer zone of the specimen dries while the inner core is still wet. Due to the moisture gradient, the outer part of the specimen will be in tension, while the core is in compression. The wet inner core will restrain the tension from the shrinking outer zone. When the developed stresses are higher than the strength of the concrete, drying damage will occur in the outer zone of the specimen.
- Damage due to aggregate restraint.
  Aggregate restraint occurs in cement-based composites with aggregate particles that have a higher modulus of elasticity than the cement paste itself. The aggregates will restrain the shrinkage of the cement past and, therefore, cracking can occur.

In most cases, the drying damage is caused by a combination of self- and aggregate restraint.

2.2.6 Drying at what temperature?

For the dynamic and static tensile test presented in this research, specimens are needed that are dry, but preferably also not damaged. Any damage introduced during drying can influence the strength results and obscure the analysis of the rate dependency of the tensile strength or fracture energy. The author wants to minimize the damage that can be introduced due to drying at high temperatures to be able to properly compare the results from the specimens with different moisture contents. Therefore, tests are conducted to determine the most effective drying temperature and relative humidity.

ESEM tests were conducted to determine the effect of the different drying temperatures and low relative humidity's on the microstructure of the concrete. Nuclear Magnetic Resonance tests were conducted on specimens to determine whether the specimens were completely dry. The measured temperatures and relative humidity's in the different ovens where the different specimens were kept are:

- 35°C and a relative humidity of 20%;
- 50°C and a relative humidity of 15%;
- 105°C and a relative humidity of 2%.

The different ESEM samples are visually inspected for drying damage at the surface of the specimens. The results show that drying damage can be found in the specimens dried at 50°C and 105°C. In Figure 2.5 and Figure 2.6, the damage in case of these two drying temperatures is visualized. The damage in Portland cement concrete dried at 105°C is much more severe than the damage in concrete dried at 50°C. When drying occurs at 105°C, the cement paste is separated from the aggregate particles (see Figure 2.6). The thermal expansion coefficients of the aggregate particles and the cement paste are different, causing stresses in the cement paste and damage around the particles. Also, the cement paste shrinks on drying, while the aggregate particles keep their original volume, causing cracks around the aggregate particles (see also literature of Bisschop [Bisschop 2002] in previous paragraph).

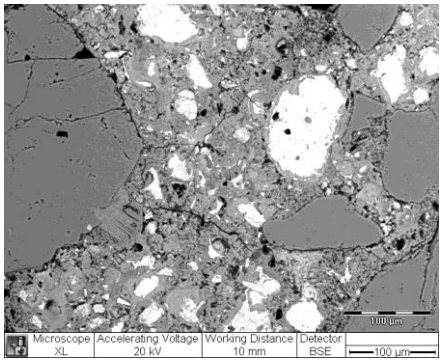

Figure 2.5 Surface drying damage in concrete dried at 50°C, determined by ESEM.

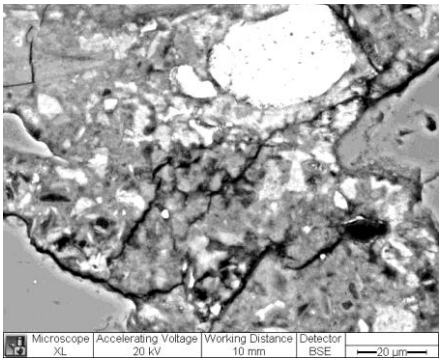

Figure 2.6 Detail of surface damage in concrete dried at 105°C, cracks between aggregates and cement paste, determined by ESEM.

Thin sections are made to quantify the damage found. Thin sections are very thin slices of concrete, used to study cracks in concrete. For more detailed information on thin sections and the method of fabrication, see paragraph 3.8.1. The different thin sections show that in all dried samples small damage around large particles can be observed, even in the samples dried at 35°C and the samples kept under 20°C and 50% RH.

The drying damage of the specimens was quantified by digitalizing the fracture patterns and then analyzing the fracture patterns by hand and visual (see also paragraph 3.8.2). The total length of the cracks was measured and the depth of the damage, measured from the surface of the specimen, was determined. The depth of the damage from the surface and the total length of cracks found in the thin sections are summarized in Table 2.3 for the different curing conditions.

Table 2.3 Drying damage of specimens cured under different conditions, Portland cement concrete; number of cracks, total and average crack length (analysis from microscopic research on thin sections), age 7 weeks.

Concrete	Damage depth [mm]	Number of cracks [-]	Total crack length [mm]	Average crack length [mm]
Dry 105	0.6	44	9.0	0.20
Dry 50	0.3	26	5.8	0.22
Dry 35	-	34	7.1	0.21
Normal	-	38	6.6	0.17
Wet	-	21	3.2	0.15

The thin sections of the samples dried at 35˚C, 50˚C and 105˚C show that the damage of the drying process is superficial. The depth of the damage from the surface is dependent on the drying temperature. For the concrete samples dried at 50°C, damage is found at approximately 0.3 mm from the surface and for the samples dried at 105°C at approximately 0.6 mm. The number of cracks found in the sample dried at 105°C is higher than in the sample dried at 35°C or 50°C (see Table 2.3). The 'Normal' (kept at 20°C and 50% RH) and 'Wet' (submersed in water) conditions are used as a reference.
Literature supports the conclusion that the damage due to drying remains superficial, even at a drying temperature of 105°C [Bisschop 2002] (crack depth < 8 mm).

For the tests performed in this research, completely dry samples are needed. The question remains whether the lower drying temperatures of 35°C and 50°C, which cause less damage due to drying, will still result in dry samples. Therefore, Nuclear Magnetic Resonance tests have been conducted on samples subjected to the previously described conditions in the different ovens. The 'Normal' condition (kept at 20°C and 50% RH) is again used as a reference.

The NMR results are visualized in Figure 2.7 and Figure 2.8. The volume of water is proportional to the NMR output variable (a.u.). The pore size is linked to the relaxation time T_2. For a detailed description of the NMR method and the different parameters, see paragraph 3.4. In Figure 2.7 the moisture distribution for the 'Normal' condition shows the filled gel pores ($T_2 = 10^2 - 10^{3.1}$), the filled capillary pores ($T_2 = 10^{3.1} - 10^{3.8}$) and the filled air voids ($T_2 = 10^{3.8} - 10^5$). The results from the NMR research show that the specimens dried at 50˚C and 105˚C are completely dry (see Figure 2.8), while the specimen dried at 35˚C contains almost the same amount of water as the specimen that was kept under controlled conditions of 20˚C and 50% RH (see Figure 2.7).

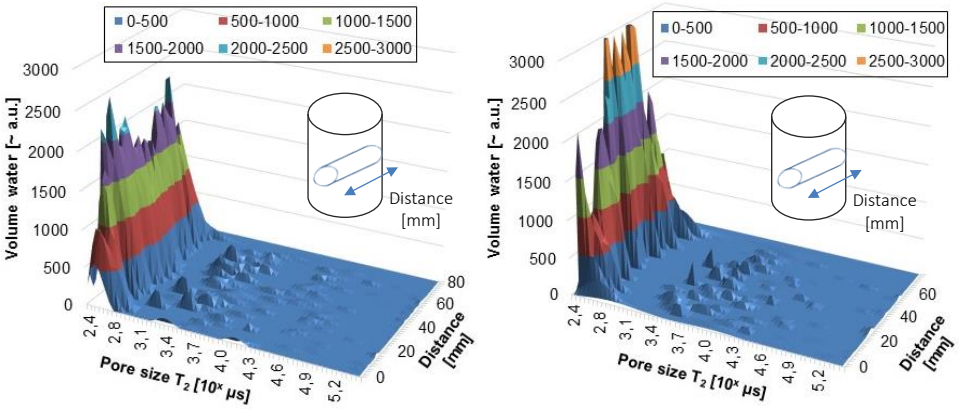

Figure 2.7 Moisture distributions measured with NMR method, Volume of water vs Pore size and distance in specimen. Portland cement concrete kept at 20°C and 50% RH (left) and dried at 35°C and 20% RH (right).

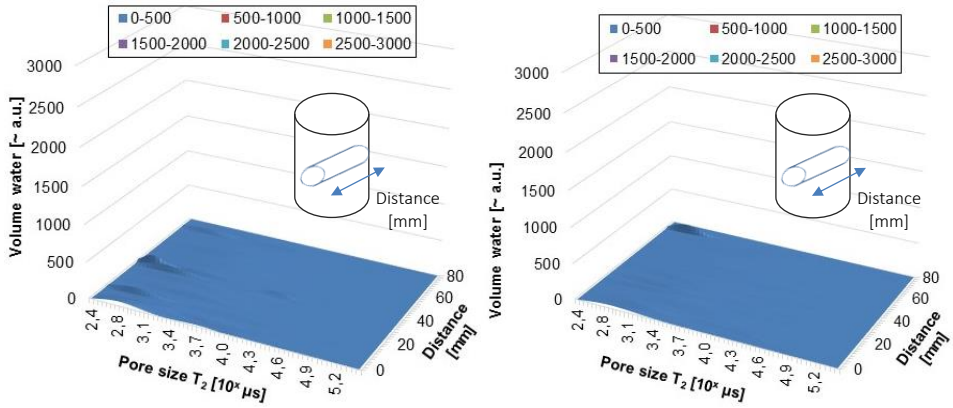

Figure 2.8 Moisture distributions measured with NMR method, Volume of water vs Pore size and distance in specimen. Portland cement concrete dried at 50°C and 15% RH (left) and dried at 105°C and 2% RH (right).

The conducted microscopic research on specimens dried at drying temperatures of 105˚C, 50˚C and 35˚C shows that drying at 105˚C will lead to drying damage. Drying at 50˚C will lead to small and superficial damage and drying at 35˚C will not lead to any visible damage. When specimens are dried at 35˚C, they are not completely dry at the day of testing. Therefore, a temperature of 50˚C is believed to be the best option to dry the specimens. When drying at 50˚C, the samples are completely dry and the induced damage is minimal. Based on the performed tests, a temperature of 50˚C is chosen by the author to dry the specimens for the experimental research.

2.3 Fracture of concrete in tension

The fracture process of concrete in tension is studied and described extensively in literature [Hillerborg 1985, Bazant 1983, Hordijk 1991, Van Mier 1997, Weerheijm et al. 2013, Shah et al. 1995]. In this section a summary is given of the concrete response up to failure, as a reference for the dynamic behaviour of concrete.

2.3.1 Meso and micro level

Most of the classical material models are based on the assumption that the material can be represented as a continuum. However, concrete consists of aggregate particles, sand, cement and pores. Therefore, the heterogeneous structure of concrete should be taken

into account. The scale at which the concrete can be modelled can be the macro level, meso level and micro level. According to Van Mier [Van Mier 1997] the smallest level, the micro level, shows the structure of the (hydrated) cement grains and the pores. The scale is about the micro-meter scale (10^{-6} m). When concrete is considered at meso scale ($\approx 10^{-3}$ m), individual sand and aggregate particles can be distinguished. Also, large pores are found. The interface between aggregate and cement matrix (ITZ) plays an important role at this scale. For the macro scale ($\approx 10^{1}$ m), the concrete is considered to be a continuum. This means that no internal structure is recognized and the material has the same properties at each point of the concrete specimen. The different scales are summarized in Figure 2.9.

In this thesis, the observations and analysis of the results mostly take place at meso level. Some mechanisms are also considered at micro level, for instance the inertia effects.

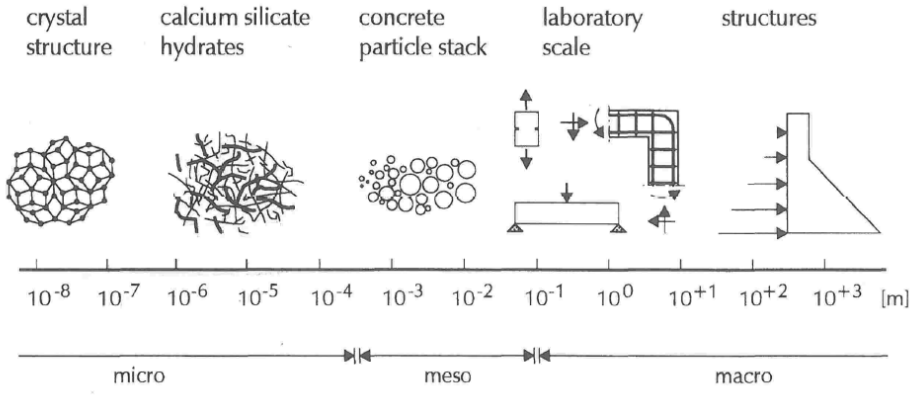

Figure 2.9 The different scales of observation for concrete, from macro to micro scale, according to [Van Mier 1997].

2.3.2 Failure process in tension

The concrete response up to failure under tensile loading is dictated by its heterogeneous composition and starts with the initiation of cracks at initially existing damage. The mechanical response of concrete is mainly dominated by the response at meso scale which is characterized by aggregates, mortar matrix, the ITZ, the larger pores and initial damage.

Due to differences in stiffness of the aggregate and cement paste and the induced stresses during hardening, initial micro cracks and defects exist. Damage will start to grow when the strength of the material is locally exceeded at these micro cracks and defects. Energy will flow into the fracture zone and is absorbed during fracture. Due to the heterogeneity of concrete the fracture zone does not consist of one single crack but exists of multiple cracks. These (micro) cracks are formed in the zone in front of the macro crack, the fracture process zone (FPZ). First the micro cracks start to grow, interfering with each other, with defects and aggregates. Due to the aggregate particles the cracks tend to 'avoid' each other and crack overlapping or crack branching takes place [see Van Mier 1997]. After a certain time the micro cracks coalescence to form a dominant macro crack. This process is well represented in the fictitious crack model of Hillerborg [Hillerborg 1985], see Figure 2.10.

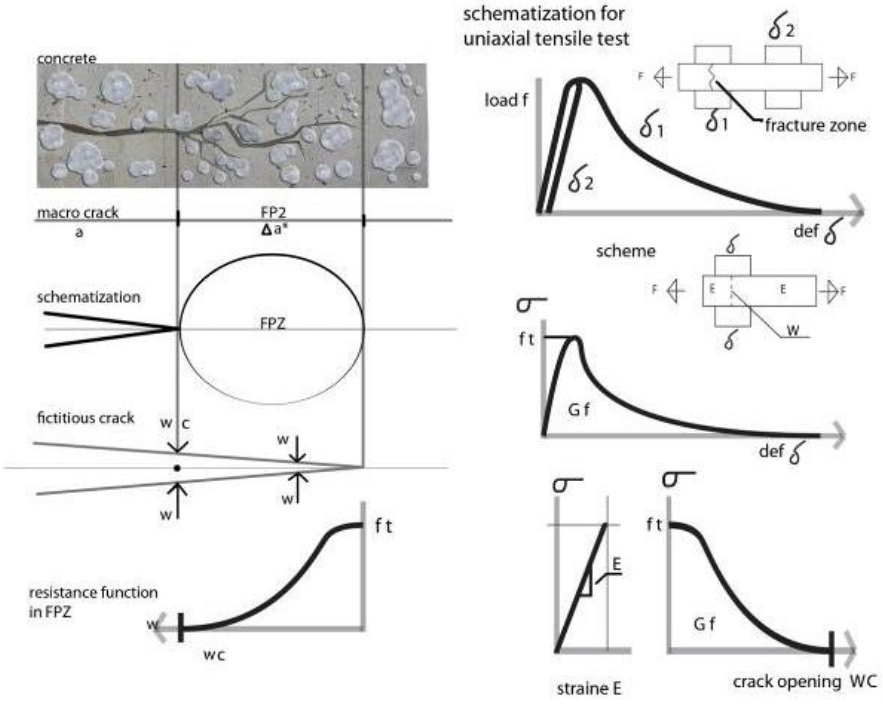

Figure 2.10 The fictitious crack model according to Hillerborg [Hillerborg 1985] figure from [Weerheijm 2011].

In the fictitious crack model the crack initiation is controlled by the strength, f_t. According to Hillerborg [Hillerborg 1985], the fracture energy is the energy needed during the fracture process. This energy is absorbed in the fracture zone and is equal to the area under the load deformation relation.
To recall and to summarize, the following definitions are suggested:

- The fracture process zone (FPZ) is the zone in front of the (macro) crack tip and contains multiple micro cracks (see also Figure 2.10).
- The fracture zone (FZ) is the zone that covers the material that is involved in the energy exchange during the fracture process. The FZ contains the dominant macro crack and the accompanying collection of micro cracks. When in this thesis the word 'fracture' is used, this refers to the fracture zone. A fracture can consist of multiple cracks.
- A 'crack' is a single crack with one defined length and width.
- The fracture energy G_f is the energy absorbed in the fracture zone and equals the area below the load-deformation curve for uniaxial tensile loading.

The tensile facture energy G_f is discussed by many researchers. However, the definition of fracture energy and method to determine the fracture energy is not consistent, which makes it hard to compare data [Weerheijm 2011]. In the next section the definition of fracture energy used in this thesis is given. Also, it is explained how to interpret the stress-deformation relation.

2.3.3 Stress-displacement and stress-deformation curves

The response of concrete up to complete failure is represented by a stress-deformation relation. In tension pre peak non-linearity starts at about 80% of the maximum strength, when matrix fracture starts [Weerheijm et all. 2013]. At this point micro cracks are initiated. These micro cracks grow with increasing load. When the maximum stress is reached, the micro cracks start to coalesce and the macro crack starts to form. The macro crack proceeds until finally total fracture is reached. The macro crack is preceded and surrounded by micro cracks.

The above described failure process is reflected in the stress-deformation relation. From a uniaxial deformation controlled static test, a complete stress-deformation relation can be

obtained (see for instance the static curve from Figure 2.11 (red curve) and the stress-deformation relation from Hillerborg in Figure 2.10). The ascending branch reflects the linear elastic behaviour of the material. The Young's modulus is determined by the slope of the ascending branch between $0.1f_t$ and $0.8f_t$. At about $0.8f_t$ damage starts and non-linear behaviour can be expected. When substantial non-linear behaviour has taken place before the maximum strength is reached, the peak of the stress-deformation relation is not sharp, but will be more rounded or 'blunt'.

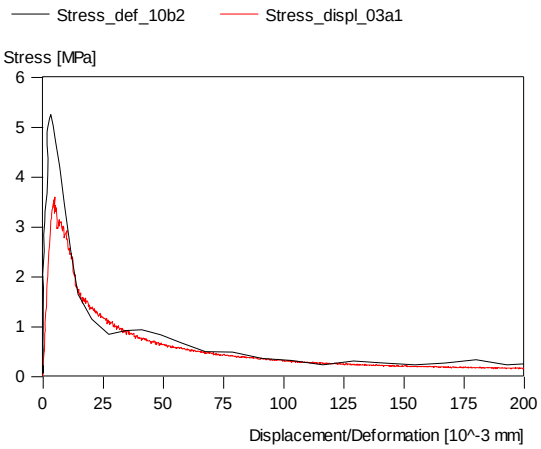

Figure 2.11 Stress-displacement curve for static test 03a1 (red), compared with stress-deformation curve for dynamic SHB test 10b2 (black).

The failure behaviour of concrete is captured in the softening part, the second part of the stress-deformation relation (descending branches). The failure or softening behaviour of concrete is usually schematized as presented in Figure 2.12, with two branches. The first steep branch is coupled to the micro cracking phase (branch I), when micro cracks grow and coalesce. The second long tail branch (branch II) represents the formation of the macro crack and final failure.

The fracture energy G_f can be obtained from the softening relation. As stated before, according to the fictitious crack model (FCM) of Hillerborg [Hillerborg 1985] the area under the stress-deformation relation equals the fracture energy. Following the FCM, the measured stress-deformation relation can be divided into an elastic part and a crack

opening part (see Figure 2.10). The area under the stress-crack opening curve also represents the fracture energy.

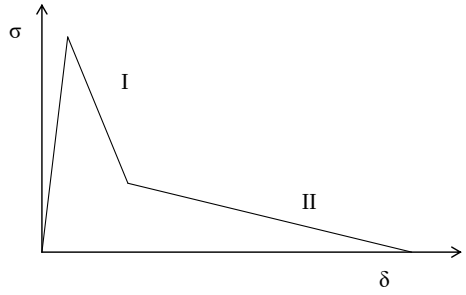

Figure 2.12 Schematized stress-displacement relation; two softening branches I and II.

Both curves, i.e. the stress-deformation relation and the stress-crack opening relation, are used in this thesis. The static uniaxial tensile tests are deformation controlled tests and, therefore, a complete stress-displacement curve can be determined. The displacement measurements in the static tests consist of two parts; the contribution of the crack opening and the contribution of the elastic deformation over the total measuring length. For the dynamic tests, the elastic deformations are subtracted from the total deformations, resulting in a stress-crack-opening curve or stress-deformation-of-fracture curve. For the static tests, the elastic deformation and elastic unloading after fracture are not specifically measured and they can, therefore, not be subtracted from the total displacement measurements. To emphasize the difference between the curves of the different tests, the curves from the static uniaxial tensile tests are named stress-displacement curve and the curves from the dynamic tensile tests stress-deformation-of-fracture curve, in short stress-deformation curve (see also Figure 2.13). The author has not chosen the term 'stress-crack-opening-curve' because this would imply that only one crack is formed which 'opens', while in reality the fracture zone consists of multiple cracks and deformation is spread over this fracture zone.

Although the method to obtain the static stress-displacement curves is different from the method to obtain the dynamic stress-deformation curves, according to Hillerborg the area under both the static (Figure 2.13a) and dynamic (Figure 2.13c) curves represents the fracture energy (see also Figure 2.10 and Figure 2.13).

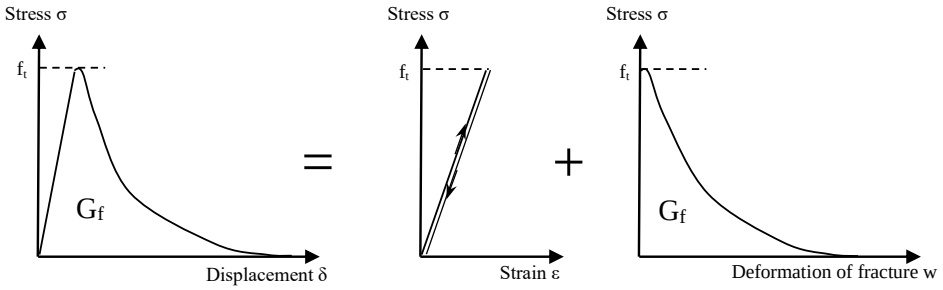

(2.13a) (2.13b) (2.13c)

Figure 2.13 Stress-displacement curve and stress-deformation-of-fracture curve or stress-deformation curve.

2.3.4 Parameters that influence failure of concrete in tension

The failure process of concrete in tension is described in the previous sections. The main properties to describe the failure behaviour of concrete in tension are: the tensile strength f_t, the tensile fracture energy G_f and the softening behaviour as captured in the stress-displacement and stress-deformation curves. The fracture time t_{frac} is also an important property. During the fracture time, energy exchange can take place in the fracture zone to form micro and eventually macro cracks.

Other important parameters that influence the fracture behaviour are the pore structure, the concrete composition and the curing conditions. The effect of curing conditions has been described in the paragraphs 2.2.4 and 2.2.5. The ratio between cement, water and aggregate particles highly dictates the properties of concrete. For instance, larger aggregate particles will increase the fracture energy G_f [Van Mier 1997]. In ordinary concrete, around aggregate particles the cement paste is less dense (ITZ). The (micro) cracks will start and propagate in these weaker zones. Therefore, in case of coarse aggregates, crack branching becomes more important and the fracture energy will increase.

The water-cement ratio also influences the static tensile strength (see Figure 2.14). In mixtures with high water-cement ratios, more capillary pores are created during hydration. This makes the cement paste weaker and lowers the tensile strength.

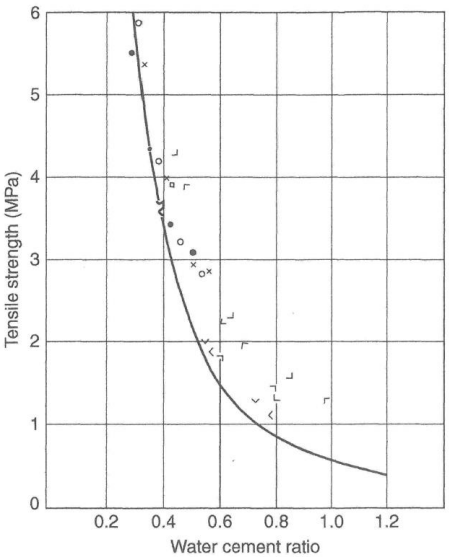

Figure 2.14 Influence of water-cement ratio on the static tensile strength of mortar of various compositions [Graf et al. 1960], figure reprinted from [Weerheijm et al. 2013].

With the above mentioned properties the failure behaviour of concrete is largely captured. However, under the influence of the loading rate, the failure behaviour of concrete changes. The stresses in front of the crack tip change with increasing loading rate. Inertia effects at meso- and micro level can become important. Also, several researchers mentioned the influence of moisture on the rate dependency of concrete fracture behaviour [Cadoni 2001b, Rossi 1992, Toutlemonde 1995a]. For a proper prediction of the failure behaviour of concrete under impact loading it is, therefore, important to quantify and understand the influence of the loading rate on the fracture properties of concrete loaded in tension.

The following mechanical properties are experimentally studied to characterize the fracture behaviour of concrete:

- Tensile strength;
- Fracture energy;

– Softening behaviour.

To quantify the influence of the loading rate on the mechanical properties and to identify the mechanisms behind the rate dependency of concrete, the following parameters have to be varied:

– Loading rate;
– Pore structure/ water-cement ratio;
– Moisture content.

The rate dependency of concrete properties and the influence of moisture on this rate dependency will be discussed in the next paragraph.

2.4 Rate dependency of concrete

Concrete is probably one of the most rate dependent structural materials. Especially in tension a pronounced increase of the fracture properties is found for loading rates exceeding 50 GPa/s [Brara 2006, Cadoni 2001b, Chen 2011, Erzar 2010, Klepazcko 2001, Schüler 2004, Weerheijm 2007]. For concrete, two regimes can be distinguished from literature; one for loading rates ranging from static (10^{-4} GPa/s) to an intermediate loading rate of 50 GPa/s. And a second regime with a steep increase in fracture properties beyond loading rates of 50 GPa/s. These regimes are clearly visible in Figure 2.15. Figure 2.15 also shows the loading rate of for instance a gas explosion or an earthquake, to be able to refer the loading rates used to situations in practice.

In this paragraph the influence of the loading rate on the failure behaviour is discussed and the experimental data found in literature presented. Also, some models on rate dependency are shortly addressed.

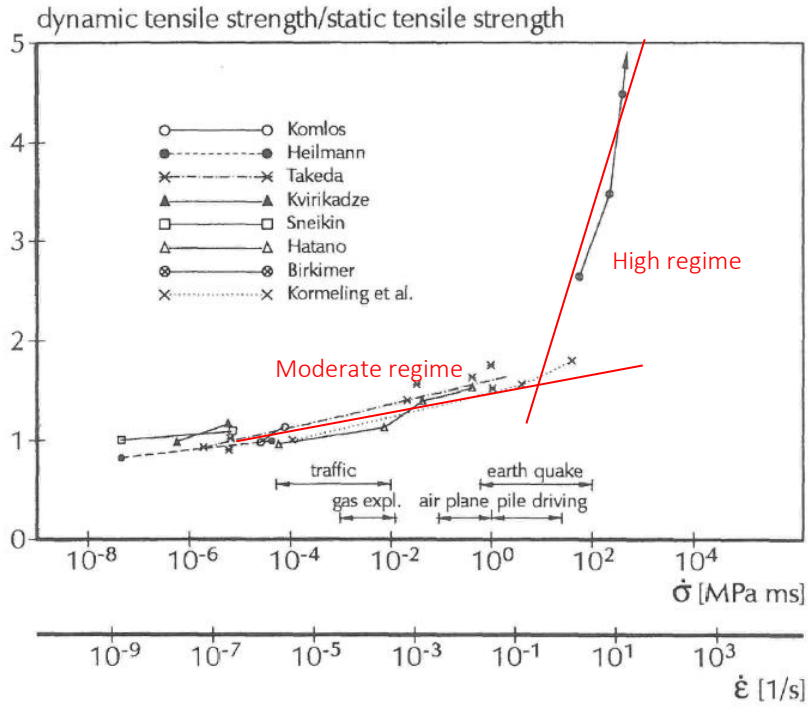

Figure 2.15 Effect of the loading rate on the relative tensile strength of concrete [Van Mier 1997].

2.4.1 Failure process at high loading rates

The fictitious crack model of Hillerborg [Hillerborg 1985] can properly describe the failure behaviour of concrete in tension, as mentioned in the previous paragraph 2.3.2. In this model, damage starts from the largest defects. When loading rates are low, the load will not change much during failure and the size of the defects that will be activated first, does not change. When damage starts to grow from these particular representative defects, the adjacent material will release stress and no other, smaller defects are initiated.

When loading rates are higher, as is the case in dynamic tests, the failure process changes [Weerheijm 1992, Weerheijm et al. 2013]. According to the model of Weerheijm [Weerheijm 2006], when the loading rate increases, also smaller defects become critical and initiate crack formation. This will lead to more (micro) cracking in the fracture zone and an increase in fracture energy.

Damage starts when the maximum strength is (locally) reached. This maximum strength is influenced by the loading rate. Additional resistance at meso and micro level against crack growth cause an increase of the maximum tensile strength at high loading rates. This additional resistance is, for instance, due to water in the pores or due to micro inertia effects.

Although the *mechanisms* behind the rate dependency of the tensile strength and initial failure process are indicated by several researchers (see paragraph 2.4.2), the influence of the loading rate on the softening curve or fracture energy has not been quantified extensively so far. Especially the influence on the fracture characteristics like fracture lengths and width of the fracture zone is not specified yet. In the next sections the data from literature on tensile strength and fracture energy at high loading rates is presented. Also, the underlying mechanisms according to literature are described.

2.4.2 Tensile strength

The tensile strength is one of the properties to describe the fracture behaviour of concrete under tensile loading. The tensile strength appears to be very rate dependent. Also, the tensile strength is the fracture property which is the easiest to determine experimentally. Therefore, most research on the rate dependency of concrete properties is focussed on the tensile strength. Many researchers have determined the influence of the loading rate on the compressive or tensile strength of concrete [Brara 2006, Cadoni 2001b, Chen 2011, Rossi 1992, Erzar 2010, Klepazcko 2001, Schüler 2004, Weerheijm 1992, Körmeling 1980, Körmeling 1984, Zielinsky 1981]. Loading rates exceeding 1000 GPa/s are successfully reached by several researchers who study the tensile strength [Schüler 2004, Weerheijm 2001, Erzar 2010, Klepaczko 2001].

The results on tensile strength found in literature are presented in Figure 2.16, supplementary to the results presented in Figure 2.15. The test data shows the two regimes. Obviously, the scatter in the results is large. The high scatter is most probably caused by the difference in test set-up, concrete mixture, diagnostic techniques, specimen size and moisture content.

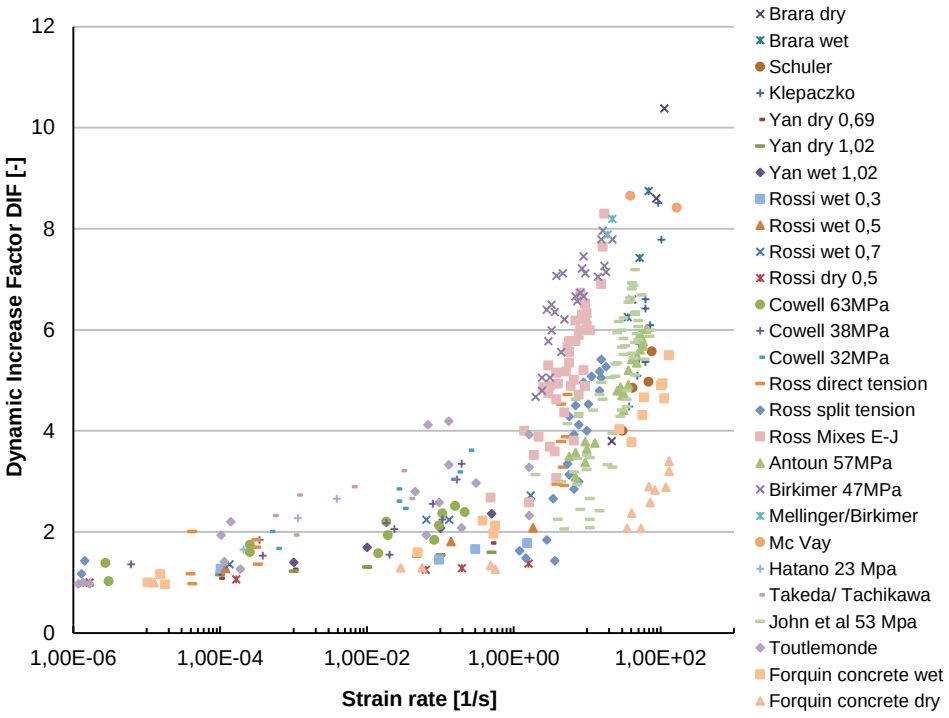

Figure 2.16 Experimental data on the DIF for tensile strength as a function of the strain rate [Weerheijm et all 2013].

The mentioned cause behind the rate effects on tensile fracture properties is diverse. Ross and Rossi, among others, believe that moisture in the pores or/and voids plays an important role in the rate dependency of concrete tensile strength [Rossi 1997, Ross 1996, Toutlemonde 1998, Zheng 2004a].

Another cause mentioned for the tensile strength increase in the high loading rate regime is micro inertia effects in the fracture process zone [Weerheijm 1992, Zheng 2004a, Cotsovos 2008b]. With increasing loading rate inertia effects at micro level can become dominant. Inertia affects the stress fields in the heterogeneous material, around the material defects and the (micro) cracks. Stress singularities decrease and damage initiation and growth might be delayed. This can cause an increase in the maximum strength reached. Structural inertia effects in the fracture process zone are also causing the tensile strength to increase, according to Ozbolt [Ozbolt 2013].

Cadoni, on the other hand, believes that the cause for the strength increase can be found in multiple fracture [Cadoni 2001a and Cadoni 2001b]. Due to the high loading rate there is no time for the cracks to localize at the weakest points. Therefore, more simultaneous cracks are found in the samples that are loaded in dynamic tension. Also, fracture does not only take place in the cement paste, but also through aggregate particles [Zielinsky 1984].

The scatter in experimental results on tensile strength found in literature is high and, also, there is no consensus between researchers on the causes behind the observed rate effects on tensile strength. Based on the fact that different causes are mentioned by several researchers and that the mentioned mechanisms are not quantified yet, it was decided to study the causes behind the rate dependency of concrete in more detail in the presented research.

2.4.3 Fracture energy at high loading rates

When comparing the fracture processes in static and dynamic tests, the mechanisms are basically the same [Weerheijm 2011]. For both, damage proceeds when deformation energy is released into the fracture zone and absorbed in the fracture process. For high loading rates, part of the available energy is stored into kinetic energy. The key difference is the factor time, which does not play a role in statics, but is very important in dynamics. At very high loading rate, the fracture time is very short and stress redistribution cannot take place. Therefore, fracture patterns can change.

A large amount of data on the influence of the loading rate on the tensile strength is available in literature. The experimental data on the influence of the loading rate on the *fracture energy* or the *softening relation* of concrete, on the contrary, is scarce (see Figure 2.17). Data on how the loading rate affects the fracture characteristics, like fracture lengths and width of the fracture zone, is not found in literature. The softening curve, which represents the fracture behaviour of concrete, is most probably also affected by the loading rate. However, data on the softening curve for high loading rates is also scarce.

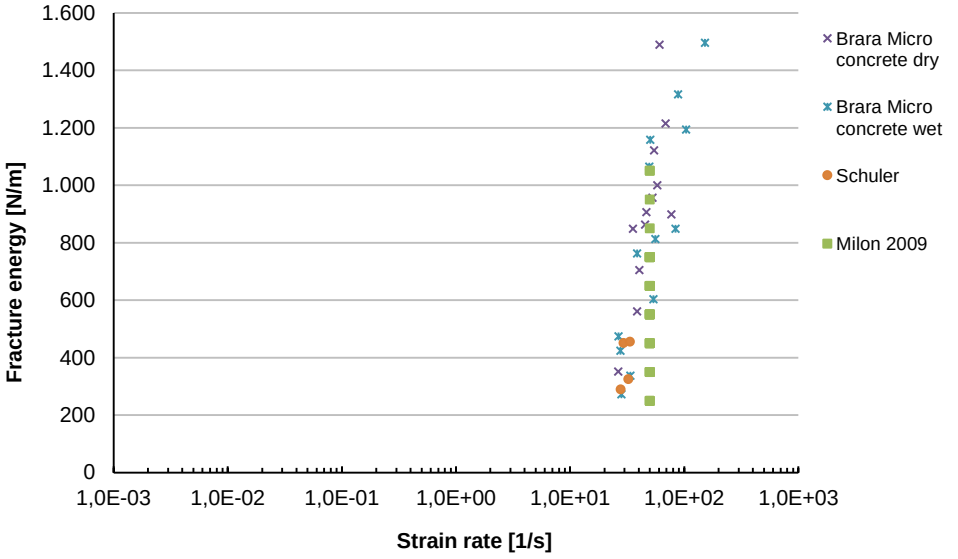

Figure 2.17 Experimental data on the fracture energy as a function of the strain rate [Weerheijm et all 2013].

The influence of the loading rate on the softening behaviour and fracture characteristics should be studied, along with the properties like strength and fracture energy, to be able to comprehend the underlying mechanisms and use the data as input for models.

2.4.4 Moisture and rate dependency

Hordijk and Reinhardt already concluded in 1990 that the moisture content and curing condition of concrete highly influence the fracture properties for static tensile tests [Hordijk 1990 and Hordijk 1991]. In Figure 2.18 the stress-deformation relations for concrete cured under different conditions (wet, lab, dry) are presented. Figure 2.18 from Hordijk and Reinhardt shows that the tensile strength is lowest for the wet concrete. Also, the fracture energy G_f is somewhat lower for dried concrete as for 'lab' cured concrete. They also showed that high drying temperatures cause small cracks in concrete. This is in accordance with the results from the author, presented in paragraph 2.2.5.

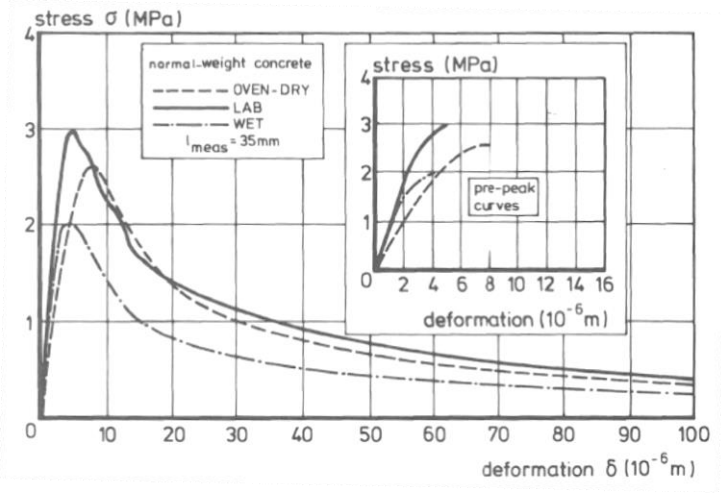

Figure 2.18 Influence of moisture on stress-deformation relation [Hordijk 1991], static tests.

As stated in the paragraph 2.4.2, several researchers recognized the influence of moisture content on the rate dependency of concrete tensile strength. Rossi and Toutlemonde claim that the water in the *gel pores* cause the observed rate effects on tensile strength [Rossi 1997, Toutlemonde 1995a]. The water in the gel pores experiences the so called Stefan effect and, therefore, adds to the resistance against cracking.

According to Cadoni [Cadoni 2001a] the rate effects on tensile strength are caused by moisture that affects the wave propagation. Cadoni used the Hopkinson Bar Bundle technique, where a bundle of small bars is loaded in dynamic tension. Cadoni claimed that the wave propagation is disturbed due to the voids. In empty voids reflection of waves takes place, which increases stresses locally. When voids are filled with moisture, the waves are not or only partly reflected. The reflected stresses are not big enough to cause the increase in stress that locally provokes the damage of the material. Therefore, the strength increases.

Ross [Ross 1996] states that the presence of moisture in concrete has a tendency to amplify inertia effects of wet specimens. In addition, the moisture increases the stiffness and fracture toughness of the concrete. This also leads to an increase in strength for wet concrete [according to the equations proposed in Ross 1996].

As can be seen from the above presented arguments, several researchers agree that moisture is an important parameter when studying the rate dependency of concrete tensile fracture properties. However, there is no common explanation of the underlying mechanisms. There is agreement that the dominant mechanisms happen at the meso level of concrete, although the determination of the mechanical properties takes place at macro level. Therefore, a combination of experimental research at macro level and microscopic research of the fracture patterns at meso level is chosen for the presented research to discover the real mechanisms behind the rate dependency of concrete tensile fracture properties.

2.4.5 Modelling fracture of concrete and the rate effects on tensile fracture properties

Theoretical and numerical models can be quite helpful in giving a better understanding of experimental results. With these models, the rate effects on fracture properties and the fracture process can be studied *inside* the concrete specimens, even *during fracture*. A numerical model can also be used to *predict* fracture behaviour, even for large concrete structures where experimental testing is not possible or has not been done yet.

There are various types of numerical models [Van Mier 1997]. One of the most commonly used approaches to model concrete fracture is the application of continuum models. The properties and behaviour of the elements in a continuum model are defined by a constitutive law, which also determines the change in properties when fracture takes place. For modelling fracture under dynamic loading conditions, the mechanisms behind the rate effects on concrete tensile properties should be incorporated into the constitutive material model, depending on the scale at which modelling takes place. This means that, for instance, when modelling takes place at macro level, the effects of micro cracking, moisture and/or inertia should be included into the constitutive material model to get a proper prediction of the failure behaviour under dynamic loading.

It is of great importance that the constitutive model is based on the right mechanisms and material properties. Without the right material properties, even the most complicated models are not able to predict the fracture response of concrete under dynamic loading conditions accurately. A complete set of material properties, that shows the effects of

moisture and loading rates, is, therefore, very important. One of the objectives of this thesis is, therefore, to contribute to a more complete set of material properties.

The data provided by the presented research has been used by Pedersen for his numerical study on the dynamic fracture behaviour of concrete [Pedersen 2010a, Pedersen 2010b]. Pedersen used the data to validate his rate dependent continuum visco-elastic visco-plastic model [Pedersen 2010a]. He included the rate dependency of concrete by means of visco-elastic and visco-plastic constitutive relationships. The moisture-dependent behaviour of concrete under dynamic loading (Stefan effect) is included into his mesoscopic finite element model by using a visco-elastic model. An additional rate effect comes from the visco-plastic contribution which can be related to the micro inertia effects of the material surrounding the crack tip. This results in increasing tensile strength with increasing load. Pedersen's in essence macroscopic model has been applied to a mesoscopic structure, consisting of aggregates surrounded by an interfacial transition zone in a bulk material. Three model parameter sets, based on the results from this thesis, have been used to study the influence of moisture at two different loading rates and to validate his model.

2.5 Conclusions and missing links

From the data and theory summarized in this chapter can be concluded that the loading rate highly influences the behaviour of concrete loaded in tension. A great deal of data is available in literature on the influence of the loading rate on the tensile strength. The question what happens to concrete loaded by a dynamic tensile load after the tensile strength is reached has not been answered by studying literature. A lot of literature can be found on the influence of the loading rate on the tensile strength, but what about the influence of the loading rate on the softening behaviour and fracture energy? This question remains unanswered. Therefore, in the presented research the focus is on the quantification of the rate dependency of not only the tensile strength, but also the fracture behaviour and softening behaviour of concrete, captured in the stress-deformation curves.

Besides experimental data on how the fracture behaviour of concrete changes when the loading rate increases, also a detailed analysis of the causes behind the rate dependency of concrete is missing in literature. For instance, there is no common explanation of the underlying mechanisms of the rate dependency of concrete tensile properties. Some

researchers believe that micro inertia effects play an important role [Weerheijm 1992, Zheng 2004a, Cotsovos 2008b], while others assume that structural inertia is one of the main causes for the observed rate effects on tensile strength [Ozbolt 2013]. A commonly accepted explanation for the tensile strength increase in the moderate loading rate regime is the moisture in the pores that resists fracture (Stefan effect) [Rossi 1997, Toutlemonde 1995a, Cadoni 2001a]. However, the influence of the Stefan effect and the other mechanisms behind the rate dependency of concrete properties have not been quantified yet. Therefore, one of the objectives of this study is to identify the different mechanisms behind the rate effect on tensile strength and to quantify the influence of the different mechanisms. To gain detailed information on the mechanisms behind the rate dependency of concrete properties and to quantify the contribution of the different mechanisms, the fracture characteristics (width of the fracture zone, crack distribution and crack /fracture lengths) are studied under different loading rates. The experimental research (at macro level) is, therefore, combined with microscopic research at meso level.

The acquired knowledge on mechanisms behind the rate effects on concrete properties and the obtained complete data set can then be used to develop, improve and validate dynamic material models, to be able to properly predict failure of concrete structures under dynamic loading in the future.

To summarize, the following 'missing links' are studied in the research presented in this thesis:

- Acquire a complete data set on the rate dependency of concrete fracture properties. Not only the tensile strength is studied, but also the rate effects on the fracture behaviour of concrete (softening, fracture energy).
- A detailed analysis of the mechanisms behind the rate dependency of concrete is missing in literature. Loading rate, moisture content and pore structure are varied to identify and quantify the mechanisms behind the rate effects on tensile fracture properties.
- To be able to quantify the influence of the different mechanisms, information on the rate effects on fracture characteristics (width of the fracture zone, crack distribution and crack /fracture lengths) is needed.

CHAPTER 3: EXPERIMENTAL PROGRAM TO STUDY THE RATE DEPENDENCY OF CONCRETE TENSILE PROPERTIES

3.1 Scope of the experimental program

To study the previously described missing links in the behaviour of concrete under dynamic loading conditions, an experimental program is conducted. The experimental program is focused on two aspects. First, the influence of the loading rate on the mechanical properties, like tensile strength, Young's modulus and fracture energy, is quantified at medium and high loading rates. Also, the stress-displacement curves and fracture behaviour of concrete is studied and quantified at different loading rates. Secondly, the program is devoted to a better understanding of the physical mechanisms behind the rate effects. To understand the mechanisms, not only the data on mechanical properties and the characteristics of the fracture planes are studied, but also the reconstructed fracture behaviour is combined with data on the composition and pore structure of the concrete to fully understand the mechanisms that take place at meso level. To understand and analyse the experimental data a simple model is developed and used. Knowing and understanding the physical mechanisms that cause the rate effects on concrete properties make it possible to influence the dynamic behaviour, design a proper numerical material model and predict the behaviour of concrete under explosive loading conditions.

In chapters 4 and 5 the experimental data and the analyses of this data are presented and discussed. In the current chapter the experimental techniques are described. The experimental program is described in paragraph 3.2. In paragraph 3.3 the concrete composition and conditioning of the specimen are discussed. The moisture content in the concrete samples is varied in order to study the influence of moisture on the rate

dependency of concrete tensile properties. The pore structure of concrete stored at different conditions and the moisture distribution in the pore system, which is relevant information for understanding the underlying mechanisms, is studied by means of Mercury Intrusion Porosimetry (MIP) and Nuclear Magnetic Resonance (NMR). Since NMR is a relatively unknown method for concrete analysis, the experimental method is described in paragraph 3.4. Paragraphs 3.5, 3.6 and 3.7 present the static set-up, the gravity driven Split Hopkinson Bar set-up (SHB) and the Modified Split Hopkinson Bar set-up (MHSB) and their accompanying measuring methods, respectively. In paragraph 3.8 the microscopic methods used to determine the fracture characteristics are described.

3.2 Experimental program

As stated in chapter 1 and 2, the tensile properties of concrete have a major influence on the failure mode and response of concrete structures under impact loading. Therefore, the research is focussed on determining *tensile* mechanical properties and gaining insight in the failure behaviour under *tensile loading* only. To study the rate effect on the tensile properties of concrete, uniaxial tensile tests are conducted at three different loading rates:

- Static loading rate as a reference; loading rate 10^{-4} GPa/s;
- Moderate loading rate with the gravity driven Split Hopkinson Bar set-up (SHB) at the Delft University of Technology; loading rate 50 GPa/s;
- High loading rate with a newly developed Modified Split Hopkinson Bar set-up (MSHB) at the laboratory of TNO in Rijswijk; loading rate > 1000 GPa/s.

As has been mentioned in the previous chapter, the moisture in the pores is supposed to be one of the causes of the strength increase in the moderate loading rate regime and possibly also influences the response in the high loading rate regime. Therefore, the moisture content in the concrete specimens is varied to study the influence of the moisture on the rate dependency of concrete tensile properties.
The four moisture conditions are:

- “Normal” condition;
- “Wet” condition;
- “Dry-50” condition;
- “Dry-105” condition.

The conditioning of the specimens is described in detail in paragraph 3.3.3.

To study the influence of the microstructure, two types of concretes are used; Portland cement concrete and Blast Furnace Slag (BFS) cement concrete. BFS cement concrete has a denser microstructure with less capillary pores. Portland cement concrete is studied using four different moisture contents and at three loading rates, except the concrete dried at 105°C, which is only tested at static and moderate loading rates. The BFS cement concrete is studied only for wet and normal conditions at three different loading rates. The conditions are summarized in Table 3.1.[1]

Table 3.1 Conditions and loading rates for Portland cement vs BFS cement concrete.

	Portland cement concrete				BFS cement concrete			
	Normal	Dry50	Dry105	Wet	Normal	Dry50	Dry105	Wet
Static	*	*	*	*	*			*
SHB	*	*	*	*	*			*
MSHB	*	*		*	*			*

For the three described loading rates, Portland cement and BFS cement concrete and the different moisture conditions, the strength and fracture energy are determined. Also, the fracture behaviour and stresses during the fracture process of the SHB and MSHB test are studied in real time. These real time measurements are possible with the developed measuring methods (see paragraph 3.6 and 3.7). After the tests are finished, the fracture patterns are studied by impregnating the cracks with epoxy and studying them by microscope. The fracture characteristics and fracture behaviour give insight in the mechanisms behind the rate effects.

The results of Portland cement concrete stored under normal conditions are discussed and presented in chapter 4. The influence of the moisture content and microstructure on the rate dependency of the concrete properties and the experimentally determined moisture distribution and microstructures are discussed and presented in chapter 5.

[1] *From now on, the terms 'normal concrete', 'normally cured concrete', 'normal condition' or 'normal' refer to the normal moisture condition (see also paragraph 3.3.3).*

3.3 Concrete and specimens

3.3.1 Concrete

The composition of the Portland cement concrete that is used for the static and dynamic experiments is similar to the concrete used in earlier research [Weerheijm 1992, Zielinski 1984, Körmeling 1980]. This enables comparison of the results from the experiments with results obtained in the past. In studies reported in literature, micro-concrete is often used for dynamic testing, which only contains sand. In this study, the concrete composition is chosen to resemble as much as possible ordinary concrete used in practice, containing not only sand but also gravel aggregates. For the Portland cement concrete a Portland cement CEM I 32.5R is used. For the BFS cement concrete a cement CEM III/B 42.5N is used. The concrete compositions and the aggregate grading are shown in Table 3.2 and Table 3.3.

Table 3.2 Aggregate grading (for Portland as well as BFS).

Aggregate grading [%]							
8-16mm	4-8mm	2-4mm	1-2mm	0.5-1mm	0.25-0.5mm	0.13-0.25mm	<0.13mm
3	28	18	15	15	16	5	0

Table 3.3 Concrete composition.

Type of cement	Cement content CEM I 32.5 R/ CEM III/B 42.5N [kg/m^3]	Aggregate content 0 – 4mm [kg/m^3]	Aggregate content 4 – 8mm [kg/m^3]	Water-cement ratio [-]	Air content [%]
Portland	375	1268	543	0.5	2.0
Blast Furnace Slag	375	1248	535	0.5	2.0

The size of the largest aggregate grain used in the concrete mixture is dictated by the size of the specimens. Usually, to avoid substantial influence of the heterogeneity on the experimental results, the smallest geometric length of the specimen must be at least five times bigger than the largest grain size (NEN5950). Therefore, for specimens with a diameter of 74 mm the largest grain size used is 8mm. However, an analysis of the aggregates used in the laboratory shows that the aggregate with a size of 4 – 8 mm contains a small percentage of 8 – 16 mm aggregate. In Table 3.2 the contamination of a

certain fraction with larger aggregates is taken into account. The composition of the concrete and the aggregate grading are determined following the NEN5950 regulation.

The mechanical properties of the concretes are determined at 28 days and 42 days (with the exception of the Young's modulus, which is only determined at 28 days for the BFS cement concrete). The cube compressive strength and tensile splitting strength are determined from a standard cube (rib length 150 mm), following the recommendations EN-12390-3, EN-12390-4 and EN-12390-6. The static Young's modulus is obtained by prism compressive tests. A prism 100 x 100 x 400 mm is loaded, measuring the strains by LVDT's at four sides of the prism. From these measurements, the Young's moduli were obtained. The mechanical properties are summarized in Table 3.4. For the general characterization, the specimens were cured in a controlled environment until the day of testing: 95% RH and 20°C.

Table 3.4 Mechanical properties of concrete.

Concrete	Time [days]	Cube strength [MPa]	Tensile splitting strength [MPa]	Young's modulus [GPa]
Portland	28	45.7	3.4	34.6
	42	49.7	3.5	35.7
Blast Furnace Slag	28	43.2	4.1	36.4
	42	44.8	4.2	-

3.3.2 Specimens

The size of the specimens for the uniaxial tensile tests is dictated by the available equipment and the concrete composition. The composition of the concrete mixture contains not only sand but also gravel aggregates. Therefore, the diameter of the specimen should be large enough to get a homogeneous concrete mixture. The diameter of the loaded bar in the SHB and MSHB equipment is 74 mm, which is a larger diameter than usual for Split Hopkinson Bar testing [Brara 2006, Cadoni 2001b, Klepazcko 2001, Ross 1996, Rossi 1992, Schuler 2004]. To match the set-up, the specimens for all three set-ups are cylindrical and have a diameter of 74 mm. The length of the specimen is determined by the length of the loading wave and is chosen to be 100 mm for the static and SHB tests and 300 mm for the MSHB tests.

The 100 mm and 300 mm cylindrical specimens are drilled out of concrete cubes (length 200 mm and 400 mm respectively), to make sure that casting-effects that will occur at the sides of the moulds are not included in the specimens. Therefore, the specimens have the same composition in the entire cross-section. The direction of the drilling is parallel to the casting direction.

Not only the tensile strength of the concrete is measured in the experiments, but also the fracture energy is determined. To determine the fracture energy of the concrete the deformation of a single fracture zone, with potential micro cracks and the resulting macro crack, has to be measured. Notches are applied to avoid multiple fractures and to obtain data for a single fracture. To enable deformation measurements at the failure zone, the location has to be predefined, which is realized by applying the notch.

A notch can introduce stress-concentrations and can, therefore, influence the experimental data. For practical reasons, the wet and dry specimens had larger notch depths, especially for the static tests. Static tests conducted on specimens with notch depths of 2, 4 and 6 mm showed that the influence of the notch depth on the static tensile strength is in the same range as the strength standard deviation (about 10%) (see Appendix A). Therefore, the influence of the different notch depths on the static test results is disregarded when comparing the results.

3.3.3 Conditioning the specimens

The casted concrete cubes are demoulded after one day and placed in a wet environment of 95% RH for 14 days, to avoid drying. Next, the cubes are subjected to a controlled environment of 50% RH and 20°C for another 14 days. At an age of 28 days, the cylindrical specimens (Ø74 mm, length 100 mm or 300 mm) are drilled out of the cubes and are foreseen with notches at a height of 35 mm from the bottom of the specimens for the static and SHB tests and at a distance of 65 mm from the free end for the MSHB tests.

To study the influence of moisture in the pore system on the rate effects on concrete tensile properties, the cylindrical specimens have been subjected to four different moisture conditions for approximately 21 days (after being drilled out of the cubes at an age of 28 days).

The four different moisture conditions are:

- "Normal" condition: specimens are stored under controlled conditions of 20°C and 50% RH;
- "Wet" condition: specimens are immersed in water;
- "Dry-50" condition: specimens are dried in an oven of 50°C and 15% RH;
- "Dry-105" condition: specimens are dried in an oven of 105°C and 2% RH.

In studies reported in literature specimens are often dried at a temperature of 105°C. Therefore, this temperature is chosen in order to be able to compare the experimental results with data mentioned in literature. However, a drying temperature of 105°C can also introduce damage when eigenstresses due to temperature or moisture gradients exceed the tensile strength. To determine the temperature at which the specimen are properly dried but minimally damaged, the effect of different drying temperatures on the moisture distribution and microstructure is studied. The results of this study have been presented in chapter 2. From the results it can be concluded that at a temperature of 35°C the samples will not be damaged, but also will not be completely dry. Nuclear Magnetic Resonance (NMR) tests proved that the specimens dried at 35°C contained almost the same volume of water as the specimens stored under normal conditions (see also paragraph 2.2.6). Therefore, a drying temperature of 50°C is chosen instead of 35°C, to get dry specimens but with minimal damage.

Dried specimen

The dried specimens are taken out of the oven at approximately 49 days to enable cooling of the specimens before being tested. The specimens are wrapped in plastic bags and silica-gel is added to the bags to avoid any moisture uptake during cooling. Tests showed that, when dry specimens are subjected to laboratory conditions (± 20°C and 40 - 50% RH), the moisture uptake will be reduced from 0.2% to 0.02% in 500 hours if they are wrapped in plastic bags. The specimens dried at 105°C are wrapped in foil during preparation and testing, to avoid moisture uptake. However, tests performed by the author showed that the moisture uptake is negligible during preparation and testing. That's why, for the concrete dried at 50°C, it was decided not to wrap the dried concrete in foil anymore during preparation and testing. The concrete dried at 50°C is subjected to laboratory conditions for about one hour.

Wet specimen

The wet specimens are immersed in water and are kept in water until testing. For the static and SHB tests, the wet specimens are wrapped in plastic foil during preparation and testing to avoid drying out of the specimen (see Figure 3.1 and Figure 3.2). Strain gauges are glued on the concrete through small holes in the foil and, surrounding the hole, the loose ends of the foil are glued to the specimen to avoid drying. For the MSHB tests, the strain gauges and wires are applied at the specimens and sealed off with an epoxy material (see Figure 3.3). Subsequently, the specimen are immersed in water and regularly checked to see if the strain gauges are still working properly. During tests, the MSHB specimens are kept wet with soaked blankets.

Normal specimen

The specimens stored under normal conditions are placed in a controlled environment (20°C and 50% RH) after being drilled from the concrete cubes and left in this environment until the day of testing. These specimens are subjected to laboratory conditions for about one hour, just like the dried specimens. The laboratory conditions are almost the same as the conditions in which the normally conditioned specimens are kept. Therefore, the moisture loss due to drying of the normally conditioned specimens in this hour is negligible.

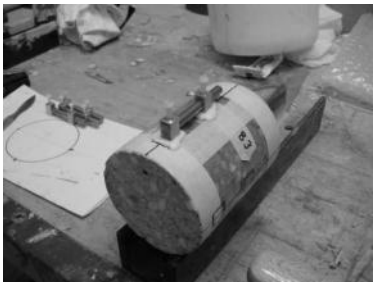

Figure 3.1 Wet static specimen.

Figure 3.2 Broken wet SHB specimen.

Figure 3.3 Wet MSHB specimen.

3.4 Nuclear Magnetic Resonance (NMR)

The moisture distribution in the concrete samples has been studied by using the so called Nuclear Magnetic Resonance method. This paragraph explains the NMR method and the set-up used.

3.4.1 NMR set-up

The NMR set-up used is situated at the group 'Transport in Permeable Media' of the department of applied physics at the Technical University of Eindhoven (Figure 3.4 and Figure 3.5). The Nuclear Magnetic Resonance method is based on the magnetic dipole moment of nuclei, which is different for every type of nuclei. Almost all nuclei have a magnetic dipole moment, resulting from their spin-angular momentum.

The NMR technique is based on two sequential steps:

- The alignment of the magnetic nuclear spins in an applied, constant magnetic field.
- The disturbance of the alignment of the nuclear spins by employing an electro-magnetic radio frequency pulse. The required perturbing frequency is dependent on the static magnetic field and the nuclei of observation.

Subsequently, the NMR technique can be made sensitive to a certain nuclei, in this case hydrogen, and, therefore, to water.

In a pulsed NMR experiment the magnetic moments of the hydrogen nuclei are manipulated by a suitably chosen alternating radio-frequency field, resulting in a so called spin-echo signal. The initial amplitude of the spin-echo signal is proportional to the magnetic spin moment density and, therefore, to the water density. The water density, or number of hydrogen nuclei, is a measure for the volume of moisture present in the sample at a certain position. By moving the specimen stepwise up and down in the NMR apparatus (see Figure 3.5), the volume of water in the pores at a certain position of the specimen can be determined and, therefore, also the moisture gradient in the specimen [Valckenborg 2001a and 2001b]. In this case the specimen is taken from the cross-section of the cylindrical specimens (see Figure 3.6 and paragraph 3.4.2) and the moisture gradient and moisture distribution in the pores of the cross-section, along the diameter, are determined.

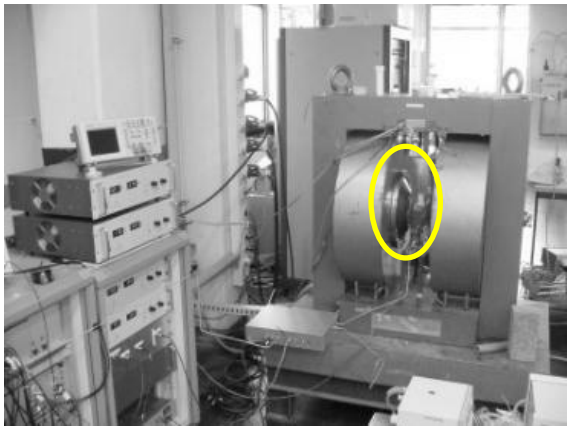

Figure 3.4 NMR set-up at the Technical University of Eindhoven. In yellow the location of the specimen (see Figure 3.5).

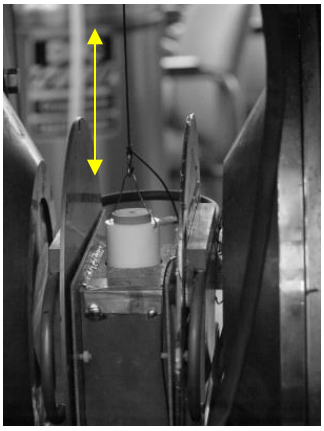

Figure 3.5 Detail of the specimen in between the magnets, moving stepwise up and down. Concrete specimen is placed in white Teflon holder.

The text below gives a summary of the theory and procedure how to derive the pore size distribution and moisture distribution inside the pores. The text is based on the article and thesis from Valckenborg [Valckenborg 2001a and 2001b].

Not only the total volume of water and moisture gradient can be determined from the spin-echo signal during a NMR experiment. It is also possible to determine the size of the pores that are filled with water from the so called relaxation time T_2. After disturbing the system by the radio frequency pulse, the system will return to its magnetic equilibrium by two mechanisms; interaction between the nuclei themselves and interaction between the nuclei and their environment. The longitudinal relaxation time, T_1, is the time spins need to exchange energy with the surrounding material. The transverse relaxation time, T_2, is the time in which the spins diphase due to interactions with neighbours and the presence of fast changing molecular fields. During a NMR experiment a water molecule moves through the pore space due to diffusion.

Assuming that both mechanisms contribute to the NMR signal, the magnitude of the NMR spin-echo signal is given by:

$$M \approx M_0 \left\{1 - exp\left(-\frac{T_R}{T_1}\right)\right\} exp\left(-\frac{T_E}{T_2}\right) \tag{3.1}$$

in which T_R is the repetition time of spin-echo experiments and T_E the spin-echo time. If $T_R > 4 \cdot T_1$, the influence of T_1 relaxation on the signal intensity M can be neglected, which is the case in the conducted experiments.

The initial decay of the magnetization is proportional to the volume-to-surface ratio, which is a property of the pore geometry. Assuming spherical pores with diameter d, the volume-to-surface ratio V/S is d/6. The measured relaxation time of magnetization in a pore is then directly related to the pore size d, when a liquid is confined in a porous material:

$$T_{2,pore} = \frac{V}{S\rho_2} = \frac{d}{6\rho_2} \tag{3.2}$$

with d the diameter of the pore (assuming spherical pores) and ρ_2 the surface relaxivity.

In a porous material a variety of pore sizes exists. Each pore contributes to the total signal intensity with its own transverse relaxation time $T_{2,i}$.

$$M(t) = \sum_i M_i exp\left(-\frac{t}{T_{2,i}}\right) \tag{3.3}$$

For a continuous distribution of pores, the summation over all pores, with their own relaxation time $T_{2,i}$ and weight factor P_i, corresponding to the volume of the pore, can be given by the following integral:

$$M(t) = M_0 \int_0^\infty P(T_2) exp\left(-\frac{t}{T_2}\right) dT_2 \tag{3.4}$$

This is the Laplace Transform of the probability distribution $P(T_2)$ of the relaxation times. The T_2 distribution is measured using a so called Carl Purcell Meiboom and Gill (CPMG) sequence. A CPMG sequence is a series of Hahn spin echoes, which is designed to self-correct pulse accuracy errors. The T_2 distribution is obtained by numerically calculating the inverse Laplace Transform of the CPMG signal by using the program CONTIN [Valckenborg 2001b]. Using Formula 3.2, the T_2 distribution can be converted into a pore size distribution.

With the above described NMR method the moisture gradient and the moisture distribution in the pores can be determined. However, the magnetic dipole moment of hydrogen nuclei in free and physically bound water (capillary and gel water) is different from that of chemically bound water. The water, chemically bound to the cement gel, has a very fast transverse relaxation time ($T_2 \approx 20$ µs) and cannot be detected by the used equipment. Therefore, according to Valckenborg [Valckenborg 2001b] only evaporable water can be determined and divided into two parts; the water physically bound to the surface of the gel particles and the free water outside the gel structure in the capillary pores (see also chapter 5, paragraph 5.4.2).

3.4.2 NMR samples and tests

The NMR set-up has a restriction of maximum diameter of 2 cm; therefore the applied diameter of the samples is 2 cm. When samples would be drilled from the specimens after being conditioned as described in paragraph 3.3.3, the water used during drilling will ruin the results. Therefore, the NMR samples are drilled from concrete cubes, *before* being exposed to different conditions as described in paragraph 3.3.3. The length of the NMR samples is 74 mm, the same as the diameter of the specimens. To simulate the real situation of the middle part of a specimen, where moisture uptake will only take place at the surface of the specimen, the drilled NMR specimens are wrapped in 6 layers of plastic to avoid any moisture transfer with the environment besides from the side edges of the samples (see Figure 3.6). To make sure that the plastic would stay on tightly, metal wires are wrapped around the samples at three different places. The samples are placed back into holes in the cylindrical specimens to make sure that the samples do not experience a temperature shock when placed into the oven.

When a NMR test is performed, the plastic layers are taken off and the sample is placed inside a Teflon holder. In steps of 2 mm, the sample is moved up and down in between the magnets (see Figure 3.5), to determine the total volume of moisture and the distribution of the water in the pores at various locations in the sample. The results of the NMR tests are presented in chapter 5.

Figure 3.6 NMR samples wrapped in plastic and placed back into the cylindrical specimen.

3.5 Static test set-up

3.5.1 The static set-up at the TUDelft

To determine the post-peak softening curve of the concrete specimens, a deformation controlled tensile test is required. The static loading device used in the experiments is situated at the Stevin Laboratory of the Delft University of Technology and is suited for deformation controlled testing.

The device was first built at the end of the nineteen seventies and has been modified over the years. The initial device consisted of two parallel plates, with a specimen glued in between, which could be loaded uniaxially in compression or tension. For the deformation controlled uniaxial tests, it was important to create a crack or softening zone, while the deformation over this zone would be uniform during the test. Therefore, a guiding system was applied to prevent rotation of the loading plates (see Figure 3.7 and Figure 3.8).

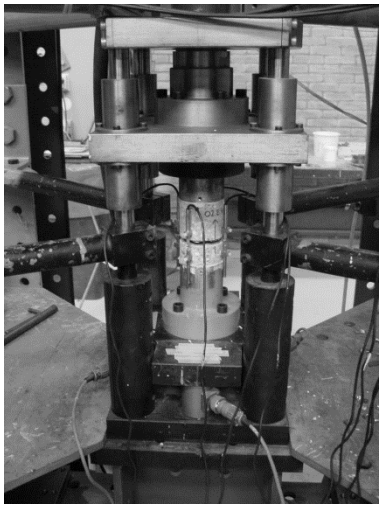

Figure 3.7 Static test set-up at Delft University of Technology, faculty Civil Engineering.

Figure 3.8 Detail of static specimen glued into set-up.

Uniaxial tensile test equipment can be categorized into two groups according to the boundary conditions that have been applied: rotational loading plates and non-rotational loading plates. The two types of equipment show similar results, but only before fracture. Because concrete is heterogeneous, crack initiation will start from a certain point along the circumference of the specimen and propagate through the specimen. In case of the rotational loading plates the loading of the specimen is highly non-uniform during the entire fracture process: the crack opening at one side of the specimen increases, whereas on the opposite side compressive deformations are measured (see Figure 3.9). For the test with non-rotational loading plates the crack also starts at the weakest point along the circumference of the specimen. Because the loading plates are forced to remain parallel during the experiment, a closing bending moment develops. The bending moments prevent the crack to propagate further, until the other side of the specimen starts to fracture. The two crack tips tend to avoid each other, until they finely meet. Due to the non-uniform cracking of the heterogeneous material and the ability for stress-redistribution, the stress-displacement curves show a bump in the descending branch. This bump has been observed by many researchers [Hordijk 1990, Mier van 1997]. Figure 3.9(a) and Figure 3.9(b) schematically show the fracture of the rotational and non-rotational loading plates. Figure 3.9(c) shows the difference between the stress-displacement curves.

The TUDelft equipment used in the static tests has “non-rotational” loading plates with a rotational stiffness of about 106 Nm/rad. The fracture behaviour of the test-specimens is as described before. The bump in the stress-displacement curves is visible in the results of the individual static tests.

With the described equipment for static tests several researchers have conducted tensile experiments, e.g. Hordijk [Hordijk 1991] and Körmeling [Körmeling 1980]. Specially designed plates are applied to the set-up in order to be able to test the cylindrical specimens (Ø74mm, length 100mm). Notches are applied at a height of 35 mm from the bottom of the specimens, to avoid multiple fracture.

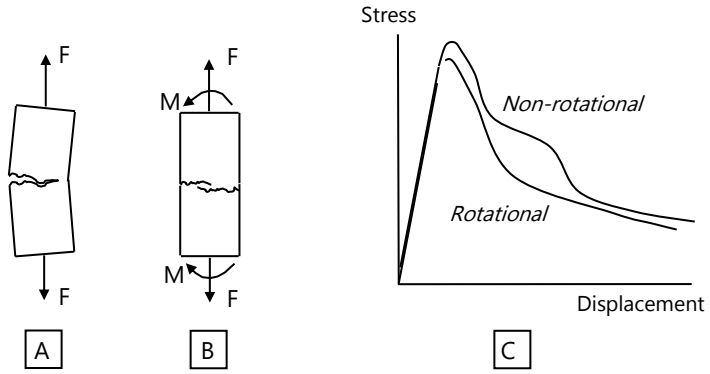

Figure 3.9 Schematic stress-displacement curves (c) for rotational (a) and non-rotational loading plates (b).

3.5.2 Measuring system

The type of experiment is determined by the control variable chosen. To obtain the fracture energy from static tests, a stable deformation controlled tensile test is needed and the deformation rate is chosen as a control variable. To get a stable deformation controlled test, the response time of the controlling system plays an important role and should be fast enough to be able to keep the deformation stable during crack propagation. One of the measures that can be taken to ensure a stable test is reduction of the measuring length. When the measuring length is too long, snap-back behaviour is observed. Snap-back behaviour means that after reaching the maximum strength at a certain deformation, not

only the measured stresses decrease, but also the measured deformations. The deformation decreases because the elastic unloading is larger than the opening of the crack. For the standard tensile test set-up at the Stevin Laboratory a measuring length of 35 mm has proven to give stable results [Hordijk 1991].

To measure the load, a 100 kN load cell is placed above the guiding system. For the deformation measurements four LVDT's (linear variable differential transducers) are placed at four sides of the specimen. The control parameter in the tensile static tests is the average of these four deformation measurements. Small supports are used to glue the LVDT's to the specimen (Figure 3.8). The deformation-controlled tests are conducted with a deformation rate of 0.1 μm/s. For a stiffness of 35 GPa and a measuring length of 35 mm this corresponds to a loading rate of 10^{-4} GPa/s. The measuring frequency was 0.5 s^{-1}. Figure 3.8 shows a detail of the specimen glued into the set-up.

The output from the static tests consists of four deformation measurements and one force measurement. From the force measurement, the tensile stresses in the specimen can be determined by dividing the measured force by the net area of the specimen at the notch. From the average of the deformation measurements and the calculated tensile stresses in the specimen the stress-displacement curve is obtained. The strength of the specimen is determined by the maximum value of the tensile force reached in the stress-displacement curve. Not only the strength, but also the fracture energy is derived from the stress-displacement curve: the area under the curve represents the fracture energy (see also chapter 2, paragraph 2.3).

In Figure 3.10 an example of the average of the displacement measurements and the force measurement from a static test on concrete which is kept under normal conditions is presented. In Figure 3.11 the obtained stress-displacement curve of the same static test is shown.

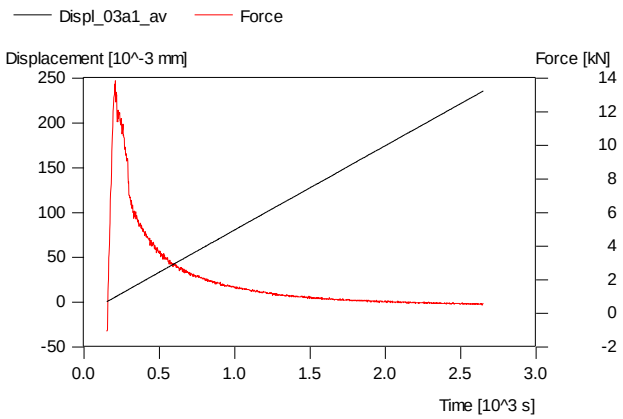

Figure 3.10 Example of average displacement- and force measurements static test, test 03a1, normal condition.

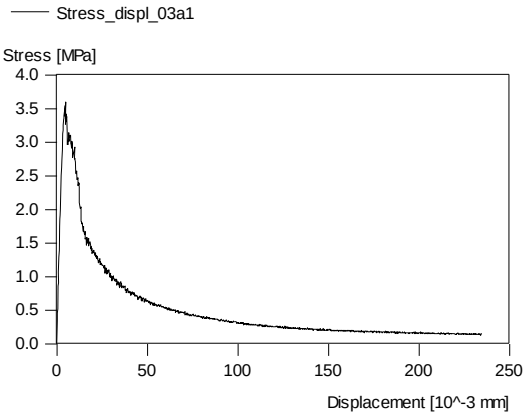

Figure 3.11 Example of stress-displacement curve for static test, test 03a1, normal condition.

Since the load cell is placed outside the guiding system, it is important that the friction in the system is minimized. Nevertheless, a small frictional force (≈ 250 N) was still active in the system [Hordijk 1991]. For the cross-section used in the tests, this means an average stress of about 0.06 MPa. This error in the measured stresses is not significant compared to the maximum tensile stress (the strength) but could be important in the tail of the descending branch.

3.5.3 Non symmetric failure of specimen in static tests due to set-up

The static uniaxial tensile tests are deformation controlled tests. This means that the direct experimental output from these tests are the force-displacement curves. Figure 3.12 shows an example of the output of the uniaxial static tests. The force-displacement curves show a distinct bump, which can be attributed to the test set-up having non-rotational loading platens, as described in paragraph 3.5.1. The shapes of the force-displacement curves of the individual LVDT's (linear variable differential transducers) are different. This is caused by non-symmetric failure of the specimens and by the specimen not being able to rotate.

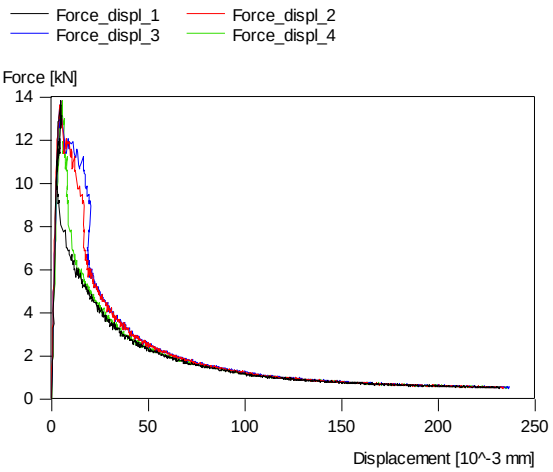

Figure 3.12 Four force-displacement curves from one static test have different shapes due to the fracture process.

The test set-up with non-rotational loading platens influences the fracture energy results, forcing the initiation of a second crack at the opposite side of the concrete specimen after occurrence of the first crack instead of the first crack traveling through the specimen as is the case for the Split Hopkinson Bar tests. In the case of a set-up with non-rotational loading platens, the fracture energy will be slightly higher than when the specimen is free to rotate. However, although the bumps in the force-displacement curves caused by the non-rotational set-up are distinct in the individual curves (see Figure 3.12), the average of the four curves hardly shows any sign of a bump (see Figure 3.10). Therefore, the bumps

in the force-displacement curves do not have an effect on the calculated strength and fracture energy and are disregarded in the analysis of the results.

3.6 Split Hopkinson Bar

3.6.1 Description of set-up

The Split Hopkinson Bar (SHB) technique has been used to generate the moderate loading rates. The Split Hopkinson Bar method has been used in the past by many researchers to subject specimens to dynamic loading conditions. Mostly, the SHB technique has been used to determine the effect of the loading rate on the compressive strength.

The gravity driven Split Hopkinson Bar at the Stevin Laboratory of the Delft University of Technology (TUDelft) consists of two cylindrical aluminium bars (Ø 74 mm) between which the concrete specimen (length 100 mm) is glued (Figure 3.13 and Figure 3.14).

Figure 3.13 The Split Hopkinson Bar set-up at the Delft University of Technology.

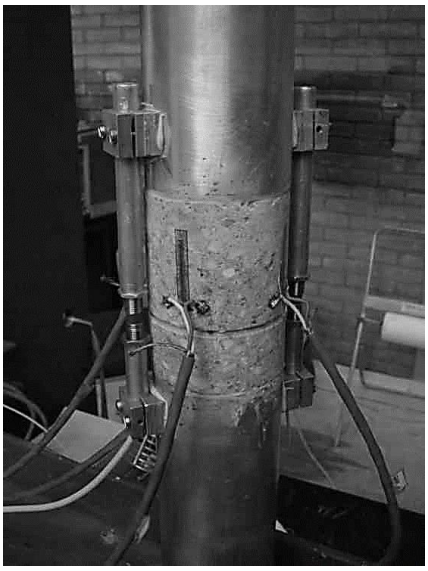

Figure 3.14 Detail of the specimen glued into the set-up.

The tensile stress wave is generated with a drop weight, which slides along the lower bar and hits an anvil at the bottom end. The tensile wave travels upwards through the aluminium bar and through the specimen, fracturing the specimen when the tensile strength of the concrete is reached. The part of the tensile wave that continues and is measured in the upper aluminium bar represents the strength of the concrete specimen. This SHB set-up at the TUDelft has been used by several researchers in the past [Kormeling 1980 and 1984, Weerheijm 1992]. Weerheijm first used the described set-up not only for determining the strength but also the fracture energy [Weerheijm 1992]. The SHB apparatus is described in more detail in [Kormeling 1980 and Weerheijm 1987].

It is important that the bars of the SHB set-up are well aligned, to ensure that the tensile tests are uniaxial. The set-up has been extensively tested and the bending moment in the concrete specimen is proven to be small in comparison with the uniaxial tensile strain (< 5%). Therefore, the tests will be regarded as uniaxial and any effect of bending moments will be disregarded.

The shape and size of the loading pulse depends on the drop weight mass, the drop height and the layers of rubber applied between the drop weight and the anvil. The drop weight has a mass of 27.4 kg. The drop height is set on 75 cm. Two layers of rubber with a total thickness of 1 cm are applied. In this way a stress wave can be generated with an approximate constant loading rate that has enough energy to fracture the specimen. The loading rate that can be generated with the SHB at the TUDelft is about 50 GPa/s, which corresponds with a strain rate in the order of 1 m/m·s.

3.6.2 Measuring system

The measuring technique of the Split Hopkinson Bar is based on uniaxial wave theory and the propagation of waves in the cylindrical bars. The classical SHB data analysis is explained by Meyers [Meyers 1994] and Chen [Chen 2011].

In the TUDelft SHB set-up the strain-time relation during a SHB test is measured at three different locations: at the lower bar, the upper bar and the concrete specimen (see Figure 3.15). Strain gauges are applied in the directions north, east, south and west, in total 12 strain gauges. The strain gauges at the aluminium upper and lower bar (FLA-10-23,

Tokyo Sokki Kenkyujo Co.) have a length of 10 mm. The strain gauges at the specimen (PFL-30-11, Tokyo Sokki Kenkyujo Co.) have a length of 30 mm and are especially suited to measure strains in concrete. The required length of the strain gauges is determined by the largest grain size, which is 8 mm. The length should be at least five times bigger than the largest grain size to minimize the influence of the heterogeneity of the concrete. However, the available area on the specimen also restricts the length of the strain gauges. The strain gauges should be placed at a certain distance from the edges of the specimen, because of the influence of the glue and the possible reflections at the transition zone of aluminium and concrete. Therefore, the maximum length of the strain gauges at the concrete specimen is set on 30 mm, although it does not satisfy the guideline requirements.

The deformations of the fracture zone are measured directly. Notches are applied to avoid multiple fracture and to obtain data for a single fracture zone, like was the case for the static tests. To measure the deformation of the fracture zone, two transducers (LVDT's) are placed at both sides of the specimen (directions north-east and south-west, measuring length 15 cm) and glued to the aluminium bars (see Figure 3.14). The measuring frequency is 90 kHz, or 90.000 s^{-1}. The strains and deformations of the SHB tests are measured at different locations and at different times (see Figure 3.15). This implies that the measurements have to be synchronized in order to be able to obtain the desired stress-deformation curve. There are different methods to synchronize the signals. Initially, the tops of the signals are chosen as reference points. After completion of the tests, a small correction is necessary due to a time delay in the LVDT's (see paragraph 4.2.1).

As long as the stresses in the aluminium bar are in the linear elastic range, the stresses in the concrete specimen can be determined from the strain measurements in the upper bar, by multiplying the strains with the Young's modulus of the aluminium and correcting them for the smaller diameter of the specimen at the notch (according to Kolsky's equations 3.5 and equation 3.6) [Meyer 1994, Chen 2011].

The strain measurements of the upper bar are synchronized with the strain measurements of the specimen. To determine the deformation of only the failure zone, the elastic deformation (measured with the strain gauges at the specimen) should be subtracted from the total deformation.

$$\sigma_{spec}(t) = E_{upbar} \cdot \frac{A_{upbar}}{A_{spec}} \cdot \varepsilon_T(t) \tag{3.5}$$

$$\sigma_{notch} = \varepsilon_T \cdot E_{upbar} \cdot \frac{{D_{bar}}^2}{\left(D_{spec} - 2 \cdot notchdepth\right)^2} \tag{3.6}$$

with E_{upbar} being the Young's modulus of the upper bar, ε_T the strains transferred into the upper bar, D_{spec} being the diameter of the specimen and D_{bar} the diameter of the bar.

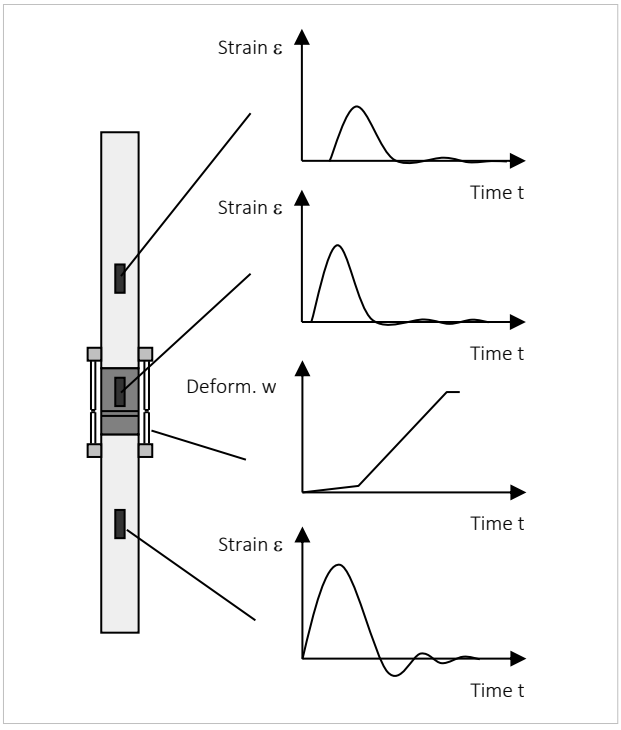

Figure 3.15 Scheme of measurement system of SHB.

An example of an average total deformation measurement (def_tot_10b2_av), the subtraction of the elastic deformation (def_elas_10b2) and the resulting deformation of the fracture zone (def_notch_10b2) is presented in Figure 3.16 for a representative SHB test. When the signals are synchronized, the deformation of the fracture zone can be

combined with the stresses in the upper bar to obtain the stress-deformation curve (see Figure 3.17 and Figure 3.18).

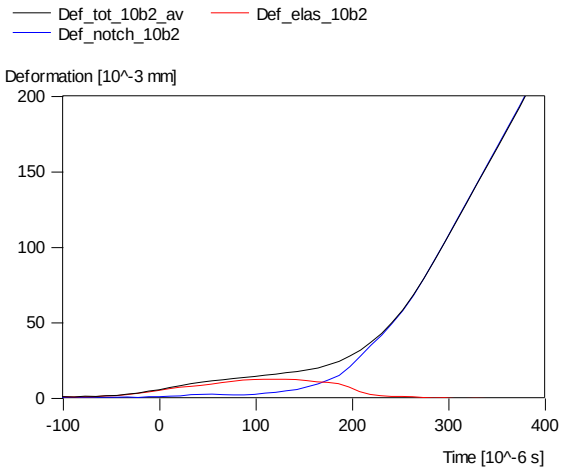

Figure 3.16 Example of deformation measurements for SHB test 10b2, normal condition.

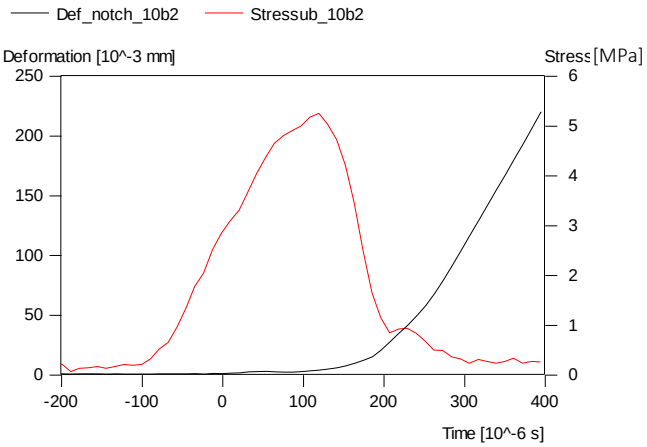

Figure 3.17 Example of stresses and deformation of fracture for SHB tests 10b2, normal condition.

The fracture energy is determined from the stress-deformation curve (area under the curve, see Figure 3.18) and the tensile strength from the maximum stress reached.

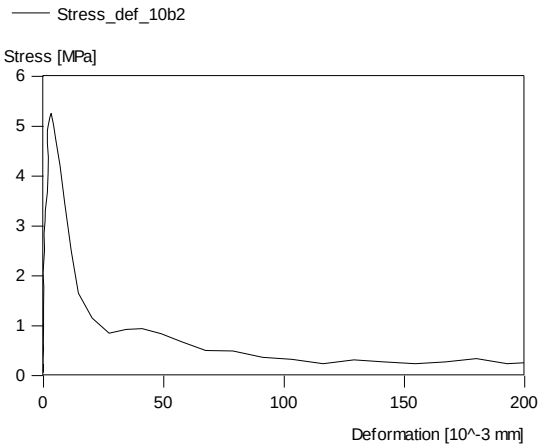

Figure 3.18 Stress-deformation curve for SHB test 10b2, normal condition.

The advantage of the described measurement method to determine the strength and/or fracture energy from the SHB signals compared to other methods, is the obtained stress-time relation and deformation-time relation of the specimen. From these relations, the duration of the fracture process can be established, the rate of inelastic deformation determined and the fracture process reconstructed.

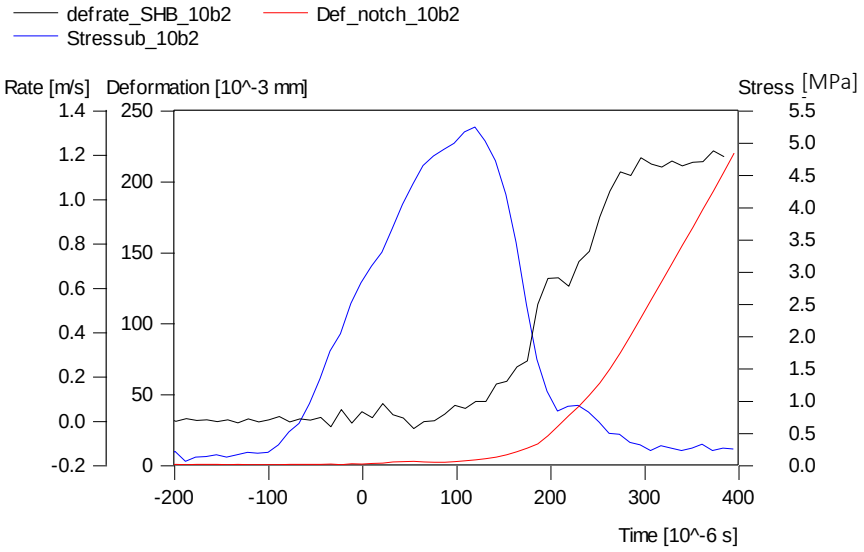

Figure 3.19 Stress-time (Stress_ub), deformation-time (Def_nocth) and fracture speed (defrate_SHB) of SHB test 10b2.

Figure 3.19 gives an example of the stress-time and deformation-time relation and an example of the fracture speed, determined from the deformation-time relation.

The shape of the obtained stress-deformation curve is different from the stress-displacement curve of the static tests, which is mainly visible in the ascending branch of the curves (see Figure 2.11, paragraph 2.3.3). The displacement measurement in the static tests consists of two parts; the contribution of the crack opening and the contribution of the elastic deformation over the total measuring length. In the SHB tests, on the contrary, the elastic deformations are subtracted from the total deformations, resulting in a stress-deformation-of-fracture curve, in short stress-deformation curve. Although the method of obtaining the curves is different, according to Hillerborg the area under both the static and SHB curves represents the fracture energy, as has been explained in chapter 2.

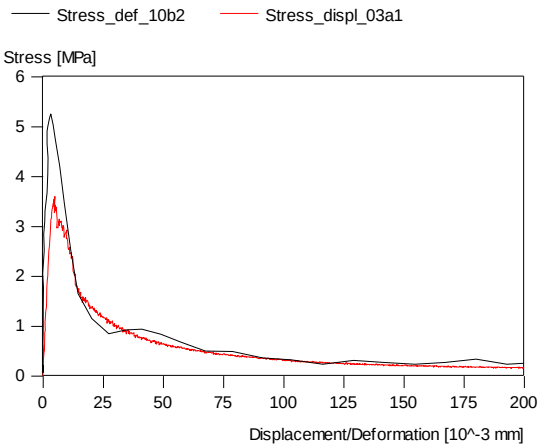

Figure 3.20 Stress-displacement curve for static test 03a1, compared with stress-deformation curve for SHB test 10b2.

3.6.3 Acoustic impedance

From uniaxial wave theory it follows that when two materials have the same acoustic impedance (I), a wave is completely transmitted when traveling from one material to the other. Aluminium is chosen for the SHB bars, because the acoustic impedance of aluminium is close to that of concrete (aluminium $13.6 \cdot 10^6$ kg/s·m^2, concrete $10.1 \cdot 10^6$ kg/s·m^2). Due to the slight mismatch in acoustic impedance between the

aluminium bar and the concrete specimen, reflections occur at the interface during transmission of the pulse into the concrete specimen, following equations 3.7 and 3.8 [Meyers 1994].

$$\sigma_{transmitted} = \frac{2}{1+\alpha} \cdot \sigma_{incoming} \tag{3.7}$$

$$\sigma_{reflected} = \frac{1-\alpha}{1+\alpha} \cdot \sigma_{incoming} \tag{3.8}$$

$$\alpha = \frac{I_{aluminium}}{I_{concrete}}$$

$$I = \rho \cdot c \tag{3.9}$$

with $c = wave\ velocity\ [m/s], \quad \rho = density\ [kg/m^3]$

Tests have shown that the stress rate measured in the specimen is the same as in the transmitted pulse from the lower bar, only a time delay occurs. This is also demonstrated by Weerheijm [Weerheijm 1987 and 1989].

3.6.4 Dispersion of signals

In the classic SHB theory, the strain data measured at the middle of the bars are used to determine the transmitted wave, the reflected wave and the incident wave. This classical SHB data analysis is based on 1-D wave propagation in long rods. However, for finite bar diameters, wave propagation in cylindrical bars is a two-dimensional process; not only axial stresses but also radial stresses are generated when a stress wave travels along the bar. The material acceleration in radial direction causes inertia induced stresses in the axial direction. These two dimensional effects result in wave dispersion when propagating along the bars.

Furthermore, the wave velocity depends on the wave frequency. Due to the fact that a wave actually consists of multiple waves with different frequencies and, therefore, with different wave velocities, the shape of the wave changes as it travels along the axial direction. [Chen 2011]

Wave dispersion has been studied extensively by several researchers, like Pochhammer (1876) and Chree (1889). They solved the equation of motion for a sinusoidal wave propagating in an infinitely long cylinder. Figure 3.21 shows the solution of Pochhammer-Chree for wave dispersion, where Λ is the wavelength (inversely proportional to the frequency), a is the diameter of the bar, C_p is the elastic wave speed of wave components and C_0 is the elastic wave speed of the bar, $C_0 = \sqrt{E/\rho}$.

The Pochhammer-Chree solution shows that dispersion increases with increasing bar diameter a and decreases with increasing wave length Λ. When $a/\Lambda < 0.1$, dispersion is minimal ($C_p/C_0 \cong 1.0$) and the stresses along the cross-section of the bar can be assumed constant. For $a/\Lambda < 0.1$, the difference is less than 5% [Meyers 1994] (see Figure 3.21).

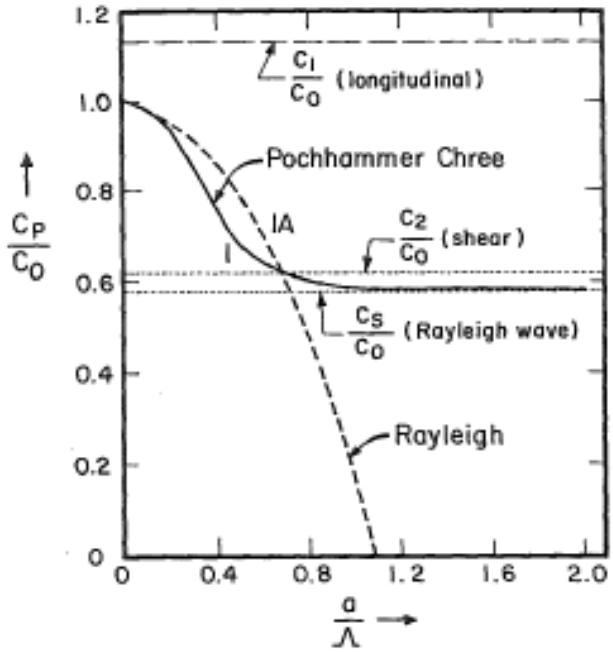

Figure 3.21 Phase velocity as a function of the ratio between cylindrical bar diameter a and wavelength Λ, Pochhammer-Chree solution [Meyers 1994].

In the case of the SHB tests at the TUDelft, the diameter of the bar a is 74 mm. The duration of the wave is approximately 300 μs, which corresponds to a wave length Λ of 1.5 m ($C_{aluminium}$ = 5000 m/s). Therefore, $a/\Lambda = 0.05$, which means that the dispersion effects on the SHB results are minimal (see Figure 3.21, $C_p/C_0 \cong 1.0$).

Due to dispersion effects and the fact that a wave can be decomposed in a set of waves with different wave velocities, a stress wave can change shape when propagating along the bar. However, for the SHB tests the distance between the strain gauges on the upper and lower bar and the specimen is about 0.75 m, which is only half the length of the stress wave. The wave will not change shape when travelling such short distance. Therefore, and because the wave length is long with respect to the bar radius, the dispersion effects are not taken into account for the SHB tests.

3.7 Modified Split Hopkinson Bar

3.7.1 Description of set-up

For the very high loading rates (> 1000 GPa/s) a new Modified Split Hopkinson Bar (MSHB) set-up is developed at TNO Defence Security and Safety in Rijswijk. The feasibility of the set-up was demonstrated by the TNO prototype test set-up [Weerheijm 2001, Weerheijm 2003, Weerheijm 2004]. Based on the results from the feasibility study, TNO decided to build a small and large scale test set-up (Ø 74 mm and 300 mm). The Modified Split Hopkinson Bar is based on a different principle than the Split Hopkinson Bar; i.e. the principle of spalling.

The small MSHB set-up consists of a horizontal steel bar (length 2 m, diameter 74 mm), supported by strings and a (concrete) specimen which is supported by low friction bearings (see Figure 3.22, Figure 3.24 and Figure 3.27). The strings and bearings make sure that the rod and specimen can move freely in the horizontal direction. Therefore, the wave propagation will not be influenced by the supports.

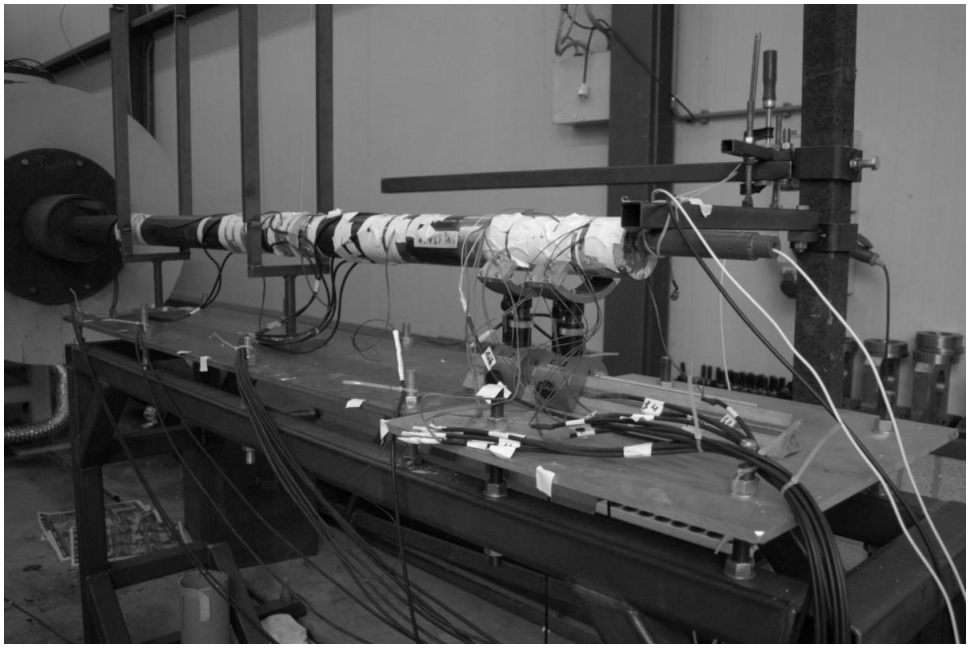

Figure 3.22 Modified Split Hopkinson Bar set-up at TNO laboratory.

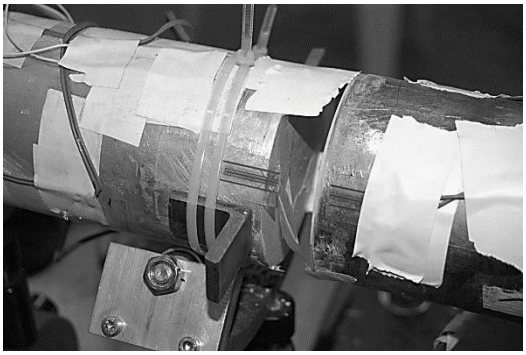

Figure 3.23 Detail of deformation measuring device with strain gauges and supporting foil.

The shock wave is introduced into the steel rod by detonating an explosive charge at one end of the bar. The explosives used are casted TNT and the amount is 10 g. The explosive charge is cylindrical and is installed at a distance of 20 mm from the end of the bar. At the other end, a concrete specimen (length 300 mm, diameter 74 mm) is attached to the bar with a plaster that has very low tensile strength. The plaster will break when tensile

stresses are introduced, making sure that only the compressive part of the impact wave will travel into the specimen. The concrete specimen is first loaded in compression and will fail in tension due to the reflected tensile wave (spalling).

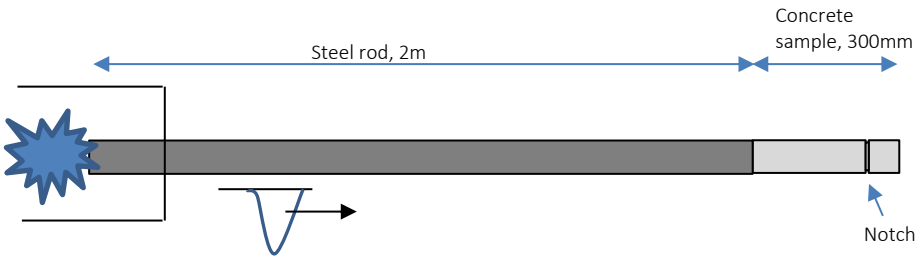

Figure 3.24 Scheme of MSHB test set-up, diameter 74mm.

The MSHB test set-up is specially designed for very high loading rates; loading rates of 1000 GPa/s and higher are reached. The set-up is extensively tested, to make sure it is working properly.

The stresses in the fracture zone are determined by the interaction of the compressive and the reflected tensile wave. Therefore, the shape of the loading pulse in the concrete specimen is very important and should be reproducible. Modified Split Hopkinson Bar tests are repeated several times to test the reproducibility of the test set-up and the introduced load. The conducted experiments showed that the shape and amplitude of the introduced load in the steel bar is almost the same in all the experiments (see for example test N12, N13, N14 and N15 in Figure 3.25, at 200 mm from the end of the steel bar).

The loading pulse in the concrete specimen is also almost the same for every test. Only the amplitude of the compressive wave differs slightly (see tests N12, N13, N14 and N15 in Figure 3.26). The loading pulse needs a steep ascending branch to make sure the loading rate is high enough. The area under the curve of the pulse, which represents the energy of the pulse, needs to be large enough to fracture the specimen. With the type of explosive used in the tests and the distance of the charge to the bar of 20 mm, both criteria are satisfied. Due to the induced compressive load pulse the maximum strain in the concrete specimen, at 35 mm from the interface at location R1-15, is approximately

600 +/- 30 µstrain (see Figure 3.26 and Figure 3.28 for location R1-15). This is low enough to make sure that no damage due to the compressive wave is introduced, but still sufficient to get the required loading rate and energy to fracture the specimen.

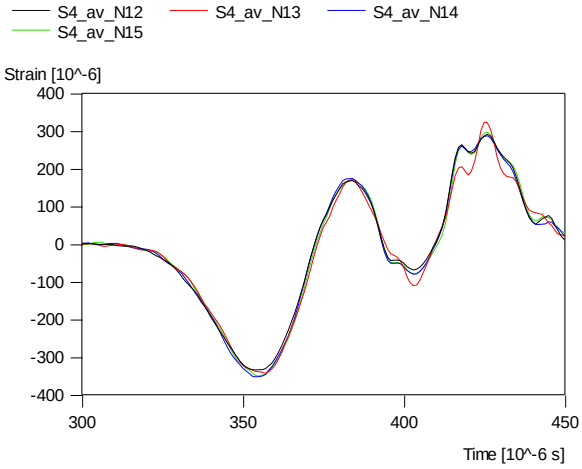

Figure 3.25 Strain measurements in steel bar for four different tests; N12, N13, N14 and N15.

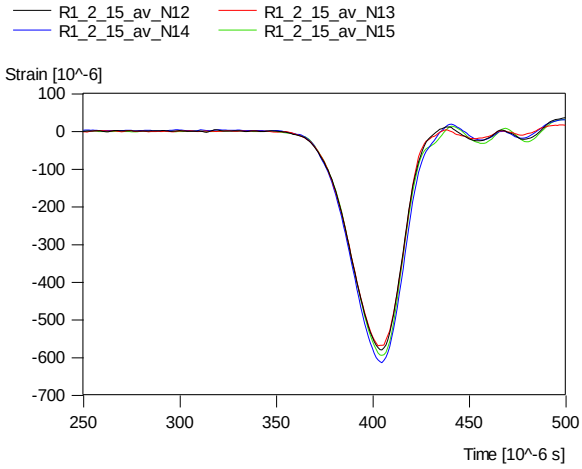

Figure 3.26 Strain measurements at location R1-15 (see Figure 3.28 for location at the specimen) for four different tests; N12, N13, N14 and N15.

3.7.2 Measuring system

The measuring equipment of the MSHB is based on the equipment of the SHB. Similar to the method used for the SHB, the deformations are combined with the stresses in the notch to obtain the desired stress-deformation curve. The transmitted pressure wave in the concrete specimen, the wave propagation and reflection process are recorded with a number of strain gauges distributed along the notched specimen (Figure 3.27 and Figure 3.28).

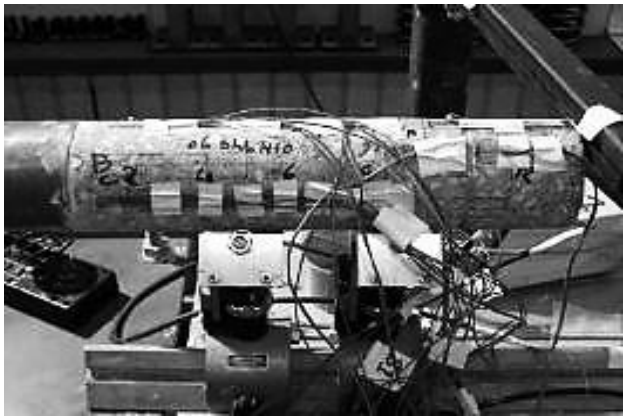

Figure 3.27 Detail of the concrete MSHB specimen (length 300 mm, diameter 74 mm).

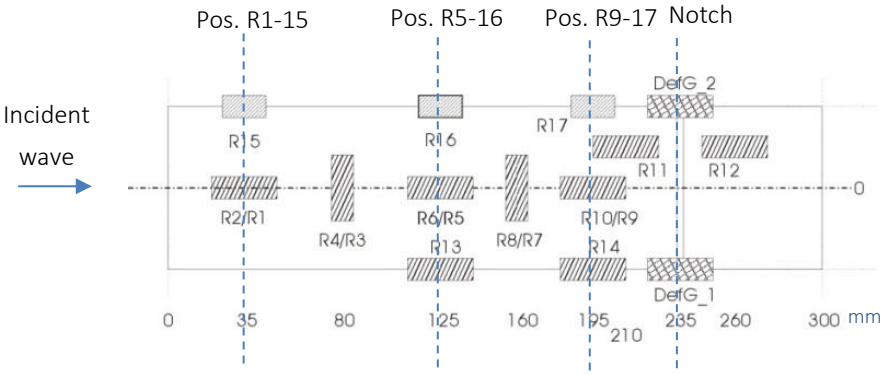

Figure 3.28 Scheme of the locations of the strain gauges on the specimen and the position (pos. x) of the relevant cross-sections.

The strain gauges (PFL-30-11, Tokyo Sokki Kenkyujo Co.) are applied at various positions not only because of the method to determine the stress-deformation curve and fracture energy (see paragraph 3.7.3), but also to cross-check the measurements to verify the set-up and exclude some inaccuracies (see paragraph 4.2). Thirdly, the strain gauges enable us to reconstruct the compressive and tensile waves in time and give detailed information on the strains in the concrete specimen just before, during and after fracture.

The applied load can be derived from the strain measurements on the incident bar and the specimen. The resulting stress at the failure zone (notch) is determined using the uniaxial wave theory to quantify the wave interaction process (see paragraph 3.7.3).

The stresses at the notch are combined with the deformation of the fracture zone, to get the desired stress-deformation curve. The deformations are measured directly at the notched area. The strains as well as the deformation are measured with a frequency of 1000 kHz or 1.000.000 s^{-1}. The Linear Variable Differential Transformers (LVDT's) of the SHB cannot be used in case of high dynamic loading. Even though the masses of the LVDT's are small, they start to vibrate due to the high accelerations. These vibrations interfere with the measurements in such a way, that no useful data can be obtained. Therefore, a new measuring device has been developed that is almost weightless and linear within its measuring range. The new device consists of a strain gauge glued on a supporting material (see Figure 3.23). The ends of this supporting material are glued onto the specimen, leaving a certain unglued area of about 0.5 cm around the notch. Static tests on different support materials showed that 3 cm strain gauges and a synthetic foil for support fulfil the requirements. The deformation gauges are pre-stressed, to be able to measure the elastic tensile deformation as well as the elastic compressive deformation of the specimen before fracture occurs.

The dynamic Young's modulus of the concrete E, necessary to determine the stresses from measured strains, can be determined with the average wave speed c, measured at the specimen, for 1D problems:

$$c = \sqrt{\frac{(1-\nu)}{(1+\nu)(1-2\nu)}} \sim \sqrt{\frac{E}{\rho}} \tag{3.10}$$

The average wave speed is determined from the large as well as the smaller strain gauges. However, the wave speed can change due to the fracture process. Therefore, it is necessary to check whether the average wave speed can be applied before as well as beyond the fracture zone (at position R5-16 and R9-17). When moving the compressive and tensile waves at position R1-15 to position R5-16 and R9-17 (see Figure 3.28), using the determined average wave speed, and comparing them with the measured strains at these locations, the wave speed was slightly adjusted until best fit is accomplished.

The stress-deformation curve is obtained from the calculated stresses at the notch and the deformation of the fracture zone. From the stress-deformation curve (see Figure 3.29), the strength and fracture energy can be determined. The determination of the stress-deformation curve is described in detail in the next subparagraph.

However, it is also possible to determine the stresses and deformations with time and, therefore, reconstruct the failure behaviour of the concrete specimen. By differentiating the deformation with time, it is possible to get insight in the deformation rate of the fracture zone of the concrete. Figure 3.30 shows an example of the stress, deformation and deformation rate with time for a MSHB test. The determination of these signals with time is a unique feature of the designed MSHB set-up at the laboratory of TNO in Rijswijk.

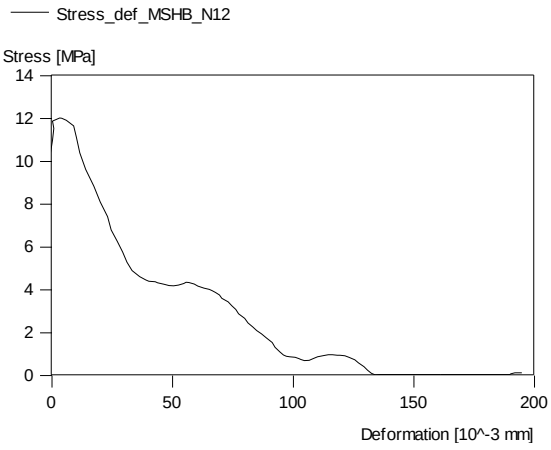

Figure 3.29 Stress-deformation curve of tests 06SHBN12.

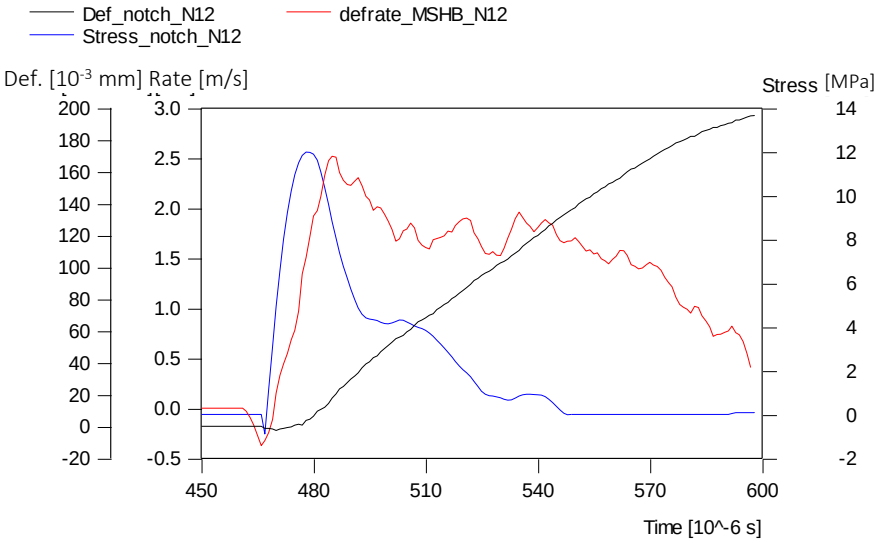

Figure 3.30 Stress-time, deformation-time and deformation rate-time of a MSHB test N12 determined at the notch.

To summarize, the MSHB measuring method enables us to determine:

- Strength;
- Dynamic Young's modulus;
- Stress-deformation curve;
- Fracture energy;
- Wave speed;
- Stresses, strains and deformation with time and, therefore, also the deformation rate of the fracture zone with time.

3.7.3 Determination of stress-deformation curve

The stress-deformation curve is determined using the uniaxial wave theory. To obtain the stress-deformation curve it is necessary to determine both the stresses with time at the notch and the deformations with time at the notch.

First the average of the strains measured by the strain gauges is determined at each cross-section. According to the uniaxial wave theory, wave recordings can be moved to other positions if the material behaves linear elastic. When no damage has occurred, the

concrete material will behave linear elastically. It is assumed that beyond the fracture zone the damage is minimal and the concrete has behaved linear elastic during the entire test (see also paragraph 4.2.2).
Similar to the SHB test, the transmitted pulse is measured beyond the fracture zone. This transmitted stress represents the dynamic resistance of the concrete. In this case, the strains at position R9-17, 105 mm from the free end of the specimen (see Figure 3.28), are used. With these strain gauges the strains at the notch are determined since this is the position closest to the notch and, therefore, the difference due to material damping will be smallest (see paragraph 4.2.3 and 4.2.4).

The method to determine the strains at the notch is schematized in Figure 3.31.

Step 1
To be able to determine the strains at the notch, by moving the tensile and compressive wave to the position of the notch according to the uniaxial wave theory, first the average measured strain at R9-17 (see Figure 3.28) has to be split into a compressive and tensile part (see step 1 in Figure 3.31).

Step 2
However, at position R9-17, the tensile and compressive waves are slightly overlapping (see Figure 3.32). When the wave is split into a compressive and tensile part, the 'tail' is missing (see step 2 in Figure 3.31). The next step is, therefore, to determine the missing tails and correct the waves, using the wave at position R5-16 (125 mm from the front face of the specimen).

At position R5-16, the tensile and compressive waves are not overlapping and can easily be split (see Figure 3.32). The compressive wave at R5-16 should be the same as at R9-17, except in amplitude (see Figure 3.33). The waves are disturbed due to the heterogeneity of concrete, which causes a decrease in maximum strain amplitude (material damping). The difference in amplitude is determined and the strains of R5-16 are multiplied by this damping factor to obtain an 'adjusted compressive wave' (see Figure 3.34).

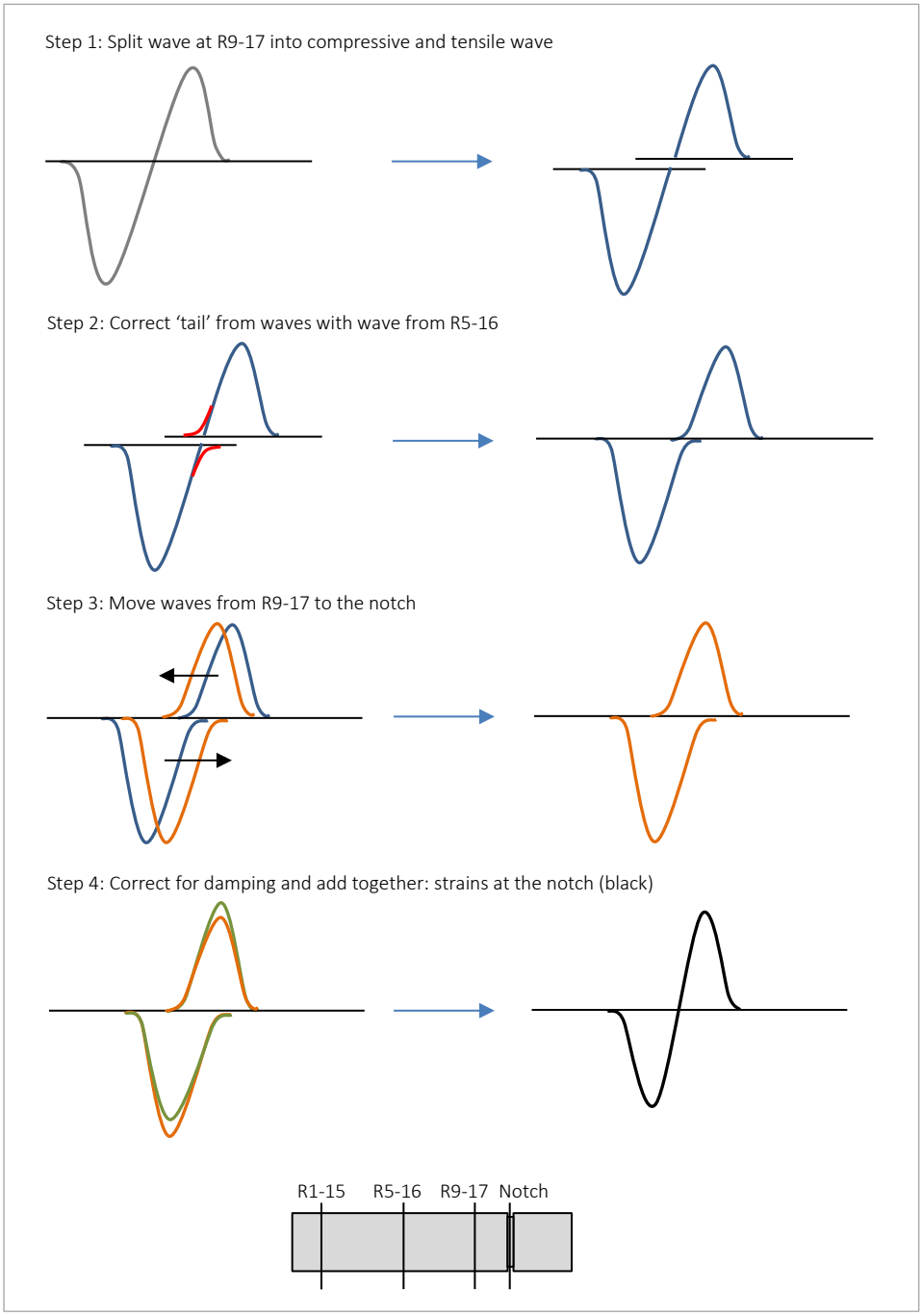

Figure 3.31 Scheme how to determine the strains at the notch.

With this 'adjusted compressive wave' the part of the compressive wave at position R9-17, which is 'missing' due to the overlapping of the waves, is determined. The same part which is missing from the compressive wave is also missing from the tensile wave, with an opposite sign, following the uniaxial wave theory. Now the compressive and tensile waves at position R9-17 can be corrected and fully determined.

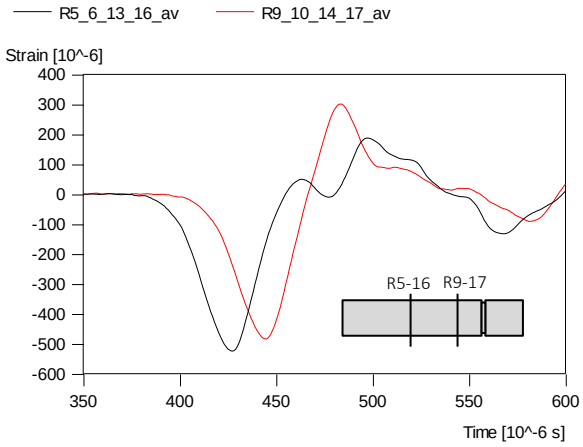

Figure 3.32 Average measured strain at R5-16 and R9-17; at position R9-17 compressive and tensile waves are overlapping.

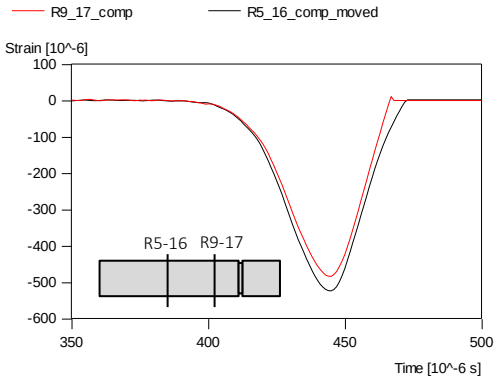

Figure 3.33 Measured compressive strain at R9-17 and moved compressive strain at R5-16; the same except the amplitude.

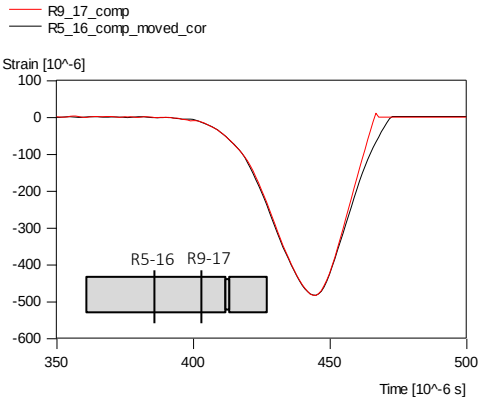

Figure 3.34 Measured compressive strain at R9-17 and adjusted compressive strain at R5-16.

Step 3

Assuming linear elastic behaviour of the concrete specimen, the uniaxial wave theory can be used to shift the compressive and tensile waves to the position of the notch (see Figure 3.35 and Figure 3.31, step 3).

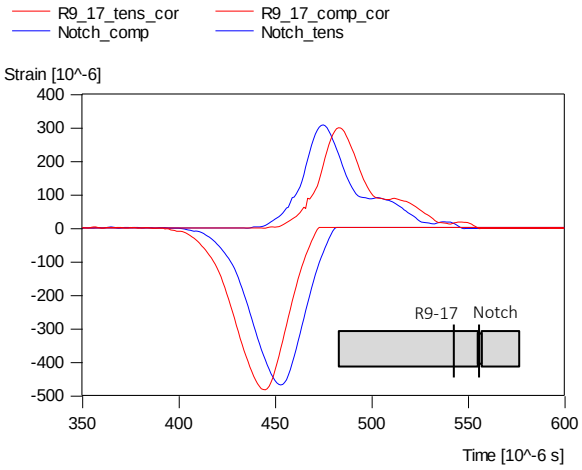

Figure 3.35 Compressive and tensile strains at position R9-17 and at the notch.

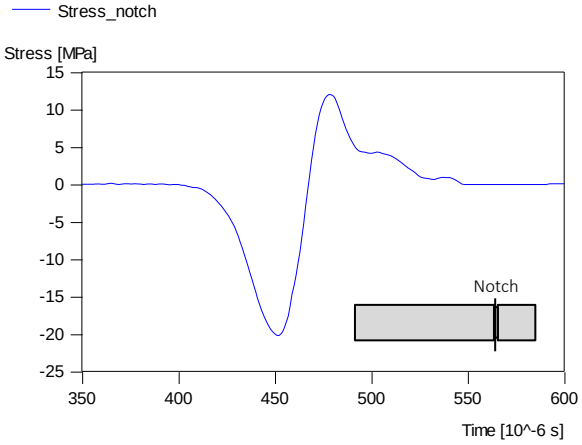

Figure 3.36 Calculated stresses at the notch.

Step 4

The shifted compressive and tensile waves are corrected for material damping and then added up to determine the final strains at the notch (see Figure 3.31, step 4). By multiplying the strains with the dynamic Young's modulus, the stresses at the notch are determined (see Figure 3.36).

The total deformation of the fracture zone is measured directly at the notch, using the newly developed deformation gauges with a measuring length of 30 mm. The elastic deformation is determined by the calculated strains at the notch:

$$\delta_{el,notch} = \varepsilon_{notch} \cdot l_{def\ gauges} \tag{3.11}$$

The elastic deformation is subtracted from the total measured deformation to obtain the deformation of the fracture at the notch (see Figure 3.37).

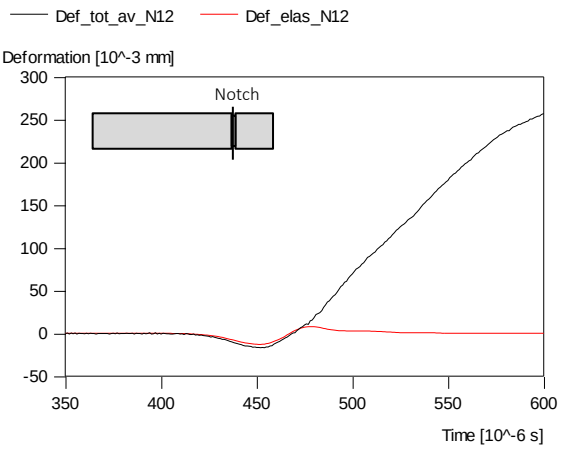

Figure 3.37 Average total deformation and calculated elastic deformation at the notch, measuring length 30 mm.

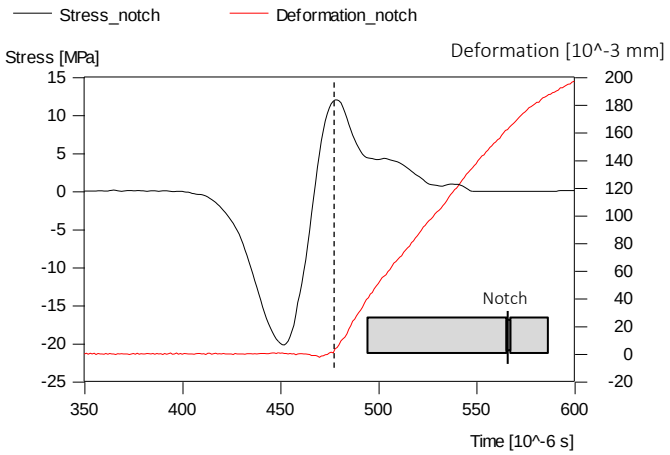

Figure 3.38 Stresses and deformation at the notch, test N12.

The calculated stresses at the notch are then graphically presented as a function of the deformation of the fracture zone, in a so called stress-deformation curve (see Figure 3.38 and Figure 3.39).

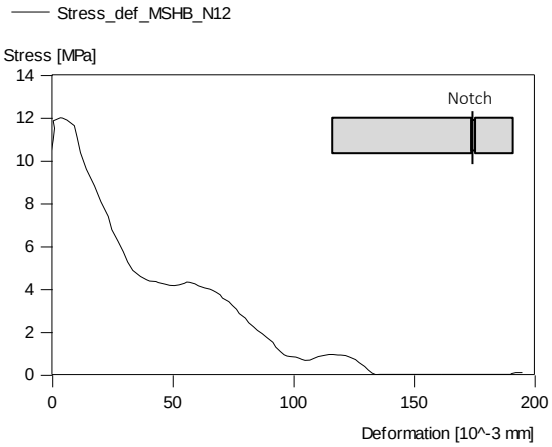

Figure 3.39 Stress-deformation curve of test 06SHBN12.

3.7.4 Dispersion of signals

The dispersion of dynamic waves becomes more pronounced when the diameter of the bar increases or the wave length decreases. When the ratio of the diameter of the bar *a*

divided by the wave length Λ is smaller than 0.1, dispersion effects can be ignored (see paragraph 3.6.4, Figure 3.21). For the MSHB tests, the diameter of the bar *a* is 74 mm, the same as for the SHB tests. The duration of the wave is shorter than for SHB, approximately 70 µs. This corresponds to a wave length Λ of 0.28 m ($C_{concrete}$ = 4100 m/s). Therefore, $a/\Lambda = 0.26$, which means that dispersion effects could be important (see Figure 3.21). When dispersion effects are pronounced, the shape of the wave changes when the wave propagates along the length of the bar. This effect can be seen in Figure 3.40, which shows the wave at different locations in the steel bar (S_1, S_2, S_3 and S_4 are located at respectively 1300 mm, 700 mm, 500 mm and 200 mm from the end of the steel bar and the attached concrete sample).

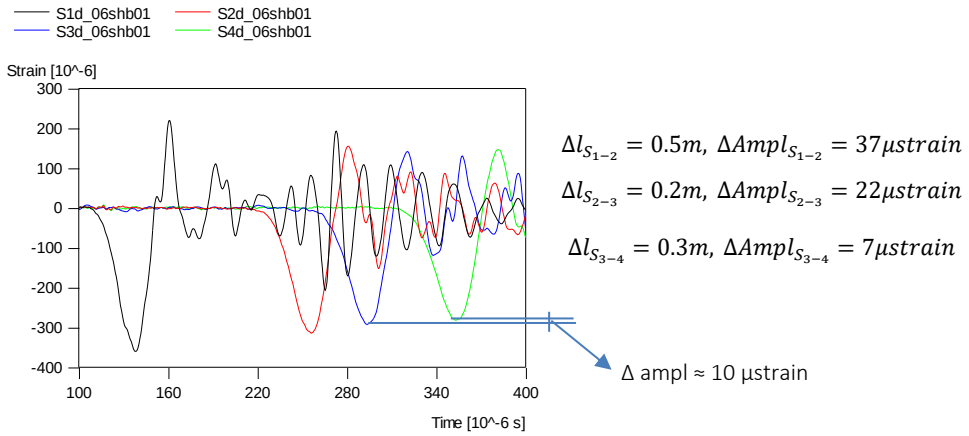

Figure 3.40 Wave dispersion in steel MSHB bar.

Also, the amplitude of the wave decreases as a result of the dispersion. The amplitude decreases rapidly when the wave is just introduced into the steel bar. When a stable situation is achieved at the end of the steel bar, the amplitude decreases about 10 µstrain over a length of 0.3 m due to dispersion effects.

As stated before, dispersion effects can become important when the wavelength is short or the specimen diameter is large. As can be seen from the measurements in the steel bar shown in Figure 3.40, dispersion effects do occur in the MSHB tests. However, the method to determine the strength, fracture energy and stress-deformation curve is different from

the classical SHB method and, therefore, the dispersion effects in the MSHB tests – although present– only minimally influence the results. The waves in the concrete specimen are transferred over short distances compared to classical SHB tests, especially the wave at location R9-17, which is transferred only 4 cm to the location of the notch. For the separation of the compressive and tensile wave at location R9-17 (see Figure 3.28), the waves at position R5-16 are used. The distance between these positions is also short, 7 cm. Compared to the distances the wave travels in the steel, the travel distances in the concrete specimen are short, and wave dispersion will have a negligible effect (<10 µstrain on an average compressive amplitude of 600 µstrain). Therefore, wave dispersion effects are disregarded in the MSHB analysis.

Figure 3.41 shows an example of the waves in the concrete specimen at three locations. As can be seen, the shape of the waves does not change when propagating along the concrete specimen. The amplitude of the waves decreases along the concrete specimen. However, this is not attributed to wave dispersion effects, but to material damping. Material damping exists when a material is heterogeneous and/or inelastic deformation occurs.

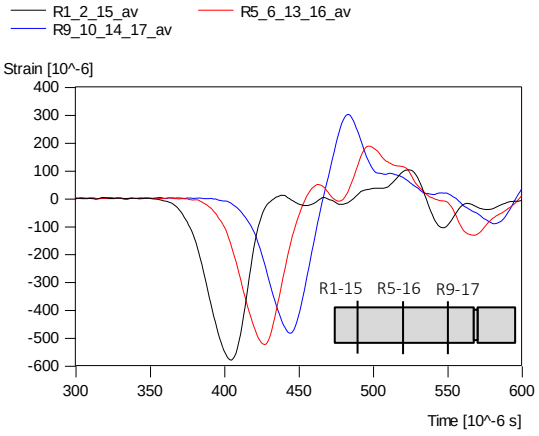

$$\Delta l_{1-2} = 0.09m,\ \Delta Ampl_{1-2} = 55\mu strain$$
$$\Delta l_{2-3} = 0.07m,\ \Delta Ampl_{2-3} = 41\mu strain$$

Figure 3.41 Strain waves in concrete specimen (test 06MSHBN12).

3.7.5 Comparison with Metz set-up and measuring method

The Hopkinson Bar method is used by many researchers to determine dynamic strength of materials. In Metz a new dynamic testing facility has been developed in LEM3 laboratory (Metz University) to test concrete specimens by means of spalling, reaching strain rates ranging from 30 /s to 200 /s [Klepaczko 2001, Erzar and Forquin 2010, Erzar 2010]. The method used to determine the strength is developed by Novikov [Novikov et al. 1966] and is based on the particle velocity and pull back velocity, measured on the rear free face of the specimen, using laser equipment (see Appendix B).

Tests have been conducted in Metz with wet concrete specimens made in Delft, using the same concrete composition as used for the tests conducted in Delft and at TNO (see paragraph 3.3.1), to be able to compare the results of both testing facilities. The diameter of the SHB bars in Metz is 46 mm and, therefore, the diameter of the Metz specimens is also 46 mm.

The average tensile strength found with the Metz set-up for the notched specimens is 12.6 MPa, at a loading rate of approximately 2380 GPa/s (see Appendix B). The average strength from the MSHB tests performed at TNO for wet notched specimens is 17.1 MPa, at a loading rate of approximately 2460 GPa/s (see chapter 5). The average tensile strength results for the TNO and Metz set-ups are similar, although the results for TNO are slightly higher. This is due to the concrete composition; the largest aggregate particle in the concrete is 8 mm, which is probably too large to get a homogeneous material for a specimen with a diameter of 46 mm. This is the diameter needed for the Metz set-up. However, in order to compare results obtained with the two test facilities, the concrete composition was kept the same for both set ups.

The advantages of the TNO set-up, compared to the Metz set-up, is the possibility to directly determine the fracture energy from the experimental data and also to measure the deformation and strains with time. These measurements provide insight in the behaviour of concrete during failure, which cannot be deduced from the experimental signals in Metz. In Metz, the experimental results are combined with numerical simulations, to determine fracture energy or to reconstruct failure behaviour.

The advantage of the Metz set-up is the easy determination of the strength. No costly strain gauges are needed and the method to determine the strength from the experimental results is short and simple.

3.8 Microscopic research

The aim of the experimental program is to get a better understanding of the physical mechanisms behind the rate effects on concrete tensile properties. To get a better understanding, not only the strength, fracture energy and stress-deformation curves are determined for different loading rates, but also the characteristics of the fracture planes. With the combination of the stress-deformation curve, the deformations and stresses with time and the characteristics of the fracture planes, the fracture behaviour of the concrete can be reconstructed and the influence of the loading rate on the fracture behaviour can be determined and quantified.

Microscopic research is necessary to characterize and quantify the fracture patterns. Therefore, samples suitable for microscopic research are fabricated from the specimens after the tensile tests were carried out. The samples are impregnated with epoxy and the fracture patterns are studied using a light microscope. The fabrication of the samples and the method used to determine the fracture characteristics are explained in detail in this paragraph.

3.8.1 Fabrication of samples

To be able to determine the fracture characteristics, like length and width of the fracture zone, samples are fabricated from the fractured specimens. The fractured concrete specimens are first impregnated with a fluorescent epoxy to fixate the fractured pieces together and to make the cracks more visible. The epoxy is composed of a resin with a fluorescent dye. Impregnation of the specimen is carried out in a vessel under low vacuum, to make sure that the pores and cracks are filled with the fluorescent resin.

The macro cracks are photographed, using a black light. Black light turns the parts of the specimen where the fluorescent epoxy is permeated into a very bright yellow, while the parts with no epoxy stay dark. This method increases the visibility of the smaller cracks.

When studying the macro cracks it was observed that only the distinct increasing amount of micro cracks for the MSHB tests compared to the static and SHB tests could be deduced from the pictures. For a proper analysis and quantification of fracture characteristics it was necessary to study the fracture in more detail at meso level (level of grains, cement paste and interfacial transition zone).

To study the cracks in more detail, so called thin-sections are fabricated. Thin-sections are very thin slices of concrete with a thickness of about 30 µm. The thin-sections can cover an area of about 45 mm x 30 mm. The preparation starts by sawing a sample with a thickness of approximately 15 mm from the concrete specimen (see Figure 3.43).

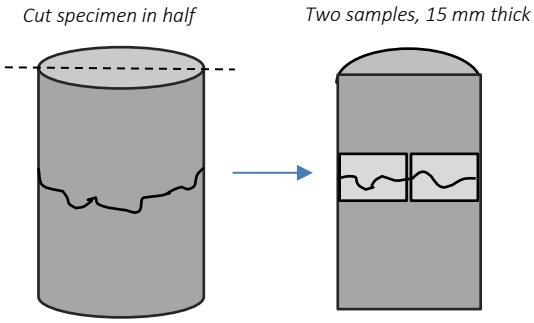

Figure 3.42 Cutting two samples from the concrete specimens to cover the crack.

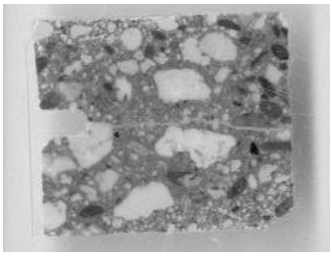

Figure 3.43 Sample sawn out of impregnated specimen, 15 mm.

In this case, because the size of the thin-sections is limited, two samples are chosen next to each other, to cover the whole crack area (see Figure 3.42). The surface of the sample is grinded until it is smooth. Next, the sample is impregnated with fluorescent epoxy. The impregnated surface is grinded to remove the excessive epoxy and a piece of glass is glued to the smooth surface. The sample is sawn to a thickness of about 0.3 mm and subsequently grinded until a thickness of about 30 µm remains. To finish, a very thin piece of glass is glued onto the surface of the sample to preserve it. An example of a finished thin-section is shown in Figure 3.44.

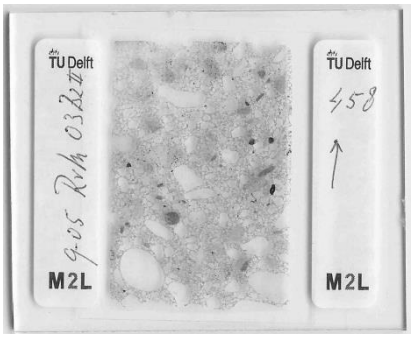

Figure 3.44 Example of thin-section.

Figure 3.45 Example of thick-section.

The fabrication of the thin-section will not lead to the initiation of more micro cracks. The sample is grinded to get a smooth surface and to remove any damage introduced due to the sawing process. Damage which is introduced after the impregnation will not be filled with epoxy and will, therefore, not be visible.

Thin-sections accurately show the micro cracks present in the samples. However, the fabrication of these thin-sections is very time consuming. Therefore, after finalizing the fabrication of the thin-sections for the static and SHB tests for Portland concrete, an alternative method has been considered for the remaining tests, so called thick-sections. These thick-sections have an area of about 75 mm x 65 mm and a thickness of approximately 25 mm (see Figure 3.45). The surface is grinded until it is smooth and any damage due to the sawing removed. Next, the sample is impregnated with fluorescent epoxy. The impregnated surface is grinded to remove the excessive epoxy and get a clear view of the cracks. When comparing the results of a thin-section and a thick-section for the same concrete specimen, it appears that the results are approximately the same. The amount of visible micro cracks is slightly smaller for the thick-sections. However, the difference in measured crack length between the thick-sections and the thin-sections is in the same range as the standard deviation. Therefore, thick-sections are accurate enough for the purpose of determination of fracture characteristics. Thin-sections have been used for the determination of the fracture characteristics of the static and SHB tests for Portland concrete. The thick-sections have been used for the remaining tests (MSHB tests for Portland concrete and all tests for BFS concrete).

3.8.2 Analysis of thin- and thick-sections

The thin- and thick-sections are first studied qualitatively. The sections are studied under a light microscope and the overall impression of the fracture patterns is determined. The main differences between the different loading rates and different curing conditions are identified.

Next, the thin- and thick-sections are quantitatively analysed. The fracture patterns are digitalized (see for example Figure 3.46 and Figure 3.47) and the lengths of the cracks and width of the fracture zone are determined. It was first attempted to digitalize the fractures with computational facilities. However, the fracture patterns could not be traced properly because of the limitations of the software available. The epoxy will penetrate all empty spaces in the concrete. This means that not only cracks, but also pores are filled and will show the same colour when exposed to a black light. The available software could, therefore, not distinguish between pores and cracks. Furthermore, the software could determine the amount of pixels in a range of colours (the epoxy has a slightly different colour, depending on the depth of the crack), but could not determine lengths of cracks.

Therefore, it was chosen to analyse the fracture patterns by hand and visual. To make sure the analysis was carried out the same for every section, the same person analysed all the sections. When starting a new series of sections, already completed series are used as a reference. Also, at the end of a series, all sections are studied a second time to ensure the same basic assumptions are applied.

After the fracture patterns are digitalized, the cracks are subdivided into three categories:

- Macro crack: the crack which physically separates the concrete specimen into two parts;
- Connected micro cracks: cracks that are directly connected to the macro crack;
- Isolated micro cracks: cracks that are isolated in the fracture zone.

Next, the total length of the three different types of cracks are determined and the width of the fracture zone established. The width of the fracture zone is defined as the width of the macro crack with accompanying connected micro cracks and long isolated micro cracks. The lengths of the different types of cracks and the width of the fracture zone are expressed in numbers of pixels.

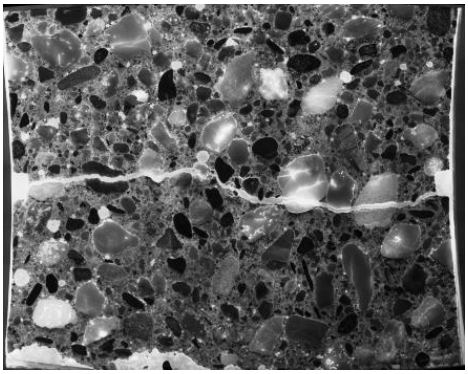

Figure 3.46 Photo of thick section exposed to light microscope (MSHB test N14).

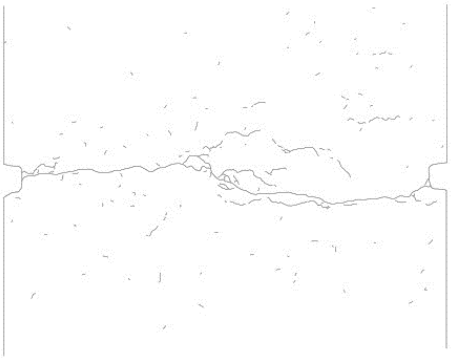

Figure 3.47 Digitalized fracture pattern (MSHB test N14).

The mm/pixels factor is estimated by photographing a marking gauge at the same scale as has been used for the analysis of the sections and accurately determining the distances between the marks. With this factor the lengths of the cracks and width of the fracture zone can be properly determined in metric numbers (mm).

The lengths of the macro crack, connected micro cracks and isolated micro cracks and the width of the fracture zone for the different loading rates and curing conditions are presented in chapter 4 and 5.

3.9 Conclusions

The described set-ups for static testing and dynamic testing (Split Hopkinson Bar and Modified Split Hopkinson Bar) enable us to test concrete at three different loading rates. The experimental results from tests conducted with these set-ups, combined with microscopic research of the fracture planes, provide information not only of the rate dependency of the tensile properties of concrete, but also on how the fracture behaviour of concrete is influenced by the loading rate.

The MSHB set-up has an advantage compared to set-ups used by other researchers because of the direct method to measure strains and deformations. The direct measurement method used in the SHB and MSHB set-ups also generates important information on real-time strains and deformations, which makes it possible to reconstruct

failure behaviour and give insight in the different causes of the observed rate effects. An approximate quantification of some of the causes is also possible when using the direct measurement method (see next chapters).

Experimental quantification of the rate dependency of concrete tensile properties and understanding of the physical mechanisms behind the rate dependency is needed to develop a proper material model and to be able to numerically predict the failure behaviour of concrete under high loading rates.

One of the causes of the rate dependency of concrete tensile properties is assumed to be moisture in the pore system of the concrete (see chapter 2). Therefore, the pore system and the moisture in the pores play an important role in the study of the rate effects for concrete and the understanding of underlying mechanisms. Methods like NMR or Mercury Intrusion Porosimetry provide the required information on pore structure and moisture distribution for a proper analysis of the experimental results and of the influence of moisture.

In chapter 4 and chapter 5 the experimental results on rate effects and the influence of moisture on the rate dependency of concrete tensile properties are presented and discussed.

CHAPTER 4: RATE EFFECTS ON TENSILE PROPERTIES OF NORMALLY CURED CONCRETE

4.1 Introduction

In this chapter the experimental results for static tests, Split Hopkinson Bar (SHB) tests and Modified Split Hopkinson Bar (MSHB) tests on concrete stored under normal conditions (20°C and 50% RH) are presented, analysed and discussed. Paragraph 4.2 presents the experimental output of the different set-ups and gives a critical review of the output and of the main reliability issues related to the dynamic test set-ups and data analysis. The accuracy of the various dynamic output parameters is addressed in the corresponding paragraphs, where the results of the different experiments are presented. The results on Young's modulus, tensile strength and fracture behaviour for three different loading conditions are presented in paragraphs 4.3, 4.4 and 4.5.

By combining the obtained experimental results on strength and fracture characteristics with real-time measurements on stresses and strains, the different causes for the rate effects on concrete tensile strength are identified and discussed by means of simple analysis. This analysis of the tensile strength results is presented in paragraph 4.6. Finally, the fracture behaviour is analysed in the same manner and is discussed in paragraph 4.7.

4.2 Dynamic experiments: critical review and reliability of dynamic data

The different set-ups and their accompanying measurement systems are described in chapter 3. Dynamic testing and the method to process the data to obtain the tensile strength and fracture energy are complex. Therefore, the processing of the data can lead to some inaccuracies. Especially for the reconstruction of the stress-deformation curves of

the SHB tests and MSHB tests, when synchronization of data or moving stress-waves within a time frame is necessary, the introduction of inaccuracies is inevitable.

In this paragraph, a critical review of the output of the Split Hopkinson Bar and Modified Split Hopkinson Bar tests is presented and the inaccuracies most likely to occur are identified and quantified. This paragraph will show that most inaccuracies are small enough to be disregarded or that they can be excluded from the results by combining the numerous and detailed experimental data measured at different locations on the concrete specimen.

4.2.1 Split Hopkinson Bar correction on synchronization

The dynamic experiments, the Split Hopkinson Bar tests as well as the Modified Split Hopkinson Bar tests, give detailed information on the fracture behaviour, by capturing the stresses and deformations with time using strain gauges and transducers (see chapter 3). The stresses and deformations are combined to obtain the stress-deformation curves and fracture energy. Figure 4.1 presents the average strains at the upper bar (Sub), at the lower bar (Slb) and at the specimen (Ssp) as well as the total deformation of the specimen (Def) for a representative SHB test '10c2' (for the location of the measured stresses, see Figure 4.2). The signals presented in Figure 4.1 are used for processing the experimental data, as has been explained in paragraph 3.6.2.

The strain signals of the upper bar, from which the strength of the specimen can be determined, are moved to the position of the strain gauges on the specimen, by synchronizing the tops of the signals using the linear elastic wave theory (see paragraph 3.6.2). Next, the stresses are calculated from the strains and combined with the deformation of the specimen measured by the Linear Variable Differential Transformers (LVDT's). However, the middle of the LVDT's is not exactly the same as the position of the strain gauges at the specimen (difference of 1.75 cm), which position is used to synchronize the strain signals. Therefore, a time correction on the LVDT-signals has to be executed.
The LVDT's also seem to display a small time delay, before capturing the deformation of the fracture plane. The deformation value is captured properly. However, a small time delay in the first part of the ascending branch is observed between the strain gauges at the specimen and the deformation measurements of the LVDT's.

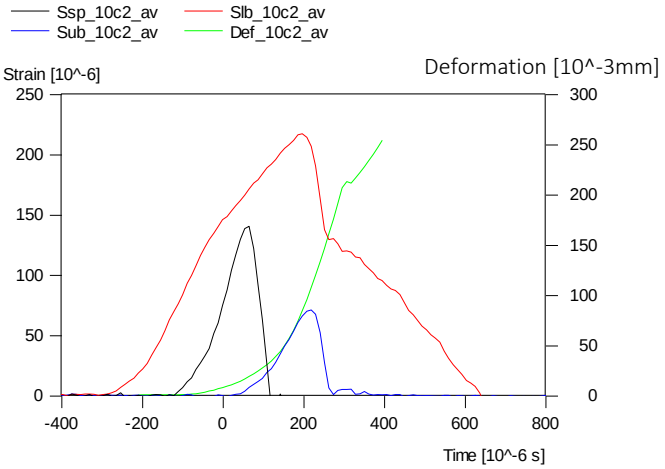

Figure 4.1 Output representative SHB tests (Ssp_av = average strains specimen; Slb_av = average strains lower bar; Sub_av = average strains upper bar; Def_av = average total deformation of the specimen).

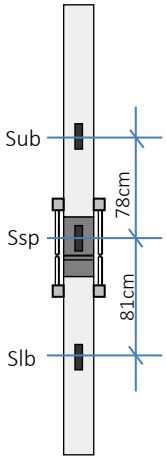

Figure 4.2 Location of the measured strains in SHB test.

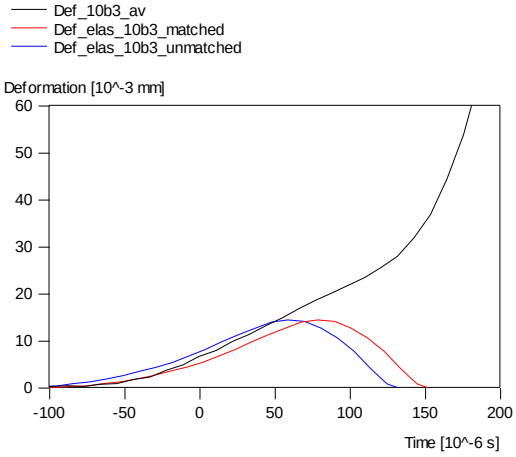

Figure 4.3 Time delay in LVDT's and synchronization difference excluded by manual best fit of elastic part deformation.

To correct the small difference due to synchronization as well as the time delay of the LVDT's, the strain measurements are manually synchronized with the deformation measurements by best fit of the starting point and the first part of the ascending branch of the deformation with the elastic deformation calculated from the strain measurements

at the specimen (see the difference between def_elas_matched (red) and def_elas_unmatched (blue) in Figure 4.3). The time difference, with an average of 17 µs, is hereby known and can be used to properly synchronize the strains from the upper bar with the deformation. This manual correction has an influence on the shape of the stress-deformation curve and, therefore, on the fracture energy. Due to the correction, the fracture energy values decrease with an average of 5%, considering all performed Split Hopkinson Bar tests for Portland as well as Blast Furnace Slag cement concrete.

4.2.2 Linear elastic behaviour in MSHB tests

Assuming linear elastic behaviour of the concrete specimen, the uniaxial wave theory can be used to shift the compressive and tensile waves to obtain the strength and the stress-deformation curve, as explained in paragraph 3.7.3. Therefore, it is important to check whether the concrete material is behaving linear elastic outside the fracture zone.

Concrete will behave linear elastic until it is damaged. To check whether damage has occurred, the residual strains of the strain gauges are examined. No residual strains are observed for the induced compressive wave at position R1-15 (see Figure 4.5). This means that with a maximum compressive strain of approximately 600 µstrain no damage is introduced. It is assumed that tensile damage has occurred when a residual strain larger than 5% of the maximum tensile strain reached in a MSHB test (approximately 400 µstrain) is observed in a particular strain gauge. Strain gauges that have a residual strain outside the range of 20 µstrain are, therefore, not taken into account for the determination of the strength and fracture energy.

The average strain of the strain gauges is determined at various cross-sections of the specimen, for instance the average of strain gauges R9, R10, R14 and R17 at the cross-section 40 mm from the notch (position R9-17, see Figure 4.5). Figure 4.4 shows an example of the different strain measurements at the cross-sections of a representative MSHB test. The location of the different strain gauges and the important cross-sections are indicated in Figure 4.5. On average, for the cross-sections beyond the notch at respectively 40 mm and 75 mm distance three out of four strain gauges have a residual strain smaller than 20 µstrain and, therefore, it is assumed that no severe damage has been introduced at these positions and that the concrete can be considered to have behaved elastically.

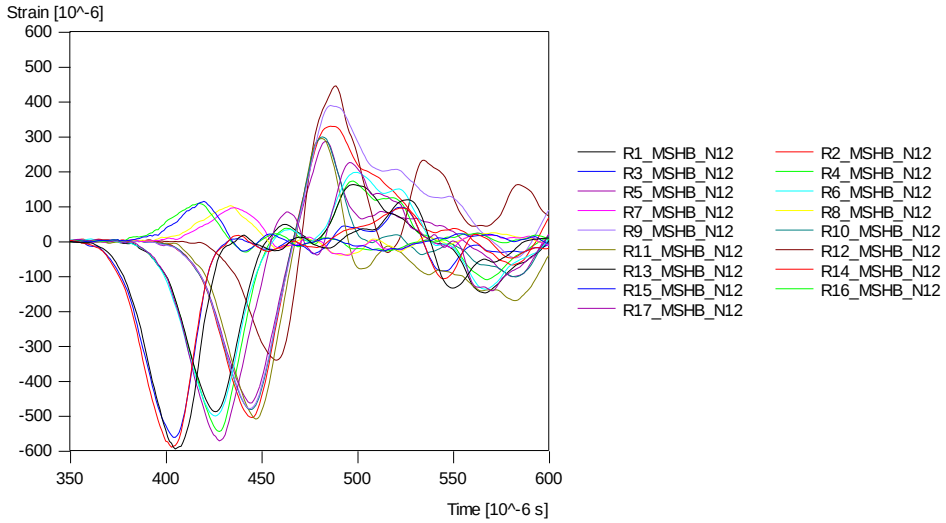

Figure 4.4 Example of experimental output of the strain gauges of a representative MSHB tests.

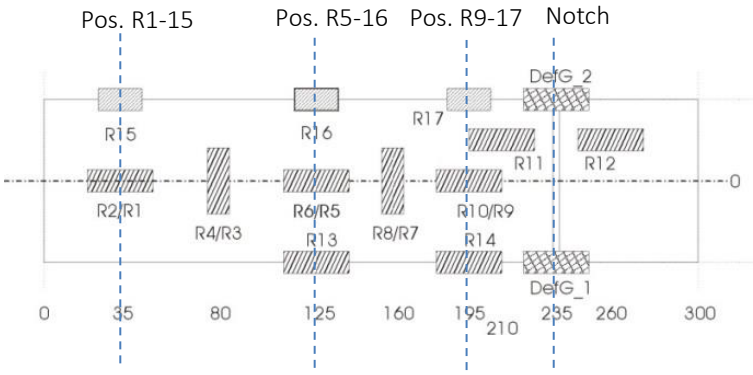

Figure 4.5 Scheme of the locations of the strain gauges on the specimen and the position (pos. x) of the relevant cross-sections.

The small residual strains at cross-section R9-17, although smaller than 20 µstrain, might influence the strength. The average residual strain in the concrete at cross-section R9-17 is 6 µstrain. A residual strain of 6 µstrain can indicate a permanent elongation of the fracture zone of 0.18 µm, the measuring length being 30 mm. This damage is very small compared to the total deformations reached in the fracture zone (150 µm).

A residual strain of 6 μstrain can give an overestimation of the tensile strength of about 0.24 MPa (assuming Young's Modulus 40 GPa), which is smaller than the standard deviation of the tensile strength results (see Table 4.2).

The residual strain outside the notched cross-section is small compared to the maximum deformation. Also, the corresponding delta stress Δσ due to this small residual strain is smaller than the standard deviation on tensile strength. Therefore, it is assumed that the residual strains are small enough to have negligible effect on the strength and fracture energy results and they are, therefore, disregarded.

4.2.3 Compressive damping in Modified Split Hopkinson Bar tests

The maximum compressive strain is decreasing when the compressive wave is propagating along the specimen (see Figure 4.6). The decrease is not due to the signal dispersion, but due to material damping, as has been explained in paragraph 3.7.3.
For the reconstruction of the response of the failure zone at the notch, the stress conditions are derived from the strain records along the specimen. Therefore, the material damping has to be taken into account.

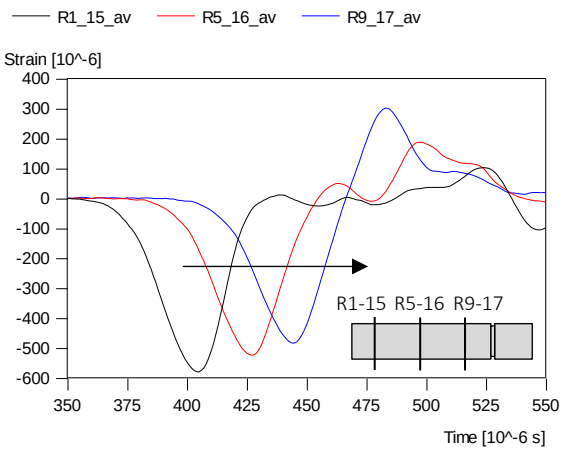

Figure 4.6 Average strains at each cross-section of MSHB test.

The average reduction of the maximum compressive strain, i.e. the compressive damping, between cross-section R5-16 and cross-section R9-17 is 6%, which is 0.8% /cm (see

Figure 4.7). Assuming that the compressive damping is a material parameter and, therefore, constant, the compressive damping from cross-section R9-17 to the notch would be 3%. This dispersion effect due to heterogeneity of the material, or compressive material damping, has been taken into account when processing the signals and moving the compressive strain signals to the location of the notch.

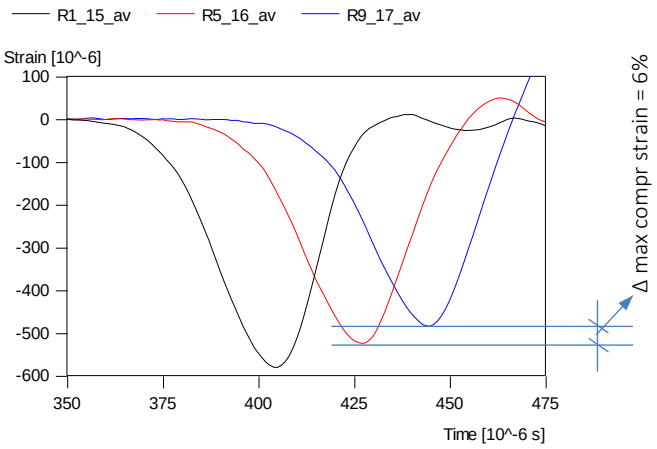

Figure 4.7 Compressive damping; maximum compressive strain decreases from position R1-15 to position R5-16 and R9-17.

4.2.4 Tensile damping in Modified Split Hopkinson Bar tests

Not only the maximum strain of the compressive part of the incident wave decreases due to material damping, the maximum tensile strain also decreases (see Figure 4.6). The tensile material dispersion seems to be even higher, as can be seen from the significant decrease of the tensile maximum strain in Figure 4.6.

In the MSHB tests on concrete specimens, the tensile amplitude decreases with an average of 28% from cross-section R9-17 to cross-section R5-16 (see Figure 4.8). This corresponds to a tensile damping of 4% /cm.

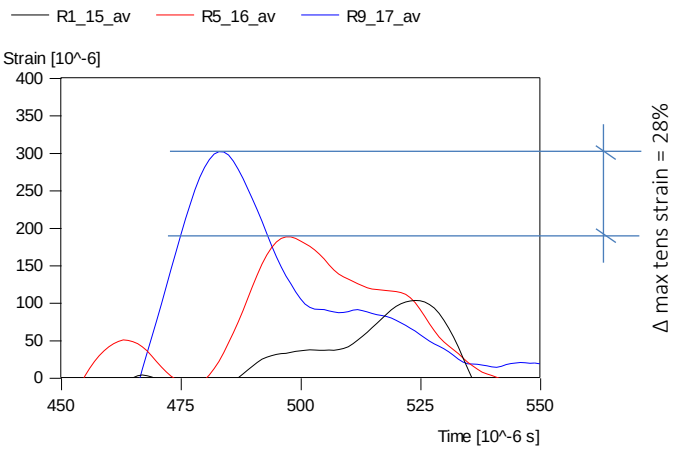

Figure 4.8 *Tensile damping; maximum tensile strain decreases from position R1-15 to position R5-16 and R9-17.*

Three different phenomena cause the decrease of the maximum in the recorded tensile strain data;

1) the interaction of waves;
2) tensile material damping;
3) disturbance of waves due to the fracture process.

Part of the decrease in maximum tensile strain is due to the interaction of the tensile wave and the returning compressive wave from the front of the specimen. To prove this, calculations of the interaction of the waves have been made, assuming linear elastic behaviour and no material damping. For these calculations the compressive part of cross-section R5-16 has been used as an incident wave. The incident wave travels to the free end of the specimen and returns as a tensile wave. This tensile wave then travels to the other end of the specimen, which is now also free due to the fact that the plaster has broken, and returns as a compressive wave, and so on (see Figure 4.9).

At position R1-15, which is located 35 mm from the end of the specimen, the interaction of the waves causes a strong decrease of the maximum tensile strain (see tensile part of the blue curve in Figure 4.9). However, at cross-section R5-16 and cross-section R9-17, the maximum tensile strain is only slightly affected by the returning waves (see black and red curve in Figure 4.9).

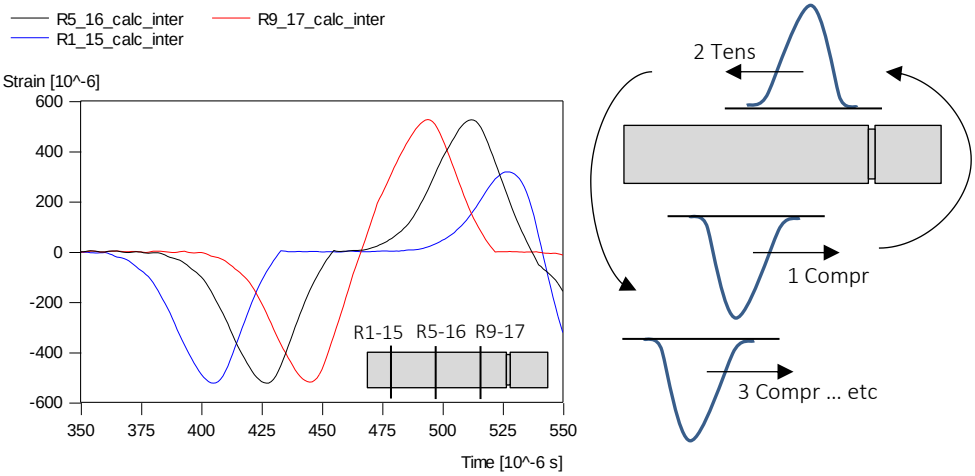

Figure 4.9 *Interaction of waves strongly influences the maximum tensile strain at position R1-15 (blue: position R1-15, black: position R5-16 and red: position R9-17).*

The interaction of the tensile wave with the compressive wave returning from the front of the specimen only contributes to a small extent to the decrease of the maximum tensile strain. Therefore, the substantial decrease in maximum tensile strain from position R5-16 to position R9-17 cannot be explained by the interaction of the waves but must be due to material damping or disturbance of the waves due to the fracture process.

The tensile material damping will probably be of the same order as the compressive material damping when no damage occurs. This means that the disturbance of the linear wave due to the fracture process is the main cause of the reduction of the maximum tensile strain.

The non-homogeneous fracture process is illustrated in Figure 4.10; the individual strain measurements have very different shapes at cross-section R9-17. The non-homogeneous fracture process influences the linearity of the tensile wave and, therefore, the tensile damping and decrease of the maximum tensile strain. The non-linearity of the tensile wave behind the fracture zone is also shown by the strain measurements at position R11 (see Figure 4.10); the maximum strain at this position should be higher than the average strain at cross-section R9-17, because it is closer to the notch and less influenced by tensile damping. However, the maximum strain at position R11 is sometimes higher than the maximum strain at R9-17 and sometimes lower. Not only does this show that the fracture

process influences the strain measurements behind the fracture zone dramatically, it also proves that it is important to use four strain gauges at one cross-section to be able to average the strain measurements and get a fair image of the average strains at that particular cross-section.

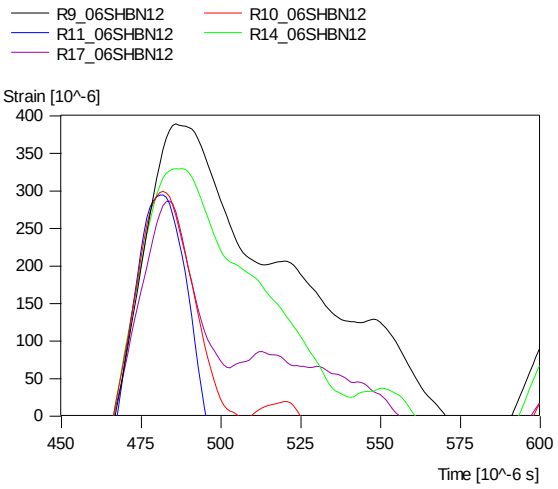

Figure 4.10 Individual strains vary at cross-section R9-17 and strain at position R11 is lower than average at cross-section R9-17.

When assuming that the tensile material damping is constant and 4% /cm, the maximum tensile strain at the notch would be 16% higher than calculated in the presented results. However, it is not sure that the tensile material damping is constant, or that the reduction of the maximum tensile strain increases or decreases when traveling away from the notch area. Therefore, it is hard to accurately quantify the effect on the presented experimental results. Combining the experimental results with numerical modelling might give more information on the tensile material damping and the influence of the fracture process on the linearity of the wave.

For the present research, the tensile material damping is considered to be the same as the compressive material damping, which is 0.8% /cm for normally cured Portland concrete (see paragraph 4.2.3). In the experiments the wave speed is the same for tensile or compressive waves, which means that material properties like the Young's modulus are also the same. Therefore, we can assume that concrete will probably also behave similar

for compressive as well as tensile loading when considering material damping. The assumed tensile material damping of 0.8% /cm will only lead to a moderate increase in maximum tensile strain when moving the tensile strains from cross-section R9-17 to the notch. Since the influence of the non-homogeneous fracture process on the amplitude is not taken into account, which is probably the main cause for the decrease in maximum tensile strain, the presented results will be conservative and in reality stresses at the notch and the calculated strength will be higher.

4.2.5 1D analysis

The analysis of the dynamic tests presented in this thesis is based on 1D wave propagation, assuming that the process is most dominant in the axial direction. For this 1D analysis it is assumed that the stress distribution is homogeneous in the radial direction; this means that the stresses are equal in each point of a certain cross-section. In reality, in the static as well as the dynamic SHB and MSHB tests, the stresses are influenced by the presence of the notch and the stress distribution at this cross-section will not be homogeneous.

Influence of notch

It is well known that a notch will introduce higher stresses at the notch tip. Consequently, before the peak load is reached, damage will be introduced at an earlier stage at the notch tip and a lower strength will be measured than when no notch is applied. However, this effect is mitigated by the fact that concrete exhibits pre-peak non-linearity. Minor damage is introduced before the peak stress is reached. But due to this pre-peak damage, the local higher stresses at the notch tip will decrease and the effect on the final strength result will be less than for a linear elastic fully brittle material. The influence of the notch on the measured stresses in the concrete specimens will be even less after the peak stress is reached, due to softening in the fracture zone and around the notch.

For the static loading conditions, tests have been conducted with different notch depths. The results from these tests have shown that the influence of the notch depth is small, compared to the standard deviation in the static tests (see Appendix A). Also, Weerheijm has conducted tests with different notch depths and types of concrete for the SHB test set-up. He found that the dynamic strength was affected by the application of notches, but mainly for the higher quality concrete he tested and not for the lower quality concrete [Weerheijm 1992].

Since a notch is needed to gain information on the fracture behaviour of a single fracture zone, it is accepted by the author that the notches influence the tensile strength results and that the results will be somewhat lower than when no notch would have been applied.

Although the stress distribution in the notch cross-section is not homogeneous, it is assumed that the general behaviour of the concrete is captured in the dynamic tests because the measurements of the strains are taken *outside* of the fracture zone and not directly in the notch area or in the fracture zone.

Surface vs inside of specimen

Another question is whether the measurements on the surface of the concrete specimen are representative for the entire cross-section. The data is collected with measurement devices attached at the outside surface of the concrete specimens, while the fracture process and the transmitting of waves take place inside the specimen. The analysis of the dispersion effects has already shown that the SHB tests can be considered 1D, based on the ratio between the bar diameter and the wave length (see paragraph 3.6.4). For the MSHB tests, this ratio indicates that dispersion effects can be expected (see paragraph 3.7.4). However, linear elastic numerical 3D simulations for the spalling test load conditions, which are proven most critical, have shown that there is some variation in strains within a cross-section, but that the differences in the strains is limited (less than 5%). Therefore, it can be assumed that the measured strains at the surface are representative for the entire cross-section.

Summarized, although it is recognized by the author that the notches will influence the results to some extent, the effect is believed to be small enough to allow 1D analysis.

4.2.6 Summary of reliability of experimental data

The experimental data of the dynamic SHB and MSHB tests is extensive and the reliability of the measurements is very good; the strain gauges and LVDT's measure the real time deformations and strains. Due to the extensive data from a single test, like for instance from the large number of strain gauges in the MSHB tests, it is possible to correct the data when needed. The processing of the data for the reconstruction of the stress-deformation curves, when synchronization of data or moving stress-waves within a time frame is

necessary, can lead to some inaccuracies. Most of the inaccuracies are negligible or can be excluded, as has been explained in this paragraph. Only one large inaccuracy cannot be quantified and excluded from the available experimental data, i.e. the influence of the non-homogeneous fracture process on the decrease of the maximum tensile strain in the MSHB tests. This means that the tensile strength and fracture energy results are underestimated and will be higher in reality.

4.3 Young's modulus

In this paragraph the results on Young's modulus measurements are presented. The Young's modulus is determined from the experimental data of the static, SHB and MSHB tests. The slope of the ascending branch of the static stress-strain curve determines the static Young's modulus. The part of the ascending branch where no matrix fracture has occurred yet, which is from $0.1 \cdot f_{t,max}$ up to $0.8 \cdot f_{t,max}$, has been used to determine the slope and the Young's modulus (see paragraph 2.3.3).

The Young's modulus from the MSHB tests is calculated using the concrete wave speed and equation 3.10, the average density of the concrete being 2330 kg/m^3.

For the Split Hopkinson Bar tests, the moderate loading regime, it is more difficult to accurately determine the Young's modulus from the experimental data. The concrete wave speed in the SHB tests cannot be determined and the stress-deformation curve has no linear ascending branch and is, therefore, not suitable for the determination of the Young's modulus (see also paragraph 2.3.3). Since these methods used for the static and MSHB tests cannot be applied for the SHB tests, the Young's modulus is calculated by combining the available strain data. The measured strains at the specimen, as well as the measured strains at the upper bar are located behind the fracture zone. Therefore, it is assumed that the strain measurements at the upper bar and the strain measurements at the specimen both determine the strength of the specimen.

This means that with the strain data from the specimen and the aluminium upper bar, the Young's modulus of the concrete can be related to the Young's modulus of the aluminium bar, which is not affected by rate effects (see equation 4.1).

$$\sigma_{specimen} = \sigma_{upper\ bar} \quad \leftrightarrow \quad \varepsilon_{specimen} \cdot E_{concrete} = \varepsilon_{upper\ bar} \cdot E_{aluminium} \tag{4.1}$$

When using equation 4.1, the dynamic Young's modulus of concrete for the SHB tests can be determined.

4.3.1 Experimental results

The average results for the Young's modulus (E) are presented in Table 4.1. The results for the SHB tests appear to be less accurate than for the static and MSHB tests, which is shown by the higher standard deviation for the SHB tests. The number of tests (n) on which the average is based is also presented in Table 4.1.
The results on Young's modulus show that the Young's modulus increases with increasing loading rate.

Table 4.1 Average results for the Young's modulus, E.

Series	d_{notch} [mm]	n [-]	$\dot{\varepsilon}$ [1/s]	E [GPa]	St.dev. [GPa]	E_{dyn}/E_{stat} [-]
Stat	2	6	$2.7 \cdot 10^{-6}$	32.6	2.6	1.0
SHB	2	6	1.1	35.7	4.2	1.1
MSHB	3	8	46.2	40.0	1.5	1.2

The concrete wave speed is used to determine the Young's modulus from the MSHB tests. A small error in the determination of the wave speed has an effect on the accuracy of the Young's modulus results. An error of 10 m/s on an average wave speed of 3900 - 4200 m/s causes an over- or underestimation of the Young's modulus of 0.2 GPa, which is approximately 0.5% and, therefore, negligible.

4.3.2 Results from literature and standards

The Young's modulus in the previous section is determined experimentally. Previous research has resulted in the following empirical formula [CEB-FIP 1988];

$$\frac{E_{dyn}}{E_{stat}} = \left(\frac{\dot{p}}{\dot{p}_0}\right)^{0.016} \tag{4.2}$$

with $\dot{p} = loading\ rate$ and $\dot{p}_0 = 0.1\ MPa/s$.

The average loading rate for SHB tests being 39 GPa/s and for MSHB tests 1860 GPa/s, the dynamic Young's Moduli according to equation 4.2 are E_{SHB} = 40.1 GPa and E_{MSHB} = 42.6 GPa respectively, assuming E_{stat} = 32.6 GPa (see Table 4.1). These values are higher than the experimentally determined Young's moduli for the SHB and MSHB tests presented in Table 4.1 (E_{SHB} = 35.7 GPa and E_{MSHB} = 40.0 GPa).

4.4 Tensile strength

The results on tensile strength are presented in this paragraph. The tensile strength of the specimens is determined by the peak value of the stress-displacement and stress-deformation curves. Although some inaccuracies are included which have led to an over- or underestimation of the tensile strength results (see paragraph 4.2), it is believed that the results give a realistic view of the rate effects on the tensile strength.

4.4.1 Experimental results

The average values on tensile strength for the static, moderate and high loading rates are summarized in Table 4.2. The results show that the strength slightly increases in the loading regime up to about 1 /s and that the strength increases rapidly in the high loading rate regime. These results are similar to the results found in literature (see next subparagraph).

Table 4.2 Average results for tensile strength, f_t.

Series	d_{notch} [mm]	$\dot{\varepsilon}$ [1/s]	St.dev. [-]	n [-]	f_t [MPa]	St.dev. [MPa]	f_t/f_{stat} [-]
Stat	2	$2.7 \cdot 10^{-6}$	$1.0 \cdot 10^{-8}$	6	3.30	0.32	1.0
SHB	2	1.1	0.26	6	5.58	0.21	1.7
MSHB	3	47.3	4.20	8	10.87	0.90	3.3

For the Modified Split Hopkinson Bar tests, the high loading rate regime, the concrete wave speed is used to move the compressive and tensile waves to the position of the notch and to calculate the strength and fracture energy (see paragraph 3.7.3). Therefore, the determination of the wave speed is very important and should be done carefully. The wave speed is experimentally determined by dividing the distance between the strain gauges by the time difference between the tops of the compressive waves. With this method, nine different values of the wave speed are calculated. The average from these calculated wave speeds is taken as starting point. Next, the value of the wave speed is manually adjusted to make sure that the strains at cross-section R5-16 can be correctly transferred to cross-section R9-17 and location R11 and , therefore, also to the notch. The calculated strains at position R9-17 and R11, using the calculated and adjusted wave speed, have to be in accordance with the real measured strains. The adjusted concrete wave speed is rounded off to the nearest multiple of 10 m/s. The correction varies between 10 - 30 m/s (average concrete wave speed approximately 4100 m/s).

The inaccuracy in the calculated strength, when an error in the determination of the wave speed of 10 m/s has been made, will be about 0.06 MPa. This can be an overestimation as well as an underestimation, but only has a small influence on the strength results and is, therefore, disregarded.

The experimental results on tensile strength are presented in Figure 4.11. This figure clearly shows an increase in strength, for the moderate regime as well as the high loading rate regime. The mild increase in tensile strength in the moderate regime is believed to be due to *free water in the pore system*. This has been proposed and experimentally investigated by other researchers in the past [Ross 1996, Rossi 1992]. In the next chapter, the influence of the moisture content on the rate dependency of concrete tensile properties is extensively studied and quantified.

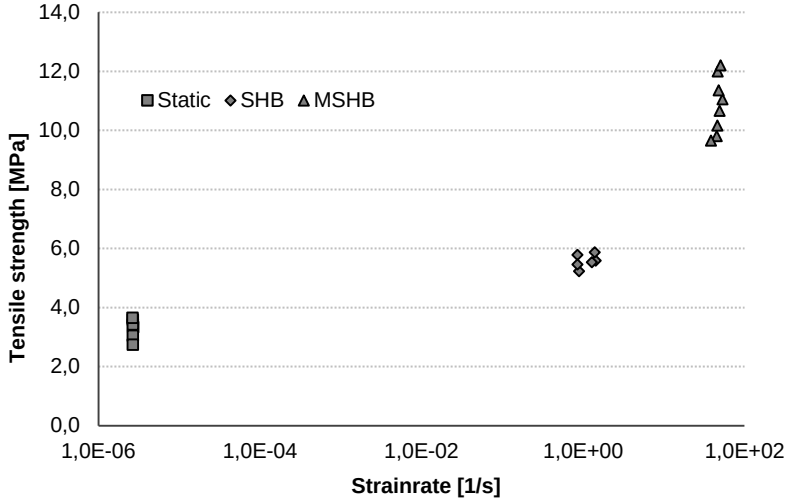

Figure 4.11 Experimental results on tensile strength for static, SHB and MSHB tests as a function of the strain rate.

The strength increase in the high loading rate regime (strain rate higher than approximately 1 /s) is believed to have several causes. One of the causes of the strength and fracture energy increase is believed to be *structural inertia of the failure zone* [Ozbolt 2013, Cotsovos 2008a, Cotsovos 2008b, Weerheijm et al 2013]. Structural inertia effects can significantly change the stress state and strains of the concrete in this zone. There are various sources of inertia, like for instance the radial inertia in a cylindrical specimen, but also the inertia of the accelerated material of the fracture zone itself. Structural inertia effects in the fracture zone develop when the fracture zone is formed, deformation concentrates and the deformation rate increases. In this experimental research the focus concerning the inertia effects is on the possible contribution of the structural inertia of the weakened fracture zone (axial direction) to the enhanced strength and fracture energy. Effects of dynamics on macroscopic stress distribution are not considered. The possible contribution of structural inertia of the fracture zone to the enhanced strength is discussed in paragraph 4.6.

4.4.2 Results on tensile strength from literature

Figure 4.12 shows the results found in literature on dynamic loading and tensile strength (see also paragraph 2.4.2) and the experimental data from the presented research. The results are presented as Dynamic Increase Factor (DIF), which is the dynamic strength

divided by the static strength. The test data from literature in Figure 4.12 show two regimes; a moderate and a high strength increase. However, the scatter in the results is large. The high scatter is caused by the difference in concrete mixture, testing techniques, size of specimens and moisture content.

The tendencies that can be derived from the experimental data are:

- The transition from moderate to high rate dependency of concrete properties occurs at strains in the order of 1 /s. This point shifts to higher strain rates when the heterogeneity of concrete decreases and strength increases. Therefore, rate dependency of concrete tensile properties increases with decreasing concrete quality and decreases for mortars or micro-concretes.
- The rate dependency of concrete tensile properties strongly depends on the moisture content of the material (see also chapter 5).

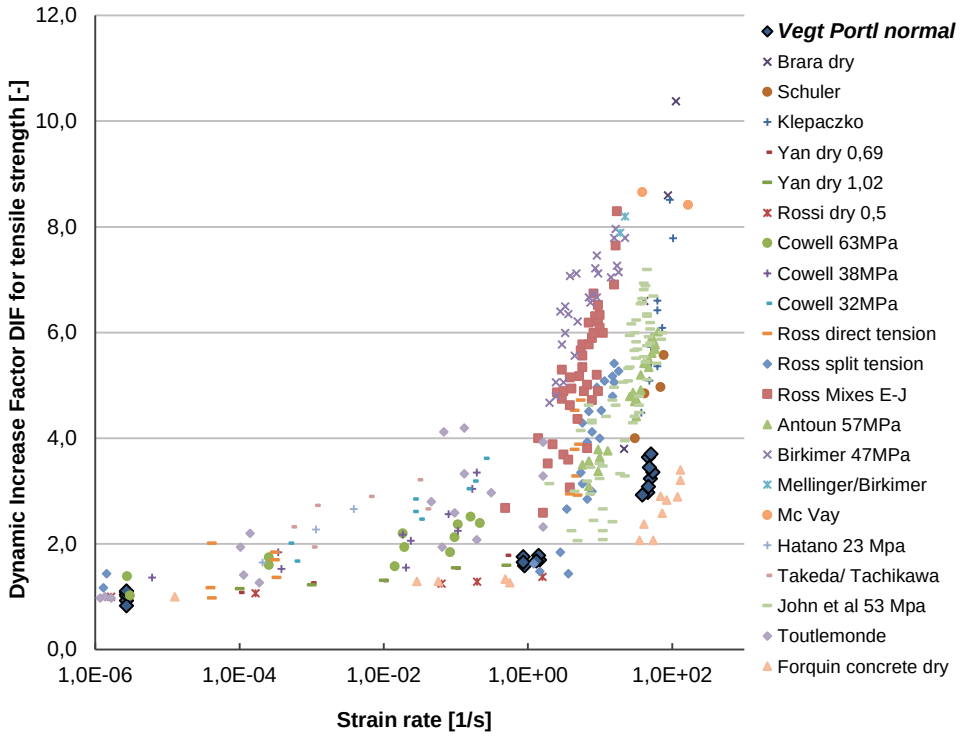

Figure 4.12 Experimental data on the DIF for tensile strength as a function of the strain rate [Weerheijm et all 2013].

4.5 Failure behaviour

This paragraph presents the experimental results on failure behaviour; the stress-displacement and stress-deformation curves as well as the fracture energy and fracture characteristics. A few conclusions are drawn from the experimental results. The reconstruction of the failure behaviour and some simple analyses to determine and quantify the causes of the rate effects on fracture behaviour are presented in paragraph 4.7.

4.5.1 Stress-displacement and stress-deformation curves

The failure behaviour of the concrete at three different loading rates is reflected in the stress-displacement and stress-deformation curves. For static, Split Hopkinson Bar as well as Modified Split Hopkinson Bar tests, these curves are presented in respectively Figure 4.13, Figure 4.14 and Figure 4.15. For mixtures see paragraph 3.3.1.

The shape of the stress-displacement and stress-deformation curves, which reflects the failure behaviour, is very similar for the three representative static tests (see Figure 4.13).

The shape of the individual stress-deformation curves are also similar to each other for the SHB as well as the MSHB tests, as is shown in Figure 4.14 and Figure 4.15.

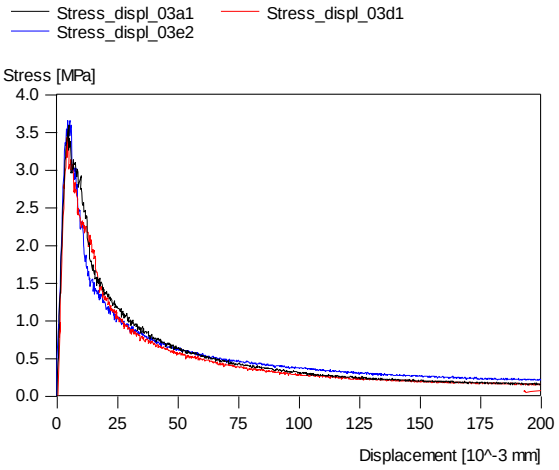

Figure 4.13 Stress-displacement curves of three representative static tests.

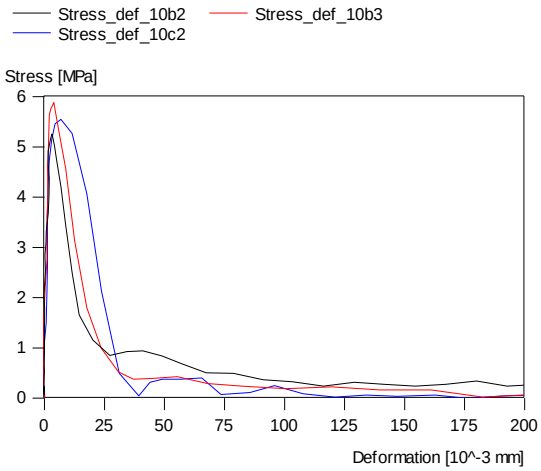

Figure 4.14 Stress-deformation curves of three representative SHB tests.

Even the stress-deformation curves of the MSHB tests, which have the highest standard deviation for strength and fracture energy, have a similar descending branch, although the bumps occur at different deformations (see Figure 4.15). The similarity in the first part of the descending branch means that, even though the fracture energy is different, the coalescence of the micro cracks is similar for each individual test within a certain loading rate regime.

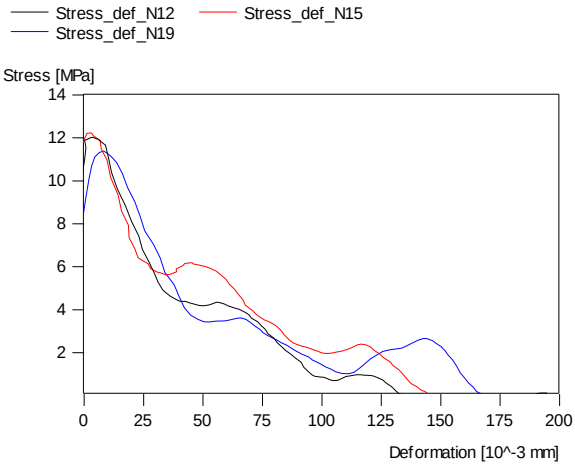

Figure 4.15 Stress-deformation curves of three representative MSHB tests.

A comparison of the stress-displacement curve of the static test and stress-deformation curves of the SHB and MSHB tests (see Figure 4.16) can give insight in the changes in failure behaviour due to the increased loading rate. The softening curve for the static and moderate regime has two branches. As has been explained in paragraph 2.3, the first branch represents the formation and coalescence of the micro cracks and the second branch reflects the final formation and opening of the macro crack, followed by final failure.

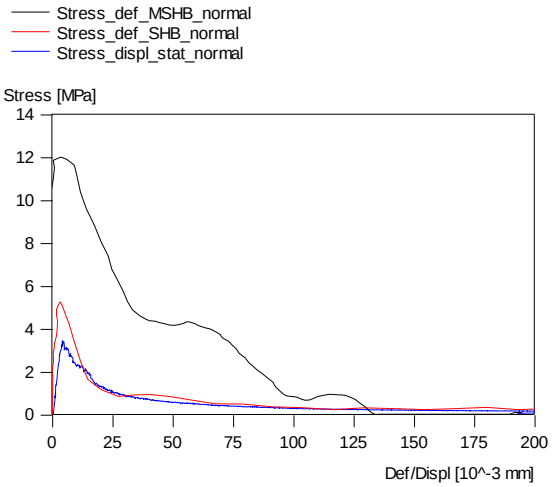

Figure 4.16 Comparison of representative static, SHB and MSHB tests.

The data for the moderate regime shows that the second branch of the softening curve is not affected up to a loading rate of 50 GPa/s (see Figure 4.16). The macro crack is fully opened at a deformation of approximately 150 – 200 mm and is not affected by loading rate.

For the high loading rate regime, the two branches are still present but much less obvious than for the moderate regime. The stress-deformation curve of the MSHB tests also shows a wider and rounder peak compared to the sharper peaks of the static and SHB tests (see Figure 4.16). This wider peak indicates pre-peak nonlinearity and a higher amount of micro cracking for the high loading rate regime.

4.5.2 Bumps in the Modified Split Hopkinson Bar tests

When considering the stress- or strain signals from the MSHB tests, not one, but two or three peaks are displayed in the descending branch (see Figure 4.15, Figure 4.16 and Figure 4.17). These peaks reflect the fracture process, when part of the tensile wave is reflected as a compressive wave at the growing fracture zone, travels to the free end and returns to the notch as a 'second' tensile wave. When the fracture process is not completed, this 'second' wave can partly travel through the notch area and is measured by the strain gauges. The effect of partial reflection of the tensile wave on the fracture zone can be repeated until the fracture process is finished and the specimen is split in two separate parts.

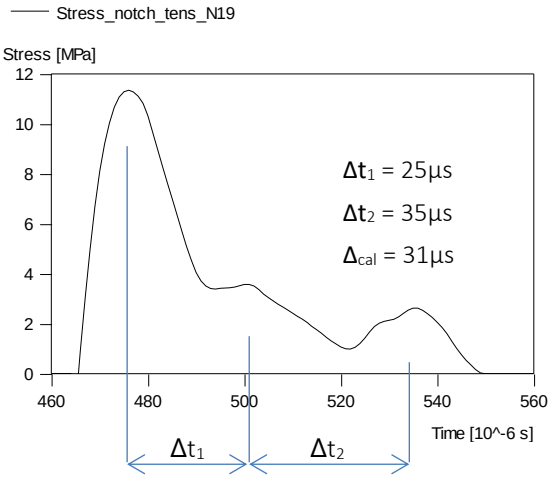

Figure 4.17 Stress-time at the notch, for MSHB test (N19).

Figure 4.17 shows the stress-time relation at the notch for a representative MSHB test. The time differences between the peaks are Δt_1 and Δt_2. The calculated time for a wave to travel up and down from the notch to the free end of the specimen, depending on the determined concrete wave speed for each specific test (approximately 4100 m/s), varies from 30 µs to 32 µs. The position of the second peak in the stress-deformation curve is difficult to determine accurately, since the 'second' tensile wave is interacting with and added to the first main tensile wave. The 'third' wave does not interact with the first tensile wave and the peak is, therefore, easier to determine. The average of the time differences between the peaks matches with the calculated time to travel up and down from notch to

end, for all MSHB tests. This proves that the cause of the multiple peaks, or 'bumps', can be found in reflecting tensile waves during the fracture process.

The question remains why the strains can actually increase after the fracture process has started and the concrete is damaged. This is probably partly due to structural inertia effects. When the fracture zone is formed, the deformation rate increases. Due to this increase in deformation rate in the fracture zone, inertia forces are initiated to maintain equilibrium. Inertia effects will affect the shape of the stress-deformation curve and, therefore, the value of the fracture energy. The effect of structural inertia of the fracture zone on the experimental results is discussed in detail in paragraph 4.6 and paragraph 4.7.

4.5.3 Fracture energy

The fracture energy (G_f) is determined by calculating the area under the stress-displacement and stress-deformation curves (see paragraph 2.3.3 and previous paragraph). The average results are summarized in Table 4.3.

Table 4.3 Average results for fracture energy, G_f.

Series	d_{notch} [mm]	$\dot{\varepsilon}$ [1/s]	n [-]	G_f [N/m]	St.dev. [N/m]	G_f/G_{fstat} [-]
Stat	2	$2.7 \cdot 10^{-6}$	6	120.2	12.1	1.0
SHB	2	1.1	4	133.2	9.7	1.1
MSHB	3	47.3	8	551.3	176.4	4.4

A small inaccuracy can be included in the fracture energy results of the MSHB tests, if the wave speed of concrete is not determined accurately (see paragraph 4.4.1). However, an error in the determination of the wave speed of 10 m/s on an average wave speed of approximately 4100 m/s will lead to an increase or decrease of the fracture energy of approximately 3 N/m, which is much smaller than the standard deviation of the experimental results and can, therefore, be neglected.

Also, the stress-displacement curves of the SHB tests may include a small inaccuracy due to the synchronization process of the deformation measurements (see paragraph 4.2.1).

An error in synchronizing of +/-2 µs, will lead to an over- or underestimation of the fracture energy of about 3 N/m. This is negligible, compared to the standard deviation for the fracture energy results of the SHB tests (see Table 4.3).

The results in Table 4.3 and Figure 4.18 show that in the moderate regime (loading rates up to 50 GPa/s) the fracture energy does not increase when the loading rate increases. After this threshold, the fracture energy is highly rate dependent. This is also found in literature (see next paragraph).

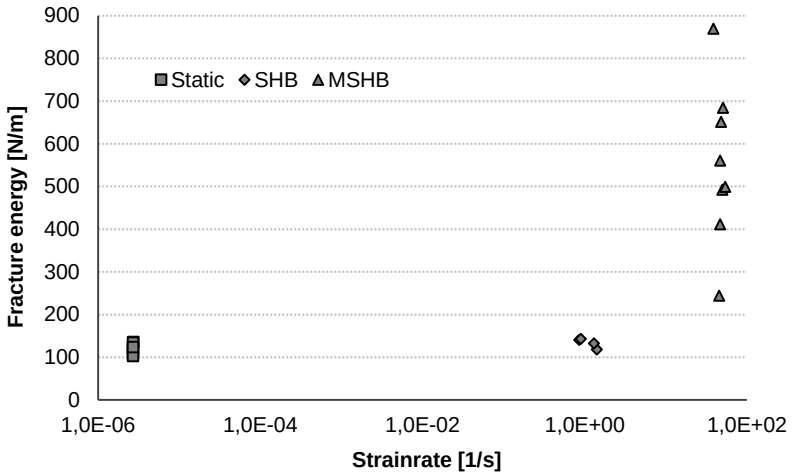

Figure 4.18 Experimental results on fracture energy for static, SHB and MSHB tests as a function of the strain rate.

4.5.4 Results from literature on fracture energy

Results on the influence of loading rate on fracture energy is scarce. The fracture energy results from literature and the experimental data are presented in Figure 4.19.

The results exhibit a large scatter, due to differences in concrete composition and test set-up. For instance, Schuler used a similar concrete composition and specimen size as used in the research from Delft presented in this thesis, but different diagnostics [Schuler 2004, Schuler 2006]. Schuler derived the separation velocity and failure time from high speed recordings and assumed a linear time dependency of the separation velocity and force. As

can be seen from the recordings of the MSHB tests, the separation velocity is not linear in time (see paragraph 4.6). This will probably cause an underestimation of the fracture energy in the data of Schuler.

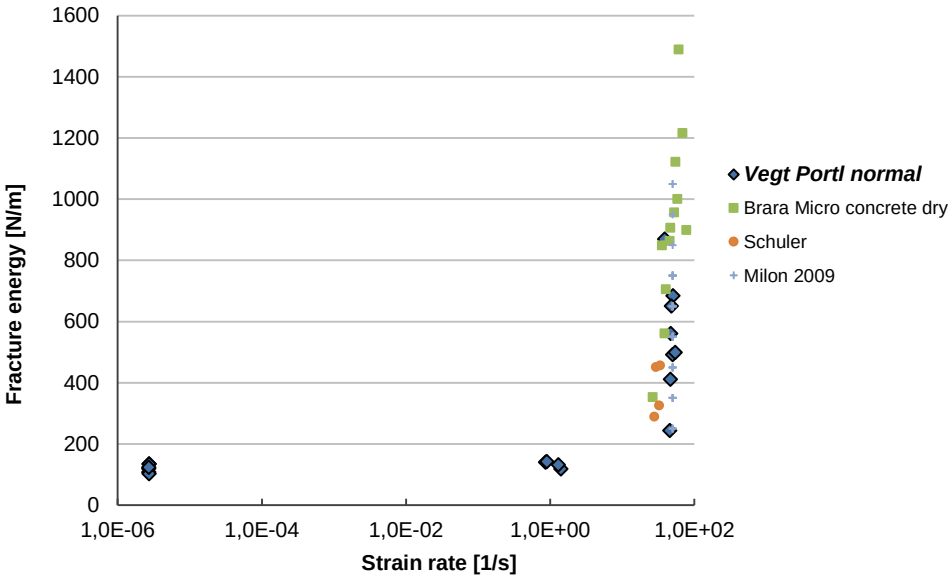

Figure 4.19 Experimental data on the fracture energy as a function of the strain rate [Weerheijm et all 2013].

The comparison between Delft data and the data of, for instance, Brara [Brara 2006, Brara 2007] is even harder, because not only the test set-ups and diagnostics used are different, but also the concrete composition and the specimen sizes. Therefore, to be able to properly compare the experimental data on fracture energy of different researchers, it is essential to standardize the test methods and start international cooperation for dynamic experiments.

Although the scatter is large and standard test methods would make comparison of the fracture energy results easier, still similar results are found by other researchers.

4.5.5 Fracture characteristics

Geometrical characteristics of the fracture zone have been derived from the specimens after the static, Split Hopkinson Bar and Modified Split Hopkinson Bar tests are completed. The fracture zone is captured and exposed by using fluorescent epoxy, as has been explained in chapter 3.

The fracture patterns are first studied qualitatively. This means that the fracture patterns are studied by a light microscope and an overall impression is obtained. From this qualitative study it is concluded that there are only small differences between static and SHB fracture characteristics. These small differences are probably caused by the set-up being rotational or non-rotational.

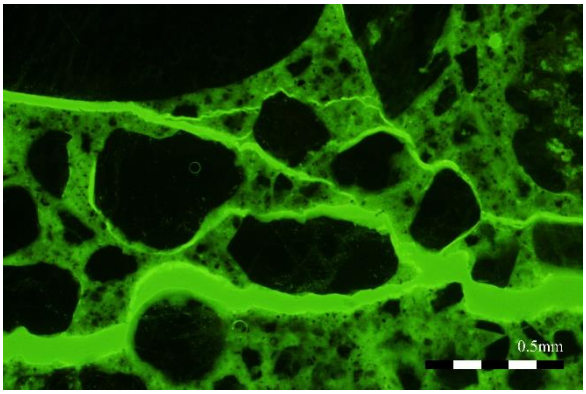

Figure 4.20 Cracks in static test develop from two sides (magnification 25x).

The non-rotational static test set-up causes crack branching; which means that when a crack starts from one side, the set-up forces another crack to start from the other side as well (see Figure 4.20), making sure the loading platens stay parallel. The two cracks meet somewhere in the middle (see Figure 4.21 and Figure 4.22).

Figure 4.21 Static fracture: crack branching (test 03D2).

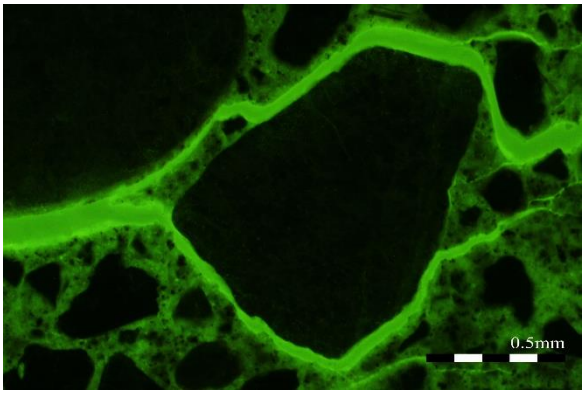

Figure 4.22 Detail crack branching in static test; cracks develop from two sides, around a particle, and meet (magnification 25x).

For the Split Hopkinson Bar tests, the orientation of the micro cracks that are connected to the macro crack, is mostly in the same direction. This means that the SHB fracture starts from one side of the specimen, travels along the specimen and ends close to or inside the notch at the other end, meanwhile creating some extra micro cracks. The fracture pattern for a SHB test and the growing of the fracture in one main direction is shown in Figure 4.23 and Figure 4.24.

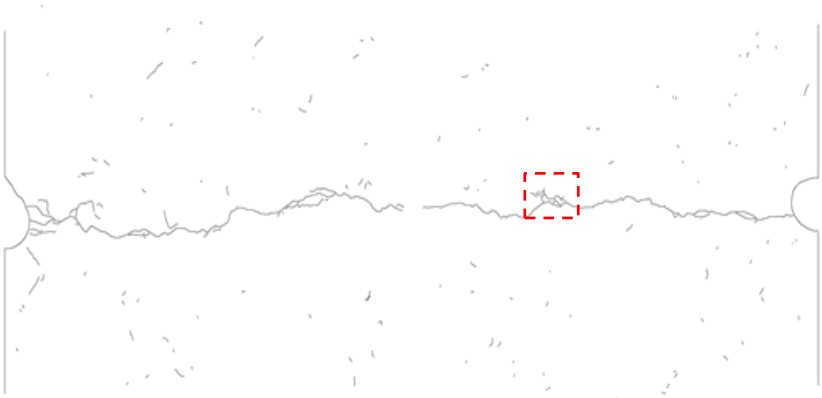

Figure 4.23 SHB fracture (test 10A4).

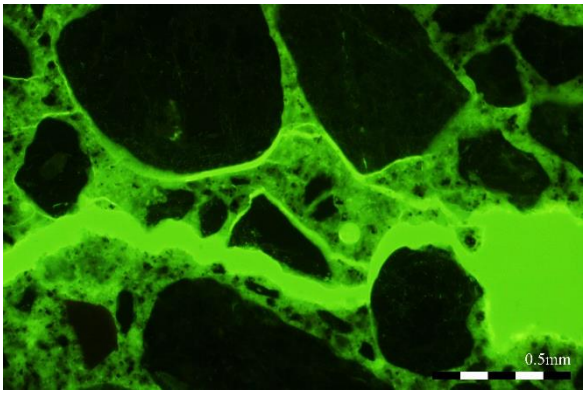

Figure 4.24 Detail SHB fracture: cracks develop mainly in one direction (magnification 25x).

The fracture patterns of the Modified Split Hopkinson Bar tests show much more and longer micro cracks which are not all connected to the final macro crack, creating a much wider fracture zone (see Figure 4.25 and Figure 4.26). The individual micro cracks are longer than the ones found in the static and SHB tests.

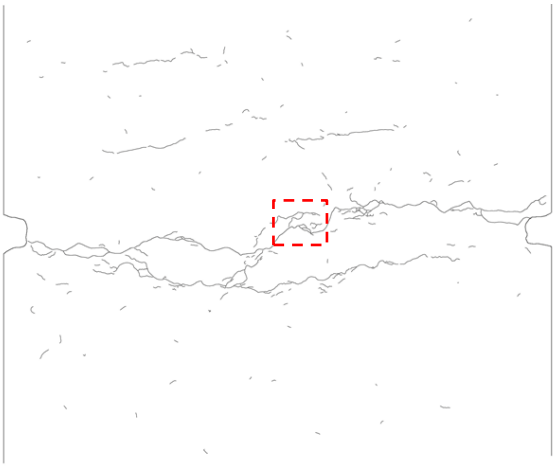

Figure 4.25 More micro cracking and wider fracture zone for MSHB test (N18).

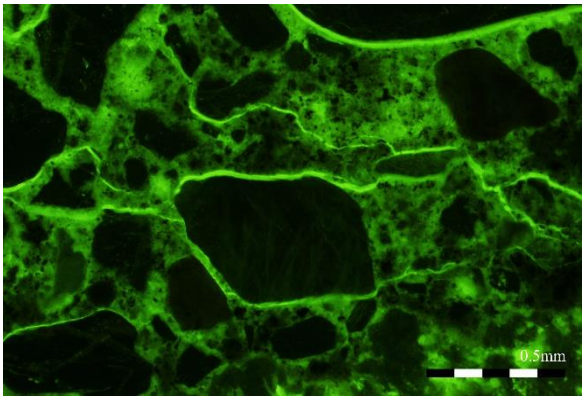

Figure 4.26 Detail of MSHB fracture: more isolated micro cracks besides the macro crack (magnification 25x).

To obtain quantitative results on fracture lengths and widths of the fracture zone, the crack patterns are manually digitalized (see also paragraph 3.8.2).

To quantify the fracture patterns, the cracks are subdivided into:

(1) macro crack, which is the crack where physical separation of the two parts of the specimen has taken place;

(2) connected micro cracks, which are connected to the macro crack;

(3) isolated micro cracks, which are not connected to the macro crack but found isolated in the concrete sample.

The fracture characteristics, like total length of cracks, amount of cracks and width of the fracture zone, are determined for each of these categories by counting and measuring each fracture in the fracture zone (see paragraph 3.8).

The results for total length of the different cracks (which is the sum of the individual cracks of each category) are summarized in Table 4.4 (L_{mac} = length of macro crack, L_{con} = length of connected micro cracks, L_{iso} = length of isolated micro cracks, L_{tot} = total length of cracks, $L_{tot,stat}$ = total length of cracks for static test) and visualized in Figure 4.27.

Table 4.4 Average results for fracture lengths, Portland cement concrete.

Series	$\dot{\varepsilon}$	L_{mac}	L_{con}	L_{iso}	L_{tot}	$L_{tot}/L_{tot,stat}$
	[1/s]	[mm]	[mm]	[mm]	[mm]	[-]
Stat	$2.7 \cdot 10^{-6}$	82	45	91	218	1.0
SHB	1.1	86	32	68	186	0.85
MSHB	46.5	81	51	127	259	1.19

NB: the macro fracture lengths of the MSHB tests are recalculated to match the 2 mm notch. This means that for the MSHB tests (notch depth of 3 mm) 2 mm is added to the macro fracture length.

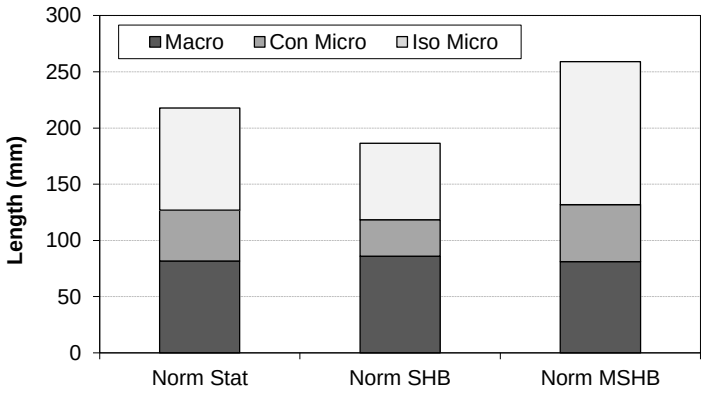

Figure 4.27 Average total length of fracture for Static, SHB and MSHB test.

Table 4.5 Average results for number of cracks (N) and average crack length (l_{av}), Portland cement concrete.

Series	$\dot{\varepsilon}$	N_{con}	N_{iso}	$l_{av,con}$	$l_{av,iso}$
	[1/s]	[-]	[-]	[mm]	[mm]
Stat	$2.7 \cdot 10^{-6}$	35	205	1.6	0.4
SHB	1.1	29	160	1.2	0.4
MSHB	46.5	24	130	2.1	1.0

From the results on fracture lengths, number of cracks (N) and average crack length the following conclusions can be drawn:

- The length of the final macro fracture L_{mac} is not affected by the loading rate (see Table 4.4). Apparently, the length of the macro fracture is only dominated by the concrete meso structure or aggregate grading and not by the loading rate.
- The number of micro cracks (N), shown in Table 4.5, decreases with increasing loading rate.
- The average length (l_{av}) of an individual micro crack does not significantly change for the moderate regime, but increases for the high loading rate (see Table 4.5).
- The total length of the micro cracks decreases for the moderate regime and increases for the high loading rate regime. The decrease of total fracture length in the moderate regime might be partly due to the set-up, which forces the crack to travel from one side to the other without forming many branches, as in case of the static tests. The fracture patterns also show that more very small isolated micro cracks are present in the static samples, compared to the SHB samples (compare Figure 4.21 with Figure 4.23). For the high loading rate regime, the increase in total fracture length is not as pronounced as expected (based on difference in load-deformation curve) due to the fact that, although the length of the micro cracks increase, the amount of micro cracks and, therefore, the crack density actually decreases.

When comparing the results of the fracture energy (see Table 4.3) with the results on total fracture length (see Table 4.4) it is concluded that the increase in fracture energy is *not* linearly proportional to the length of additional (micro) cracks. The increase in fracture energy can, therefore, *not* be fully ascribed to an increase in fracture length.

The results for the width of the fracture zone for the macro crack (WFZ_{mac}), the width of the macro and connected micro cracks ($WFZ_{mac+con}$) and the total width of the fracture zone including long isolated micro cracks (> 5 mm) (WFZ_{tot}), are presented in Table 4.6 and visualized in Figure 4.29. An example of the determination of the width of the fracture zone for the different crack categories is shown in Figure 4.28.

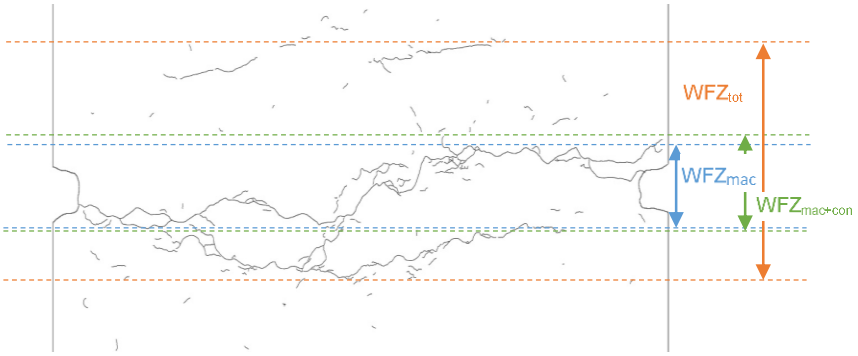

Figure 4.28 Example of width of fracture zone for macro crack (WFZ_{mac}), macro and connected micro cracks ($WFZ_{mac+con}$) and total width including long isolated cracks (WFZ_{tot}).

Table 4.6 Average results for width of fracture zone (WFZ).

Series	$\dot{\varepsilon}$	WFZ_{mac}	$WFZ_{mac}+_{con}$	WFZ_{tot}	WFZ_{tot}/ $WFZ_{tot,stat}$
	[1/s]	[mm]	[mm]	[mm]	[-]
Stat	$2.7 \cdot 10^{-6}$	4.5	6.2	6.7	1.0
SHB	1.1	6.3	7.4	8.1	1.2
MSHB	46.5	6.6	8.6	19.1	2.9

The results show that the width of the total fracture zone (WFZ_{tot}), including the macro crack and the connected and isolated micro cracks, increases significantly for the high loading rate regime. The width of the macro crack is hardly affected by the loading rate (see Table 4.6), as was the case for the length of the macro crack.

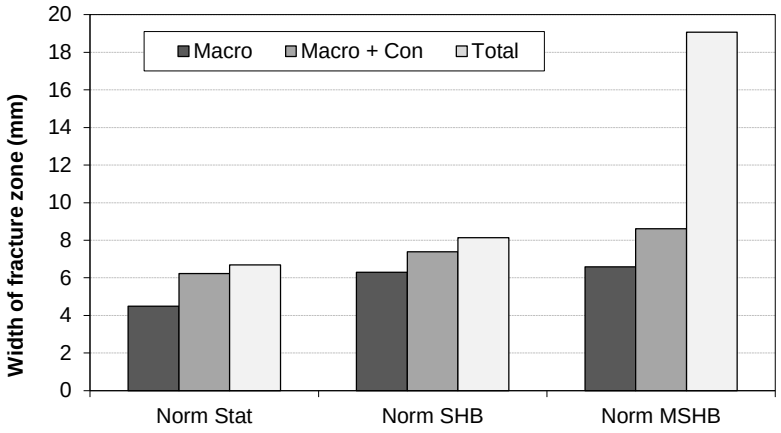

Figure 4.29 Average width of fracture zone for Static, SHB and MSHB test. (width macro crack, width macro and connected micro cracks and total width including long isolated cracks)

From the data presented in this paragraph on the geometry of the fracture zone it is concluded that the width and length of the macro crack are not affected by the loading rate. The width of the total fracture zone, including long isolated micro cracks, increases for the high loading rate regime, although the crack density (= total length of cracks divided by width of the total fracture zone) actually decreases.

The fracture data gives insight in the rate dependency of the fracture process. However, it can also be combined with the experimental data on strength, fracture energy, stress-deformation curves and data on stresses and deformations measured in real time, to be able to reconstruct the mechanisms behind the rate effects on tensile concrete properties (see paragraph 4.6, paragraph 4.7, paragraph 5.9 and paragraph 5.10).

4.6 Analysis of loading rate effects on tensile strength: apparent and true dynamic strength

In the previous paragraphs the experimental results on Young's modulus, tensile strength and failure behaviour are presented and some conclusions are drawn. The question remains whether the measured increase in strength, Young's modulus and fracture energy can be fully ascribed to the material response itself or that the increase is partly due to the structural response at macro and micro scale level. Some effects, like size of the specimen,

geometry of the specimen and structural inertia of the specimen, are not related to the material response itself and should be taken into account when analysing the results. Especially at higher loading rates, the observed response can be affected by (structural) inertia effects.

Besides structural inertia effects at macro level, inertia at micro level can also contribute to the observed strength increase. Inertia at micro level affects the local stress distribution and, therefore, induces limitations in crack initiation and propagation.

In dynamics, the observed increase in tensile strength is believed to be due to:

(1) the influence of (structural) inertia forces, which are generated when the material starts to weaken by micro cracking in the fracture zone. [Reinhardt 1990, Cotsovos 2008a, Cotsovos 2008b, Ozbolt 2013 and Weerheijm et all 2013]
(2) influence of inertia at micro level, which delays crack initiation. [Weerheijm 1992]
(3) influence of inertia at micro level, which delays crack propagation. [Weerheijm 1992]
(4) the viscous behaviour of the material (viscosity due to the water content). [Cadoni 2001a, Ross 1996, Rossi 1992, Toutlemonde 1995a, Toutlemonde 1995b, Vegt 2006b, Vegt 2006d, Weerheijm et all 2013]

Structural inertia effects can significantly change the state of stresses and strains of the material. As stated in paragraph 4.4.2, in this research the focus concerning inertia effects at macro level is on the possible contribution of structural inertia of the fracture zone, generated by large and localized deformations, to the enhanced strength and fracture energy.
If structural inertia effects are included in the experimental results they might lead to a misleading conclusion on the rate dependency of concrete properties. Therefore, it is important to distinguish between the apparent tensile strength and the true material strength. The true strength is defined as the load bearing capacity of the material itself, represented in the constitutive relation. When due to dynamic effects and accelerations the material resistance is combined with structural inertia forces, the total resistance is recorded as apparent strength. When in numerical models the structural inertia effects are explicitly dealt with by the model itself, only the true strength should be included in the material model, which is the constitutive relation.

Besides structural inertia of the fracture zone, other structural inertia effects, like for instance radial inertia in the cylindrical specimen, can also be recorded as 'apparent' strength. However, in this thesis the effects of dynamics on macroscopic stress distribution are not considered and only the structural inertia of the fracture zone in the *axial* direction is determined to obtain the 'true' strength (see also paragraph 4.2.5).

In [Weerheijm and Vegt 2011, Vegt and Weerheijm 2015] inertia phenomena in the fracture zone and the inertia that influences crack initiation and crack propagation have been dealt with. The initial interpretation in [Weerheijm and Vegt 2011, Vegt and Weerheijm 2015] on structural inertia of the fracture zone is incomplete and not very accurate. In the next paragraph, the structural inertia of the fracture zone will be discussed in more detail and conclusions are drawn. The line of thoughts proposed in [Weerheijm and Vegt 2011, Vegt and Weerheijm 2015] will be followed and forms the bases for paragraph 4.6 and 4.7. Paragraph 4.6.4 will shortly describe how the moisture content can influence the fracture behaviour of concrete. The influence of moisture on the rate effects of concrete will be studied and described extensively in chapter 5.

4.6.1 Structural inertia in the fracture zone

This paragraph focusses on the inertia effects in the fracture zone which are generated when micro cracks start to form, deformation concentrates in the fracture zone and the deformation rate increases.
To be able to interpret the strength and fracture energy data and to determine whether structural inertia of the fracture zone influences the recorded data, the equilibrium in the spalling tests is first analysed.

For a bar segment dx, with a cross-section A, the dynamic equilibrium along the bar is given by the following equation, where u is the particle displacement and ρ is the density of the concrete:

$$A \cdot \frac{\partial \sigma}{\partial x} \cdot dx = A \cdot \rho \cdot \frac{\partial^2 u}{\partial t^2} \cdot dx \qquad (4.3)$$

This equation describes how the stress gradient between the surfaces of the bar segment is balanced by inertia forces.

Using the definition of the engineering strain $\varepsilon = \partial u/\partial x$, equation 4.3 becomes the equation of motion for a longitudinal stress wave in a rod:

$$\rho \cdot \frac{\partial^2 u}{\partial t^2} = \frac{d\sigma}{d\varepsilon} \cdot \frac{\partial^2 u}{\partial x^2} \tag{4.4}$$

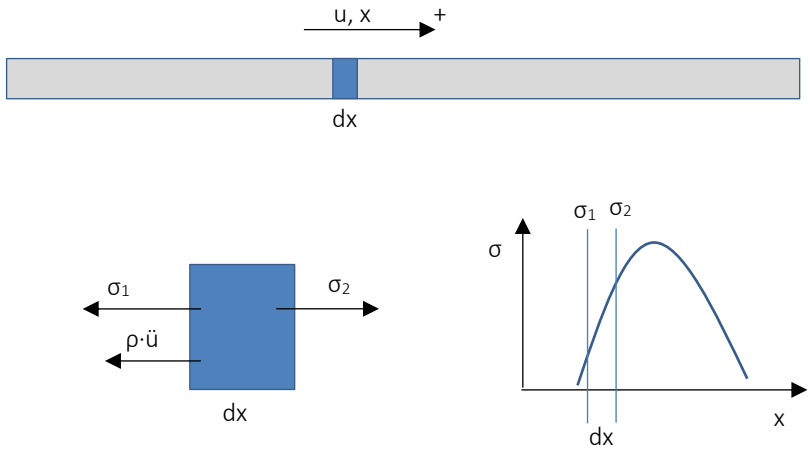

Figure 4.30 Equilibrium of bar segment dx.

The longitudinal wave velocity c_p is given by:

$${c_p}^2 = \frac{1}{\rho} \cdot \frac{d\sigma}{d\varepsilon} \tag{4.5}$$

For a linear elastic material, with a constant Young's modulus E and density ρ, the longitudinal wave velocity c_p is constant and equals $c_p = \sqrt{E/\rho}$.

When damage is induced before the maximum concrete strength is reached, the stress-strain relation deviates from the linear function and bends into a concave shape. Due to this bend in the curve $d\sigma/d\varepsilon$ will decrease with increasing stress. This means that the longitudinal wave velocity decreases with increasing stress. Although the wave velocity is decreasing, $d\sigma/d\varepsilon$ remains positive until the maximum strength is reached. Subsequently, the wave can still propagate and stresses are transferred.

Against this background the issue is addressed whether the maximum recorded stresses in the dynamic tests represent the 'true' tensile strength. In the SHB and MSHB tests, the stresses are measured beyond the failure zone in the linear elastic material. To determine whether inertia of the fracture zone is included in the measured maximum stress or that the 'true' material behaviour is captured beyond the failure zone, the equilibrium of the failure zone is analysed.

First, let us assume that the cracks are concentrated in a fracture zone with a length 2·dx. Outside the fracture zone, the material is linear elastic. The load is a linearly increasing tensile load, traveling in the negative x-direction. Figure 4.31 shows the equilibrium of half of the failure zone with a length dx.

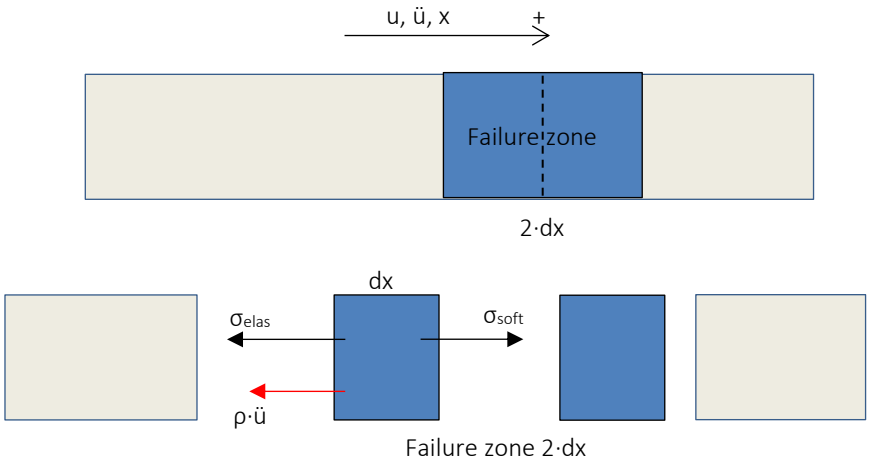

Figure 4.31 Equilibrium of failure zone with length 2dx.

The measured stress in the elastic material σ_{elas}, just beyond the fracture zone, is balanced by the 'true' material behaviour in the softening zone σ_{soft} and the inertia forces, with dx being half the fracture zone and u the particle displacement.

$$\sigma_{elas}(t) = \sigma_{soft}(t) - \rho \cdot dx \cdot \ddot{u}(t) \tag{4.6}$$

The inertia contribution equals the stress gradient in the element with length dx, i.e. the stress gradient induced by the linearly increasing tensile loading wave. When the specimen response is linear elastic, no damage has occurred, the inertia forces will work in the negative x- or u-direction as indicated in Figure 4.31. However, when the material fractures, additional deformation occurs and both 'parts' of the failure zone in Figure 4.31 move in opposite direction. For the considered left part, the additional inertia forces will work in the positive u-direction, adding to the 'true' material behaviour. The question is whether these inertia forces due to the fracture process obscure the measured results in the elastic material beyond the fracture zone.

The wave equation 4.4 for non-linear material response tells us that waves will be transferred as long as $d\sigma/d\varepsilon$ is positive. The additional deformation due to cracking leads to a reduction in $d\sigma/d\varepsilon$, or a reduction in stiffness. The deformation increases and inertia is activated, as explained before. Although deformation has taken place, the wave equation 4.4 still holds. This means that the total inertia contribution, i.e. due to the loading and the fracture process, is still working in the negative u-direction and represents and equals the stress gradient in the bar segment. Therefore, the change in resistance might not be immediately recorded at the location beyond the inelastic zone, but the 'true' stresses will be transferred to the location beyond the fracture zone after a small (unknown) time delay.

The above presented reasoning shows that for the SHB tests the measured maximum stress in the aluminium bar is not influenced by structural inertia of the fracture zone and therefore, representative for the 'true' tensile strength.

When, just like for the SHB tests, only a single tensile loading wave would be applied to the specimen in the MSHB tests, the maximum stress beyond the failure zone, thus also the maximum measured stress in R9-17, would be equal to the maximum stress in the failure zone and representative for the tensile strength. However, in the MSHB tests the specimen is loaded sequentially by an incident compressive as well as the reflected tensile wave. At the failure zone, these waves are still interacting with each other. Just beyond the fracture zone, the compressive wave and the tensile wave are interacting in a different manner than at the position of the notch (see difference between Figure 4.32 and Figure 4.33 for the total strain at the notch 'Strain_tot_notch' and the total strain beyond the fracture

zone 'Strain_tot_outFZ'). Therefore, the recorded tensile stresses outside the fracture zone are not fully representative for the stress conditions in the notch. The stress conditions at the notch have to be determined. This can be done if the wave speed c_p is known (see paragraph 3.7.3).

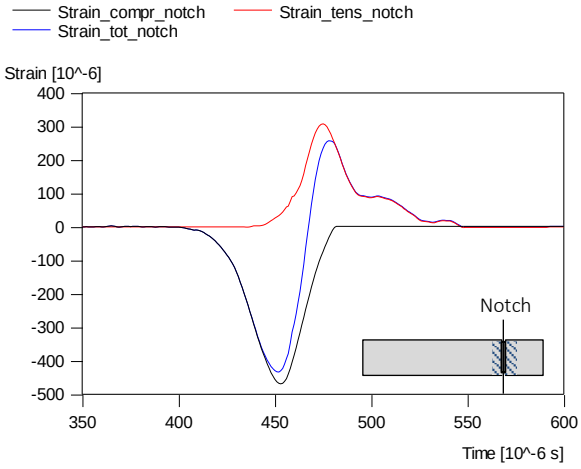

Figure 4.32 Interaction of waves at the notch.

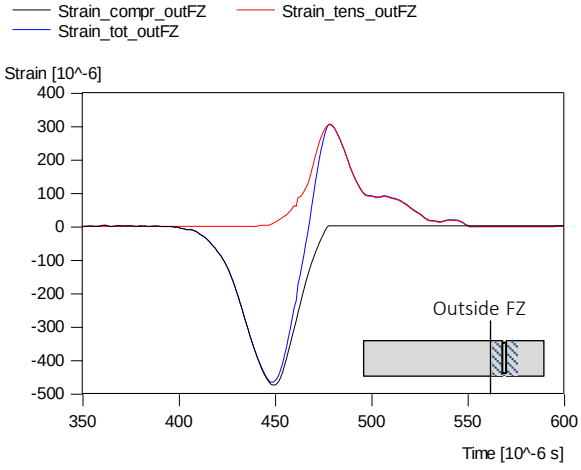

Figure 4.33 Interaction of waves outside the failure zone.

The remaining question is whether the possible damage in the pre-peak phase affects the wave velocity.

The average wave velocity, used to transfer the waves to the notch, is determined using the time difference between the tops of the compressive waves (elastic parts). When the wave speed is constant and not influenced by any damage, the compressive wave should perfectly fit the ascending branch of the returning tensile wave beyond the fracture zone. To get a good fit, small adjustments of the average wave velocity were necessary. However, the correction varies between 10 – 30 m/s on an average concrete wave speed of approximately 4100 m/s, which is only 0.5%. This proves that until the maximum tensile stress is reached, the wave speed is almost constant. Therefore, it is assumed that the wave speed is constant in the pre-peak phase and that the tensile strength, determined at the notch for the MSHB tests, can be considered as the true material strength.

The experimental data on wave velocity and the (1D) analysis of the equilibrium of the fracture zone show that structural inertia of the fracture zone in the pre-peak concrete response does not contribute to the recorded tensile strength increase for the medium or high loading rates. The tensile strength increase is, therefore, probably caused by micro inertia and/or the viscous behaviour of the concrete. In the next paragraphs, inertia effects on crack initiation and crack propagation are discussed.

4.6.2 Crack initiation

In concrete defects are formed during the hydration process. When loading concrete, these initial flaws and the heterogeneity of concrete cause irregularly distributed internal stresses. With increasing load, the defects will lead to crack initiation. The question is whether inertia effects in the zone around the crack tips, at the so called micro level, will lead to a delayed crack initiation and, therefore, an increase of the dynamic strength.

Chen and Sih studied the effect of dynamics on the stress distribution around cracks [Chen and Sih, 1977]. The stress intensity factor (K) is used in fracture mechanics to predict the stress state near the tip of a crack caused by an external load or residual stresses. The magnitude of K depends on the sample geometry, the size, shape and location of the cracks and the magnitude and distribution of the load. The work of Chen and Sih showed that the

dynamic stress intensity factor (K_{Id}) around defects initially increases after impact until it rapidly approaches the static value.

Chen and Sih also proved that the dynamic stress intensity factor decreases with increasing crack velocity. This means that with increasing velocity, less energy is available for cracking than for a similar stress level with static loading. This implies that cracking is delayed and, since dynamic strength is directly coupled to crack initiation, the dynamic strength increases.

The loading rate at which the crack initiation is delayed can be determined from the work of Chen and Sih [Chen and Sih, 1977]. Chen studied the situation of a shock load hitting a penny shaped crack. He scaled the time with shear wave velocity (c_2) and the crack radius (a). When the shock hits the flaw, initially the stresses are lower than in statics (see Figure 4.34). Until the threshold of $c_2 \cdot t/a = 1$ is reached, the reduced stresses will result in delayed crack initiation. After some time, stress equilibrium according to statics is reached and stresses will not be reduced. This means that the effect of discontinuities in geometry, stiffness or loading is smoothened.

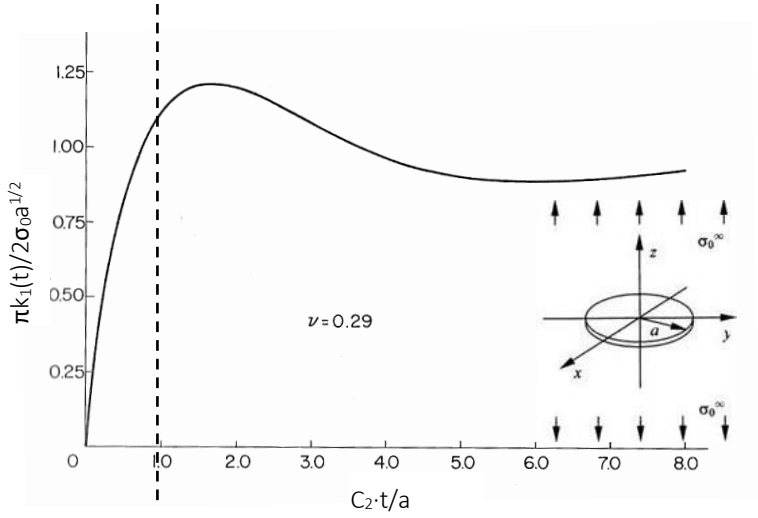

Figure 4.34 Ratio of dynamic and static stress intensity factor as a function of time, i.e. $c_2 \cdot t/a$, for normal impact on a penny-shaped crack [Chen and Sih, 1977].

When using this point $c_2 \cdot t/a = 1$ to determine the loading rate at which rate effects on crack initiation might occur, the following thresholds can be obtained (assuming $f_t = \dot{\sigma} \cdot t_{ft}$, with f_t = static tensile strength and t_{ft} = time of fracture):

$t \leq \frac{a}{c_2} \rightarrow \dot{\sigma} \geq \frac{c_2 \cdot f_t}{a}$ (4.7) *rate effects will occur on crack initiation due to micro inertia*

$t > \frac{a}{c_2} \rightarrow \dot{\sigma} < \frac{c_2 \cdot f_t}{a}$ (4.8) *no rate effects will occur on crack initiation due to micro inertia*

When applying these equations to concrete, it can be determined whether this mechanism is relevant for the material concrete and the presented experimental results. For concrete the characteristic flaw size or crack radius is assumed to be in the order of 10 percent of the largest aggregate size, in this case about 1 mm. The static tensile strength is 3 MPa and $c_2 = C_R$ = Rayleigh wave velocity = 1800 m/s. Rayleigh wave velocity is used because this phenomenon is about a wave at the surface of the penny shaped crack and not a shear wave in a solid. When applying these concrete properties to equation 4.7, only beyond a loading rate $\dot{\sigma} = 5000\ \mathrm{GPa/s}$ rate effects can occur due to delayed crack initiation. However, the experimental data shows that significant rate effects can be observed at loading rates beyond 50 GPa/s. Therefore, it is concluded that inertia effects on crack initiation are not the factor that dominates the enhanced rate dependency on tensile strength at rates beyond 50 GPa/s [Weerheijm et all 2013, Weerheijm and Vegt 2011].

4.6.3 Crack propagation

In the pre-peak phase micro cracking occurs, until the tensile strength is reached and macro cracks start to form. As has been described in the previous paragraph, delayed crack initiation itself is not the cause for the observed strength increase with increasing loading rate. However, before reaching the maximum strength, the micro cracks have to grow and coalescence, which takes time. During this time the load increases. Therefore, the strength increase might be caused by delaying or decelerating crack propagation due to inertia effects.

In statics the energy dissipation rate by fracture, or strain energy release rate, is in balance with the energy supply rate of the loading. This means that the energy that has to be

supplied to a crack tip for it to grow is balanced by the amount of energy dissipated due to the formation of new fracture surfaces. In dynamics, due to the limitations in crack velocity, this balance is disturbed and crack propagation is limited. At a certain load, the maximum cracking velocity is reached and a minimum amount of time is needed to form the final macro crack. Increasing the load beyond this threshold, will not lead to an increase in cracking velocity and crack propagation. When the load increases beyond the threshold, during the minimum time which is needed for the cracks to coalescence and form the final macro crack, the measured strength also increases.

To determine the threshold at which loading rate the strength might increase due to limitations in crack velocity, a simple analysis is applied. The time duration (Δt_{frac}) of the pre-peak phase of the fracture process depends on the velocity at which the crack grows, i.e. the crack velocity $(\dot{a})$, and the required crack growth (Δa) for cracks to connect and start forming macro cracks. Weerheijm studied dynamic crack growth in the past [Weerheijm 1992] and showed that crack growth velocities, or in short crack velocities, varied from 500 – 1000 m/s during fracture (see also [Curbach 1990]). Forquin [Weerheijm et al 2013] studied crack velocities in various materials and concluded that the velocity ranges from 0.23 - 0.35C_0, which is 800 – 1200 m/s for concrete. In the following analysis average crack velocities in the range of 500 – 1000 m/s are used.

For a significant rate effect due to limitations in crack propagation, an increase in strength of at least 0.1f_t (≈ 0.3 MPa) should be achieved in a time $\Delta t_{frac} = \Delta a/\dot{a}$. The assumed initial flaw size a is again 1 mm. The required crack growth then probably ranges from about 5a to 15a before cracks start to connect with another (propagating) crack or flaw and create a macro crack. Following equation 4.9, for a crack velocity of 1000 m/s and required crack growth Δa of 5 mm, a loading rate of at least 60 GPa/s is necessary to achieve 10% strength increase in the pre-peak phase.

$$\Delta t_{frac} \cdot \dot{\sigma} \geq 0.1 f_t \; ; \; \Delta a = \Delta t_{frac} \cdot \dot{a} \;\; \rightarrow \;\; \dot{\sigma} \geq \frac{0.1 f_t \cdot \dot{a}}{\Delta a} \tag{4.9}$$

where a = initial flaw size, Δa = required crack growth, $\dot{a}$ = crack velocity, Δt_{frac} = pre-peak fracture time, $\dot{\sigma}$ = loading rate and f_t = tensile strength.

Results for different crack velocities $\dot{a}$ and required crack growth Δa are summarized in Table 4.7. The results in Table 4.7 show that limitation of the crack velocity (not higher than approximately 1000 m/s), can lead to a strength increase at loading rates in the range of 10 – 60 GPa/s. The simple analysis shows that, beyond loading rates of 10 – 60 GPa/s, rate effects on tensile strength due to limitations of crack propagation are likely to occur.

Table 4.7 Loading rate beyond which the tensile strength f_t becomes rate dependent due to limitation of crack propagation.

Δa	$\dot{a}$	$\dot{\sigma}$
[mm]	[m/s]	[GPa/s]
5	500	30
5	1000	60
10	500	15
10	1000	30
15	500	10
15	1000	20

In reality the rate dependency of micro cracking is more complex. The crack velocity is not constant during the fracture process [Weerheijm et all 2013] and the dynamic stress intensity factor K_{Idyn} depends on the crack velocity. The results of Freund [Chen 1977] show that the stresses in front of the crack tip decrease with increasing crack velocity. Ultimately, at crack velocity of C_R, the information on the 'geometry and dimensions' of the crack cannot be transferred in time to the material in front of the crack tip, resulting in K_{Idyn}=0. Weerheijm developed a model [Weerheijm 1992] that predicts crack growth by calculating the energy flux into the fracture zone and takes all the effects on the dynamic stress field (K_{Idyn}) into account. The more thorough analysis showed that the changes in K_{Idyn} due to dynamic loading and crack velocity become important for loading rates beyond 50 GPa/s, which is similar to the threshold found in the simple analysis for crack growth.

The presented experimental results show a steep strength increase after the threshold of 50 GPa/s, which is in accordance with the simple analysis presented before and with the research by Weerheijm [Weerheijm 1992]. Hence, micro inertia related to limitations in crack propagation could be one of the main causes of the observed rate effects for the high loading rate regime.

4.6.4 Moisture content

The above described analyses on the inertia effects show that for the loading rates up to 50 GPa/s all inertia effects can be ignored and, therefore, the observed rate effects in dynamics should be ascribed to the material response itself and included into the constitutive material model. The strength increase in the moderate regime must be caused by an enhanced resistance to crack initiation and/or crack propagation, which is not micro inertia. The moisture content and the pore structure are the probable explanations for the observed strength increase in the moderate regime.

For the high loading rate regime (> 50 GPa/s), structural inertia of the fracture zone does not contribute to the enhanced strength. The observed tensile strength is, therefore, the 'true' material strength and should be included into the constitutive material model. The rate effects on tensile strength are probably dominated by micro inertia effects on crack propagation. However, moisture content can also influence the strength and fracture behaviour for high loading rates. This will be discussed in the next chapter, where the effect of moisture content and pore structure on strength will be examined and analysed.

4.7 Analysis of loading rate effects on failure behaviour

The behaviour of concrete up to complete failure is represented by the stress-deformation curve, as has been explained in chapter 2. The characteristic parameters are ultimate strength, stiffness in the ascending branch and fracture energy. The rate effects on strength and the fracture behaviour before ultimate strength is reached have been discussed in the previous paragraph. In this paragraph, the post-peak failure behaviour will be addressed.

The schematized softening curve has two branches (see Figure 4.35); (I) the first steep branch which is coupled to the phase of micro cracking and (II) a long tail branch which represents the formation of the final macro crack (see also paragraph 2.3).

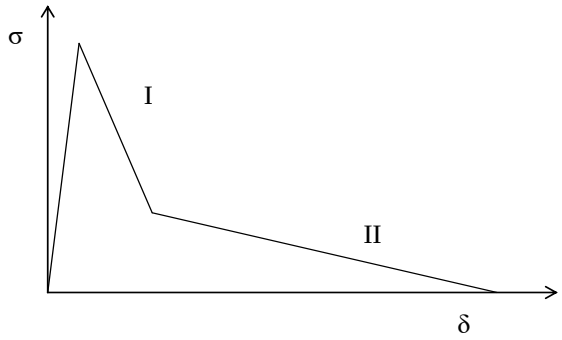

Figure 4.35 Schematized softening curve.

The first branch of the softening curve is determined by micro cracking (initiation and growth). The observed increase in fracture energy in the first part of the softening curve is probably caused by the additionally absorbed energy to form more micro crack surfaces and by the rate effects affecting the ultimate strength f_t, as explained in paragraph 4.6. The reduced number and length of the micro cracks for the moderate loading rate (≈ 50 GPa/s) (see Table 4.4) combined with a fracture energy that almost equals the static value (see Table 4.3), illustrates that both components contribute to the fracture energy.

4.7.1 Additional micro cracking

The experimental results show that the total length of micro cracks decreases for the moderate loading rate and increases for high loading rates (see Table 4.4), as stated before. In this paragraph simple analyses are used to determine whether the experimental data is supported by fracture mechanics.

Cracks start to grow from representative defects; first the larger defects will be initiated and with increasing dynamic load, also smaller defects will contribute. The energy that must be supplied to a crack tip for it to grow is balanced by the amount of energy dissipated due to the formation of new surfaces. To initiate also cracks from smaller defects, the stress should be higher than necessary in static tests, assuming that the critical stress intensity factor K_{Ic} does not change.

For a penny shaped crack with crack radius a in a 3D infinite solid and uniform uniaxial tension, K_{Ic} is:

$$K_{Ic} = \frac{2 \cdot \sigma}{\pi}\sqrt{\pi \cdot a} \tag{4.10}$$

When considering cracks with sizes a_1, a_2, a_3,..., a_i and assuming $a_i = 2 \cdot a_{i+1}$ (the assumption of $a_i = 2 \cdot a_{i+1}$ is indicative and only used to roughly determine at what loading rate the initiation of smaller cracks can be expected), the required stress to activate a set of smaller cracks a_{i+1} is:

$$\sigma_{i+1} = \sqrt{2} \cdot \sigma_i \tag{4.11}$$

This means that the load should be about 40% higher to be able to initiate the smaller set of defects. The stress and loading rate needed to initiate a new set of smaller cracks compared to static tests is described by equations 4.12 and 4.13, assuming the critical intensity factor K_{Ic} does not change.

$$\sigma_i = \sigma_1 \cdot \frac{\sqrt{a_1}}{\sqrt{a_i}} = \left(\frac{a_1}{a_i}\right)^{\frac{1}{2}} \cdot \sigma_1 \tag{4.12}$$

$$\dot{\sigma_i} \geq \frac{\sigma_i}{t_{frac}} = \left(\frac{a_1}{a_i}\right)^{\frac{1}{2}} \cdot \frac{\sigma_1}{t_{frac}} = \left(\frac{a_1}{a_i}\right)^{\frac{1}{2}} \cdot \frac{f_t}{t_{frac}} \tag{4.13}$$

Experiments and numerical simulations indicate that the fracture time t_{frac} for the dynamic tests is in the order of 100 µs (see Figure 4.39 and Figure 4.40). For a tensile static strength f_t = 3 MPa and a fracture time of approximately 100 µs, the loading rate needed to initiate a smaller set of cracks ($a_2 = 0.5 \cdot a_1$) is about 42 GPa/s, according to equation 4.13. This is about the same order as the loading rate of the SHB experiments. Therefore, in the SHB tests no additional micro cracking is expected, based on the previous analysis.

Experimental data supports this conclusion. The data shows that the total length of micro cracks decreases for the moderate loading rate and only increases for high loading rates

by approximately 30% (see paragraph 4.5.5). The width of the total fracture zone (including long isolated micro cracks) for the high loading rate regime increases significantly with a factor three. Since the total length of the micro cracks is only increasing by 30%, the average crack density in the fracture zone is decreasing for the high loading rate regime. This is also visible in the digitalized fracture patterns, as shown in paragraph 4.5.5.

According to the experimental data and the simple analysis, additional micro cracking is unlikely to occur for the moderate regime. For the high loading rate regime, the simple analysis indicates more micro cracking. This conclusion is supported by experimental data, although the increase in total micro crack length was found to be lower than could be expected from the analysis. The total fracture length increases with a factor 1.2 for the high loading rate regime (see Table 4.4). Assuming that the cracks are penny shaped cracks in a 3D medium and that the total length of the macro and micro cracks is also increasing with a factor 1.2 in the other direction, this increase in total crack length can increase the fracture energy by approximately 40% (factor 1.2 x 1.2 = 1.44), assuming a constant K_{Ic} and E_{mod}. Therefore, the apparent increase in fracture energy for the high loading rate regime with a factor 4.4 (see Table 4.3), cannot be explained by the formation of extra micro cracks only.

4.7.2 Structural inertia of fracture zone

Structural inertia effects in the fracture zone do not influence the stresses in the pre-peak phase, as has been explained in paragraph 4.6.1. Therefore, in the pre-peak phase, the 'true' stresses $\sigma_{soft}(t)$ are measured outside the fracture zone and can be used to determine the strength at the notch.

However, the aim is not only to determine the strength, but also to reconstruct the stress-deformation relation. The experimentally obtained stress-deformation curves show a different shape of the softening branch for the MSHB tests than for the static and SHB tests. However, the macro crack length is similar for all three loading rates (see Table 4.4). The combination of no increase in macro crack length and still a difference in shape of the softening curve indicates that another mechanism contributes to the enhanced resistance, like for instance structural inertia effects of the fracture zone.

To obtain the 'true' stress-deformation relation, the 'true' material stresses $\sigma_{soft}(t)$ in the pre-peak as well as the post-peak phase have to be synchronized with the deformation $\delta(t)$ and inertia effects have to be excluded. When the failure zone consists of a single fracture and the adjacent material is linear elastic, the wave velocity c_p is constant for the LE material and the signals can be synchronized.

In reality, however, the cracks are distributed along the fracture zone (FZ). Due to this distributed damage, the properties change and the wave velocity c_p is variable in the FZ and unknown. Furthermore, when the material is in the softening phase, the stiffness reduces and no wave velocity c_p can be derived from the equation of motion:

$$c_p = \sqrt{\frac{1}{\rho} \cdot \frac{d\sigma}{d\varepsilon}}$$

Equation 4.14 (= equation 4.6) still holds, even in the softening phase. This means that when the acceleration of the 'damaged material' in the FZ is known as a function of time, equation 4.14 can be applied and the 'true' material stress $\sigma_{soft}(t)$ is also known from the equilibrium of 'half the failure zone' (see Figure 4.36):

$$\sigma_{elas}(t) = \sigma_{soft}(t) - \rho \cdot dx \cdot \ddot{u}(t) \tag{4.14}$$

The contribution of structural inertia is given by:

$$\sigma_{inertia}(t) = \rho \cdot dx \cdot \ddot{u}(t) = \int_{x1}^{x2} \rho(x,t) \cdot \ddot{u}(x,t) \cdot dx \tag{4.15}$$

Assuming that the density is not or hardly affected during the experiments, the inertia contribution is represented by:

$$\sigma_{inertia}(t) = \rho \cdot \int_{x1}^{x2} \ddot{u}(x,t) \cdot dx \tag{4.16}$$

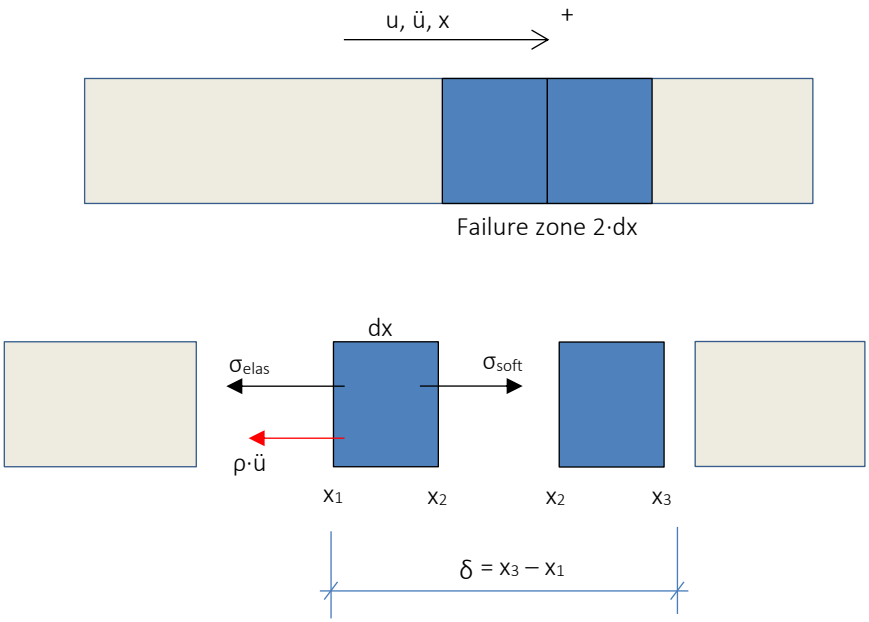

Figure 4.36 Equilibrium of half of the failure zone and measured deformation.

If the displacement distribution $u(x,t)$ is known as a function of time, also $\ddot{u}(x,t)$ can be derived, the contribution of inertia can be determined and the true stresses $\sigma_{soft}(t)$ can be quantified using equation 4.14 for the pre-peak as well as the post-peak phase.

However, in the MSHB tests, we did not record $\ddot{u}(x,t)$ but we recorded the total deformation of the damage zone, δ_{dam}, by the difference in movement between points x_1 and x_3 (see also Figure 4.36 and Figure 4.37):

$$\delta_{dam} = u_3 - u_1 \tag{4.17}$$

Although only the total deformation is recorded, we can use this information to estimate the inertia effect on the recorded softening process.

When fracture starts from the centre of the fracture zone, δ_{dam} will be symmetrical and equal for both parts of the failure zone. However, the damage distribution is not equally distributed within the fracture zone (see Figure 4.37).

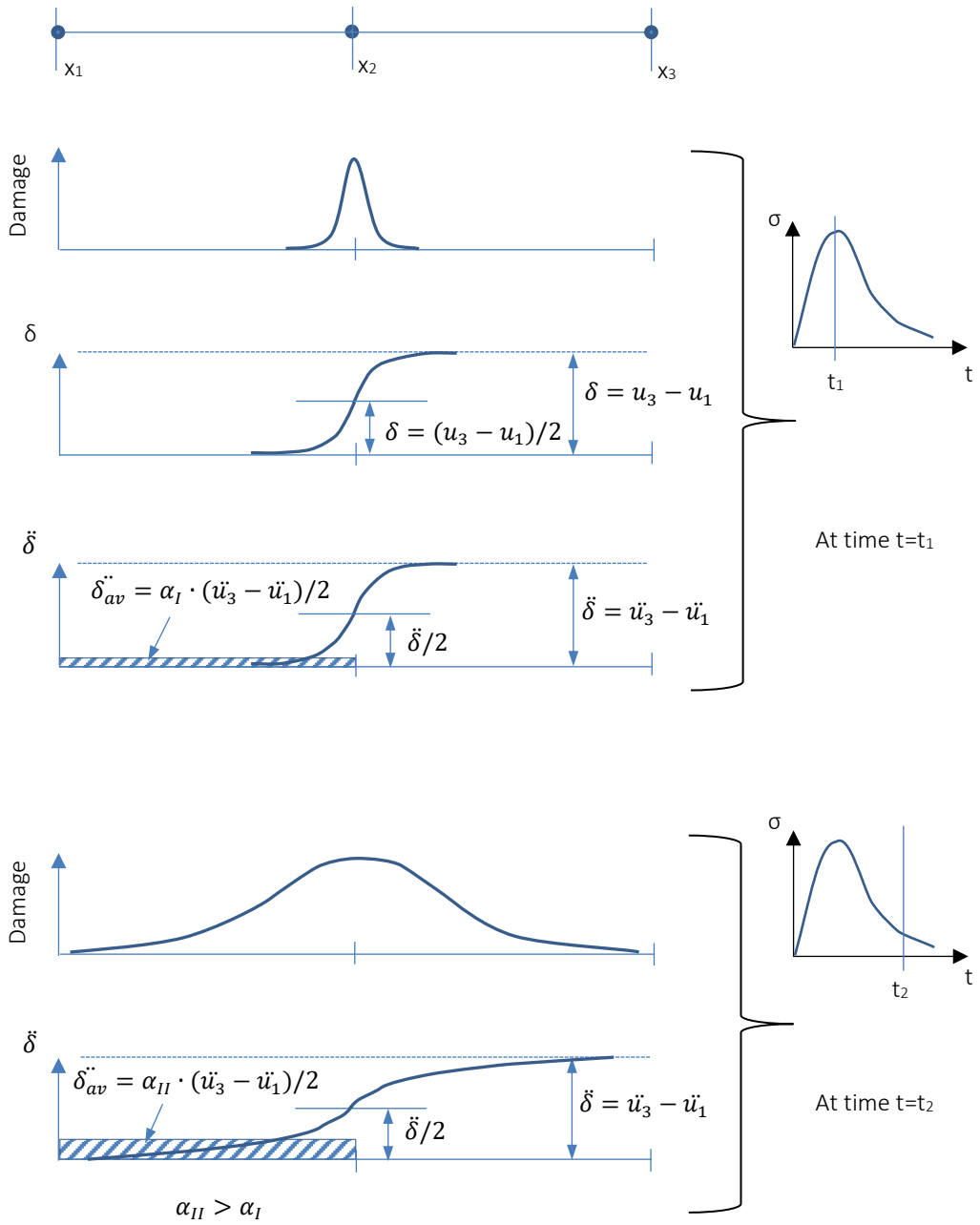

Figure 4.37 Damage distribution, deformation and acceleration of the fracture zone at time t_1 and time t_2.

The fracture will start at the centre of the notch and will extend to a wider zone during the softening process. The consequence of the damage concentration to the deformation δ(x,t) is schematically illustrated in Figure 4.37 for time $t=t_1$ and $t=t_2$. The acceleration distribution $\ddot{\delta}$ will have a similar shape as the deformation distribution δ (see also Figure 4.37).

In order to estimate the inertia contribution to the tensile strength, the average value of the acceleration of half the fracture zone (between point x_1 and x_2) has to be known. Then the inertia contribution can be estimated according to the following equation:

$$\sigma_{inertia}(t) \approx M \cdot \ddot{\delta}_{av}(t) = \rho \cdot \ddot{\delta}_{av}(t) \cdot \frac{1}{2} \cdot WFZ \tag{4.18}$$

The average value of the acceleration can be determined by FEM analysis or advanced digital image correlation (DIC) and high speed camera images. This information is currently not available and, therefore, the average acceleration value is expressed with a factor α (see also Figure 4.37):

$$\ddot{\delta}_{av}(t) = \alpha \cdot \frac{1}{2} \ddot{\delta}(t) \tag{4.19}$$

Thus, the inertia contribution can be written as.

$$\sigma_{inertia}(t) \approx \rho \cdot \alpha \cdot \frac{1}{2} \ddot{\delta}(t) \cdot \frac{1}{2} \cdot WFZ \tag{4.20}$$

As Figure 4.37 shows, the wider the damage distribution, the higher the average value for acceleration of half of the fracture zone. When the damage distribution approaches an evenly distributed crack pattern, the factor α will be 0.5. However, the deformation of the fracture zone is not equally distributed, but concentrated around the final macro crack (see Figure 4.38). Therefore, the fracture zone will not be fully activated and the factor α, which determines the average acceleration, will be less than 0.5.

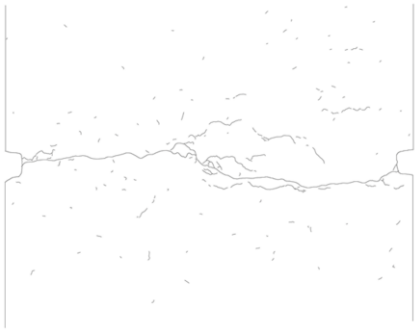

Figure 4.38 Fracture pattern N14, fracture concentrated around macro crack.

A precise value of factor α cannot be determined from the data, because the displacement distribution $u(x,t)$is not recorded, but the total deformation of the damage zone. To estimate the value of factor α, which determines the average value of the acceleration for half of the fracture zone, the available information on final crack distribution is used. The final crack distribution is determined and quantified with microscopic analysis. The largest deformations will occur around the macro crack and the micro cracks connected to the macro crack. The value of the average acceleration factor α is estimated by comparing the width of the zone holding the macro crack and the connected micro cracks to the corrected total width of the fracture zone. For instance, normal Portland cement concrete has a total WFZ of approximately 19.1 mm and the width of the macro crack with connected micro cracks is 8.6 mm. The cracks are not evenly distributed and, therefore, factor α will be less than 0.5. The average acceleration factor α is estimated to be α = 0.25.

As stated in paragraph 4.6.1, structural inertia effects do not contribute to the enhanced strength in the pre-peak phase. In the post-peak phase, the inertia contribution is estimated by equation 4.20. The acceleration $\ddot{\delta} = \ddot{u}_3 - \ddot{u}_1$ is determined from the experimental data on deformations. The measured deformation was differentiated two times and the results smoothed over a time frame of 9 μs (9 sample points), to get rid of the scatter. The smoothing procedure used is a so called moving average filter, which smooths data by replacing each data point with the average of the neighbouring data points defined within the span.

In Figure 4.39, the deformation of the fracture zone (Def_notch_N12), which is the measured deformation minus the elastic deformation, and the deformation velocity are

plotted against the stresses in the notch (right axis). Regarding the accelerations, four different phases in the pre-peak and post-peak behaviour can be identified.

In phase I, the pre-peak phase, the deformation velocity data show that the deformation velocity increases. However, although accelerations do occur, the contribution of inertia to the recorded tensile strength is negligible in this pre-peak phase and will be disregarded (see also paragraph 4.6.1).

After reaching the maximum strength, in the post-peak phase, three different phases are identified. In phase II the deformation velocity increases further in the first branch of the softening curve. In phase III the deformation velocity drops, which means negative accelerations, to a more or less constant value in phase IV. In this last phase the accelerations are approximately zero.

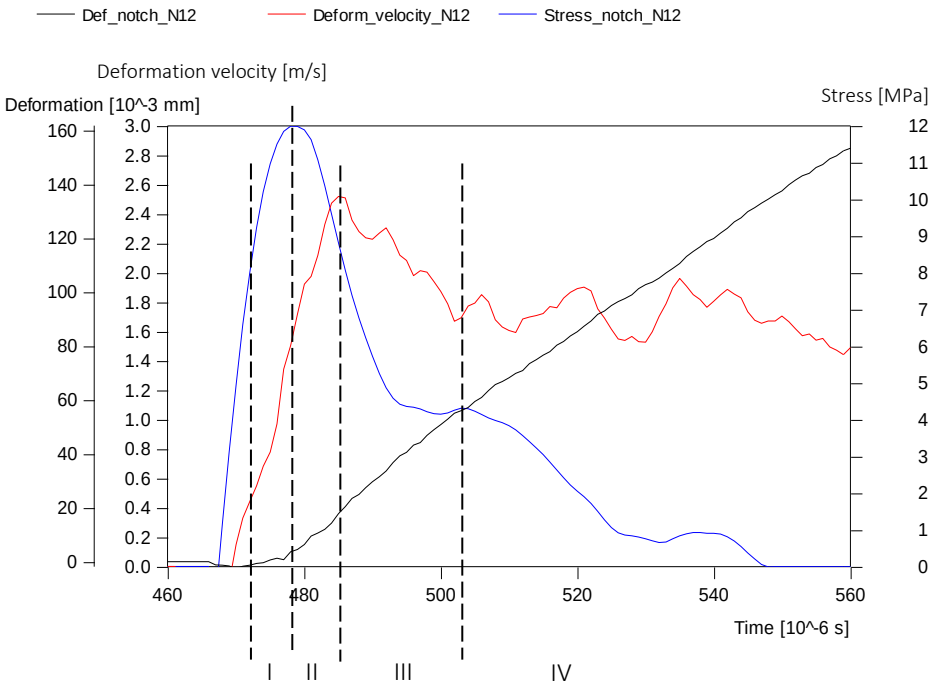

Figure 4.39 Different phases for deformation velocity in MSHB test; I: acceleration in the pre-peak phase, II: acceleration in post-peak phase, III: deceleration, IV: constant deformation velocity, thus acceleration = 0.

Using equation 4.20, the contribution of structural inertia in the different phases is estimated. With the experimental data on fracture patterns, we are able to estimate the factor α for the *final* crack pattern (phase III and phase IV). However, there is no information available on the variation of the width of the fracture zone *during the fracture process*. This information can be obtained from numerical simulations. At the current state of research, the factor α is estimated to be 0.25 (final distribution) for phase III and phase IV. For phase II, when the peak stress is reached but the deformations are still small, the factor α is assumed to be 0.1.

The average contribution of the structural inertia of the fracture zone to the stresses in the different phases of the stress-deformation curve is summarized in Table 4.8 for the MSHB tests on normally cured Portland concrete. The width of the fracture zone is approximately 20 mm and the concrete density is 2330 kg/m^3.

Table 4.8 Estimation of the average contribution of structural inertia of the fracture zone to apparent tensile resistance in MSHB tests for different phases in stress-deformation curve using the average acceleration factor α.

$\Delta ft_{inertia}$	Average Acceleration [$\cdot 10^5$ m/s^2]	α [-]	$\sigma_{inertia}$ [MPa]	Δσ [%]
Pre-peak (phase I)	1.58	0.0	0.0	0
1st post peak (phase II, acc)	1.11	0.1	0.1	1
2nd post peak (phase III, dec)	-0.64	0.25	-0.2	-2
3rd post peak (phase IV)	+/-0.0	0.25	+/-0.0	0

The contribution of structural inertia in the post-peak phase to the measured stresses is in the order of 1-5% for the high loading rate regime. In phase II, the structural inertia effects will contribute to the measured stresses and the 'true' stresses can be found by subtracting the inertia contribution from the measured stresses. For phase III, when the deformation rate is decreasing and the acceleration is negative, the 'true' stresses will be higher and the inertia should be added to the measured stresses.

For the moderate regime, up to 50 GPa/s, the accelerations are much smaller in the different phases. In Figure 4.40, the deformation of the fracture zone and the deformation velocity are plotted against the stresses in the upper bar (shifted to the notch) for a

representative SHB test. The deformation velocity data of the SHB tests shows that almost no acceleration takes place in the pre-peak phase. In the post-peak phase, phase II, the deformation rate increases and then stays more or less constant when the stresses are almost zero and fracture is complete.

The average acceleration in the post-peak fracture phase (phase II) is much smaller than for the higher loading rates; $\ddot{\delta}$ = 1.03 m/s /158 µs = 6.5*10^3 m/s^2, see Figure 4.40. Also, the width of the fracture zone for the SHB tests is smaller, in the order of 10 mm (see Table 4.6).

When using equation 4.20 to determine the contribution of structural inertia, the contribution to the apparent stresses in the post-peak phase appears to be in the order of 0.01 - 0.05 MPa for the SHB tests, which is negligible.

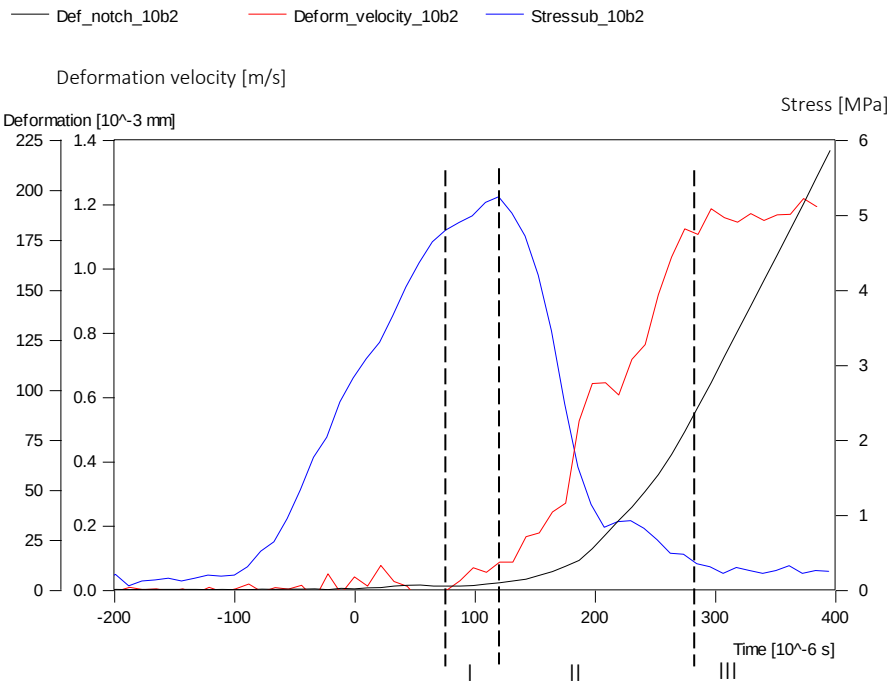

Figure 4.40 Different phases for deformation velocity in SHB test 10b2: I: acceleration in pre-peak phase, II: acceleration in post-peak phase, III: constant deformation velocity: acceleration = 0.

From the presented analysis of the deformation velocity data and corresponding accelerations, it can be concluded that inertia effects only have a small influence on the stress-deformation relation in the post-peak phase for the high loading rate regime. The deformation velocities and estimated contributions to the apparent tensile stresses in Table 4.8 also show that in the second branch of the softening curve (phase IV) the velocity is approximately constant and, therefore, the accelerations are zero and structural inertia is negligible in this phase. This means that the enhanced resistance found in the tail of the stress-deformation curve for the high loading rate regime must be due to another mechanism than structural inertia of the fracture zone.
For the moderate loading rate regime, structural inertia effects are negligible and can be disregarded.

4.7.3 Stress-deformation curve and bumps

The contribution of the inertia effects of the fracture zone to the measured stresses can be estimated as explained in the previous paragraph. To quantify the contribution of the structural inertia of the fracture zone to the stress-deformation relation, the acceleration in time is determined by differentiating the deformation measurements two times. Subsequently equation 4.20 is used to establish the structural inertia for the post-peak phase in real time and to determine the 'true stresses', assuming factor $\alpha = 0.25$ for phase III and IV and $\alpha = 0.1$ for phase II.

In Figure 4.41 and Figure 4.42 the 'true' stresses for a representative MSHB test (N12 and N19 respectively) are shown compared to the stresses determined at the notch. The 'true' stress results are smoothed according to the same principle as used for smoothing the deformation velocity, with a moving average filter with time span 9 µs. By doing this, the high frequency flutter is removed.

From Figure 4.41 and Figure 4.42 it is obvious, that inertia of the fracture zone only has a small effect on the softening part of the stress-deformation curve and the observed bumps in the tail of the softening branch.

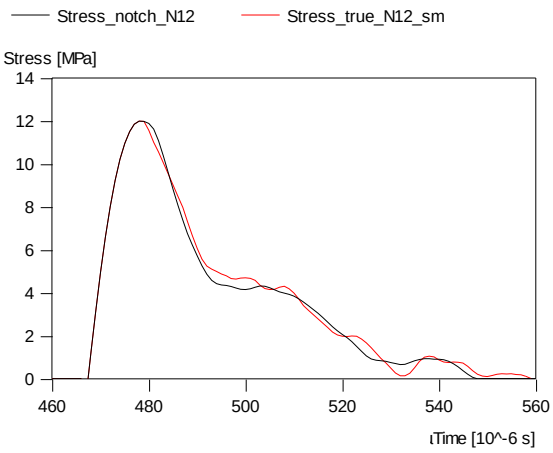

Figure 4.41 Determined stresses at the notch using waves at R9-17 (black curve) and 'true' stresses at the notch (red curve) for MSHB test Portland normal N12. (location R9-17, see Figure 4.5)

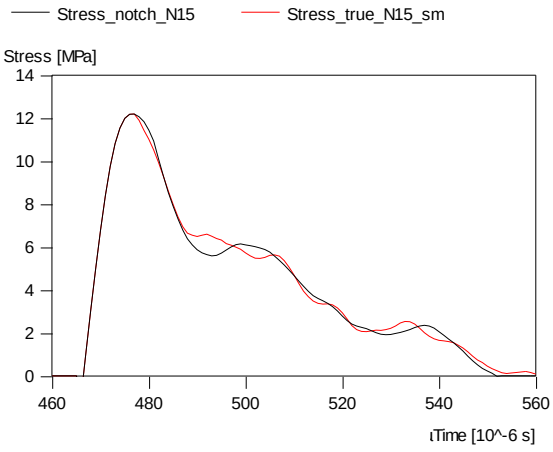

Figure 4.42 Determined stresses at the notch using waves at R9-17 (black curve) and 'true' stresses at the notch (red curve) for MSHB test Portland normal N15.

As explained in paragraph 4.5.2, the bumps in the stress-deformation curves for specimens tested in the high loading rate regime are partly caused by the fracture process, when part of the tensile wave is reflected as a compressive wave at the growing fracture surface, travels to the free end and returns to the notch as a 'second' tensile wave. The apparent increased resistance of the material when the stresses increase due to these returning

tensile waves, shown as bumps in the stress-deformation curve, are partly caused by structural inertia of the fracture zone, which can be seen in Figure 4.41 and Figure 4.42. When excluding the structural inertia using the double differentiated deformation measurements, the bumps become less distinctive.

The first bump in the stress-deformation curve is not only caused by the returning waves, but also by the negative structural inertia at approximately t = 490 µs (see Figure 4.39). This negative inertia is ascribed to the particle velocity reaching its maximum, due to the incident tensile wave and the first reflected compressive wave at the fracture surface. In order to illustrate this the records of test N12 are analysed. The complete incident wave at the notch is reconstructed using the compressive part of the loading wave at position R9-17 (35 mm from the notch) and assuming material damping of 0.8% /cm (Figure 4.43, Rnotch_inc, blue). The maximum of the incident tensile wave is reached about 17 µs after reaching the notch.

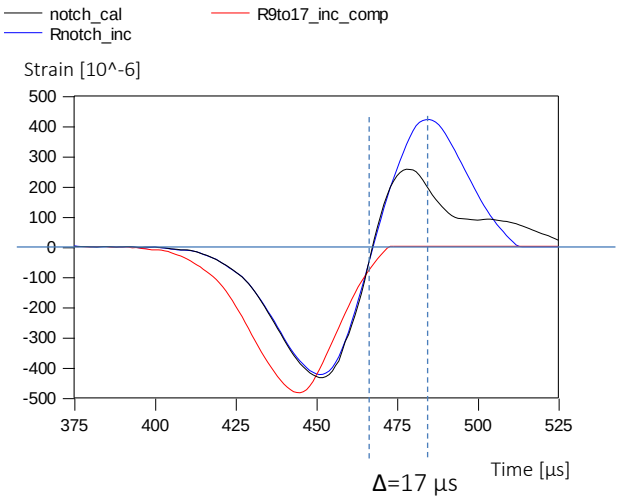

Figure 4.43 Reconstructed incident wave at the notch (Rnotch_inc, blue), the compressive part of loading wave R9-17 (R9to17_inc_comp, red) and experimentally determined strains at the notch (notch_cal, black) for representative test N12.

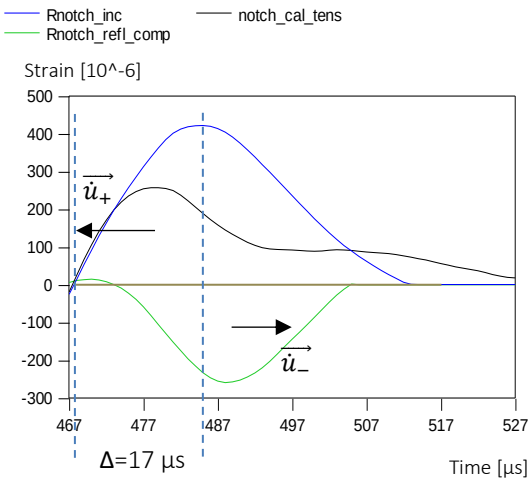

Figure 4.44 Tensile wave at the notch, incident (blue) and experimentally determined (black), and reflected compressive wave (green), each contributing to the particle velocity $\dot{u}$ in the same direction, test N12.

When the tensile strength is reached and fracture starts to grow, the incident tensile wave cannot be transferred anymore and will be partially reflected as a compressive wave (see Figure 4.44). The amplitude of the compressive wave (Figure 4.44, Rnotch_refl_comp, green) is equal to the difference between the incident tensile wave (Figure 4.44, Rnotch_inc, blue) and the experimentally determined tensile stresses at the notch (Figure 4.44, notch_cal_tens, black).

The particle velocity at the notch due to the combination of the incident tensile wave and the reflected compressive wave, each causing the particles to move in the same direction (see Figure 4.44), also reaches its maximum after approximately 17 µs. This effect is visible in Figure 4.39, where the measured deformation velocity in the fracture zone is decreasing after approximately 17 µs, resulting in a deceleration, negative inertia and a decrease in the apparent stress-deformation curve. When excluding this negative structural inertia of the fracture zone, the first bump becomes much less distinctive (see Figure 4.41 and Figure 4.42).

With the 'true' stresses at the notch, corrected for structural inertia in the post-peak phase, the 'true' stress-deformation curve can be obtained. The stress-deformation curve without structural inertia of the fracture zone (axial direction) is plotted in Figure 4.45

('Def_curve_cor_N12'). When comparing the stress-deformation curve determined from the waves at R9-17 and the stress-deformation curve which is corrected for structural inertia effects in the axial direction (see Figure 4.45, green compared to light blue), it is obvious that the structural inertia of the fracture zone only contributes to a small extent to the fracture behaviour and the determined fracture energy. The fracture energy increases with approximately 3% after correcting for structural inertia effects. This is negligible.

It is obvious that, when comparing the for structural inertia effects corrected stress-deformation curve at high loading rates with medium and static loading rates (see Figure 4.45, blue curve compared to red and orange curve), concrete becomes more ductile in the high loading rate regime. After excluding the structural inertia effects in the post-peak phase, the peak is still wider, the softening curve is less steep and the total fracture energy increases significantly at high loading rates. The enhanced fracture energy is, therefore, not attributed to structural inertia of the fracture zone.

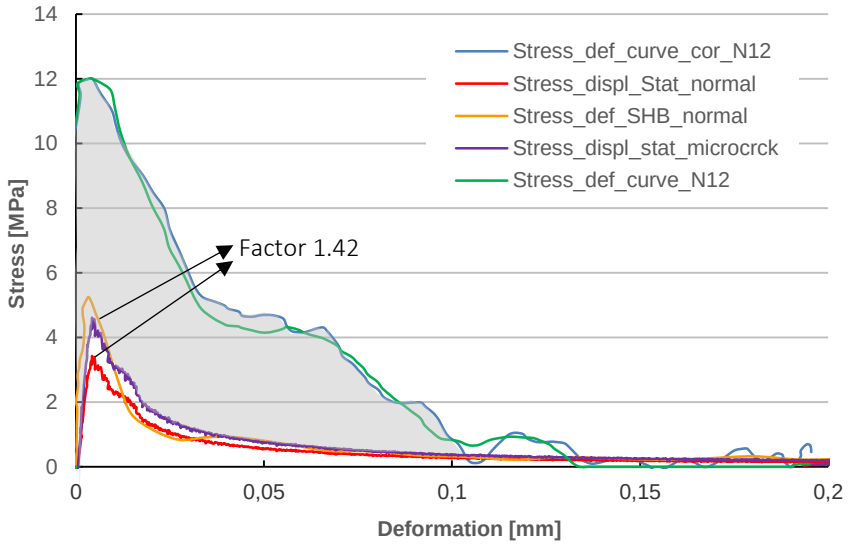

Figure 4.45 Stress-deformation curve without structural inertia for MSHB test N12 (light blue), compared with determined stress-deformation curve at the notch including structural inertia (green), static stress-displacement curve (red), SHB stress-deformation curve (orange) and static stress-displacement curve increased with factor 1.42 (dark purple).

The contribution of additional micro cracks to the enhanced fracture energy can be estimated from Figure 4.45, 'Stress_displ_stat_microcrack' (purple curve). Additional micro cracking in the high loading rate regime leads to a total increase of the fracture length with a factor 1.19 compared to the static loading rate, see Table 4.4. Assuming penny shaped cracks and that the cracks grow the same amount in the direction perpendicular to the measured fracture plane, the total fracture length in the high loading rate regime increases with a factor $1.19^2 = 1.42$ compared to the static loading rate regime. The grey area in between the corrected stress-deformation curve, inertia of the fracture zone excluded, and the static curve with '42% more fracture energy due to micro cracks' shows an increase in fracture energy due to additional resistance of the material, not being structural inertia of the fracture zone or additional micro cracks.

In this paragraph the deformation data and the fracture geometry data have been combined with the experimental data and stress-deformation curves, to study the causes of the rate effects on fracture behaviour. Although the differentiation of the deformation-time signals is limited due to the experimental constraints, valuable conclusions can be drawn;

- The shape of the softening curve is only slightly influenced by structural inertia of the fracture zone for the high loading rate regime, whether due to returning waves or the first incident wave. For a proper determination of the 'true' stresses in the post-peak phase, the contribution of structural inertia to the tensile stresses should be subtracted from the apparent stresses determined at the notch. With these stresses the 'true' shape of the descending branch of the stress-deformation curve for the high loading rate regime can be determined.
- The stress-deformation curves for the high loading rate exhibit an enhanced resistance, not due to structural inertia of the fracture zone. This additional resistance can be due to three different phenomena;
  (1) additional micro cracking, although experimental data show that increase in micro crack length is limited.
  (2) inertia at micro level in the pre-peak phase and perhaps also the softening phase, due to limitations in crack propagation.
  (3) enhanced resistance by moisture in the pores or micro cracks.

The influence of moisture will be analysed and discussed in the next chapter.

4.8 Conclusions

In this chapter the dynamic material response for concrete under tensile loading and the mechanisms behind the rate effects on tensile properties for normally cured concrete are presented and discussed. Using simple analysis, the different mechanisms and the loading rate at which they have significant effect are identified.

The dominant mechanisms for dynamic tensile strength depend on the loading rate;

- Structural inertia of the fracture zone does not contribute to the enhanced tensile strength for the moderate as well as the high loading rate regime. Therefore, the obtained strength is the so called 'true' strength and should be used in the constitutive model.
- Inertia effects at micro scale change the stress distributions around crack tips or flaws and, therefore, delay crack initiation and propagation. Inertia effects on crack initiation only occur at very high loading rates (>5000 GPa/s). Inertia effects on crack propagation due to limitation of the crack velocity can occur at loading rates exceeding the moderate regime (>50 GPa/s) and plays a significant role in the high loading rate regime.
- For the moderate regime, micro inertia and inertia of the fracture zone do not contribute to the enhancement of the tensile strength. Therefore, the observed increase in strength is most probably due to the viscous behaviour of the material (viscosity due to the moisture content).

The influence of the loading rate on the softening post-peak response was studied. The stress-deformation curves were used to quantify the fracture energy and characterize the dynamic response. The following conclusions are drawn;

- For loading rates up to 50 GPa/s, the fracture energy, shape of the stress-deformation curve, width of the fracture zone and the amount of micro cracking are hardly affected by loading rate. The rate effect is restricted to the enhanced strength. This conclusion is supported by the performed simple analyses.
- At high loading rates (>50 GPa/s), the length of the generated macro crack does not change. The width of the fracture zone increases considerably, while the amount of micro cracks increases only moderately. By using basic principles of fracture mechanics it is showed that additional micro cracking is possible, but only at higher loading rates (>45 GPa/s).

- The 'bumps' in the post-peak response of the high loading rate regime are partly caused by structural inertia of the fracture zone. Therefore, the post-peak response needs to be adjusted for structural inertia effects in the fracture zone. From the established data on deformation rate it can be concluded that this structural inertia effect is limited to the first part of the softening curve and can be ignored for the macro cracking phase (tail of the softening curve).
- The increase in fracture energy and changed shape of the stress-deformation curve can be due to; (1) additional micro cracking, (2) the structural inertia response of the fracture zone, (3) the inertia at micro level due to limited crack propagation and (4) the contribution of moisture in the pores and possibly in the micro cracks to the enhanced resistance. The contribution of the inertia of the fracture zone to the fracture energy and shape of the curve is very limited and, therefore, the structural inertia is only quantified to be able to reduce the bumps in the stress-deformation curve.

  To be able to quantify each contribution of these mechanisms properly, detailed experimental and numerical research is necessary. The current experimental method, presented in this thesis, is sufficient to experimentally determine the main contributions but could be improved to increase the accuracy of the data on the individual aspects.

In this chapter the dominant mechanisms behind the rate effect on concrete tensile properties are identified. The knowledge on the mechanisms behind the rate dependency can be used to improve numerical models. The constitutive material model used in dynamic numerical calculations should include the effects due to the rate dependency of concrete properties, dependent on the scale of the numerical model used. For instance, when modelling the dynamic behavior of mortar with (large) aggregate particles, the so called meso scale, only the mechanisms that are ascribed to the materials itself should be explicitly included into the material model. For this meso scale, the effects due to moisture and the micro inertia effects should be included in the material model. When sufficient level of detail is represented in the meso-model, the structural inertia effects should be covered by the numerical calculations itself. Else, the structural inertia effects should also be included into the constitutive material model. However, if modelling takes place at macro level and the experimental data can be reproduced with a modified constitutive

model, which includes all identified mechanisms, proper prediction of rate effects on concrete properties like strength or fracture behaviour is also possible.

In this chapter the experimental results and analysis of the results for normally cured Portland cement concrete have been given. The effect of moisture on the rate dependency of concrete is studied in detail in the next chapter.

CHAPTER 5: INFLUENCE OF MOISTURE ON RATE EFFECTS ON CONCRETE TENSILE PROPERTIES

5.1 Introduction

In the previous chapter, the rate dependency of tensile properties of normally cured concrete was studied. The main causes of the rate effects are identified and to a certain extent quantified. One of the probable causes of the rate dependency of concrete properties is moisture in the pores. Previous studies on dynamics and moisture [Cadoni 2001a, Ross 1996, Rossi 1992, Toutlemonde 1995a, Toutlemonde 1998, Vegt 2006b, Vegt 2006d, Weerheijm et all 2013] have proven that the following parameters play an important role:

- Amount of pores;
- Pore size and pore size distribution;
- Saturation degree of the pores.

In past research, it has been found that the rate dependency of concrete properties is influenced by the moisture present in the pore structure. However, the research was limited to the concrete strength. The influence of the mentioned parameters on fracture energy and fracture behaviour was not quantified. In this chapter the influence of moisture on the rate dependency of concrete strength as well as fracture behaviour is studied, analysed and quantified by using concrete specimens that are kept under different curing conditions (see paragraph 3.2). Due to the different conditions, the specimens vary from saturated to dry. Also the influence of the pore structure is studied by comparing different concrete types.

Paragraph 5.2 presents the experimental program for studying the influence of the moisture saturation level and the pore structure on the rate dependency of tensile properties. Knowledge of the microstructure of the concrete and knowing which pores are filled with moisture is crucial for a proper analysis of the experimental results and for a reconstruction of the underlying mechanisms. Therefore, the structure of the concrete and the moisture distribution in the pore structure are described in paragraph 5.3 and 5.4. The experimental results on Young's modulus, strength and failure behaviour are presented in paragraph 5.6, 5.7 and 5.8. The mechanisms behind the rate dependency of concrete and the influence of moisture are reconstructed by combining all experimental data on mechanical properties, pore structure and moisture level. In paragraph 5.9 and 5.10 the experimental results are combined and also analysed with simple models with the aim to understand and quantify the main mechanisms which cause the rate dependency of tensile strength and fracture behaviour.

5.2 Experimental test program on moisture

To study the influence of the moisture content and pore structure on the rate dependency of tensile properties, different moisture contents and concrete types are used and tested at three loading rates. To study the effect of the pore structure, Portland cement concrete is compared with Blast Furnace Slag (BFS) cement concrete, the latter having a denser pore structure with less capillary pores compared to Portland concrete (see paragraph 5.3.2). The concrete composition and aggregate grading of both types of concrete are presented in chapter 3, Table 3.2 and Table 3.3.

To recall, the different conditions used in the static and dynamic tests are:

- "Normal" condition: specimens are stored under controlled conditions of 20˚C and 50% relative humidity (RH);
- "Wet" condition: specimens are submersed in water;
- "Dry-50" condition: specimens are dried in an oven of 50˚C and 15% RH;
- "Dry-105" condition: specimens are dried in an oven of 105˚C and 2% RH.

The conditioning of the specimens starts at an age of 28 days and is described in detail in paragraph 3.3.

The rate dependency of the tensile properties of Portland cement concrete is studied using the above described four different moisture conditions and by testing at three loading rates; static ($1{\cdot}10^{-4}$ GPa/s), moderate (50 GPa/s) and high loading rates (> 1000 GPa/s). The test set-ups for these loading rates are the same as used in the previous chapter and are described in chapter 3. The concrete dried at 105˚C is only tested for static and moderate loading rates.

The rate dependency of Blast Furnace Slag cement concrete properties is studied for wet and normal conditions at the three loading rates mentioned above (see also Table 3.1).

5.3 Microstructure of concrete

The microstructure of concrete influences the properties of concrete like permeability, strength and fracture energy (see chapter 2), but has also an influence on the rate dependency of concrete properties since it is believed that the water in the pores plays an important role [Cadoni 2001a, Ross 1996, Rossi 1992, Toutlemonde 1995, Vegt 2006b, Vegt 2006d, Weerheijm et all 2013]. In this study the effects of moisture and pore structure on the rate dependency of concrete properties are analysed and quantified. To analyse the results, information on the pore structure of the concrete used is needed. The microstructure of concrete is influenced by the hydration process and the conditioning of the concrete during hydration. This is discussed in paragraphs 2.2.4, 2.2.5 and 2.2.6 and will be summarized in paragraph 5.3.1. For the determination and quantification of the pore structure of the concretes, Mercury Intrusion Porosimetry and Nuclear Magnetic Resonance (NMR) are used. The results on pore size distribution are presented in paragraphs 5.3.2 and 5.3.3.

5.3.1 Influence of conditioning on pore structure

The pore structure of concrete is created during the hydration process. The hydration process is described in detail in paragraph 2.2.1. During hydration, cement particles react with water and form a structure with gel- and capillary pores. The water-cement ratio has a large impact on the pore structure and the amount of capillary pores that are formed during hydration. When the water-cement ratio is higher than 0.4, the excess water will be stored in capillary pores. With a water-cement ratio of 0.5, as has been used for the

experiments, theoretically all cement particles could be hydrated and capillary pores are formed, which contain the additional water. However, in practice unhydrated cement particles are present in the cement paste and can be activated when rewetted. Therefore, the conditions in which the specimen are kept before testing considerably influence the final pore structure at the moment of testing. It is important to determine what the effect of the different conditions is on the final pore structure of the concrete samples. The results from microscopic research with the ESEM (see also paragraph 2.2) show the different microstructures after conditioning and help to identify the effects of drying and wetting.

The wet concrete specimens have been submersed in water at an age of 28 days, which has led to a restart of the hydration process and a denser cement structure, especially near to the aggregate particles (see Figure 5.1 compared to Figure 5.2) in the surface zone. This denser and more homogeneous structure can theoretically lead to a higher tensile strength and a different loading rate at which the rate dependency of the tensile strength becomes important. However, neither is observed in the conducted experiments (see paragraph 5.7). Still, the difference in concrete density due to the conditioning of the specimens, although not quantified in detail, should and has been considered in the analysis of the experimental results on strength, Young's modulus, fracture energy and fracture characteristics.

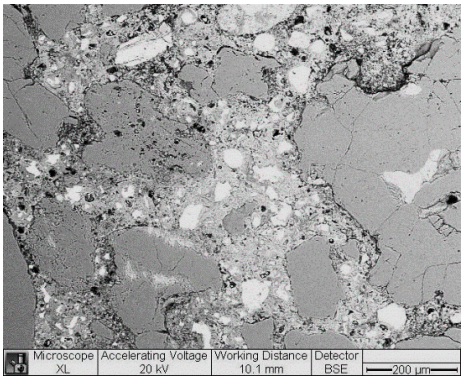

Figure 5.1 Structure of normally cured Portland cement concrete (ESEM), age approximately 7 weeks.

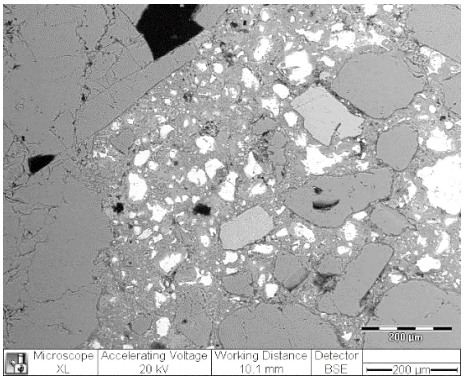

Figure 5.2 Structure of Portland cement concrete cured under 'wet' condition (ESEM), after 28 days under water, age approximately 7 weeks.

The elevated temperature in the drying oven can lead to a better hydration degree, provided that enough water is available to react with the unhydrated cement particles. This could result in a denser structure of the cement paste. However, drying at high temperature also introduces damage (see paragraph 2.2.5): (1) damage due to the difference between the thermal expansion coefficients of aggregate particles and cement paste and (2) damage due to drying shrinkage of the cement paste.

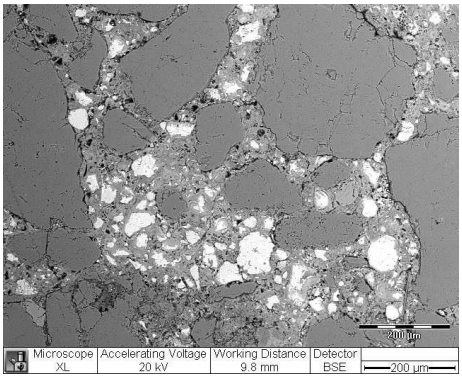

Figure 5.3 Structure of Portland cement concrete dried in oven of 50˚C (ESEM), age approximately 7 weeks.

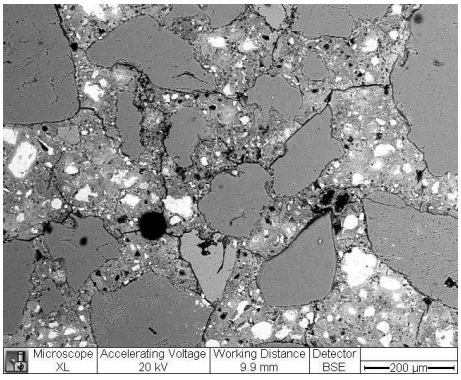

Figure 5.4 Structure of Portland cement concrete dried in oven of 105˚C (ESEM), age approximately 7 weeks.

The conducted microscopic research on specimens dried at drying temperatures of 105˚C, 50˚C and 35˚C shows that drying at 105˚C will lead to severe damage (see Figure 5.4). Drying at 50˚C will lead to small and superficial damage and drying at 35˚C will not lead to any visible damage. When combining the microscopic research of the ESEM samples with quantitative microscopic analysis of sections from the specimens cured under different conditions (see Table 2.3), it can be concluded that the specimens dried at 35˚C and 50˚C are quite similar in structure compared to normally cured concrete. The wet concrete has a denser structure and less damage at the moment of testing, while the concrete dried at 105˚C has more damage compared to normally cured concrete.

However, when specimens are dried at 35˚C, they are not completely dry at the day of testing (see paragraph 2.2). Therefore, a temperature of 50˚C is believed to be the best practical option to dry the specimens. When drying at 50˚C, the samples are completely dry after three weeks and the damage is minimal.

5.3.2 Pore structure with MIP

To be able to properly analyse the experimental results and to quantify the effects of the moisture in the pores it is necessary to know and quantify the pore structure of the two types of concrete used: Portland cement concrete and Blast Furnace Slag cement concrete.

One way to determine the pore structure and pore size distribution of concrete or cement paste is Mercury Intrusion Porosimetry (MIP). MIP is used for decades to determine the porosity and pore size distribution of cement-based materials. It is a fast method to obtain information about the pore structure. The pore diameters that can be measured vary from 0.001 µm to 1000 µm depending on the pressure used. A critical review is provided by Ye [Ye 2003], who evaluated different methods to characterize the pore structure. The MIP method is described in detail in [Aligizaki 2006]. The limitations of the MIP method are described in [Aligizaki 2006 and Ye 2003].

For the MIP tests, concrete samples are cut from the cylindrical concrete specimens and cement paste samples from casted cement paste cubes (Portland and Blast Furnace Slag cement paste cubes). The samples are shaped as small cubes, with a rib length of approximately 1 cm. The samples are freeze dried, since this is proven to be the least damaging method of drying for MIP samples [Ye 2003]. For the MIP tests, the samples are placed inside a chamber, evacuated and mercury is added. The pressure on the mercury is gradually increased. By tracking the pressures and volumes during the experiment, the porosity and pore size distribution can be determined.

Paste

The pore size distribution is defined as the pore volume per unit interval of pore diameter. The differential pore size distribution curve is obtained by taking the slope of the pore size distribution curve against the pore diameter (log scale). The peaks of the differential pore size distribution curve represent the main pore diameters. In general, for cement paste, the most right peak is considered to represent the capillary porosity, with a diameter of the pores ranging from 0.1 µm to 10 µm. The second peak corresponds to the gel pores, with a diameter of the pores ranging from 0.001 µm to 0.1 µm.
In the experimental results for the cement types used (see Figure 5.5), one large peak and a small second peak are visible for the Blast Furnace Slag cement and two less distinct

peaks are visible for Portland cement. The results show that Portland cement paste has more capillary pores and less gel pores compared to Blast Furnace Slag cement paste.

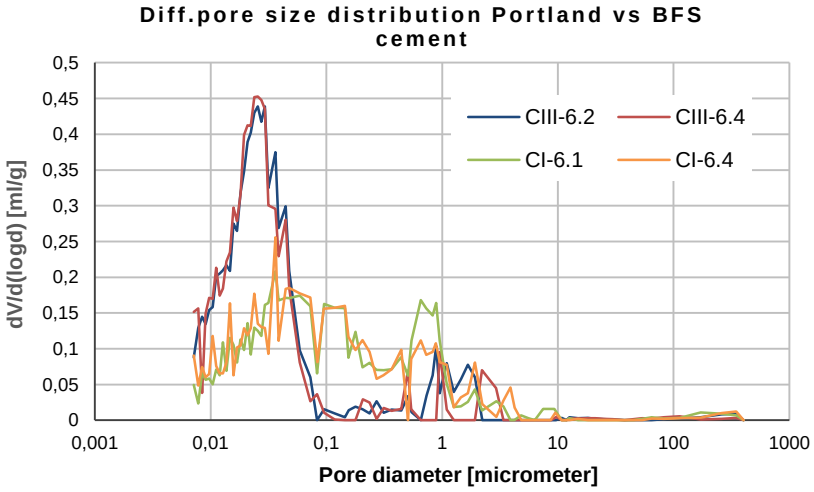

Figure 5.5 Differential pore size distribution Portland cement paste (test CI-6.1 and CI-6.4) and Blast Furnace Slag cement paste (test CIII-6.2 and CIII-6.4), age 6 weeks.

Concrete

Hydrated concrete consists of aggregate particles glued to together with cement paste. The aggregate particles have a significant influence on the pore size distribution. Around the aggregate particles a certain area is observed where the porosity is highest. Therefore, the MIP tests are repeated with small concrete samples, to determine the pore size distribution of concrete instead of the homogeneous cement paste.

The results from these MIP tests show that also in the concrete samples made with Blast Furnace Slag cement there is a significant increase in gel pores compared to Portland cement concrete. The higher amount of capillary pores for Portland cement paste compared to BFS cement paste is not found for concrete samples (see curves in Figure 5.6).

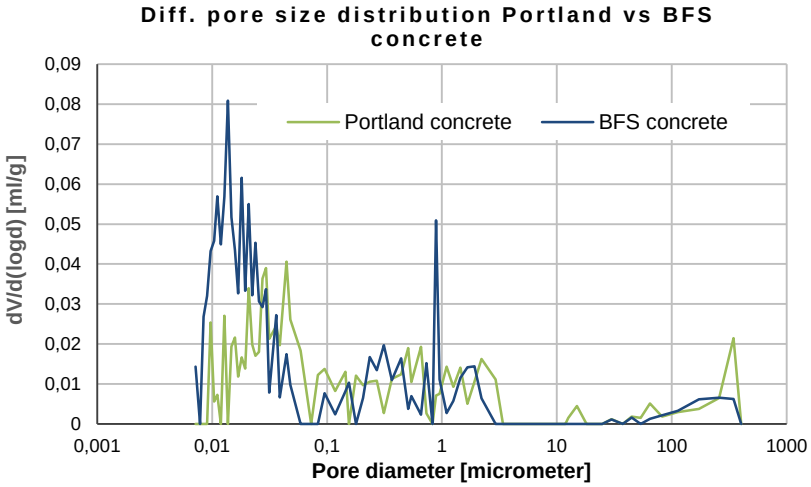

Figure 5.6 Differential pore size distribution Portland cement concrete and Blast Furnace Slag cement concrete, age approximately 3 months, max. aggregate size 8 mm.

Table 5.1 Pore diameter (median and average) and total pore area of Portland and Blast Furnace Slag concrete, age approximately 3 months.

Concrete	Median pore diameter [µm]	Average pore diameter [µm]	Total pore area [m^2/g]
Portland	0.274	0.077	2.3
BFS	0.058	0.031	6.4

When considering the data (see Table 5.1), the average pore diameter in Portland cement concrete is higher than in BFS cement concrete, as was expected. From the results in Table 5.1 it can be concluded that, at the same age of approximately 3 months, the total porosity of Blast Furnace Slag cement concrete is higher, but the average size of the pores is much smaller than for Portland cement concrete.

The results from the MIP tests for concrete samples are not as distinct as for cement paste, because of the presence of aggregate particles affecting the results. Due to the limitations of a MIP set-up, not wanting to use a lot of mercury for each test or very high pressures, the samples are very small (rib length ca. 1 cm) and the largest aggregate particles used in the concrete are in the same order. These larger particles influence the test results, having a larger density than the cement paste and almost no porosity. Although it is attempted to

avoid large particles in the small samples and to get similar compositions of the samples, the remaining aggregates do have a substantial effect on the MIP results and cause a large scatter of the results. Therefore, to quantify the pore sizes in concrete samples, a different and more accurate method is used; Nuclear Magnetic Resonance (NMR).

5.3.3 Pore structure with NMR

With NMR it is possible to determine the sizes of the pores by the differences in magnetic dipole moments and relaxation time T_2 (see paragraph 3.4). Concrete samples of substantial size (i.e. diameter 2-2.5 cm by 10 cm length) can be used with NMR, depending on the set-up. Chemically bound water cannot be detected but the evaporable water can. The latter consists of two parts: the water physically bound to the surface of the gel particles and the free water in the capillary pores (see also paragraph 3.4).

The relaxation time is proportional to the diameter of the pore, assuming spherical pores (see equation 5.1 and chapter 3).

$$T_{2,pore} = \frac{V}{S\rho_2} = \frac{d}{6\rho_2} \qquad (5.1 = 3.2)$$

with d = diameter of the pore (assuming spherical pores) and ρ_2 = surface relaxivity.

When the surface relaxivity ρ_2 is known, the T_2 distribution determined in the NMR tests can be converted into a pore size distribution. The surface relaxivity can be determined according to equation 5.2;

$$\rho_2 = \frac{\lambda}{T_{2,s}} \qquad (5.2)$$

with $T_{2,s}$ the fluid surface relaxation time and λ the thickness of the fluid layer of water interacting with the surface.

The thickness of the fluid layer, λ, is about the size of one water molecule which is approximately 0.3 nm [Valckenborg 2001b]. The fluid surface relaxation time $T_{2,s}$ has been determined by Valckenborg by measuring the relaxation time of a dry mortar sample which

was wetted with wet air flow. This experiment showed that $T_{2,s}$ = 85 ± 15 µs [Valckenborg 2001b]. When using this data, the pore distribution can be determined.

Assuming all pores of wet Portland and wet Blast Furnace Slag samples are filled, the NMR results on these samples show the difference in (filled) pores (see Figure 5.7). The initial amplitude of the spin-echo signal is proportional to the amount of hydrogen nuclei and is, therefore, a measure for the volume of moisture present in the sample, expressed as the sum of the amplitude. The sum of the amplitude is expressed as a so called arbitrary unit, a.u., or procedure-defined unit. This means that the unit is defined by the method and is not an absolute unit normally used to express volume, like for instance m^3. The results of the presented NMR tests can, therefore, only be used to indicate differences relative to each other. The results in Figure 5.7 show that BFS cement concrete has a larger amount of gel pores and Portland cement concrete a larger amount of capillary pores. This result is similar to the result found by the MIP tests, but much less scatter is present.

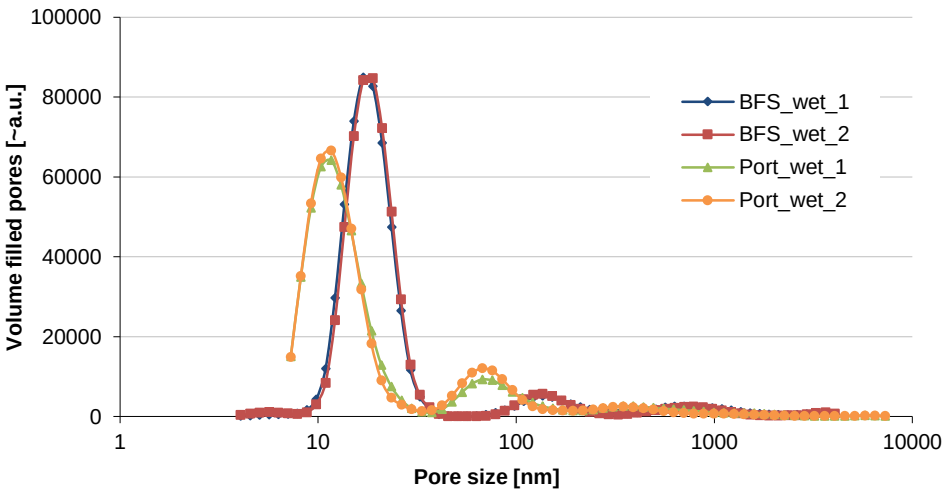

Figure 5.7 Pore size distribution wet BFS and Portland cement concrete samples, NMR tests, assuming spherical pores, age approximately 7-8 weeks.

However, the determination of the pore size distribution by converting the T_2 distribution into a pore diameter is not without difficulties. The surface relaxivity is determined from literature and not determined specifically for the types of concrete used in this research. In literature the T_2 distribution is usually not converted into pore diameters, but considered

as representative information concerning the pore size distribution. Therefore, in the next paragraphs the relaxation time T_2 will be used as a representative parameter for the pores sizes of the concrete samples used.

The differences between the NMR and MIP results can be explained by determination of the surface relaxivity, which is not specifically determined for the concretes used, but also by fundamental differences in the measuring techniques. Mercury porosimetry is based on injecting mercury into the sample at high pressures while recording the volume of fluid injected into the sample at each step. Pore sizes are then calculated from the relation between capillary pressure and pore radius, and the volume of each pore size is calculated from the volumes injected. When the connectivity of the pores deviates from ideality, the MIP technique tends to underestimate the larger pores within the sample as the volumes of larger pores are not reached at the correct corresponding pressure due to so called pore throat effects and are assigned to smaller pores (ink-bottle effect). In the NMR experiments molecules are monitored that are probing different cavities throughout the NMR measurement, resulting in a response depending on the size of the individual cavities. The connectivity and/or shape of the cavities do not influence the results, as in the case of MIP tests. Therefore, the NMR technique is believed to be more sensitive to variations in pore size distributions within concrete compared to the mercury intrusion technique. For the interpretation of the results of dynamic tests, the pore size distribution from the NMR technique will be used and the total porosity determined with the MIP technique.

5.4 Moisture in the specimens

The pore structure and pore size distribution of Portland cement concrete and Blast Furnace Slag cement concrete are determined using different techniques (see previous paragraph). For a proper analysis of the results and to quantify the influence of moisture on the rate dependency of concrete tensile properties, it is essential to know not only the pore size distribution of the concrete used, but also how much water is present in the pore system and which pores are filled; capillary or gel pores.

5.4.1 Saturation level, standard method

To determine the saturation level, which indicates the amount of pores filled, first some simple tests have been conducted. For the determination of the saturation level, pieces of concrete are cut from the cylindrical specimens. These pieces, being about half the size of a specimen used for the dynamic and static experiments, are kept in the same environmental conditions as the test specimens; wet (immersed in water), normal (50% RH and 20°C) and dry-50 (dried in oven of 50°C). All pieces will be kept in these three conditions for a duration of three weeks, like is the case for the specimens used in the static, SHB and MSHB experiments.

After being prepared the same way as the test specimens, the concrete pieces are weighted and put in an oven at 105°C to remove most of the physically-bound water (standard method). The pieces are left in the oven for 1 week. Next, the pieces are weighted and made vacuum, to make sure the water will be pulled into all the empty pores. Then water will be added and vacuum released, pushing the water into the pores of the concrete sample. The weight and volume of the saturated sample are determined.

The density (ρ), open porosity (ψ_0) and saturation level (w) are defined, using the following equations;

$$\psi_0 = V_{pores}/V_{tot} \tag{5.3}$$

$$w = V_{filled\ pores}/V_{pores} \cdot 100\% \tag{5.4}$$

$$\rho = m_0/V_{tot} \tag{5.5}$$

The results on saturation level, density and open porosity are summarized in Table 5.2. According to these results even the dry samples are not completely dry and the wet samples not completely wet.

Furthermore, it should be mentioned that drying the samples at 105°C (standard method) will damage the material by cracking (see paragraph 2.2) and, therefore, create extra porosity. To more accurately determine the volume of water present and which pores are

filled, Nuclear Magnetic Resonance is again used. The results of the NMR method are described in the next section.

Table 5.2 Density (ρ), open porosity (ψ_0) and saturation level (w), age of samples 8 weeks.

Concrete	Condition	ρ [kg/m³]	Ψ_0 [-]	w [%]
Portland	Normal	2374	0.139	62
	Wet	2428	0.141	94
	Dry-50	2286	0.140	14
BFS	Normal	2357	0.152	71
	Wet	2369	0.162	89
	Dry-50	2336	0.150	29

5.4.2 Moisture in pores with NMR

According to several authors, only the filled pores contribute to the rate dependency of concrete tensile properties [Ross 1996, Rossi 1992, Toutlemonde 1995, Vegt 2006d]. Therefore, it is important to know how much water is present in the pore system and in which pores. Nuclear Magnetic Resonance can give insight in the volume of water present *and* the location of the water. The sum of the spin-echo amplitude, a.u., represents the volume of moisture present in the different pores of the sample (see paragraph 3.4). As stated in paragraph 5.3.2, the pore size distribution can be determined from the difference in relaxation time (T_2) between capillary and gel pores. The assumptions about the size of the different types of pores and other voids (air voids and defects) for the different types of concrete are displayed in Table 5.3 [Valckenborg 2001a and Valckenborg 2001b].

Table 5.3 Relaxation time T_2 for different pores and voids, Portland and BFS concrete.

Concrete	T_2-gel pores [μs]	T_2-capillary pores [μs]	T_2-air enclosures [μs]	T_2-rest (defects) [μs]
Portland	10^2 -$10^{3.1}$	$10^{3.1}$ – $10^{3.8}$	$10^{3.8}$ - 10^5	10^5 – larger
BFS	10^2 -$10^{3.3}$	$10^{3.3}$ – $10^{4.1}$	$10^{4.1}$ - 10^5	10^5 – larger

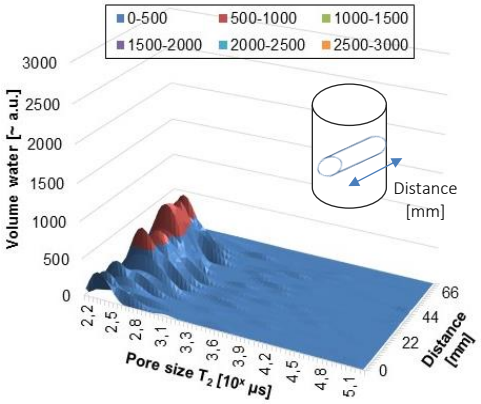

Figure 5.8 Moisture distribution BFS cement concrete dry, age approximately 7-8 weeks.

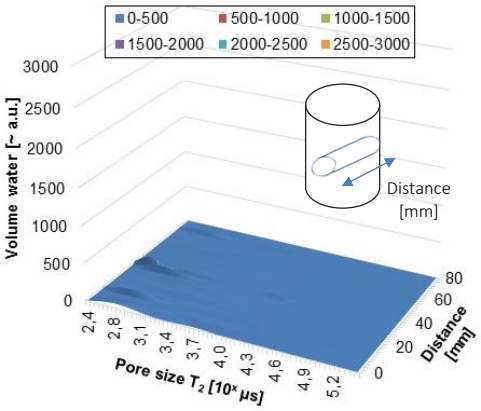

Figure 5.9 Moisture distribution Portland cement concrete dry, age approximately 7-8 weeks.

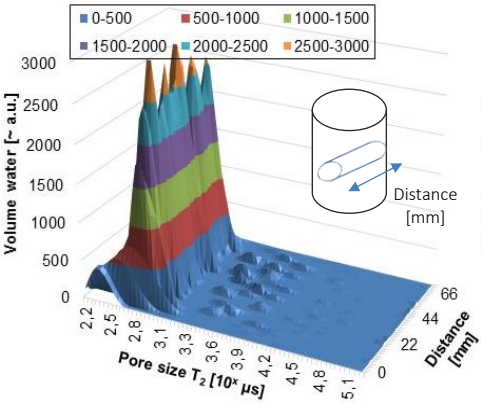

Figure 5.10 Moisture distribution BFS cement concrete normal, age approximately 7-8 weeks.

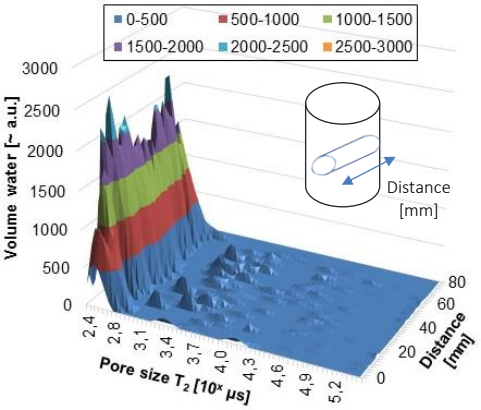

Figure 5.11 Moisture distribution Portland cement concrete normal, age approximately 7-8 weeks.

The relaxation time T_2 is determined over the diameter of the concrete samples. A 3-dimensional view of the filled pores over the diameter of the sample is obtained for concrete dried at 50˚C, wet concrete and normally cured concrete and both concrete types (see Figures 5.8 – 5.13). The vertical axis represents the volume of water (a.u.), the two horizontal axes represent the pore size T_2 and the location (= distance) in the sample over the diameter (0 – 74 mm) of the specimen. The visible peaks correspond with the different pores; gel- and capillary pores and air voids.

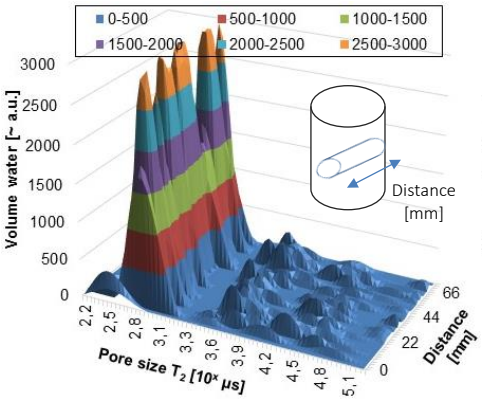

Figure 5.12 Moisture distribution BFS cement concrete wet, age approximately 7-8 weeks.

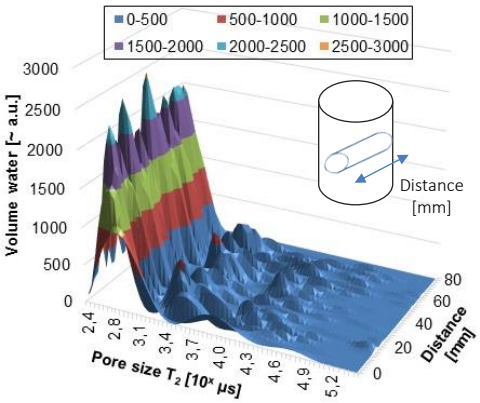

Figure 5.13 Moisture distribution Portland cement concrete wet, age approximately 7-8 weeks.

In Table 5.4 the results are quantified for normal, dry and wet conditions and for Portland as well as Blast Furnace Slag cement concrete. The total volume of water present in the sample is indicated by the sum of measured amplitude (a.u.). In Table 5.4, the different types of pores and voids are expressed as a percentage of the total volume of water present.

Table 5.4 NMR results on total volume of water (a.u.) and the distribution (% of total) of the moisture in the different voids: gel pores, capillary pores, air voids and defects, age approximately 7-8 weeks.

Condition	Total volume water in voids [$\sum$a.u. x 10^6]	Gel pores [%]	Capillary pores [%]	Air [%]	Defects [%]
Port-dry105	24.1	2.1	11.3	64.6	22.0
Port-dry50	21.3	3.6	13.8	57.3	25.3
Port-normal	35.7	37.3	9.5	28.0	25.2
Port-wet	157.7	14.9	15.9	52.7	16.5
BFS-dry50	15.1	46.8	11.7	23.8	17.7
BFS-normal	38.7	74.5	11.3	7.2	7.0
BFS-wet	191.8	20.6	12.3	46.7	20.4

NB: the sum of the measured amplitude (= a.u.) is the output of the NMR method and can be used as reference parameter for the volume of water present.

As can be seen from Table 5.4, the total volume of water present in wet BFS cement concrete is higher than in Portland cement concrete. This indicates that BFS cement concrete has a higher total pore volume, which is consistent with the results from the MIP tests. Other conclusions that can be drawn from the NMR data are:

- Portland and Blast Furnace Slag cement concrete contain approximately the same volume of water when cured normally, but the distribution of the water in the pores is very different, at an age of approximately 7-8 weeks.
- After drying at 50˚C Portland cement concrete contains less water than BFS cement concrete. For dry Portland cement concrete most of the water is free water located in the capillary pores, while for BFS cement concrete the water is located in the gel pores.
- When concrete is immersed in water, the filled air voids and defects highly contribute to the total volume of water present.

Air voids and defects are introduced due to the aggregate particles and during the casting process. They are random inclusions in the cement paste of concrete and are not part of the characteristic pore structure of the type of concrete used. Therefore, when considering the rate dependent behaviour of the different types of concrete and the influence of the moisture in the pores on the rate dependency, air inclusions and defects are not taken into account (see paragraph 5.9.2 on modelling influence of moisture).

Table 5.5 Volume of water in pore system only (no air or defects) and the distribution of the water in gel pores and capillary pores, age approximately 7-8 weeks.

Condition	Total volume water filled pores [a.u. x 10^6]	Filled gel pores [a.u. x 10^6]	Filled gel pores [%]	Filled capillary pores [a.u. x 10^6]	Filled capillary pores [%]
Port-dry50	3.71	0.77	21	2.94	79
Port-normal	16.71	13.32	80	3.39	20
Port-wet	48.57	23.50	48	25.07	52
BFS-dry50	8.84	7.07	80	1.77	20
BFS-normal	33.20	28.83	87	4.37	13
BFS-wet	63.10	39.51	63	23.59	37

When leaving out the air voids and defects and only considering gel- and capillary pores, it is obvious that Blast Furnace Slag cement concrete contains more gel pores than Portland cement concrete, (see Table 5.5), as was also found by means of MIP (see Table 5.1).

The NMR results from Table 5.5 show that when Portland cement concrete is wet, a significant volume of water is located in the capillary pores. When the samples are kept under normal curing condition, the capillary pores are almost empty and mainly gel pores are filled. The dry Portland cement concrete is almost completely dry.

Wet Blast Furnace Slag cement concrete contains filled capillary pores as well as filled gel pores, although the absolute volume of filled capillary pores is a bit less for the BFS cement concrete compared to Portland cement concrete. When the BFS samples are kept under normal conditions, the capillary pores are almost empty and the gel pores remain filled. The dried BFS cement concrete is not as dry as the Portland cement concrete, some gel pores remain filled. This is due to the denser structure of the BFS cement concrete with smaller pores, making it harder for the moisture to evaporate from the sample.

The MIP and NMR tests have provided us with the necessary information about pore structure, amount of moisture present in the sample and the distribution of this moisture in the different pores for the various curing conditions and for the two types of concrete used. This information is needed when analysing and quantifying the influence of moisture on the rate dependency of concrete fracture properties (see paragraph 5.9 and 5.10).

5.5 Dynamic experiments: critical review and reliability of experimental data

In the previous paragraphs, the pore structure and moisture distribution of the concretes used were presented. Information on pore sizes and distribution of the water in the pores is essential for a proper analysis of the experimental results.

Static experiments and experiments at moderate and high loading rates are conducted using the static, Split Hopkinson Bar and Modified Split Hopkinson Bar set-ups as described in chapter 3. The test methods are the same for all experiments on Portland and Blast Furnace Slag cement concrete and for all the different moisture contents. Therefore, the

critical review of the experimental output and the small inaccuracies, as have been explained in paragraph 4.2, also apply for the experiments described in this chapter. For instance, the correction for the synchronization in SHB tests or the residual strains in the MSHB tests are similar for all test conditions and concrete properties. Only for the damping in compression and tension, the inaccuracy is different compared to normally cured concrete (see paragraph 4.2). This will be discussed in the next paragraph 5.5.1.

5.5.1 Damping in compression and tension for the MSHB tests

The amplitude of the loading wave decreases when the wave travels through the concrete specimen due to compressive material damping. The compressive material damping is different for each curing condition and concrete type and displayed in Table 5.6. The decrease in amplitude of the tensile wave is not only due to material damping. The largest part of the decrease is caused by the disturbance of waves due to the fracture process (see paragraph 4.2.4). The decrease in amplitude (tensile 'damping') is also presented in Table 5.6.

Table 5.6 Average damping in compression and tensile 'damping' in MSHB tests.

Concrete	Condition	Compressive damping [%/cm]	Tensile 'damping' [%/cm]
Portland	Normal	0.85	4.1
	Dry-50	1.17	5.4
	Wet	1.53	7.6
Blast Furnace Slag	Normal	1.20	4.0
	Wet	1.09	5.7

To take into account the effect of the compressive and tensile material damping in the experimental results, the same method is used for all curing conditions and concrete types. For the processing of the experimental data it is assumed that the tensile material damping is equal to the compressive material damping. The decrease in amplitude of the tensile wave due to the disturbance of the waves during fracture is not taken into account.

5.5.2 Summary of reliability of experimental data

The conclusion that can be drawn from paragraph 5.5 is that for the MSHB tests, the only significant inaccuracy is the unknown decrease in amplitude of the tensile wave due to the influence of the fracture process during the tests. This inaccuracy cannot be properly quantified from the available data. This means that for all concrete types and curing conditions the strength and fracture energy results are underestimated and will be higher in reality.

The small inaccuracies included in the experimental results are similar for all curing conditions and both concrete types and were given in paragraphs 4.3.1, 4.4.1 and 4.5.3. They will not be repeated in this chapter.

The following three paragraphs will show the results on, respectively, the Young's modulus, the tensile strength and the fracture behaviour of concrete with different moisture contents under different loading rate regimes. Some conclusions are drawn, regarding the characteristics of the microstructure of the concrete. The experimental results are combined with the data on pore structure and moisture distribution in paragraph 5.9 and 5.10, to explain the failure behaviour, to quantify some of the influences on strength and fracture energy and to determine the rate effects on fracture properties that should be included in a constitutive numerical material model for a proper prediction of the failure behaviour of concrete in dynamic loading.

5.6 Young's modulus and moisture

From the data of the conducted experiments the Young's modulus can be determined at three different loading rates. It has to be emphasized, however, that the method to determine the Young's modulus is very different for static, Split Hopkinson Bar (SHB) or Modified split Hopkinson Bar (MSHB) testing (see paragraph 4.3).

5.6.1 Experimental results

The results for the average Young's modulus (E) are shown in Table 5.7. The number of tests (n) for each loading rate and curing condition of the concrete, on which the average is based, is also given.

Table 5.7 Average results on Young's modulus for Portland cement concrete, age ±49 days.

Condition	Series	d_{notch} [mm]	n [-]	$\dot{\varepsilon}$ [1/s]	E [GPa]	St.dev. [GPa]	E_{dyn}/E_{stat} [-]
Normal	Stat	2	6	$2.7 \cdot 10^{-6}$	32.6	2.6	1.0
	SHB	2	6	1.1	35.7	4.2	1.1
	MSHB	3	8	47.3	40.0	1.5	1.2
Dry 50	Stat	6	9	$2.7 \cdot 10^{-6}$	27.5	4.8	1.0
	SHB	4	10	1.1	26.1	2.2	1.0
	MSHB	3	5	40.7	33.6	1.7	1.2
Dry 105	Stat	6	5	$2.6 \cdot 10^{-6}$	24.0	1.6	1.0
	SHB	4	6	1.8	23.3	1.9	1.0
Wet	Stat	4	9	$2.6 \cdot 10^{-6}$	29.5	2.6	1.0
	SHB	2	8	1.0	35.8	2.1	1.2
	MSHB	3	7	58.1	42.5	1.0	1.4

The results show that the Young's modulus increases with increasing loading rate, with the exception of the Young's modulus for the moderate loading rate (SHB) dried at 50 degrees. The determined Young's moduli for the SHB tests are not very precise, as has been explained before (paragraph 4.3). A trend can be observed though; for moderate loading rates, the increase in Young's modulus is small (0-10%) and for the higher loading rates an increase of about 20 - 40% is observed.

Drying the samples at 105 degrees has a negative effect on the Young's modulus. The decrease in Young's modulus can be explained by the damage introduced during drying (see paragraph 2.2.5 and paragraph 5.3.1). Submersing the specimens in water, the wet condition, has little effect on the Young's modulus for Portland cement concrete when loaded at different loading rates.

The Young's modulus of Blast Furnace Slag cement concrete seems to increase when specimens are kept in water, as can be seen from the average results for the Young's modulus of the Blast Furnace Slag cement concrete, summarized in Table 5.8. The hydration process of Blast Furnace Slag cement can continue after the first 28 days, more than of Portland cement, provided that enough water is available to react with the unhydrated cement particles (see also chapter 2). This means that submersing the specimens in water will have a larger effect on BFS specimens than on Portland specimens when loading the specimens at an age of approximately 49 days.

Table 5.8 Average results on Young's modulus for Blast Furnace Slag cement concrete, age ± 49 days.

Condition	Series	d_{notch} [mm]	n [-]	$\dot{\varepsilon}$ [1/s]	E [GPa]	St.dev. [GPa]	E_{dyn}/E_{stat} [-]
Normal	Stat	4	13	$1.43 \cdot 10^{-6}$	25.5	5.6	1.0
	SHB	2	12	0.8	29.4	3.6	1.2
	MSHB	3	14	42.7	40.2	1.6	1.5
Wet	Stat	4	8	$1.43 \cdot 10^{-6}$	36.3	1.8	1.0
	SHB	2	11	1.3	26.2	2.7	0.7
	MSHB	3	8	59.5	41.5	1.2	1.1

The Young's modulus of the Blast Furnace Slag cement concrete at an age of 49 days at static and moderate loading rates is lower than for Portland cement concrete, when cured under normal conditions. This is due to the fact that, at an age of 49 days, normal BFS cement concrete has a higher total porosity, compared to Portland cement concrete (see also paragraph 5.3 and 5.4).

The results on Young's modulus for Blast Furnace Slag cement concrete under normal conditions, determined from the static tests, are very low compared to the results obtained according to standard NEN tests (see Table 3.4); 25.5 GPa compared to 36.4 GPa. The reason for this large difference lies in the procedure to determine the Young's modulus from the experiments. The Young's modulus for the static tests is determined by the slope of the ascending branch of the stress-deformation curve. The first part of the ascending branch of the static curve is usually straight and the slope is considered constant from $0.1f_t$ until about $0.8f_t$ (see also paragraph 2.3.3). However, for the Blast Furnace Slag cement

concrete cured under normal conditions, the slope of the ascending branch is almost never constant, especially after $0.5f_t$ (see Figure 5.14). Therefore, the static Young's modulus for the BFS cement concrete cured under normal conditions is determined by the slope of the ascending branch from $0.1f_t$ to $0.5f_t$ instead of from $0.1f_t$ to $0.8f_t$, which has been used to determine the Young's Modulus of the other series. By changing the procedure, the results are improved, but still not as accurate as for instance wet BFS cement concrete, which does have the constant ascending branch (see ascending branch of normal and wet BFS cement concrete in Figure 5.14).

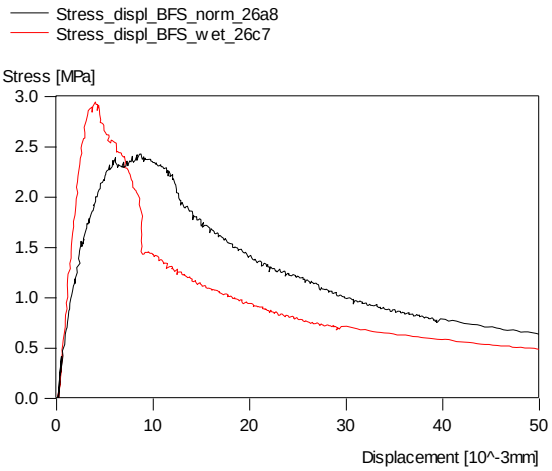

Figure 5.14 Close-up of static stress-displacement curve for normal and wet cured BFS cement concrete at an age of 49 days.

The fact that the Young's modulus for moderate loading rate is lower than for static loading rate in some series of Portland as well as Blast Furnace Slag cement concrete is due to the inaccuracy in the procedure to quantify the Young's modulus in the moderate regime. The fact that the Young's modulus is determined using different methods for the three loading rates, also makes it hard to properly quantify the differences in results. Therefore, only tendencies can be identified from the results.

From the Young's modulus data the following tendencies can be derived regarding the rate dependency:

- For moderate loading rates, the increase in Young's modulus is small (0 - 10%) and for the higher loading rates an increase of about 20 - 40% is observed.

- The Young's modulus at high loading rates is similar for Blast Furnace Slag cement concrete and Portland cement concrete for normal as well as wet conditions.
- The cement type and pore structure hardly affect the relative rate dependency of the Young's modulus (E_{dyn}/ E_{stat}) at high loading rates.

5.6.2 Results from literature on Young's modulus and moisture

In literature, data on the rate dependency of the Young's Modulus is scarce. Toutlemonde conducted several tensile tests and determined not only the tensile strength but also the Young's modulus at different loading rates [Toutlemonde 1995]. The data from Toutlemonde [Toutlemonde 1995] are presented together with the obtained experimental data in Figure 5.15.

From the available data it can be concluded that the Young's modulus is not or only slightly rate dependent in the moderate loading rate regime (loading rate up to 50 GPa/s). The increase found in the moderate regime is 0 - 10%. For the high loading rate regime, the increase is higher. From the currently obtained experimental data an increase of 20 - 40% is found.

Toutlemonde found an increase in Young's modulus of approximately 10% for the high loading rate regime and 5% for the moderate rate regime. The loading rate used by Toutlemonde in the high loading rate regime is lower than used for the MSHB experiments, which could explain the lower increase.

To fit his experimental data, Toutlemonde obtained the following equation for the dynamic Young's modulus [Toutlemonde 1995]:

$$E_{dyn} = E_{stat} + \alpha \cdot \varphi(H) \cdot log(\dot{\sigma_{dyn}} / \dot{\sigma_{stat}}) \tag{5.6}$$

$$\varphi(H) = sin(\pi H) \; for \; H < 50\%$$

$$\varphi(H) = 1 \; for \; H > 50\%$$

with H being the internal relative humidity in the pores or moisture content and α being an experimental factor.

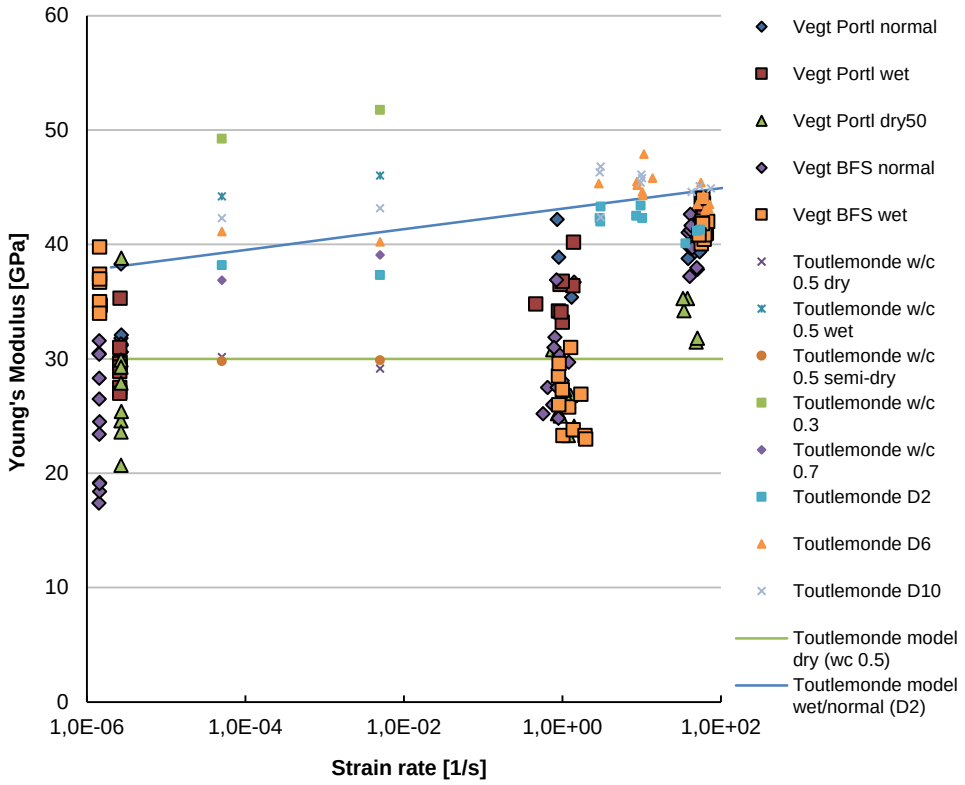

Figure 5.15 Experimental data on the Young's modulus as a function of the strain rate; experimental data Vegt, [Toutlemonde 1995] and equations 5.7a and 5.7b.

From the experimental data of Toutlemonde the factor α is determined to be approximately 0.9. Toutlemonde approximated equation 5.6 with:

$$E_{dyn} = E_{stat} + 0.9 \cdot log(\dot{\sigma_{dyn}} / \dot{\sigma_{stat}}) \quad (for\ wet\ or\ normal\ concrete) \qquad (5.7a)$$

$$E_{dyn} = E_{stat}\ (for\ dry\ concrete) \qquad (5.7b)$$

Equations 5.7a and 5.7b are visualized in Figure 5.15 for dry concrete and normal/wet concrete, using the data from Toutlemonde for dry concrete with a water-cement ratio of 0.5 and the normally cured concrete 'D2', respectively [Toutlemonde 1995].

As can be seen from Figure 5.15, equations 5.7a, 5.7b do not completely fit the experimental data of Toutlemonde as well as the obtained data presented in this research.

5.7 Tensile strength and moisture

In this paragraph the results on tensile strength for Portland and Blast Furnace Slag cement concrete are presented for three different loading rates and different moisture contents. The tensile strength is determined by the highest stress reached in the notch area; the peak value of the stress-deformation or stress-displacement curve. As has been explained in paragraph 5.5, the tensile strength determined in the Modified Split Hopkinson Bar tests are somewhat underestimated.

5.7.1 Experimental results

The average results for tensile strength (f_t) for static, moderate and high loading rates are summarized in Table 5.9. The number of tests (n) is also displayed.

Table 5.9 Average results on tensile strength, f_t, for Portland cement concrete.

Condition	Series	d_{notch} [mm]	n [-]	$\dot{\varepsilon}$ [1/s]	f_t [MPa]	St.dev. [MPa]	f_t/f_{stat} [-]
Normal	Stat	2	6	$2.7 \cdot 10^{-6}$	3.30	0.32	1.0
	SHB	2	6	1.1	5.58	0.21	1.7
	MSHB	3	8	47.3	10.87	0.90	3.3
Dry 50	Stat	6	9	$2.7 \cdot 10^{-6}$	3.05	0.43	1.0
	SHB	4	10	1.1	4.73	0.53	1.6
	MSHB	3	5	40.7	8.39	0.80	2.8
Dry 105	Stat	6	5	$3.0 \cdot 10^{-6}$	3.48	0.55	1.0
	SHB	4	6	1.8	5.04	0.12	1.5
Wet	Stat	4	9	$2.6 \cdot 10^{-6}$	2.05	0.26	1.0
	SHB	2	8	1.0	6.35	0.30	3.1
	MSHB	3	7	58.1	17.14	2.50	8.4

As explained in paragraph 4.6, the tensile strength results are not influenced by structural inertia in the axial direction generated by large and localized deformations in the fracture zone. Therefore, the determined tensile strength is the 'true' tensile strength.

The results on the relative tensile strength ($f_t/f_{t,stat}$) show that the wet Portland cement concrete exhibits much larger rate effects at medium and high loading rates than normal and dry concrete. Normal and dry Portland cement concrete show similar results for all loading rates.

The static strength for wet concrete is lower than for normal and dry concrete. This decrease in strength for wet concrete is also found by other researchers [Cadoni 2001b, Ross 1996, Hordijk 1991]. One of the possible explanations suggested by Wittmann [Wittmann 1972] and also pointed out by Hordijk and Ross [Hordijk 1991, Ross 1996] is based on the Munich Model from Wittmann [Wittmann 1977]. Wittmann proposes [Wittmann 1972] that the presence of water in the gel pores increases the distances between the CSH-molecules of the concrete and, therefore, decreases the internal VanderWaals forces that hold the structure together. This means that lower force is needed to fracture the structure and, therefore, the static strength is lower.

The conclusion that can be drawn from the results on Portland cement concrete is that the rate dependency of the tensile strength is highly influenced by the amount of moisture and the moisture distribution in the pores. When studying the moisture distribution at the different conditions (see paragraph 5.4.2, Table 5.5), it is obvious that the main difference between wet Portland cement concrete on the one hand and normal and dry Portland cement concrete on the other hand, is the free water in the capillary pores. Therefore, it is hypothesized that the rate effect on tensile strength in the moderate loading rate regime is mainly caused by the free water in the capillary pores and perhaps partly caused by water in the gel pores or (micro) fractures. This will be discussed in more detail in paragraph 5.9.

Table 5.10 Average results on tensile strength, f_t, for Blast Furnace Slag cement concrete.

Condition	Series	d_{notch} [mm]	n [-]	$\dot{\varepsilon}$ [1/s]	f_t [MPa]	St.dev. [MPa]	f_t/f_{stat} [-]
Normal	Stat	4	13	$1.43 \cdot 10^{-6}$	2.54	0.37	1.0
	SHB	2	12	0.8	4.10	0.54	1.6
	MSHB	3	14	42.7	9.87	2.01	3.9
Wet	Stat	4	8	$1.43 \cdot 10^{-6}$	3.25	0.51	1.0
	SHB	2	11	1.3	6.02	0.47	1.9
	MSHB	3	8	59.5	15.20	1.07	4.7

The results on the relative tensile strength ($f_t/f_{t,stat}$) for Blast Furnace Slag cement concrete (see Table 5.10) show that BFS cement concrete exhibits a similar rate effect on tensile strength as Portland cement concrete when stored under normal conditions. The absolute strength increase (see also Figure 5.16) for the medium and high loading rate applied to concrete cured under normal condition is also similar to Portland cement concrete, approximately 2 MPa and 7 MPa. This similarity in rate dependency and absolute tensile strength increase for Portland and BFS cement concrete stored at normal condition confirms the conclusion that the rate dependency of the tensile strength in the moderate regime is mainly caused by the free water in the capillary pores. The volume of filled capillary pores is similar for the normal Portland (3.39×10^6 a.u.) and normal BFS cement concrete (4.37×10^6 a.u.), while the volume of filled gel pores differs (13.32 vs 28.83×10^6 a.u.) (see Table 5.5).

The rate dependency of the relative tensile strength ($f_t/f_{t,stat}$) for normally conditioned Blast Furnace Slag cement concrete is similar to wet BFS cement concrete, although the absolute strength increase for the medium and high loading rate regime is higher for wet concrete compared to normally conditioned concrete. The volume of filled capillary pores is higher for wet BFS cement concrete compared to normally conditioned BFS cement concrete and, therefore, more free water is available for a possible strength increase.

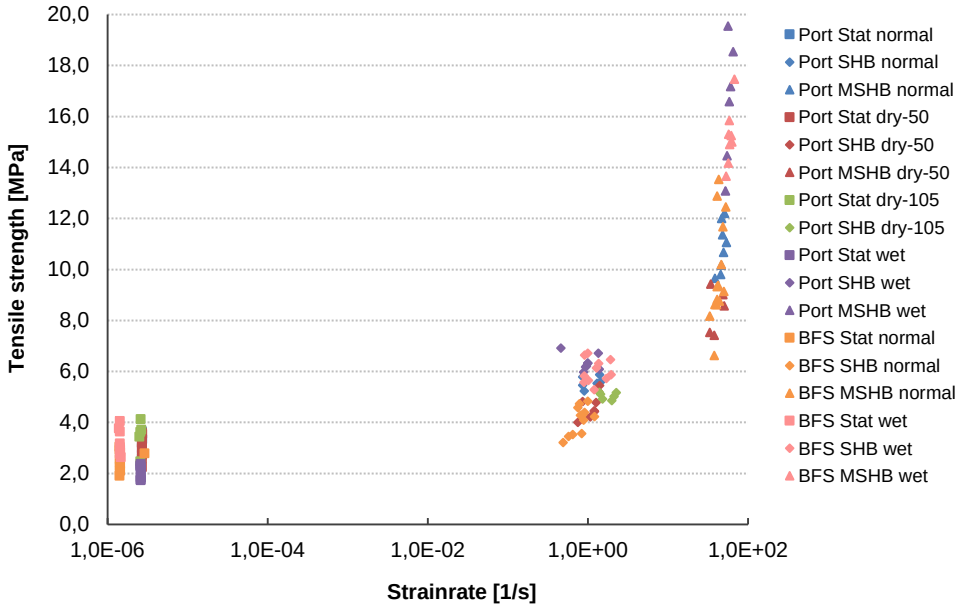

Figure 5.16 Tensile strength results for Static, SHB and MSHB tests on Portland and BFS cement concrete.

From the results on relative strength increase ($f_t/f_{t,stat}$) it seems that the curing condition has less influence on the rate dependency of BFS cement concrete than of Portland cement concrete. The somewhat lower volume of filled capillary pores in Blast Furnace Slag cement concrete compared to Portland cement concrete (see Table 5.5) might contribute to this effect. The influence of the pore structure and the filled pores on the observed rate effects will be discussed in more detail in paragraph 5.9.

5.7.2 Results from literature on tensile strength and moisture

The results from the presented research are compared to results obtained by other authors (see also paragraph 2.4.2). The results found in literature on dynamic loading, tensile strength and moisture are summarized in Figure 5.17 together with the results from the presented research. The results are presented as Dynamic Increase Factor (DIF), which is the dynamic strength divided by the static strength ($f_t/f_{t,stat}$). Two regimes can be distinguished; a moderate and high strength increase. The scatter is high due to the difference in concrete mixture, testing techniques, size of specimens and moisture content.

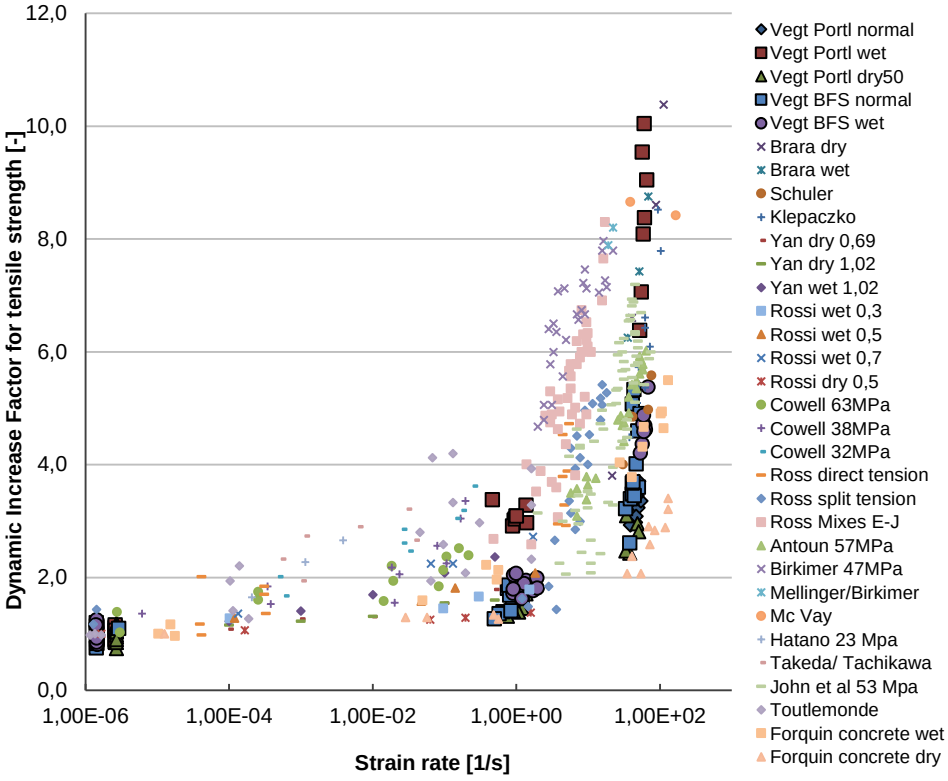

Figure 5.17 Experimental data on the DIF for tensile strength as a function of the strain rate [weerheijm et all 2013].

The tendencies that can be derived from the experimental data found in literature as well as from the presented research are:

- The transition from moderate to high rate dependency of the tensile strength occurs at strain rates in the order of 1 /s. When the heterogeneity of concrete decreases and, therefore, the static strength increases, the transition point shifts to higher strain rates.
- The rate dependency of the tensile strength increases with decreasing concrete quality and decreases for mortars; mortars have a higher static strength compared to dynamic strength.
- A higher rate dependency of the tensile strength of wet concrete is found by all researchers.

The most important conclusion on strength and pore structure that can be drawn from the experimental data found in literature as well as from the presented research:
The rate dependency of the tensile strength strongly depends on the moisture content in the (capillary) pores, on the pore structure of the concrete and, therefore, also on the concrete quality.

5.8 Failure behaviour and moisture

This paragraph presents the experimental results on failure behaviour; the stress-displacement and stress-deformation curves with a focus on the post-peak response. Also, data on the fracture energy and fracture characteristics are given. Some general observations are presented in this paragraph. The analysis and discussion of the data is given in paragraph 5.10.

5.8.1 Stress-displacement and stress-deformation curves

The failure behaviour of the concrete at three different loading rates is reflected in the stress-displacement and stress-deformation curves. The shape of the stress-deformation curves is different from the stress-displacement curve (static tests). The differences are the consequence of the method to determine the deformation or displacement; For the static stress-displacement curves the displacement measurement consists of two parts; the contribution of the crack opening and the contribution of the elastic deformation over the total measuring length. This means that elastic deformation is included in the stress-displacement curve. For the dynamic stress-deformation curves, only the deformation of the fracture zone is used to obtain the stress-deformation curve (see also paragraph 2.3.3). For Portland cement concrete loaded under static, moderate and high loading rates, the stress-displacement and stress-deformation curves are presented in Figure 5.18, Figure 5.19, Figure 5.20 and Figure 5.21 (Stat = static loading, SHB = moderate loading rate, MSHB = high loading rate). The obtained stress-deformation curves are for Portland cement concrete stored under normal conditions (normal), submersed in water (wet) and dried in an oven of 50˚C (dry50) and 105˚C (dry105).

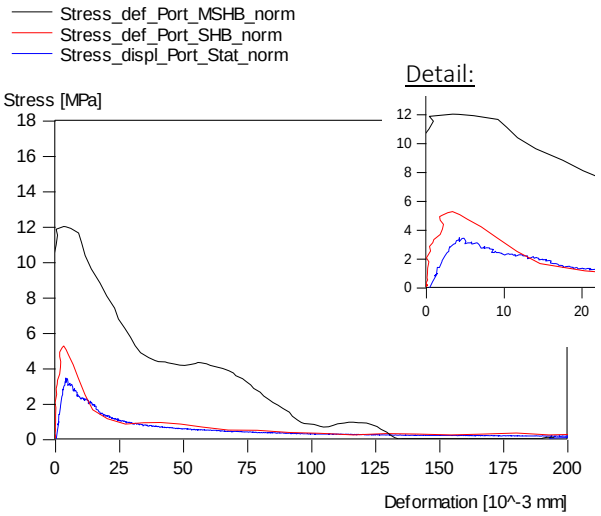

Figure 5.18 Stress-displacement and stress–deformation curves Stat, SHB, MSHB Portland cement concrete normal.

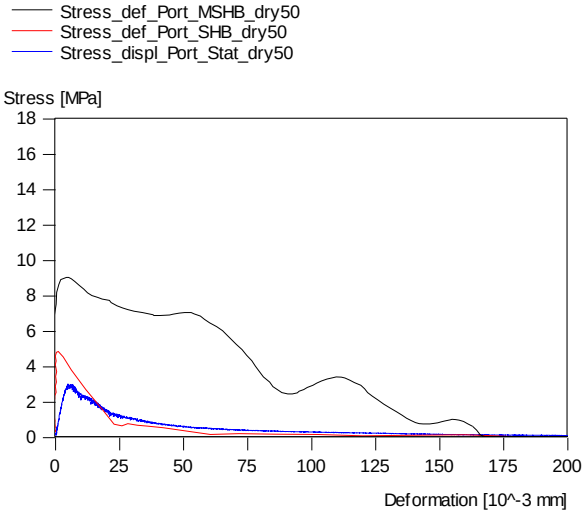

Figure 5.19 Stress-displacement and stress–deformation curves Stat, SHB, MSHB Portland cement concrete dry50.

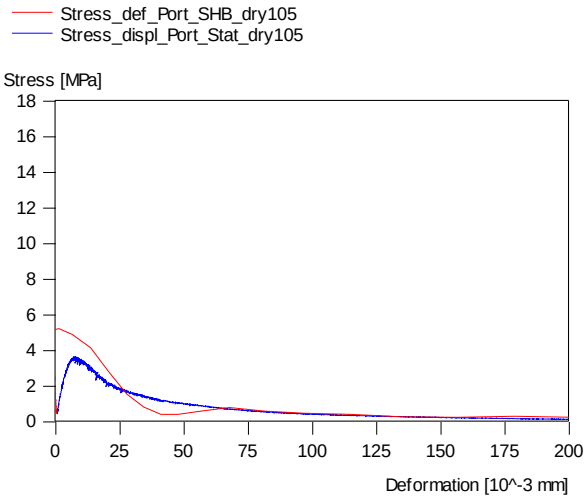

Figure 5.20 Stress-displacement and stress-deformation curves Stat, SHB Portland cement concrete dry105.

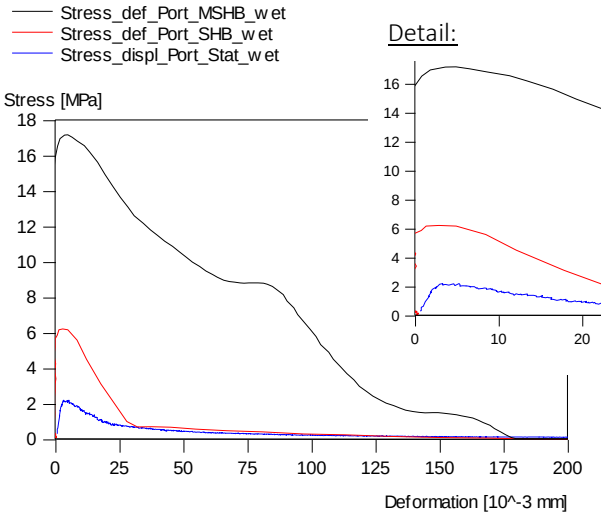

Figure 5.21 Stress-displacement and stress–deformation curves Stat, SHB, MSHB Portland cement concrete wet.

Although it seems that the SHB stress-deformation curve for normally cured Portland cement concrete has an ascending branch (see detail of Figure 5.18), in reality this is an inaccuracy which is caused by subtracting the elastic deformation (see paragraph 4.2.1).

The inaccuracy is different for each test (see detail Figure 5.18 and Figure 5.21) and will be disregarded in the analysis of the results.

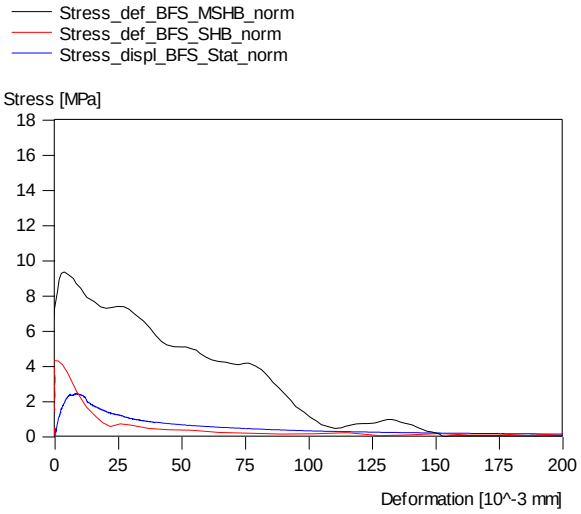

Figure 5.22 Stress-displacement and stress-deformation curves Stat, SHB, MSHB BFS cement concrete normal.

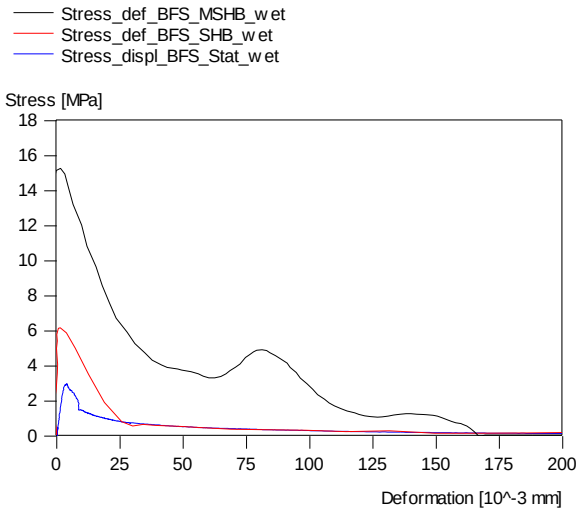

Figure 5.23 Stress-displacement and stress-deformation curves Stat, SHB, MSHB BFS cement concrete wet.

For Blast Furnace Slag cement concrete the curves are determined for normally conditioned concrete (normal) and concrete samples submersed in water (wet). These curves are presented in Figure 5.22 and Figure 5.23.

The shape of the stress-displacement curves (static) and the stress-deformation curves (dynamic) reflects the failure behaviour of the concrete at different loading rates. The first branch of the softening curve represents the formation and coalescence of the micro cracks and the second branch reflects the subsequent formation and opening of the macro crack (see also paragraph 2.3 and paragraph 4.5).

Static and moderate loading rate

For the static and moderate loading rate, the following conclusions are drawn from the obtained stress-displacement and stress-deformation curves;

General:

- The softening curve has two branches (see paragraph 2.3.3) for both types of concrete, i.e. Portland and Blast Furnace Slag cement concrete, for static as well as moderate loading rate and for all curing conditions.

Pre-peak:

- Only for normally conditioned Blast Furnace Slag cement concrete the stress-displacement curve for static loading exhibits an almost completely non-linear ascending branch (see Figure 5.14). This indicates that a lot of micro cracking has occurred before the maximum strength was reached and the macro crack developed. Note that the total micro crack length for static Blast Furnace Slag cement concrete cured under normal conditions is similar to that found in the other static tests of Portland as well as Blast Furnace Slag cement concrete. Because of the non-linear ascending branch, the Young's modulus is hard to determine from these curves, as was explained in paragraph 5.6.
- Additional micro cracking due to increased loading rate seems to be marginal in the moderate loading regime for Portland cement concrete normally conditioned and dried. This can be seen from the negligible non-linear behaviour before the maximum stress is reached ('sharp' peak) in the stress-deformation curves of the SHB tests (see Figure 5.18 and Figure 5.19).

- For the Portland cement concrete submersed in water, non-linear behaviour is observed just before the maximum strength is reached (a 'blunt' instead of a 'sharp' peak). Also, the peak is wider than for the other conditions. This indicates additional micro cracking. The experimental results on fracture lengths (see Table 5.13) support this conclusion.

Post-peak:

- The subsequent descending branch, which is associated with the formation of the final macro crack, is not affected by the loading rate in the moderate loading regime.
- Only for Blast Furnace Slag cement concrete cured under normal conditions, the static second branch is higher than for moderate loading rates. This means that the formation of the macro crack is a more ductile process for static loading than for moderate dynamic loading, at an age of approximately 49 days.
- The macro crack is fully opened at a deformation of approximately 150 – 200 µm and is not affected by the loading rate, curing condition or concrete type.

High loading rate

For the high loading rate regime the stress-deformation curves are significantly different from those for moderate loading rates. The following conclusions are drawn:

General:

- The two branches in the softening curve (see paragraph 2.3.3) are also present for the high loading rate regime but much less obvious as for the moderate loading regime.

Pre-peak:

- For Portland as well as BFS cement concrete, pre-peak non-linearity ('blunt' peak) is visible before maximum strength is reached (see Figure 5.18 - Figure 5.23), indicating an increase in micro cracking compared to the static and moderate loading rate regime.

Post-peak:

- The 'bumps' in the stress-deformation curves, partly caused by structural inertia as was explained in the previous chapter, is visible for all curing conditions and concrete types.

- The macro crack is fully opened at a deformation of approximately 125 – 175 µm and is not affected by curing condition or concrete type.
- All stress-deformation curves for the high loading rates show a significant increase in fracture energy. This will be discussed in the next paragraph.

5.8.2 Fracture energy

The fracture energy (G_f) is determined by the resistance of the material to micro cracking and the energy absorbed during micro and macro cracking. The fracture energy has to be determined from a single fracture zone. A single fracture zone is dictated by a single macro crack. However, it comprises not only the single macro crack, but also the involved micro cracks in the adjacent material. To ensure that only one fracture zone will be initiated during a test, all the specimens used have a notch. For the experiments, the fracture energy is determined by calculating the area under the stress-displacement and stress-deformation curves (see paragraph 2.3.3). The average results for Portland cement concrete and Blast Furnace Slag cement concrete are summarized in Table 5.11 and Table 5.12.

Table 5.11 Average results on fracture energy, G_f, for Portland cement concrete.

Condition	Series	d_{notch} [mm]	n [-]	$\dot{\varepsilon}$ [1/s]	G_f [N/m]	St.dev. [N/m]	$G_f/G_{f,stat}$ [-]
Normal	Stat	2	6	$2.7 \cdot 10^{-6}$	120.2	12.1	1.0
	SHB	2	4	1.1	133.2	9.7	1.1
	MSHB	3	8	47.3	551.3	176.4	4.6
Dry 50	Stat	6	8	$2.7 \cdot 10^{-6}$	105.5	21.3	1.0
	SHB	4	10	1.1	133.4	33.1	1.3
	MSHB	3	5	40.7	572.5	92.7	5.4
Dry 105	Stat	6	3	$3.0 \cdot 10^{-6}$	134.6	14.3	1.0
	SHB	4	6	1.8	254.0	53.6	1.9
Wet	Stat	4	9	$2.6 \cdot 10^{-6}$	80.3	8.2	1.0
	SHB	2	8	1.0	157.5	44.3	2.0
	MSHB	3	7	58.1	1274.4	322.3	15.9

Table 5.12 Average results on fracture energy, G_f, for Blast Furnace Slag cement concrete.

Condition	Series	d_{notch} [mm]	n [-]	$\dot{\varepsilon}$ [1/s]	G_f [N/m]	St.dev. [N/m]	$G_f/G_{f,stat}$ [-]
Normal	Stat	4	12	$1.43 \cdot 10^{-6}$	112.4	18.5	1.0
	SHB	2	11	0.8	112.6	19.9	1.0
	MSHB	3	12	42.7	568.9	208.2	5.1
Wet	Stat	4	7	$1.43 \cdot 10^{-6}$	81.1	11.7	1.0
	SHB	2	11	1.3	180.3	55.5	2.2
	MSHB	3	8	59.5	778.4	258.9	9.6

The results show only a mild increase in fracture energy for the moderate loading rates. For the normally conditioned Portland and Blast Furnace Slag cement concrete there is no increase in fracture energy for the moderate regime. Wet cured Portland and BFS cement concrete demonstrate the highest rate effect on relative fracture energy (G_f/ $G_{f,stat}$) for the moderate as well as the high loading rate regime (see also Figure 5.24).

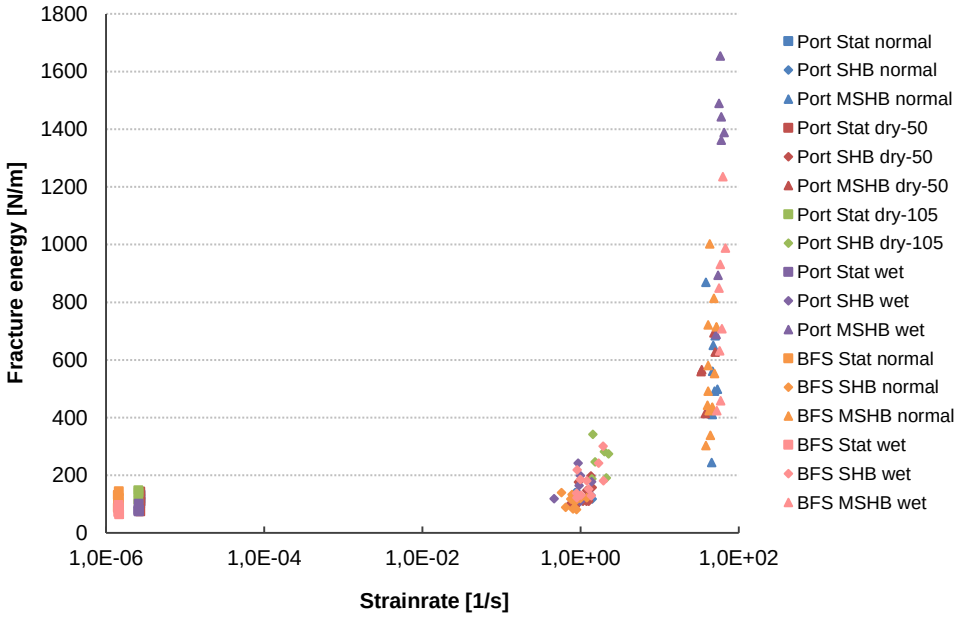

Figure 5.24 Fracture energy results for Static, SHB and MSHB tests on Portland and BFS cement concrete.

For the high loading rate regime, the fracture energy increases significantly (see also Figure 5.24). The normal and dry concrete behave similarly, when comparing the Dynamic Increase Factor (DIF = G_f/ $G_{f,stat}$) for the fracture energy results. Wet concrete has a high increase in fracture energy, for Portland cement concrete even higher than for BFS cement concrete. From these results it is concluded that the moisture and pore structure also play an important role in the rate dependency of the fracture energy.

The rate effects on fracture energy are due to additional micro cracking and additional resistance to micro crack initiation and growth due to micro inertia effects or moisture, as has been explained in the previous chapter. The influence of inertia effects and moisture on the fracture energy results will be discussed in more detail in paragraph 5.10.

5.8.3 Results from literature on fracture energy and moisture

The fracture energy results from the presented research are compared to results obtained by other authors (see also paragraph 2.4.3). As stated in the chapter 4, results on the influence of loading rate on the fracture energy are scarce. Especially data on the effect of moisture on the fracture energy of dynamically loaded concrete is scarcely found in literature. The fracture energy results obtained from the experiments and the results found in literature are both presented in Figure 5.25.

Obviously, there is a lot of scatter in the results. This scatter reflects the differences in concrete composition, test set-up and data processing.

From the published results it can be concluded that only a slight or no increase in fracture energy is observed for the moderate regime and a considerable increase is found for the high loading rate regime. For the tensile strength, a significant increase in tensile strength was observed for the moderate loading rates (see paragraph 5.7). Obviously, the rate dependency of the fracture energy starts at higher loading rates than the rate dependency of the tensile strength.
The influence of moisture on the fracture energy, i.e. a higher increase for wet concrete, is also found by Brara [Brara 2007], see Figure 5.25.

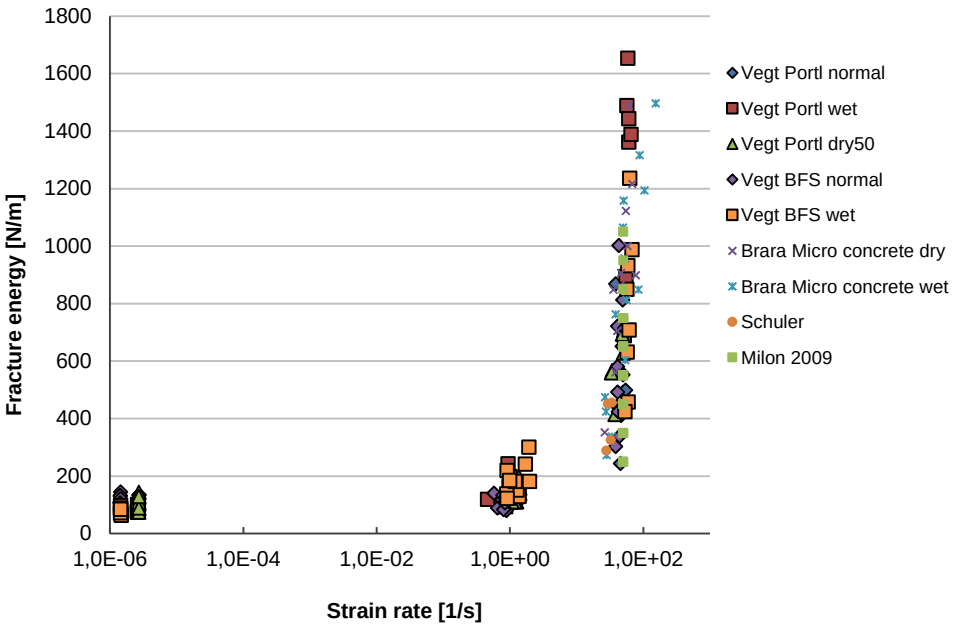

Figure 5.25 Experimental data on fracture energy as a function of the strain rate [Weerheijm et all 2013].

Whether the observed increase in fracture energy is due to additional micro cracking, moisture and/or inertia effects can only be determined by evaluating the experimental results in combination with the fracture patterns. The characteristics of the fracture patterns are presented in the next subparagraph.

5.8.4 Fracture characteristics

Geometrical characteristics of the fracture zone have been derived from the specimens after the static, Split Hopkinson Bar and Modified Split Hopkinson Bar tests of both concrete types were completed. The fracture patterns are captured and exposed by using fluorescent epoxy, as has been explained in chapter 3 (impregnated at an age of approximately 7-9 weeks). The fracture patterns are studied qualitatively as well as quantitatively.

From the qualitative results of the static and SHB tests on Portland cement concrete it can be concluded that there are only small differences between the fracture patterns for the static and medium loading rates for all conditions (see Figure 5.26 - Figure 5.31).

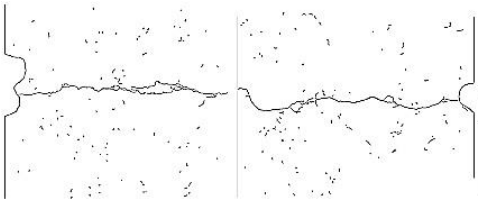

Figure 5.26 Fracture pattern for representative static test on Portland cement concrete Normal (03d2).

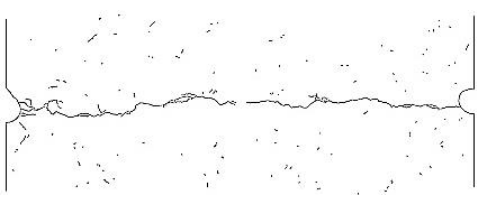

Figure 5.27 Fracture pattern for representative SHB test on Portland cement concrete Normal (10a4).

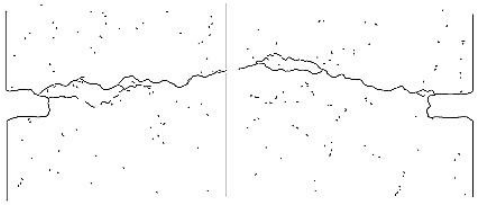

Figure 5.28 Fracture pattern for representative static test on Portland cement concrete Dry (17-17).

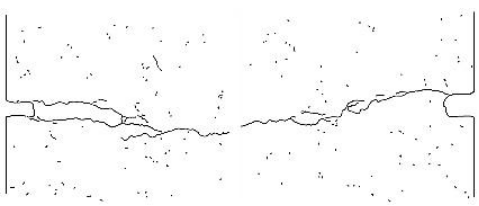

Figure 5.29 Fracture pattern for representative SHB test on Portland cement concrete Dry (17-9).

Figure 5.30 Fracture pattern for representative static test on Portland cement concrete Wet (08d4).

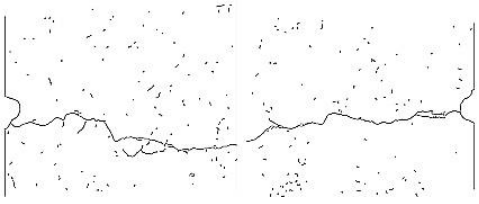

Figure 5.31 Fracture pattern for representative SHB test on Portland cement concrete Wet (08a3).

The fracture patterns for the high loading rate are different from the static and medium loading rate patterns. For all curing conditions the length of individual micro cracks in the fracture zone significantly increase (see Figure 5.32, Figure 5.33 and Figure 5.34).

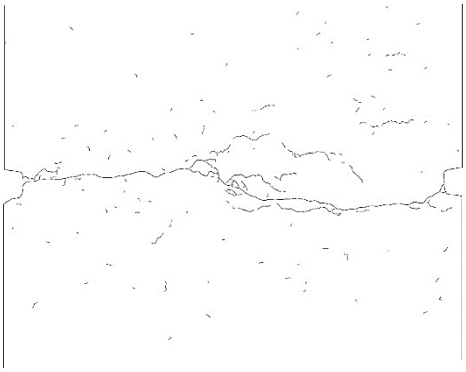

Figure 5.32 Fracture pattern for representative MSHB test on Portland cement concrete Normal (N14).

Figure 5.33 Fracture pattern for representative MSHB test on Portland cement concrete Dry (D02).

Figure 5.34 Fracture pattern for representative MSHB test on Portland cement concrete Wet (W02).

For wet Portland cement concrete tested at high loading rates the number and length of the individual micro cracks, not connected to the macro crack, are much larger than for dry and normal Portland cement concrete (see Figure 5.34). Micro cracks, parallel to the macro crack, seem to have formed during fracturing.

The fracture patterns for the static and SHB tests on Blast Furnace Slag cement concrete are shown in Figure 5.35 - Figure 5.38.

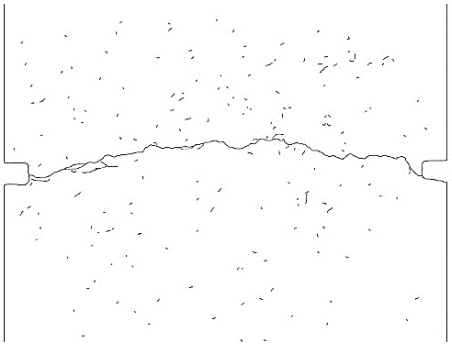

Figure 5.35 Fracture pattern for representative static test on BFS cement concrete Normal (26a6).

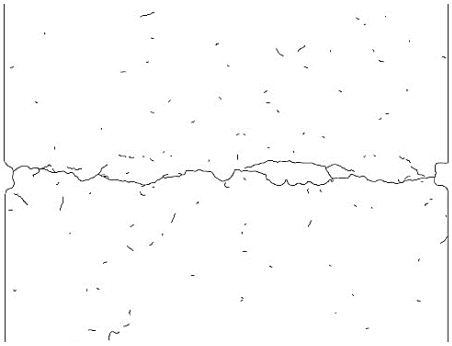

Figure 5.36 Fracture pattern for representative SHB test on BFS cement concrete Normal (26c3).

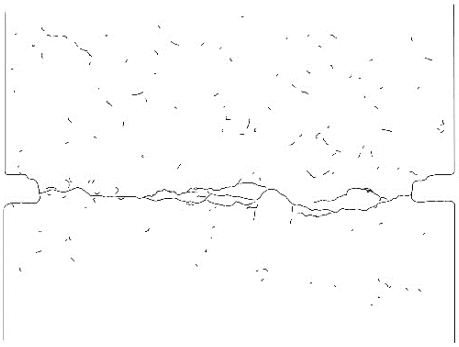

Figure 5.37 Fracture pattern for representative static test on BFS cement concrete Wet (26c7).

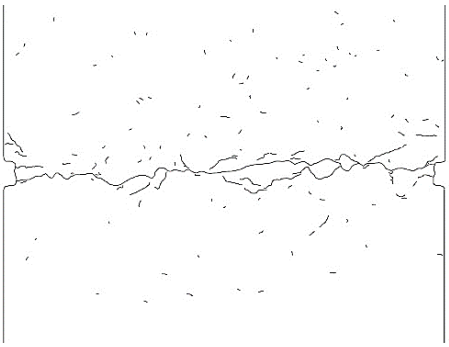

Figure 5.38 Fracture pattern for representative SHB test on BFS cement concrete Wet (26a4).

As was the case for Portland cement concrete, the differences between the fracture patterns for the static and moderate loading rates are minimal.
The wet BFS cement concrete displays more micro cracks than the normally conditioned BFS cement concrete, for the static as well as the moderate loading rates (see Figure 5.36 and Figure 5.38).

The Blast Furnace Slag cement fracture patterns for the high loading rates show a high increase in the number and length of the micro cracks (see Figure 5.39 and Figure 5.40). Normally conditioned BFS cement concrete shows the highest increase in micro crack

length. The micro cracks are not parallel to the macro crack like the fracture pattern of wet Portland cement concrete (see Figure 5.34 and Figure 5.39).

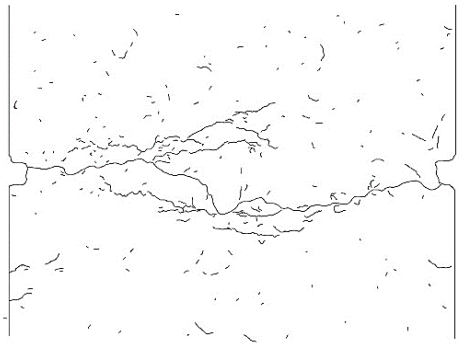

Figure 5.39 Fracture pattern for representative MSHB test on BFS cement concrete Normal (07H01).

Figure 5.40 Fracture pattern for representative MSHB test on BFS cement concrete Wet (07HW04).

To obtain quantitative results on fracture lengths and widths of the fracture zone, the crack patterns are manually digitalized and analysed, as was explained before (see also paragraph 3.8 and paragraph 4.5.5).

The cracks are again subdivided into:

(1) macro crack, which is the crack where physical separation of the two parts of the specimen has taken place;
(2) connected micro cracks, which are connected to the macro crack;
(3) isolated micro cracks, which are not connected to the macro crack, but found isolated in the concrete sample.

The fracture characteristics, total length of cracks, number of cracks and width of the fracture zone, are determined for Portland cement concrete and Blast Furnace Slag cement concrete and all curing conditions. The results for the total length of the different cracks (which is the sum of the individual cracks of all three categories) are summarized in Table 5.13 for Portland cement concrete.

Table 5.13 Average results for fracture lengths, Portland cement concrete.

Condition	Series	$\dot{\varepsilon}$ [1/s]	L_{mac} [mm]	L_{con} [mm]	L_{iso} [mm]	L_{tot} [mm]	$L_{tot}/L_{tot,stat}$ [-]
Normal	Stat	$2.7 \cdot 10^{-6}$	82	45	91	218	1.0
	SHB	1.1	86	32	68	186	0.9
	MSHB	47.3	81	51	127	259	1.2
Dry50	Stat	$2.7 \cdot 10^{-6}$	90	25	61	176	1.0
	SHB	1.1	88	27	73	188	1.1
	MSHB	40.7	80	41	136	257	1.5
Dry105	Stat	$3.0 \cdot 10^{-6}$	84	17	51	152	1.0
	SHB	1.8	84	12	44	140	0.9
Wet	Stat	$2.6 \cdot 10^{-6}$	78	35	105	218	1.0
	SHB	1.0	88	35	108	231	1.1
	MSHB	58.1	83	75	213	371	1.7

NB: the macro fracture lengths are adjusted to match a 2 mm notch.

Legend: L_{mac} = total length of macro crack, L_{con} = total length of connected micro cracks, L_{iso} = total length of isolated micro cracks, L_{tot} = total length of macro- and micro cracks together, $L_{tot,stat}$ = total length of macro- and micro cracks for static test.

Table 5.14 shows the average results for BFS cement concrete. The results are also visualized in Figure 5.41 and Figure 5.42.

Table 5.14 Average results for fracture lengths, BFS cement concrete.

Condition	Series	$\dot{\varepsilon}$ [1/s]	L_{mac} [mm]	L_{con} [mm]	L_{iso} [mm]	L_{tot} [mm]	$L_{tot}/L_{tot,stat}$ [-]
Normal	Stat	$1.4 \cdot 10^{-6}$	86	18	82	186	1.0
	SHB	0.8	92	27	84	203	1.1
	MSHB	42.7	86	67	232	385	2.1
Wet	Stat	$1.4 \cdot 10^{-6}$	80	31	109	220	1.0
	SHB	1.3	84	39	116	239	1.1
	MSHB	59.5	87	54	147	288	1.3

NB: the macro fracture lengths are adjusted to match a 2 mm notch.

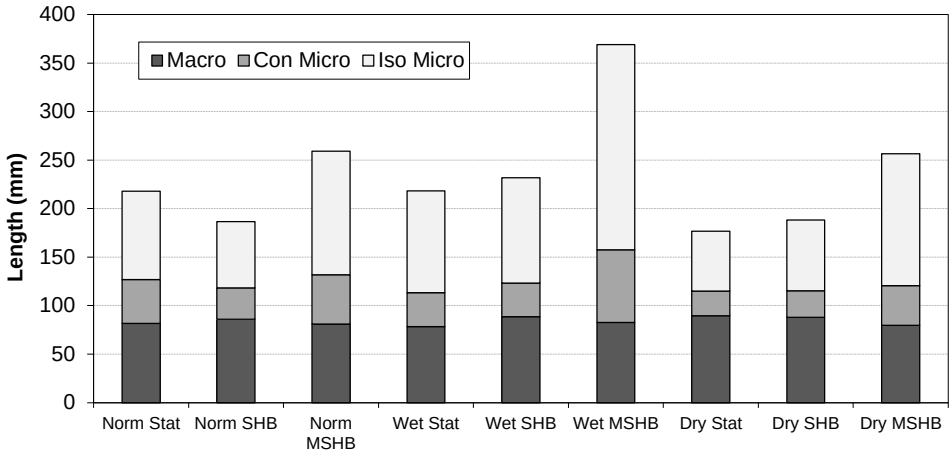

Figure 5.41 Average total length of fracture for Static, SHB and MSHB test, Portland cement concrete (normal, dry50 and wet).

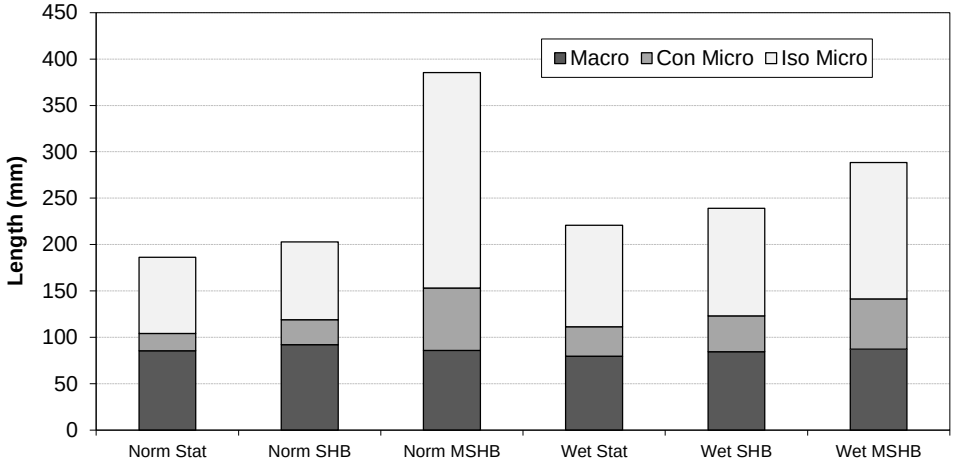

Figure 5.42 Average total length of fracture for Static, SHB and MSHB test, BFS cement concrete (normal and wet).

A notch depth of 2 mm is used in the SHB tests and is the smallest notch depth used. To be able to compare the macro fracture lengths L_{mac} shown in Table 5.13 and Table 5.14, the notch depth is supposed to be 2 mm for all conditions, both concrete types and the three described loading rates. This means that when a larger notch depth is used in the static or MSHB tests, like for instance a notch depth of 3 mm which is used for most of the

MSHB tests, 2 mm (1 mm at each side) is added to the experimentally measured macro crack length.

From the data on fracture lengths the following conclusions can be drawn;

Static and moderate loading rate

- The length of the final macro crack is not affected by loading rate or curing condition. Portland cement concrete and Blast Furnace Slag cement concrete also show similar results regarding macro crack lengths. Apparently, the macro crack length is mainly dominated by concrete composition and aggregate grading, which is similar for both concrete types.
- For Portland as well as BFS cement concrete, up to a loading rate of 50 GPa/s, additional micro cracking is not substantial for all curing conditions compared to the static loading rate. The total length of micro cracks is even slightly reduced for normal and dry105 Portland cement concrete.
- For Portland cement concrete as well as BFS cement concrete, the number of cracks decreases with increasing loading rate in the moderate regime (see Table 5.15 and Table 5.16).
- The average micro crack length, connected as well as isolated, does not substantially change for moderate loading rates for Portland and BFS cement concrete (see Table 5.15 and Table 5.16).
- The increase in fracture energy in the moderate regime is not linearly proportional to the total length of the additional micro cracks (see Figure 5.43). This is most obvious for the wet Portland cement concrete results. The fracture length increases with a factor 1.1 (see Table 5.13) compared to the static loading rate, while the fracture energy increases with a factor 2.0 (see Table 5.11).
- The fracture energy increases with a factor 2 for wet Portland and wet BFS cement concrete in the moderate regime. The length of additional micro cracks is only slightly increasing for the wet concrete types (see Figure 5.43). Micro inertia only plays a role for loading rates larger than 50 GPa/s (see chapter 4). Therefore, in the moderate regime, the increase in fracture energy is probably caused by the water in the capillary pores providing additional resistance to crack growth.

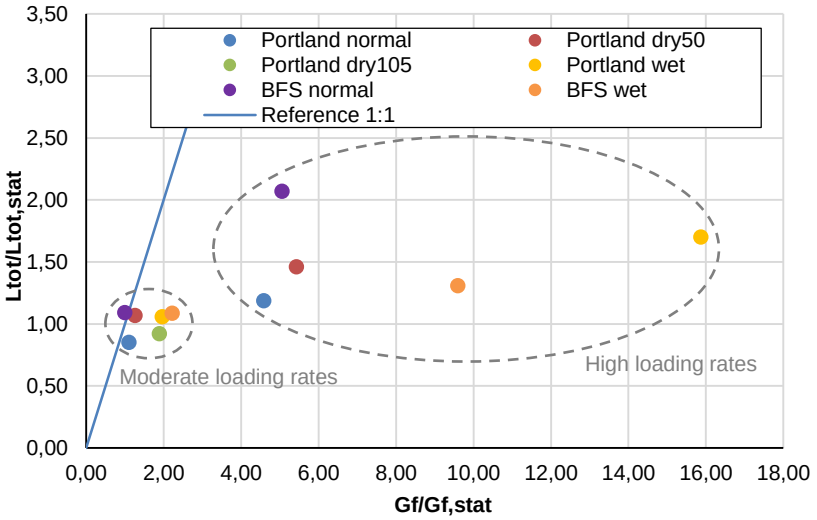

Figure 5.43 Increase in fracture energy (Gf/Gf,stat) vs additional crack length (Ltot/Ltot,stat).

Table 5.15 Average results for number of cracks (N) and average crack length (l_{av}), Portland cement concrete.

Condition	Series	$\dot{\varepsilon}$ [1/s]	N_{con} [-]	N_{iso} [-]	$l_{av,con}$ [mm]	$l_{av,iso}$ [mm]
Normal	Stat	$2.7 \cdot 10^{-6}$	35	205	1.6	0.4
	SHB	1.1	29	160	1.2	0.4
	MSHB	47.3	24	130	2.1	1.0
Dry50	Stat	$2.7 \cdot 10^{-6}$	17	155	1.5	0.4
	SHB	1.1	22	188	1.3	0.4
	MSHB	40.7	21	93	1.9	1.5
Dry105	Stat	$3.0 \cdot 10^{-6}$	15	142	1.2	0.4
	SHB	1.8	12	96	1.0	0.5
Wet	Stat	$2.6 \cdot 10^{-6}$	36	221	1.0	0.5
	SHB	1.0	35	232	1.0	0.5
	MSHB	58.1	28	107	2.7	2.0

Table 5.16 Average results for number of cracks (N) and average crack length (l_{av}), BFS cement concrete.

Condition	Series	$\dot{\varepsilon}$ [1/s]	N_{con} [-]	N_{iso} [-]	$l_{av,con}$ [mm]	$l_{av,iso}$ [mm]
Normal	Stat	$1.4 \cdot 10^{-6}$	11	144	1.6	0.6
	SHB	0.8	15	106	1.8	0.8
	MSHB	42.7	27	181	2.5	1.3
Wet	Stat	$1.4 \cdot 10^{-6}$	14	130	2.3	0.8
	SHB	1.3	15	115	2.5	1.0
	MSHB	59.5	19	147	2.9	1.0

High loading rate

Conclusions on fracture lengths for the high loading rate regime:

- The length of the macro crack is similar to the length of the macro crack observed in specimens tested under moderate loading rates.
- In the high loading rate regime the total length of micro cracks increases considerably.
- For Blast Furnace Slag cement concrete, the number of isolated micro cracks decreases for the moderate loading rate regime and only increases slightly for the high loading rate regime. (See Table 5.16)
- For Portland cement concrete, the number of isolated micro cracks decreases with increasing loading rate.
- The average micro crack length increases substantially for the high loading rate regime. For Portland cement concrete, the crack length increase is more significant than for BFS cement concrete.
- The additional micro crack length is more substantial for normally conditioned BFS cement concrete than for wet BFS cement concrete. This is contrary to Portland cement concrete, where the wet concrete exhibits a higher increase in micro crack length for the high loading regime compared to normally cured Portland cement concrete. The higher increase in micro crack length for normally cured BFS cement concrete compared to wet cured BFS cement concrete is unexpected and cannot be fully explained yet with the current experimental data.

– The increase in fracture energy is not linearly proportional to the total length of the additional micro cracks. This is more pronounced for the high loading rates than the moderate loading rates (see Figure 5.43).

The width of the fracture zone is determined in the same way as explained in the previous chapter, for the normally cured Portland cement concrete (see paragraph 4.5.5). The total width of the fracture zone (FZ) is determined by the macro crack and the accompanying connected micro cracks and long isolated micro cracks.

The data for the width of the fracture zone (WFZ) is summarized in Table 5.17 and Table 5.18. The data is also visualized in Figure 5.44 and Figure 5.45 for Portland and Blast Furnace Slag cement concrete respectively.

Table 5.17 Average results for width of fracture zone (WFZ), Portland cement concrete.

Condition	Series	$\dot{\varepsilon}$ [1/s]	WFZ_{mac} [mm]	$WFZ_{mac+con}$ [mm]	WFZ_{tot} [mm]	WFZ_{tot}/ $WFZ_{tot,stat}$ [-]
Normal	Stat	$2.7 \cdot 10^{-6}$	4.5	6.2	6.7	1.0
	SHB	1.1	6.3	7.4	8.1	1.2
	MSHB	47.3	6.6	8.6	19.1	2.9
Dry50	Stat	$2.7 \cdot 10^{-6}$	7.4	7.5	8.7	1.0
	SHB	1.1	6.8	7.6	8.8	1.0
	MSHB	40.7	6.2	7.7	43.7	5.0
Dry105	Stat	$3.0 \cdot 10^{-6}$	6.1	6.1	7.9	1.0
	SHB	1.8	5.6	6.4	7.1	0.9
Wet	Stat	$2.6 \cdot 10^{-6}$	4.5	4.7	6.0	1.0
	SHB	1.0	7.3	7.8	9.6	1.6
	MSHB	58.1	6.4	9.8	47.5	7.9

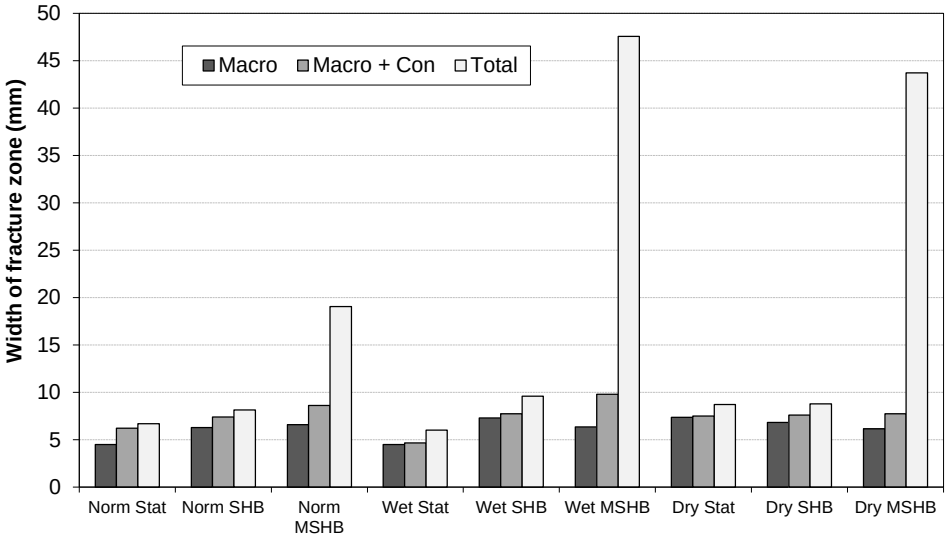

Figure 5.44 Average width of fracture zone for Static, SHB and MSHB test, Portland cement concrete (normal, dry50 and wet).

Table 5.18 Average results for width of fracture zone (WFZ), BFS cement concrete.

Condition	Series	$\dot{\varepsilon}$ [1/s]	WFZ_{mac} [mm]	$WFZ_{mac+con}$ [mm]	WFZ_{tot} [mm]	WFZ_{tot}/ $WFZ_{tot,stat}$ [-]
Normal	Stat	$1.4 \cdot 10^{-6}$	6.5	7.5	10.5	1.0
	SHB	0.8	8.2	8.7	12.2	1.2
	MSHB	42.7	7.0	9.7	33.2	3.2
Wet	Stat	$1.4 \cdot 10^{-6}$	5.3	6.5	10.8	1.0
	SHB	1.3	6.0	7.2	13.0	1.2
	MSHB	59.5	7.4	9.2	18.4	1.7

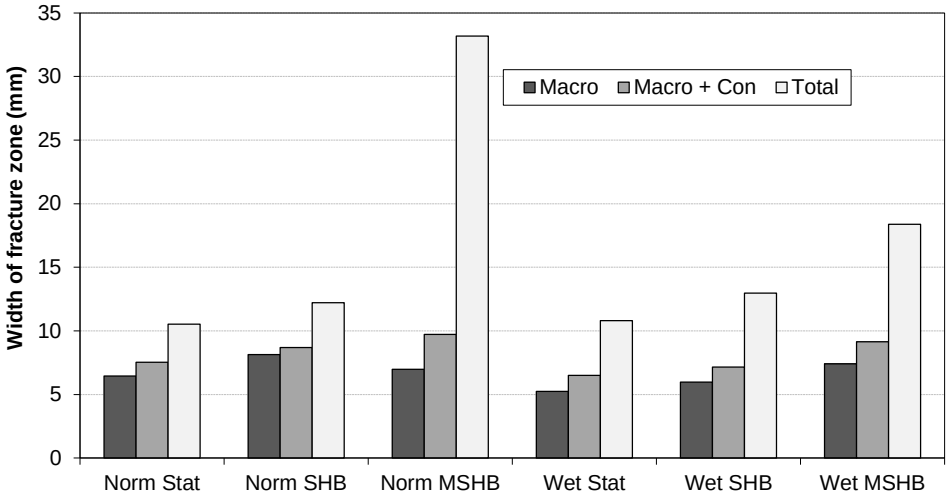

Figure 5.45 Average width of fracture zone for Static, SHB and MSHB test, BFS cement concrete (normal and wet).

Static and moderate loading rate

From the data on width of the fracture zone, the following can be concluded for the static and moderate loading rate regime:

- The width of the fracture zone (WFZ) is only moderately affected by the loading rate.
- For Portland cement concrete, the moisture content has an influence on the WFZ in the moderate regime. The WFZ for dry Portland cement concrete does not increase in the moderate regime. For normally conditioned Portland cement concrete the WFZ slightly increases and for wet Portland cement concrete substantially increases.
- For BFS cement concrete, the moisture content does not seem to influence the WFZ in the moderate regime.

High loading rate

Conclusions on width of the fracture zone for the high loading rate regime:

- The width of fracture zone (WFZ) increases significantly.
- The relative increase of the WFZ is higher than the relative increase of the total length of cracks (see Table 5.13 and Table 5.14), which means that crack density is decreasing for the high loading rate regime. The crack density is the total length

of the cracks divided by the width of the fracture zone. The decreasing crack density for high loading rates is more pronounced for Portland cement concrete than for BFS cement concrete.

At high loading rates the fracture zone (FZ) is much wider and the process of micro cracking occurs also at some distance from the macro crack. The additional micro cracking during the formation of the final macro crack explains why for the stress-deformation curve of the MSHB tests the two branches in the softening part of the curve (see also paragraph 2.3.3) are not as distinctive as for the moderate and static loading rate.

Although the width of the total fracture zone increases considerably for the high loading rate regime, most of the damage (approximately 80-90%) still occurs around the macro crack with connected micro cracks. This observation is important for numerical simulations, where the internal length scale, an important parameter to model fracture, has to be introduced. The width of the macro crack with connected micro cracks covers most of the damage and is hardly affected by the loading rate. Therefore, the internal length scale should be linked to the width of the macro crack with connected micro cracks and not to the total width of the fracture zone. Subsequently, the internal length scale of a specific model does not significantly change with increasing loading rate.

5.8.5 Corrected fracture characteristics

The fracture lengths and the widths of the fracture zones presented in the foregoing paragraphs are determined from microscopic test specimens with sizes of approximately 74 mm x 65 mm (thick sections) or 74 mm x 30 mm (thin sections). The obtained width of the fracture zone ranges between 6.0 mm for the static regime and 47.5 mm for the high loading rate regime. However, due to limited measuring lengths in the static and dynamic tests, only the cracks within the analysed zone contribute to the measured fracture behaviour. The cracks outside these measuring/analysed zone are not taken into account when comparing fracture energy results or when using the fracture characteristics to explain features from the stress-deformations curves (see also Figure 5.46). Therefore, the experimental results as presented in Table 5.13 - Table 5.18 have to be 'corrected' and all cracks outside the measuring/analysed zone are disregarded for the analysis of the results..

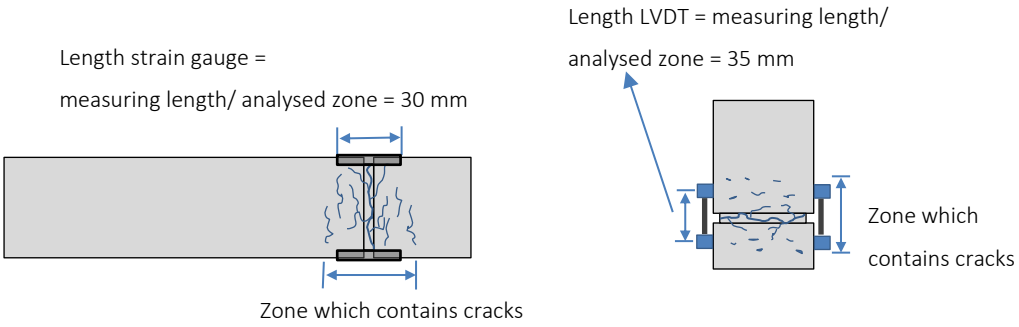

Figure 5.46 Measuring length/ analysed zone is smaller than zone that contains cracks; left: MSHB, right: static.

The fracture characteristics *within* the analysed zone are shown in Table 5.19 and Table 5.20. The 'correction' affects the results from the MSHB tests the most. The width of the fracture zone for MSHB tests cannot exceed the measuring length of 30 mm and the measured length of the isolated micro cracks within the analysed zone is about 20 – 30% smaller than when all observed cracks are taken into account. The total length of the micro and macro cracks for the MSHB tests decrease with approximately 10 – 15% due to the correction (compare the results from Table 5.13 and Table 5.14 with the results from Table 5.19 and Table 5.20).

Table 5.19 Corrected average results (*) due to restricted measuring length; WFZ, length isolated micro cracks (L_{iso}) and total length of cracks (L_{tot}), Portland cement concrete.

Condition	Series	$\dot{\varepsilon}$ [1/s]	WFZ_{tot}* [mm]	WFZ_{tot}*/ WFZ_{stat}*	L_{iso}* [mm]	L_{tot}* [mm]	L_{tot}*/ $L_{tot,stat}$*
Normal	Stat	$2.7 \cdot 10^{-6}$	6.7	1.0	75	202	1.0
	SHB	1.1	8.1	1.2	68	186	0.9
	MSHB	47.3	19.1	2.9	102	234	1.2
Dry50	Stat	$2.7 \cdot 10^{-6}$	8.7	1.0	61	176	1.0
	SHB	1.1	8.8	1.0	73	188	1.1
	MSHB	40.7	30.0	3.4	94	215	1.2
Wet	Stat	$2.6 \cdot 10^{-6}$	6.0	1.0	105	218	1.0
	SHB	1.0	9.6	1.6	108	231	1.1
	MSHB	58.1	30.0	5.0	143	301	1.4

Table 5.20 Corrected average results (*) due to restricted measuring length; WFZ, length isolated micro cracks (L_{iso}) and total length of cracks (L_{tot}), BFS cement concrete.

Condition	Series	$\dot{\varepsilon}$ [1/s]	WFZ_{tot}* [mm]	WFZ_{tot}*/ WFZ_{stat}*	L_{iso}* [mm]	L_{tot}* [mm]	L_{tot}*/ $L_{tot,stat}$*
Normal	Stat	$1.4 \cdot 10^{-6}$	10.5	1.0	56	160	1.0
	SHB	0.8	12.2	1.2	84	203	1.3
	MSHB	42.7	30.0	2.9	186	339	2.1
Wet	Stat	$1.4 \cdot 10^{-6}$	10.8	1.0	82	193	1.0
	SHB	1.3	13.0	1.2	116	239	1.2
	MSHB	59.5	18.4	1.7	107	248	1.3

The observed trends, as discussed in paragraph 5.8.4, do not change when the fracture results are corrected. However, the differences between the fracture lengths for the moderate and high loading rate regime become smaller.

The results on fracture characteristics within the defined measuring lengths (results summarized in Table 5.19 and Table 5.20 are used for the analysis of the results in the next paragraphs.

5.9 Tensile strength: influence of moisture

In the previous paragraphs the results on Young's modulus, tensile strength and fracture behaviour were presented for all moisture contents and the two concrete types. In this paragraph, different possible causes for the tensile strength increase are identified and quantified.

To recall, for the dynamic tensile strength the observed increase in strength is believed to be due to (see paragraph 4.6):

(1) the influence of (structural) inertia forces, which are generated when the material starts to weaken by micro cracking in the fracture zone.
(2) influence of inertia at micro level, which delays crack initiation.
(3) influence of inertia at micro level, which delays crack propagation.
(4) the viscous behaviour of the material due to the water in the pores (Stefan effect).

In chapter 4 it was demonstrated that structural inertia of the fracture zone (axial direction) in the pre-peak concrete response does not contribute to the strength increase for the medium or high loading rates. Since the measured maximum stress for the SHB as well as the MSHB tests is not influenced by structural inertia of the fracture zone, the measured maximum stress is considered representative for the 'true' tensile strength.

It is also shown in chapter 4, paragraph 4.6, that only beyond a loading rate of 5000 GPa/s rate effects might occur due to delayed crack initiation. Since the loading rate does not exceed 5000 GPa/s in the conducted dynamic tests, it is, therefore, concluded that inertia effects on crack initiation are not the factor that dominates the observed rate dependency of the tensile strength.

Since it was demonstrated that structural inertia of the fracture zone and micro inertia on crack *initiation* do not contribute to the tensile strength, the observed strength increase is probably caused by micro inertia on (pre-peak) crack *propagation* and/or some "viscous" behaviour of the concrete. Therefore, only the inertia at micro level which delays crack propagation and the influence of any viscous behaviour of concrete are studied and quantified in this paragraph.

5.9.1 Inertia at micro level

One of the probable causes for the observed tensile strength increase is inertia at micro level. The analysis in chapter 4 showed that, in the medium as well as the high loading rate regime, inertia at micro level is restricted to inertia on crack *propagation*. The simple analysis presented in paragraph 4.6.3 showed that for normal Portland cement concrete loaded at loading rates beyond the range of 10 – 60 GPa/s, rate effects on tensile strength due to material inherent limitations on the crack velocity (not higher than approximately 1000 m/s) and therefore limitations on crack propagation are likely to occur.

The formula used to determine the threshold for the influence of micro inertia on crack propagation to become significant is (see also paragraph 4.6.3):

$$\Delta t_{frac} \cdot \dot{\sigma} \geq 0.1 f_t \; ; \; \Delta a = \Delta t_{frac} \cdot \dot{a} \;\; \rightarrow \;\; \dot{\sigma} \geq \frac{0.1 f_t \cdot \dot{a}}{\Delta a} \qquad (5.8 = 4.10)$$

where a = initial flaw size, Δa = required crack growth, $\dot{a}$ = crack velocity, Δt_{frac} = fracture time, $\dot{\sigma}$ = loading rate and f_t = tensile strength.

Since the static tensile strength f_t is used to determine the loading rate beyond which effects on tensile strength due to micro inertia are likely to occur, the threshold will be slightly different for the different concrete types and conditions (see equation 5.8). When the static strength is lower, rate effects due to micro inertia can occur at lower loading rates. However, the minimum static tensile strength is approximately 2 MP for wet Portland cement concrete. With a static strength of 2 MPa, the threshold for effects due to micro inertia is at loading rates of 7 – 40 GPa/s. This is about the same range as the medium loading rate of the SHB tests. The effects of micro inertia will, therefore, probably only occur for the high loading rate regime and only minimally influence the results in the medium loading rate regime.

From foregoing considerations it can be concluded that beyond loading rates in the range of 10 – 40 GPa/s, rate effects due to limitations on the crack velocity and, therefore, limitations on crack propagation contribute to the observed strength increase for all moisture contents and concrete types. This means that for the medium loading rate regime, micro inertia only plays a minor role and the main cause is probably the viscous behaviour of concrete. The influence of moisture content and pore structure on the rate dependency of concrete will be analysed in the next section.

5.9.2 Moisture in pores

In the previous paragraph, inertia at micro level is indicated to be a probable cause for the strength increase in the high loading rate regime (50 – 5000 GPa/s). For the moderate loading rate regime (up to 50 GPa/s), the influence of moisture is believed to be the main cause of the increase in tensile strength [Rossi 1997, Ross 1996, Toutlemonde 1998]. In

this paragraph the influence of moisture in the pore system on the rate dependency of concrete tensile strength is studied and quantified for the moderate loading rate regime.

In Table 5.21 the tensile strength results are summarized and the dynamic strength increase is quantified for the moderate (SHB) as well as the high (MSHB) loading rate regime. In Table 5.21 the pore structure characteristics are presented. The total volume of water present in the gel- and capillary pores is defined with the NMR-output variable (a.u.).

Table 5.21 Summarized tensile strength results for Portland cement concrete (P) and Blast Furnace Slag cement concrete (BFS) and increase in strength for dynamic tests (Δf_t) combined with data on pore structure (volume filled gel pores and capillary pores).

Concrete/ condition	$f_{t,stat}$ [MPa]	$f_{t,SHB}$ [MPa]	$f_{t,,MSHB}$ [MPa]	$\Delta f_{t,SHB}$ [MPa]	$\Delta f_{t,,MSHB}$ [MPa]	Volume filled gel pores [a.u. x10^6]	Volume filled cap. pores [a.u. x10^6]
P-normal	3.30	5.58	10.87	2.3	7.6	13.32	3.39
P-dry50	3.05	4.73	8.39	1.7	5.3	0.77	2.94
P-wet	2.05	6.35	17.14	4.3	15.1	23.50	25.07
BFS-normal	2.54	4.10	9.87	1.6	7.3	28.83	4.37
BFS-wet	3.25	6.02	15.20	2.8	12.0	39.51	23.59

When considering the strength increase in the moderate regime ($\Delta f_{t,SHB}$) and the moisture present in the gel- and capillary pores, it is suggested that the water in the capillary pores and not the gel pores causes the increase in tensile strength. The arguments for this suggestion are the following (see Table 5.21):

- The volume of water present in the gel pores is much higher in BFS cement concrete than in Portland cement concrete for the normal as well as the wet cured samples, while the absolute tensile strength increase under dynamic loading for the BFS cement concrete is lower than for Portland cement concrete.
- The dry Portland and normal BFS cement concrete have the same increase in tensile strength in the moderate regime (1.7 MPa and 1.6 MPa), while the volume of filled gel pores is very different.
- The difference in volume of filled gel pores of normal and dry Portland cement concrete is high, while the strength increase under dynamic loading is limited.

– The strength increase of wet Portland cement concrete is much higher than for normal Portland cement concrete, while the difference in volume of filled gel pores is small. The difference in volume of filled capillary pores, however, is high.

The data from Table 5.21 is visualized in Figure 5.47 for the moderate loading rates. The above presented arguments and the visualized data in Figure 5.47 suggest that the water in the capillary pores, the so called free water, causes the strength increase and not the water in the gel pores. However, besides the volume of filled pores, other parameters like pore size also influence the strength increase. This will be discussed in the remainder of this paragraph by using a simple Stefan effect model.

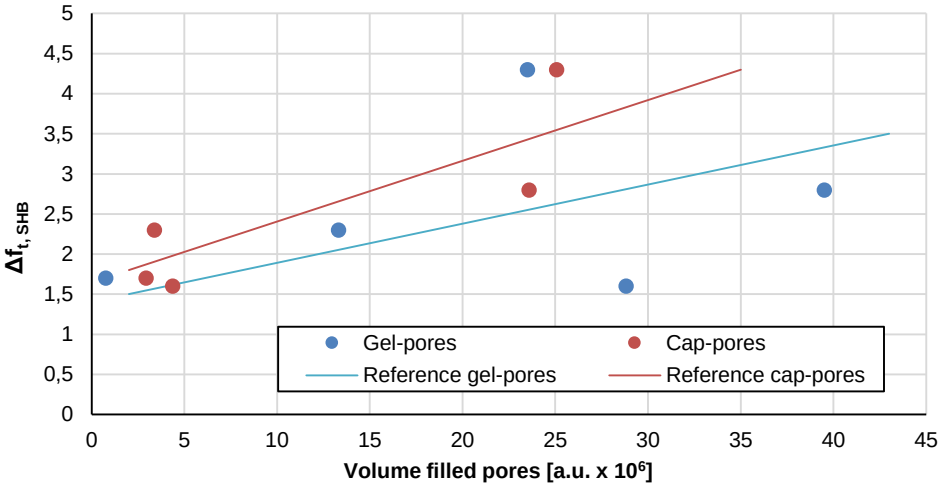

Figure 5.47 Strength increase $\Delta f_{t,SHB}$ vs volume of filled pores, gel- and capillary pores.

In a study on rate effects on tensile strength Toutlemonde and Rossi have varied the w/c-ratio of the concrete, which affects the amount of capillary pores [Toutlemonde 1995, Rossi 1997] (see also paragraph 2.4). They concluded that the moisture causing the rate effect of concrete are not found in the capillary pores but in the gel pores. This is opposite to the suggestion presented in the first part of this paragraph. The conclusion of Toutlemonde and Rossi is based on their tensile strength results that are not influenced by the w/c-ratio. The pore structure and filled pores are not quantified for the different w/c-ratios used in the research of Toutlemonde and Rossi. In the presented research the pore structure and filled pores are quantified by using NMR. This extra data gives insight in

the real filled pores and makes it possible to determine the influence of gel- and capillary pores on the tensile strength increase. It is recommended to perform research on dynamically loaded concrete using different w/c-ratios and then also determine the pore structure with NMR. From such a test program, further insight can be acquired about the type of pores which cause the rate effect.

Although there is no agreement yet about the type of pores which influence the tensile strength increase, it is believed by all researchers that the mechanism behind the moisture-induced rate effects is the so called Stefan effect. The Stefan effect is the effect of water in the pores, causing a strengthening effect when tensile load is applied. The effect can be explained as follows: when a moisture is present between two plane and parallel plates with a surface area A and a distance h between the plates, an opposing force is induced when the plates are separated with a velocity $\dot{h}$ (see Figure 5.48).

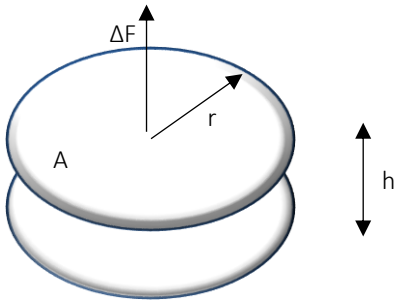

Figure 5.48 Stefan effect between plane and parallel plates.

The opposing force is dependent on the separating velocity, first derived by Stefan and Reynolds [Zheng 2004a, Zheng 2004b, Nguyen 2000]:

$$\Delta F = \frac{3 \cdot \pi \cdot \eta \cdot r^4}{2 \cdot h^3} \dot{h} \tag{5.9}$$

with η the viscosity, r the radius, $\dot{h}$ the separating velocity and h the distance between the plates (see also Figure 5.48).

When $V \approx A \cdot h$ and $A = \pi \cdot r^2$, equation 5.9 can be rewritten as:

$$\Delta F = \frac{3}{2} \cdot \frac{\eta}{\pi} \cdot \frac{A^2}{h^3} \cdot \dot{h} \tag{5.10}$$

However, the pores in concrete are not disk shaped, as assumed for the calculation of the Stefan effect, but are generally considered small tubes. Therefore, in the proposed model, the gel- and capillary pores are assumed to be long, cylindrical tubes (see Figure 5.49), which is a common assumption when modelling the pore structure of concrete, especially for modelling transport. The pores are considered filled or empty, depending on the condition. The objective of the model is to explain the trends found in the experimental data by means of the differences in pore structure and filled pores.

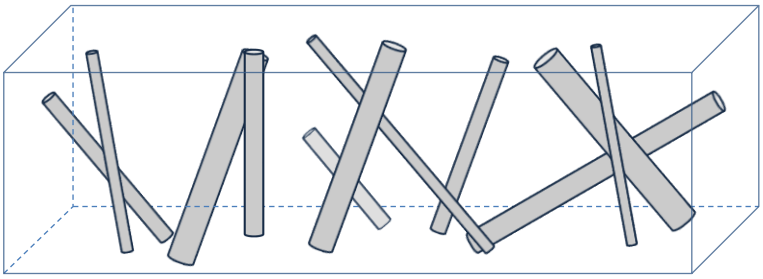

Figure 5.49 Concrete model; paste with cylindrical pores.

The Stefan-Reynolds equation (equation 5.9) is adjusted, to be applicable for concrete with cylindrical pores, schematized as tubes. The Stefan effect mechanism for long tubes is assumed to be cavitation in the pores. The cavitation stress on the pore wall is constant for the entire pore surface (see also Figure 5.50).

The force due to hydraulic stress in a single pore is:

$$\Delta F = \emptyset_p \cdot L_p \cdot \Delta\sigma \tag{5.11}$$

with $\emptyset_p$ being the pore diameter, L_p the pore length and $\Delta\sigma$ the hydraulic stress.

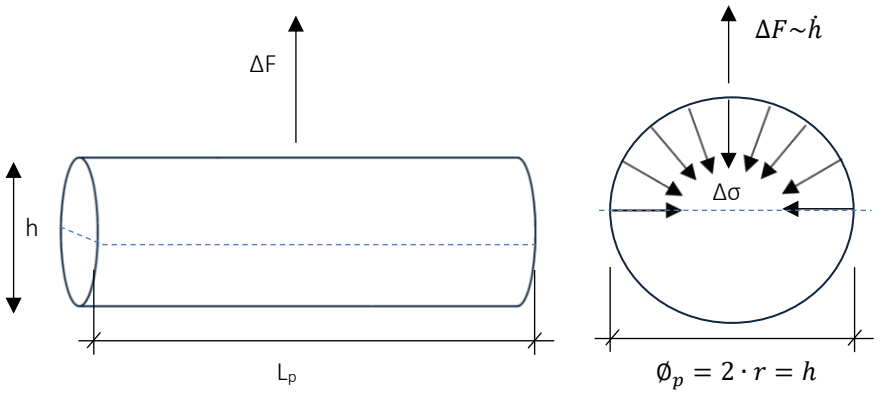

Figure 5.50 Stefan effect on cylindrical tubes.

Assuming that the Stefan-mechanism is similar for plates and cylindrical tubes, the equations should also be similar:

$$\Delta F = \Delta\sigma \cdot A = \left(\frac{3}{2} \cdot \frac{\eta}{\pi} \cdot \frac{A}{h^3} \cdot \dot{h}\right) \cdot A \qquad (plates) \tag{5.12}$$

$$\Delta F = \Delta\sigma \cdot A = \left(c_1 \cdot \frac{\eta}{\pi} \cdot \frac{\emptyset_p \cdot L_p}{{\emptyset_p}^3} \cdot \dot{\emptyset}_p\right) \cdot \emptyset_p \cdot L_p \quad (Cylindrical\ tubes) \tag{5.13}$$

For a single cylindrical pore, loaded perpendicular to its main orientation (see Figure 5.50), the additional force due to the moisture inside the pore is (assuming that the adhesion between water and pore wall is infinite):

$$\Delta F = c_1 \cdot \frac{\eta}{\pi} \cdot \frac{{L_p}^2}{\emptyset_p} \cdot \dot{\emptyset}_p \qquad c_1 \neq \frac{3}{2} \tag{5.14}$$

with η the viscosity, $\emptyset_p$ the pore diameter, L_p the pore length, $\dot{\emptyset}_p$ the separating velocity and c_1 a constant, not being 3/2 as in equation 5.10, because geometry is different than for platens.

Not all pores in the fracture zone (FZ) are loaded perpendicular to their main orientation (see also the model in Figure 5.49 and Figure 5.51).

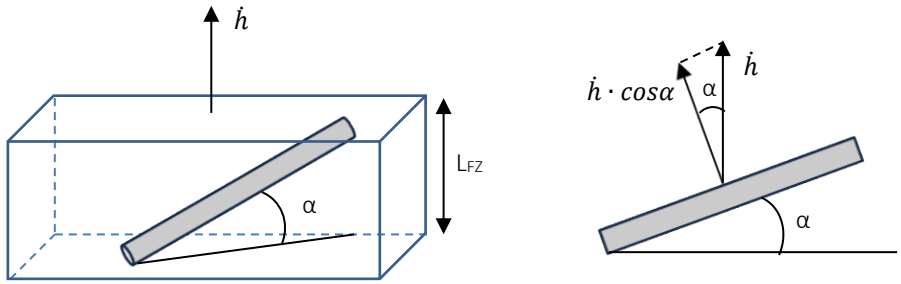

Figure 5.51 Orientation of pores in the fracture process zone.

Therefore, the additional force perpendicular to the pore length for one pore, using equation 5.14, is:

$$\Delta F\ (\perp pore) = c_1 \cdot \frac{\eta}{\pi} \cdot \frac{{L_p}^2}{\emptyset_p} \cdot \dot{h} \cdot cos\ \alpha \tag{5.15}$$

To be able to determine the contribution of one pore to the enhanced strength of the fracture zone, the part of the calculated additional force that works in the direction of the tensile loading needs to be determined (see also Figure 5.52).

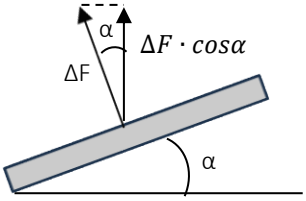

Figure 5.52 Additional force due to Stefan effect on single pore.

The contribution of the moisture in one pore to the enhanced strength is then:

$$\Delta F\ (\perp Fracture\ plane) = c_1 \cdot \frac{\eta}{\pi} \cdot \frac{{L_p}^2}{\emptyset_p} \cdot \dot{h} \cdot cos^2\alpha \tag{5.16}$$

The separating velocity $\dot{h}$ (or $\dot{\emptyset}_p$) can be expressed as follows:

$$\dot{h} = \dot{\varepsilon} \cdot L_{FZ} \tag{5.17}$$

where $\dot{\varepsilon}$ is the strain rate and L_{FZ} is the height of the fracture zone (see also Figure 5.51).

The volume of relevant, filled pores in the fracture zone n_{filled} that contributes to the enhanced tensile strength can be determined by the following equation:

$$n_{filled}/m^2 = \frac{\beta_{filled} \cdot L_{FZ}}{V_{filled}} = \frac{\beta_{filled} \cdot L_{FZ}}{L_p \cdot \frac{\pi}{4} \cdot {\emptyset_p}^2} \tag{5.18}$$

with L_{FZ} the height of the fracture zone, L_p the representative length of the pore in the fracture zone, $\emptyset_p$ the diameter of the pore and β_{filled} the 'effective porosity' when only taken into account the moisture filled pores.

The effective porosity of only the filled pores, β_{filled}, is determined as follows:

$$\beta_{filled} = \phi \cdot \frac{a.u._{filled}}{a.u._{wet}} \tag{5.19}$$

with a.u.$_{wet}$ being the NMR output of a certain type of wet concrete, representing the volume of all pores in the concrete sample, a.u.$_{filled}$ being the filled pores of that particular condition and ϕ being the total porosity of the concrete.

When the volume of relevant filled pores is combined with the additional force per pore (equation 5.16, 5.17 and equation 5.18), the following equation for the additional strength due to the Stefan effect in filled pores is obtained:

$$\Delta_\sigma = \Delta_F \cdot n_{filled} = c_2 \cdot \frac{\eta}{\pi^2} \cdot \frac{L_p}{{\emptyset_p}^3} \cdot {L_{FZ}}^2 \cdot \beta_{filled} \cdot \dot{\varepsilon} \tag{5.20}$$

with L_{FZ} the height of the fracture zone, L_p the representative length of the filled pore in the fracture zone, $\emptyset_p$ the average diameter of the pore, β_{filled} the effective porosity of the filled pores and $\dot{\varepsilon}$ the strain rate.

Equation 5.20 shows that the pore diameter $\emptyset_p$ has a big influence on the additional strength. Theoretically, the smaller (moisture filled) *gel* pores should lead to a higher resistance under dynamic tensile loading than the larger *capillary* pores. However, the data in Table 5.21 and the arguments below Table 5.21 indicate that the moisture in the larger *capillary* pores contributes to the enhanced tensile strength at medium and high loading rates (50 GPa/s and higher), not the moisture in the *gel* pores. Even when the influence of the diameter of the pores is taken into account, the presented arguments still hold. The gel pores seem to be ineffective to help withstanding the dynamic load.

Taking into account that only the capillary pores contribute to the increase of the tensile strength, the following equation for the Stefan effect in filled capillary pores is obtained:

$$\Delta\sigma = \Delta_F \cdot n_{filled,cap} = c_2 \cdot \frac{\eta}{\pi^2} \cdot \frac{L_p}{{\emptyset_p}^3} \cdot {L_{FZ}}^2 \cdot \beta_{cap} \cdot \dot{\varepsilon} \qquad (5.21)$$

$$= c_2 \cdot \frac{\eta}{\pi^2} \cdot \Lambda\,(L_p, L_{FZ}, \beta_{cap}, \emptyset_p, \bar{a}, \dot{\varepsilon})$$

with L_{FZ} the height of the fracture zone, L_p the representative length of the capillary pore in the fracture zone, $\emptyset_p$ the average diameter of the capillary pore, $\beta_{cap} = \phi \cdot (a.u._{cap}/a.u._{wet})$ the effective porosity of only the filled capillary pores and $\dot{\varepsilon}$ the strain rate.

The constant c_2 is determined as:

$$c_2 = 4 \cdot c_1 \cdot cos^2\bar{\alpha} \qquad (5.22)$$

$\bar{\alpha}$ being the average angle or orientation of the pores in the fracture zone.

Due to the fact that the constants c_2 and c_1 in equation 5.22 are unknown and that the average orientation of the pores $\bar{\alpha}$ is also not known, the additional stress due to the Stefan effect in the filled capillary pores cannot be absolutely quantified. However, trends can be established and the ratio of the strength increase for different conditions can be determined. The question is whether the differences in tensile strength for the two concrete types and different conditions can be explained by using the Stefan effect and the simple cylindrical pore model.

From equation 5.21 can be inferred that the increase in tensile strength could depend on the parameters:

- L_{FZ} the height of the fracture zone;
- $\emptyset_p$ the average diameter of the capillary pore;
- β_{cap} the effective porosity of the filled capillary pores;
- $\dot{\varepsilon}$ the strain rate;
- $\bar{a}$ the average angle or orientation of the pores in the fracture zone;
- L_p the average representative length of the pore in the fracture zone (dependent on LFZ and $\bar{a}$).

As said, the average orientation of the pores $\bar{a}$ is unknown. Yet, it is assumed that this orientation is the same for both Portland cement concrete and Blast Furnace Slag cement concrete. This implies that the average length of the pore in the fracture zone L_p is only dependent on the height of the fracture zone L_{FZ} if different concrete types and curing conditions are compared (see Figure 5.51). Equation 5.21 can be used to analyse the individual tensile strength results and to explain the differences, by filling in only parameters L_{FZ}, $\emptyset_p$, $\dot{\varepsilon}$ and β_{cap}.

First, the average diameter of the pores $\emptyset_p$ needs to be determined from the NMR results. In paragraph 5.3.3 the diameter of the pores is determined by assuming spherical pores. In the proposed model, however, the geometry of the pores is chosen to be cylindrical tubes. The cylindrical tubes in the model are small and long (d << L_p). The surface S is determined by the length and circumference of the pore.
The diameter of the pores can be determined from the relaxation time T_2 of the NMR results (see also paragraph 5.3.3 and paragraph 3.4). For the water in cylindrical tubes the relaxation time T_2 is determined as follows:

$$T_{2,pore} = \frac{V}{S \cdot \rho_2} \approx \frac{\pi r^2 \cdot L_p}{2\pi r \cdot L_p \cdot \rho_2} = \frac{r}{2 \cdot \rho_2} = \frac{d}{4 \cdot \rho_2} \tag{5.23}$$

$$\Rightarrow d = \emptyset_p = T_2 \cdot 4 \cdot \rho_2$$

with ρ_2 = 4.3·10^{-6} m/s [Valckenborg 2001b].

The pore size distribution from the NMR results, when assuming cylindrical pores instead of spheres as presented in paragraph 5.3.3, is shown in Figure 5.53.

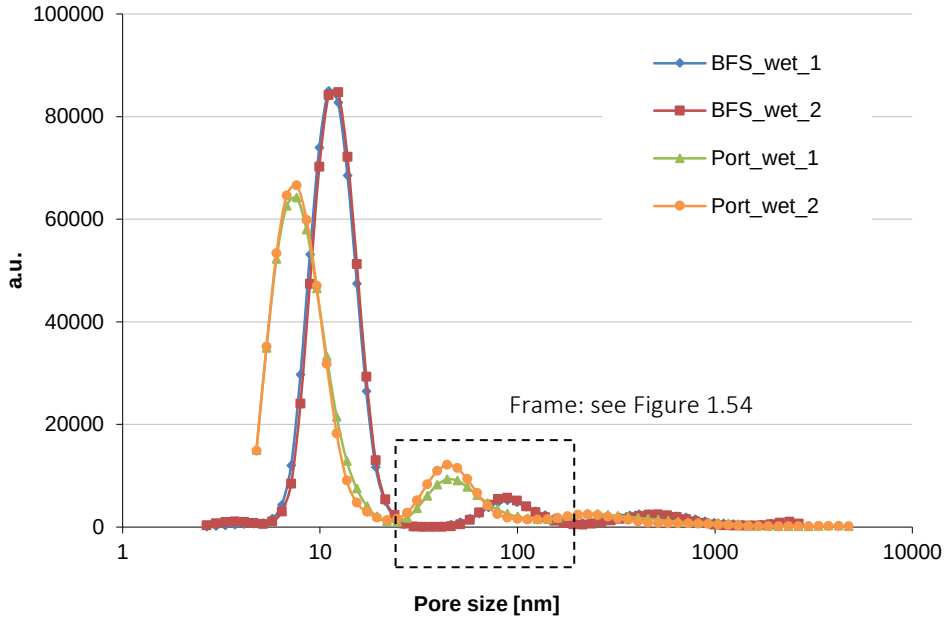

Figure 5.53 Pore size distribution wet BFS and Portland cement concrete samples, NMR tests, assuming cylindrical pores instead of spheres, age approximately 7-8 weeks.

Based on the previous analysis of the filled pores and tensile strength results, it is assumed that only capillary pores are important for the determination of the tensile strength increase due to the Stefan effect. The capillary pores are shown in Figure 5.54 for the two concrete types and the wet conditions. In Figure 5.55 the capillary pores are shown for the normally cured concretes. In Figure 5.54 and Figure 5.55, the average diameter used in equation 5.21 for wet and normally cured concrete is indicated. The same method is used to determine the average diameter for the capillary pores of dry concrete.

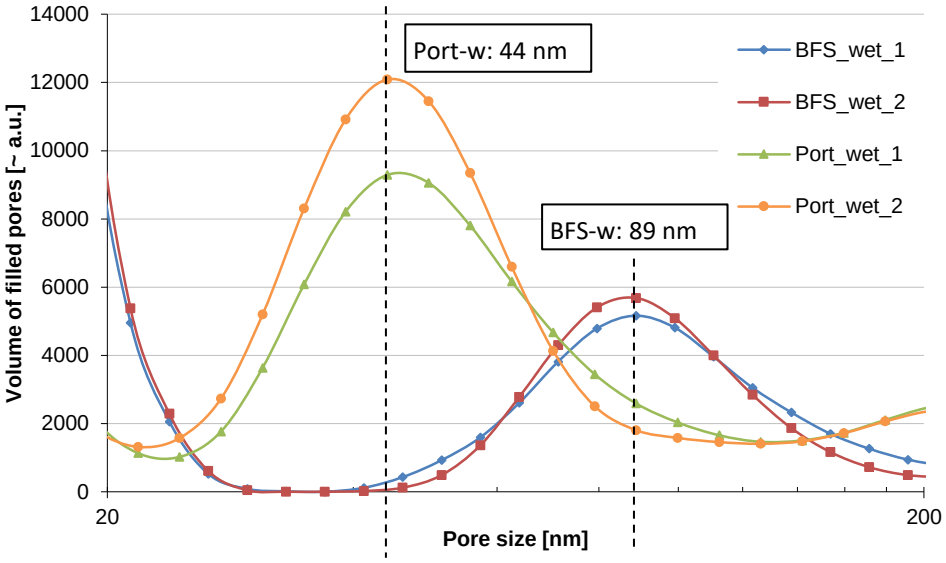

Figure 5.54 NMR-measured pore size distribution, filled capillary pores (cylindrical). Two measurements for wet conditioned BFS and Portland cement concrete. Mixtures see paragraph 3.3.1.

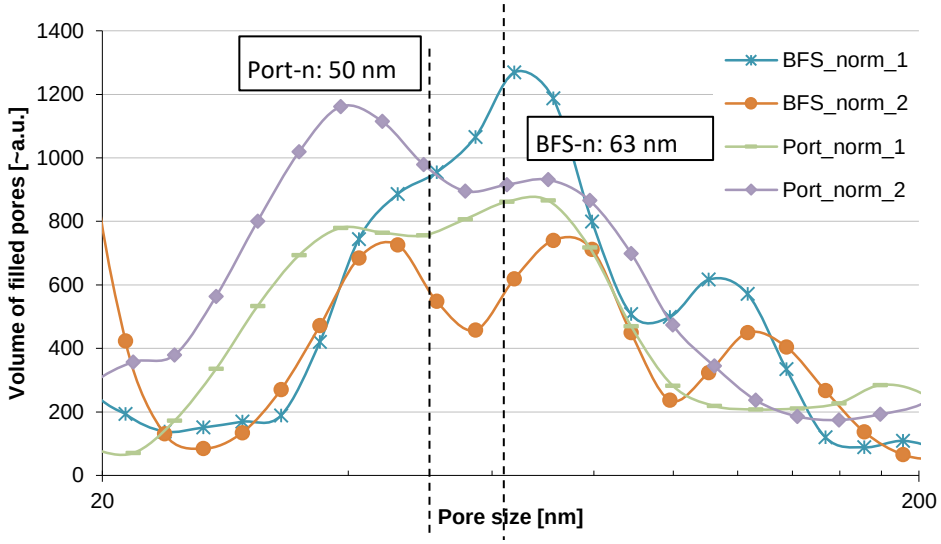

Figure 5.55 NMR-measured pore size distribution, filled capillary pores (cylindrical). Two measurements for normally conditioned BFS and Portland cement concrete. Mixtures see paragraph 3.3.1.

For the determination of the effective porosity of only the filled capillary pores β_{cap}, the total porosity of the different concrete types is needed (see equation 5.19). The total porosity φ is determined by means of Mercury Intrusion Porosimetry (see also paragraph 5.3.2). Two representative tests are shown in Figure 5.56 and Figure 5.57 for Portland and BFS cement concrete. From the MIP experiments it is concluded that the average total porosity of Portland cement concrete is 0.10 and of BFS cement concrete 0.12. This is in accordance with the results from the simple saturation tests (see Table 5.2).

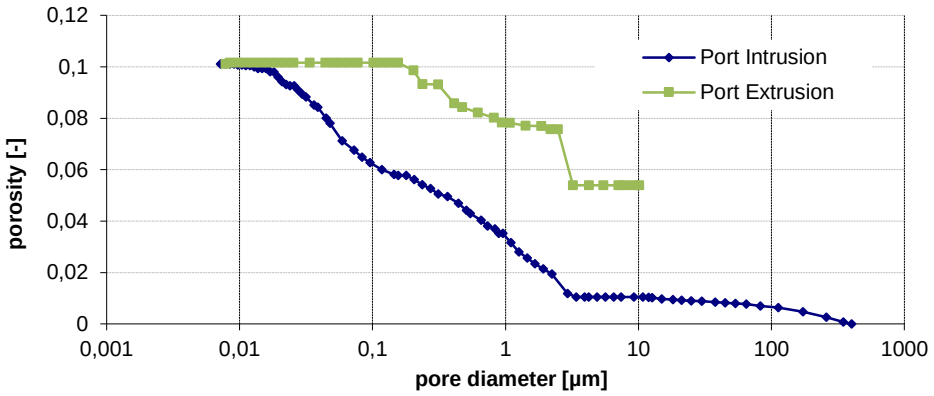

Figure 5.56 Total porosity φ of Portland cement concrete, Mercury Intrusion Porosimetry results of representative test (specimen 27-3).

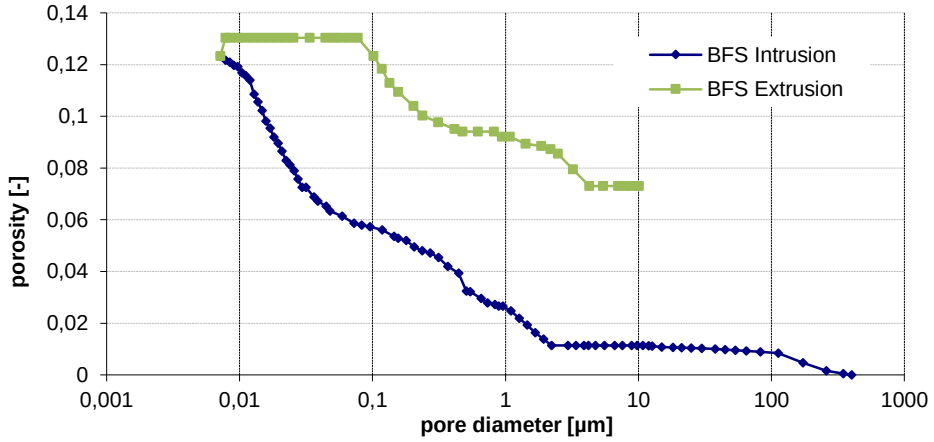

Figure 5.57 Total porosity φ of BFS cement concrete, Mercury Intrusion Porosimetry results of representative test (specimen 21-3).

The effective porosity β_{cap}, i.e. the capillary pores filled with water, can now be determined with equation 5.19 and the NMR output from Table 5.4 and Table 5.5. The length of the fracture zone L_{FZ} is taken from Table 5.17 and Table 5.18.

With β_{cap} being known, the tensile strength increase for moderate loading rates $\Delta\sigma_t$ can now be determined using equation 5.21. The parameter values used to determine the tensile strength increase due to the Stefan effect in the capillary pores for Portland as well as BFS cement concrete and for the different conditions are summarized in Table 5.22. Since the constant c_2 is unknown for both concrete types, an absolute increase cannot be determined from the results. Assuming that $L_p = L_{FZ} \cdot c_3$, c_3 being a constant depending on the average orientation of the pores $\bar{\alpha}$ and assuming that the average orientation of the pore structure $\bar{\alpha}$ does not change when the condition or type of concrete changes, the tensile strength increase due to the Stefan effect is determined by only the parameters L_{FZ}, β_{cap}, $\dot{\varepsilon}$ and $\emptyset_p$. Although the strength increase calculated with equation 5.21 cannot be compared to the absolute experimental strength increase due to the unknown variables, trends can still be established and the results can be compared to each other. From the comparison it is possible to find whether the Stefan effect is the main cause of the strength increase in the moderate loading rate regime (up to 50 GPa/s).

Table 5.22 Parameters used in equation 5.21 to determine the Stefan effect in the moderate regime.

Concrete/ condition	Length of FZ L_{FZ}	Strain rate $\dot{\varepsilon}$	Av. pore diameter $\emptyset_p$	Effective porosity β_{cap}	Exp. Strength increase, $\Delta f_{t,SHB}$	Strength increase, Calculated with equation 5.21 $\Delta\sigma_t \sim \Lambda\,(L_{FZ}, \beta_{cap}, \emptyset_p, \dot{\varepsilon})$ (Stefan effect)
	[mm]	[1/s]	[nm]	[-]	[MPa]	[x c_c x c_3 x 10^{13} MPa]
P-normal	8.1	1.12	50	0.002	2.3	1.0
P-dry50	8.8	1.09	55	0.002	1.7	0.9
P-wet	9.6	0.99	44	0.016	4.3	16.5
BFS-normal	12.2	0.81	63	0.003	1.6	1.8
BFS-wet	13.0	1.28	89	0.015	2.8	6.0

The calculated strength increase due to the Stefan effect (last column) from Table 5.22 is also visualized in Figure 5.58.

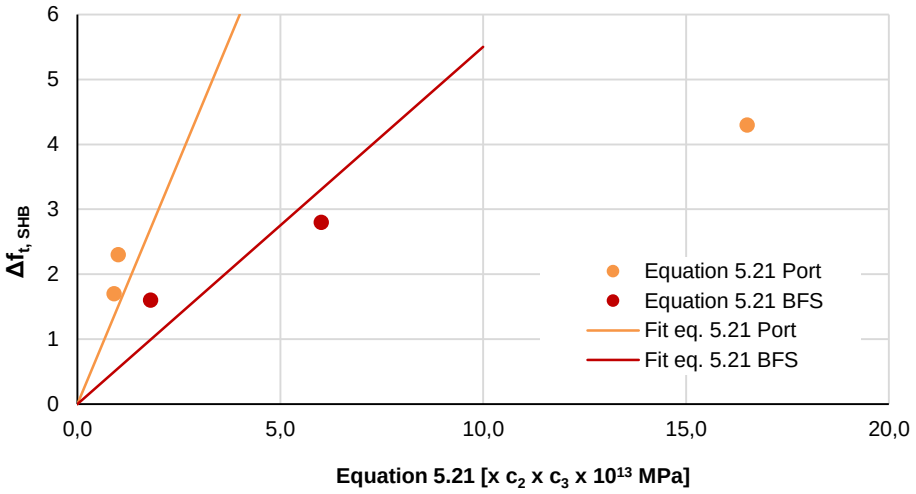

Figure 5.58 Strength increase calculated with equation 5.21 for Portland as well as BFS cement concrete vs. experimental data ($\Delta f_{t,SHB}$) and linear fit of data.

Moderate loading rate

From equation 5.21 on the Stefan effect and the data presented in Table 5.22, the following conclusions can be drawn regarding the influence of moisture and the Stefan effect in the moderate regime;

- The trends of the tensile strength increase found in the dynamic experiments is reasonably well described by equation 5.21, which calculates the strength increase due to the Stefan effect in the capillary pores.
- When calculating the tensile strength increase due to the moisture in the capillary pores with equation 5.21, the highest increase is found for wet Portland cement concrete. Wet Blast Furnace Slag cement concrete also experiences a strength increase due to the Stefan effect, but significantly lower than Portland cement concrete. This is in accordance with the experimental results.
- The average capillary diameter of the pore structure and the length of the fracture zone is determined by the concrete type used. The condition in which the specimens are stored prior to loading influences the porosity of the filled pores, β_{cap}.
- From the experimental results on the tensile strength and the NMR results, both presented in Table 5.21, it was concluded that the moisture in the *capillary* pores and not the *gel* pores cause the strength increase due to the Stefan effect. This

means that the scale at which the important mechanisms occur and decisive cracking takes place is the meso scale (capillary pores, cement paste, ITZ and grains).

– There is a strong correlation between the average diameter of the capillary pores and the strength increase due to the Stefan effect. Portland cement concrete has a similar volume of filled capillary pores as Blast Furnace Slag cement concrete (see Table 5.21, normal and wet condition) but the pores are smaller (see Table 5.22). These smaller capillary pores cause a higher increase in tensile strength.

The tensile strength increase in the moderate loading rate regime can be fully ascribed to the moisture in the capillary pores. In the high loading rate regime, however, the tensile strength increase cannot be calculated using equation 5.21. According to equation 5.21, the tensile strength increase is linearly dependent on the strain rate. Following this equation the calculated increase for the high loading rates would be approximately 50-100 times higher than for the moderate regime. This, however, is not supported by the experimental results. The strength increase due to the Stefan effect in the capillary pores most probably has a maximum. The tensile stress increase is limited due to the limited adhesion forces between the pore wall and water in the pores. In the Stefan-Reynolds equation (equation 5.9) it is assumed that the adhesion forces are infinite. In reality, however, at a certain strain rate and under certain conditions, the adhesion between the concrete pore wall and the water will be broken. Another explanation for the limitation of the strength increase due to the Stefan effect is the strength of the cement paste itself. When the strength of the cement paste is reached, the stresses cannot increase anymore and the tensile strength of the specimen is, therefore, also reached.

Although the strength increase due to the moisture in the capillary pores is limited due to the limited strength of the cement paste and the limited adhesion forces, the experimental results indicate that the moisture in the pores does contribute to the strength increase in the high loading rate regime. The higher amount of filled capillary pores for wet Portland cement concrete explains why wet Portland cement concrete exhibits a higher absolute strength increase than wet BFS cement concrete in the high loading rate regime (see Table 5.21), while the loading rate is similar.

High loading rate

For the high loading rate the strength increase for the two types of concrete and the different curing conditions are due to:

- the moisture in the pores, causing the Stefan effect. The contribution of the moisture to the dynamic strength increase is limited and probably in the range of the strength increase for the moderate regime: 1 - 5 MPa.
- the inertia effects at micro level causing limitations on crack velocities and, therefore, on crack propagation. This effect occurs for all curing conditions and moisture contents.

5.9.3 Influence loading rate on strength results, high loading rate regime

From the experiments and analyses presented in this chapter it is concluded that the tensile strength increase for the high loading rate regime is caused by the moisture in the capillary pores (Stefan effect) and micro inertia effects. The contribution of these two mechanisms to the enhanced tensile strength is proportional to the loading rate. The loading rate is not always the same for the high loading rate regime. Although the same amount of TNT is applied for each test and the stress wave in the steel rod is the same, the stress wave in the concrete specimens is influenced by the curing conditions. The wave speed and Young's modulus are different for every curing condition and, therefore, the interaction of the compressive and tensile wave at the notch is also different. This means that, for instance, the wet concrete specimens are loaded with a loading rate of approximately 2500 GPa/s, while the loading rate for the normal condition is around 1800 GPa/s. This holds for both Portland cement concrete and BFS cement concrete. The loading rate for dry Portland cement concrete is approximately 1350 GPa/s. These large differences in loading rates cause part of the variations found in strength increase for the different conditions in the high loading rate regime.

5.10 Post peak failure behaviour: influence of moisture

In paragraph 5.9 the rate effects on the tensile strength and on the behaviour before the maximum strength is reached were discussed. The tensile strength, under static and dynamic loading, is highly influenced by the moisture content. The Stefan effect, caused by the moisture in the capillary pores, is the main cause for the strength increase in the moderate loading rate regime.
The moisture in the capillary pores will help to withstand the dynamic load and delay crack initiation. Most probably the moisture in the pores will also delay crack propagation of (existing) micro cracks and, therefore, influence the post-peak behaviour of concrete. In this paragraph, the influence of moisture on the post-peak failure behaviour will be addressed.

The behaviour of concrete up to complete failure is represented by the stress-deformation curve, as has been explained in chapter 2. As we have seen in the previous paragraph and paragraph 4.7, the additional resistance reflected in the stress-deformation curves of the dynamic tests can be due to four different phenomena;

(1) Structural inertia in the post-peak response;
(2) Additional micro cracking;
(3) Inertia at micro level in the pre-peak phase and perhaps also in the softening phase, due to limitations in crack propagation;
(4) Enhanced resistance by moisture in the pores in the pre-peak and perhaps also in the post-peak phase.

These phenomena are all influenced by the moisture content, can occur together and can contribute to the enhanced post-peak performance of the concrete samples, i.e. the more ductile behaviour and the higher fracture energy. That multiple phenomena can influence the post-peak behaviour and fracture energy can be seen from the different stress-deformation curves. For instance, the stress-deformation curves (high loading rate regime) for normal and dry Portland cement concrete and for normal Blast Furnace Slag cement concrete are *different in shape*, while for the indicated curing conditions these concretes have a *similar fracture energy* of approximately 550 GPa (see Figure 5.18, Figure 5.19, Figure 5.22, Table 5.11 and Table 5.12).
In the paragraphs 5.10.1, 5.10.2, 5.10.4 and 5.10.3 the effects of the four mentioned phenomena will be discussed and quantified.

5.10.1 Structural inertia in post peak phase; stress-deformation curves

Structural inertia effects in the fracture zone do not influence the maximum stresses in the pre-peak phase, as has been explained in paragraph 4.6.1. In the pre-peak phase, the 'true' stresses $\sigma_{soft}(t)$ are measured outside the fracture zone and can be used to determine the strength at the notch for the high loading rate regime as well as the medium loading rate regime.

In the post-peak phase, structural inertia effects can influence the shape of the stress-deformation curve, as was discussed in paragraph 4.7.2 and, therefore, obscure the results. To obtain the 'true' stress-deformation relation, the 'true' material stresses $\sigma_{soft}(t)$ in the post-peak phase have to be synchronized with the deformation $\delta(t)$ and structural inertia effects have to be excluded from the results. Up to a loading rate of 50 GPa/s inertia effects of the fracture zone can be disregarded (see paragraph 4.7.2). Therefore, in this paragraph only the post-peak inertia effects in the high loading rate regime will be evaluated in more detail.

During the fracture process, the damage is not equally distributed within the fracture zone but concentrated around the macro crack, as explained in chapter 4. In order to estimate the structural inertia contribution to the tensile strength, the average value of the acceleration of the fracture zone has to be known. As explained in paragraph 4.7.2, detailed information on the average acceleration is not available. In the absence of detailed information, the average acceleration of the fracture zone is expressed by introducing a factor α. In the post-peak phase, the structural inertia contribution is then estimated by:

$$\sigma_{inertia}(t) \approx \rho \cdot \left(\alpha \cdot \frac{1}{2} \ddot{\delta}(t) \right) \cdot \frac{1}{2} \cdot WFZ \qquad (4.20 = 5.24)$$

with α = factor to determine the average acceleration, WFZ = the width of the fracture zone and ρ = density of the concrete.

When the damage distribution approaches an evenly distributed crack pattern, the factor α will be 0.5 (see also paragraph 4.7.2). However, the deformation of the fracture zone is not equally distributed, but concentrated around the final macro crack. Therefore, the factor α, which determines the average acceleration, will be less than 0.5.

To estimate the factor α, the experimental data on crack distribution is used. At the current state of research, the factor α in phase III and IV of the post peak response is based on the final crack distribution (see Figure 4.39 for the different phases). For phase II, no information on crack distribution is available. Therefore, for phase II, when the peak stress is reached but the deformations are still small, the factor α is small and assumed to be 0.1 for all conditions and concrete types.
The final crack distribution is quantified with microscopic analysis and varies with the different curing conditions. Therefore, the factor α is also different for each curing condition. The largest deformations will occur around the macro crack and the micro cracks connected to the macro crack. The factor α (less than 0.5) is estimated by comparing the width of the macro crack and the connected micro cracks to the corrected total width of the fracture zone. For a fracture process in normal Portland cement concrete the final factor α is estimated at 0.25 (see also paragraph 4.7.2). For wet BFS cement concrete, which has a larger macro crack width (with connected micro cracks) compared to the total width of the fracture zone and a more evenly distributed crack pattern than Portland cement concrete, the factor is higher and is 0.30.

The parameters used in the calculation of the structural inertia are summarized in Table 5.23, with WFZ = width of fracture zone, ρ = density of concrete and α = factor to determine the average acceleration of half the fracture zone. The WFZ is rounded off to a multiple of 5 mm. The width of the fracture zone is limited to 30 mm due to the measuring length as explained in paragraph 5.8.5.

Table 5.23 Parameters used in equation 5.24 to determine structural inertia for Portland and BFS concrete (phase III and IV, see also Figure 5.59 and Figure 5.60).

Concrete	Condition	$\dot{\varepsilon}$ [1/s]	WFZ [mm]	α [-]	ρ [kg/m^3]
Portland	Normal	47.3	20	0.25	2330
	Dry	40.7	30	0.15	2250
	Wet	58.1	30	0.20	2380
BFS	Normal	42.7	30	0.20	2350
	Wet	59.5	20	0.30	2360

The stress-deformation curves for the high loading rate regime are corrected for structural inertia effects of the fracture zone, using equation 5.24. Examples of measured stress-deformation curves and corrected stress-deformation curves are plotted in Figure 5.59 and Figure 5.60.

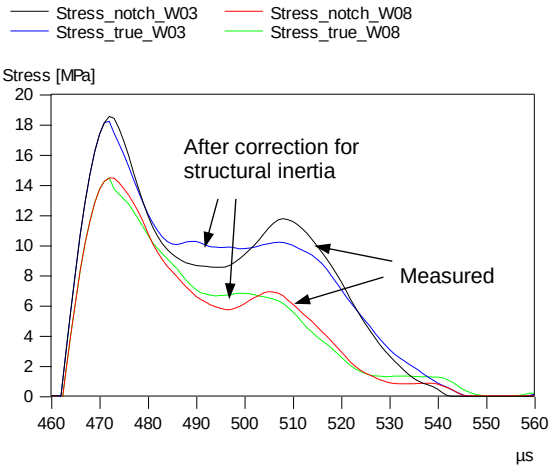

Figure 5.59 Stresses for wet Portland cement concrete, corrected for inertia of the fracture zone (measured stresses: Stress_notch, corrected stresses: Stress_true).

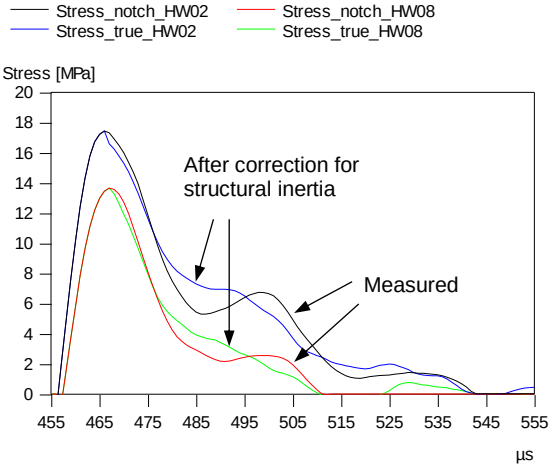

Figure 5.60 Stresses for wet BFS cement concrete, corrected for inertia of the fracture zone (measured stresses: Stress_notch, corrected stresses: Stress_true).

Figure 5.59 and Figure 5.60 show that the shape of the stress-deformation curve and especially the bumps change due to the effect of structural inertia. This effect is substantial for the wet Portland as well as the wet BFS cement concrete and less evident for normal and dry concrete. When excluding the effects of structural inertia of the fracture zone, the bumps become less distinct.

The presented results show that structural inertia of the fracture zone influences the shape of the post-peak softening curve and, therefore, also influences the fracture energy to some extent. The effect on the fracture energy results is, however, very limited. The fracture energy results show an increase of approximately 2 - 7% due to the structural inertia of the fracture zone (see Table 5.24). This is less than the standard deviation of the measured fracture energy. Therefore, the structural inertia effects of the fracture zone will be disregarded in the analysis of the fracture energy results for all loading rates.

Table 5.24 Fracture energy results, corrected for structural inertia effects, high loading rate regime.

Concrete	Condition	$G_{f,MSHB}$ [N/m]	$G_{f,MSHB,\ corr}$ [N/m]	ΔG_f [%]
Portland	Normal	551.3	567.8	+ 3
	Dry	572.5	611.5	+ 7
	Wet	1274.4	1301.5	+ 2
BFS	Normal	568.9	592.5	+ 4
	Wet	778.4	798.8	+ 3

5.10.2 Additional micro cracking

The fracture energy increases when additional (micro) cracks are formed. An increase in the total (micro) crack length, therefore, might explain the increase in fracture energy for the moderate or high loading rate regime for the different concrete types and curing conditions.

With microscopic fracture analysis the total fracture lengths are determined for the different curing conditions and concrete types. The results on relative fracture length (L_{SHB}/L_{stat} and L_{MSHB}/L_{stat}) are summarized, together with the relative dynamic fracture

energy results, in Table 5.25. The relative fracture energy results are expressed as a dynamic increase factor (DIF); the fracture energy is divided by the static fracture energy ($G_{f,SHB}/G_{f,stat}$ and $G_{f,MSHB}/G_{f,stat}$).

Table 5.25 Dynamic increase factor for fracture energy for moderate as well as high loading rate regime with accompanying enhancement factor for fracture lengths and enhancement factor for tensile strength.

	DIF Fracture energy		Relative fracture length		DIF Tensile strength	
Concrete/ condition	Moderate Gf_{SHB}/Gf_{stat} [-]	High Gf_{MSHB}/Gf_{stat} [-]	Moderate L_{SHB}/L_{stat} [-]	High L_{MSHB}/L_{stat} [-]	Moderate ft_{SHB}/ft_{stat} [-]	High ft_{MSHB}/ft_{stat} [-]
P-normal	1.1	4.6	0.9	1.2	1.7	3.3
P-dry50	1.3	5.4	1.1	1.2	1.6	2.8
P-wet	2.0	15.9	1.1	1.4	3.1	8.4
BFS-normal	1.0	5.1	1.3	2.1	1.6	3.9
BFS-wet	2.2	9.6	1.2	1.3	1.9	4.7

For the high loading rate regime, the total fracture length determined from the microscopic fracture analysis shows a significant increase for the normal Blast Furnace Slag cement concrete, namely a factor 2.1 (see Table 5.25). Assuming that the cracks are penny shaped cracks in a 3D space and that the total length of the macro and micro cracks is also increasing with a factor 2.1 in the other direction, this increase in total crack length can increase the fracture energy with a factor of approximately 2.1 x 2.1 = 4.4. A large part of the fracture energy increase for normal BFS concrete (DIF factor 5.1, see Table 5.25) can, therefore, be attributed to the larger number of (micro) cracks formed during fracture.

The results on the relative fracture energy and on the relative fracture lengths in 3D space are visualized in Figure 5.61. From Figure 5.61 it is concluded that for the moderate and high loading rate regime, the increase in fracture lengths does not proportionally contribute to the increase in fracture energy. The increase in total fracture length is limited, especially for the high loading rates.

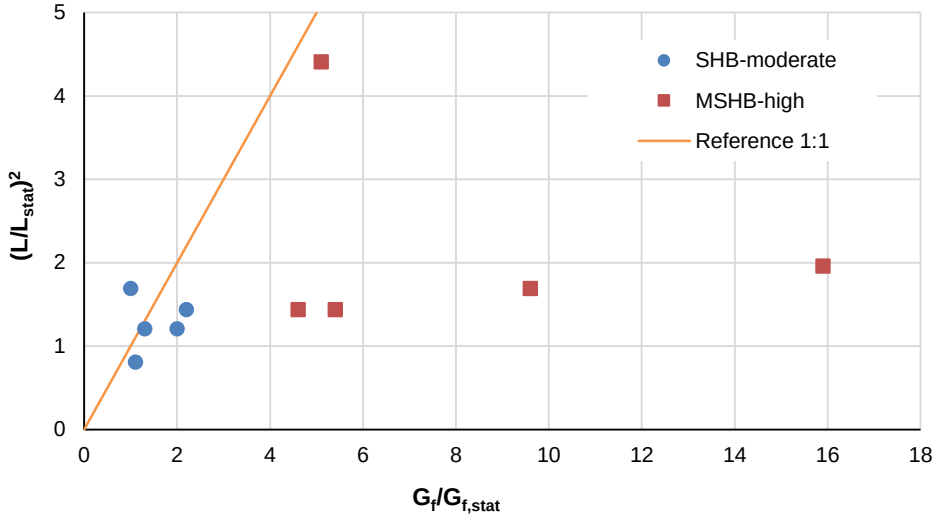

Figure 5.61 Relative fracture energy increase $G_f/G_{f,stat}$ vs increase in fracture length $(L/L_{stat})^2$ (3D medium).

Obviously, the observed increase in fracture energy is not only due to additional (micro) cracks. It is assumed that the main part of the increase is caused by the mechanisms that are also responsible for the higher strength; the Stefan effect due to moisture in the pores and micro inertia effects. Most probably, these phenomena influence the post-peak behaviour of concrete and, therefore, influence the fracture energy. This will be explained in more detail in paragraph 5.10.4 and 5.10.3.

5.10.3 Micro inertia

One of the mentioned causes for the observed tensile strength increase and the additional resistance during fracture is micro inertia, which affects crack propagation. The simple but straightforward analysis in paragraph 5.9.1 and paragraph 4.6.3 showed that only at high loading rates, beyond loading rates in the range of 10 – 40 GPa/s, rate effects due to limitations on the crack velocity and, therefore, limitations on crack propagation contribute to the observed strength increase for all moisture contents and concrete types. The limitation on the crack velocity is not only valid for the micro cracking in the pre-peak phase, but also applies to the coalescence of the micro fractures into a macro crack in the post-peak phase. Therefore, the inertia effects on crack propagation also contribute to the

enhanced resistance in the post-peak behaviour of concrete in the high loading rate regime.
The extent on which inertia effects influence the strength increase and post peak behaviour depends on the loading rate and the defect sizes in the concrete (see paragraph 4.6.3). The decisive defects, from which the cracks start propagating, are dictated by the aggregate skeleton, which is the same for Portland cement concrete and Blast Furnace Slag cement concrete.

The loading rate in the high loading rate regime ranges from 1350 – 2450 GPa/s for the different conditions and concrete types (see also paragraph 5.9.2). This means that, although the defect sizes are the same for both concrete types, the extent on which the inertia effects influence the results differs per condition.

For the high loading rate regime and wet curing condition, the micro inertia effects are probably similar, since the loading rate and defect sizes are similar for wet Portland cement concrete and wet BFS cement concrete. Also, the increase in fracture lengths is similar (see Table 5.25). This indicates that the differences in the post peak part of the stress-deformation curves between wet Portland cement concrete and wet BFS cement concrete should probably be ascribed to the moisture in the pores (see Figure 5.63). This will be explained in the next paragraph.

5.10.4 Influence of moisture on post peak

The way in which the moisture in the capillary pores can influence the maximum peak stress has been explained in paragraph 5.9.2. The higher tensile strength due to the moisture causes a higher peak and can, therefore, also influence the fracture energy and the post-peak behaviour.

The moisture in the pores will affect the toughness of the concrete. When micro cracks are propagating to form the macro crack, propagation is affected by viscous forces in the capillary pores. When the micro cracks are propagating, the capillary pores become gradually ineffective to contribute to the fracture resistance; some of the filled pores are still effective and will transfer forces, while for other pores the maximum resistance is reached and they have become ineffective. The maximum resistance of a pore can, for

instance, be reached when adhesion forces between the pore wall and water in the pores reach their maximum. This will not occur for all pores simultaneously. It might even be possible that the stresses can increase a bit in the still effective pores. This means that the moisture in the pores provides additional resistance even after the maximum strength is reached and makes that the concrete behaves more ductile. This phenomenon is visible in the moderate as well as the high loading rate regime (see Figure 5.62). In the high loading rate regime, the contribution of the moisture to the resistance is more pronounced.

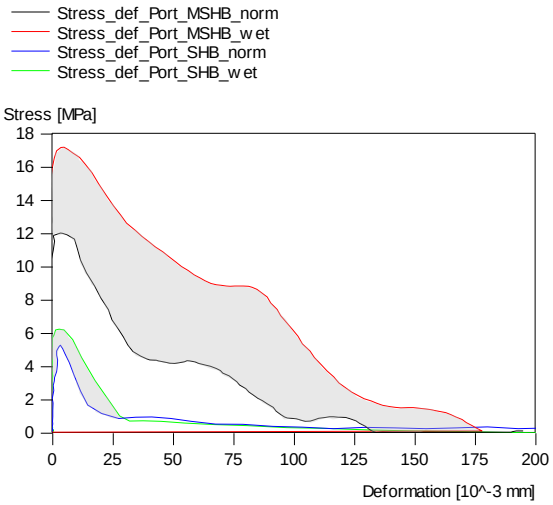

Figure 5.62 Stress-deformation curves for wet and normal Portland cement concrete. Representative SHB and MSHB tests.

The ductile behaviour in the post peak phase due to the presence of moisture in the pores is influenced by the pore structure and moisture conditions, in the same manner as for the maximum strength. Because the Portland cement concrete contains more (filled) capillary pores than the Blast Furnace Slag cement concrete, the Stefan effect and post peak ductile behaviour of concrete is more pronounced in wet Portland cement concrete than in wet BFS cement concrete (see Figure 5.63).

For the high loading rate regime, the increased fracture toughness in the post peak phase of the stress-deformation curve is due to the Stefan effect of the moisture in the pores and due to micro inertia effects. For the medium loading rate, inertia effects do not influence

the results (see paragraph 5.10.3). Therefore, the main cause for the enhanced resistance in the post peak phase in the moderate loading rate regime is the viscous behaviour of concrete due to the moisture in the pores.

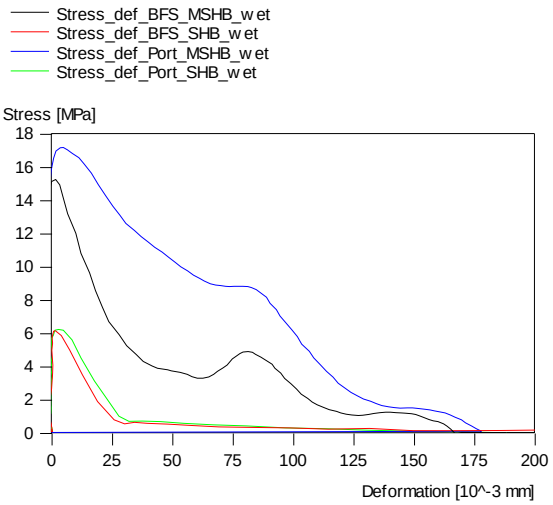

Figure 5.63 Stress-deformation curves for wet Portland cement and BFS cement concrete. Representative SHB and MSHB tests.

5.11 Conclusions

In this chapter the dynamic response of concrete under tensile loading and particularly the influence of the moisture content on the mechanisms behind the rate dependency of concrete are presented and discussed. The dominant mechanisms behind the rate effects have been identified. With a simple model of the Stefan effect, the important parameters which influence the rate dependency of concrete fracture properties have been identified and their effect approximately quantified.

For the effect of loading rate and moisture on the tensile strength, the following conclusions are drawn:

– The moisture content of concrete influences the tensile strength rate dependency, for the moderate as well as the high loading rate regime. The tensile

strength increase in the moderate loading rate regime can be fully ascribed to the viscous effects of moisture in the capillary pores of the concrete.

– The mechanism which causes the strength increase due to moisture in the pores is the so called Stefan effect. The Stefan effect is explained as the reaction force, which is induced when two plates with moisture in between are separated.
  The equation to calculate the Stefan effect is modified to fit concrete pore structure properties. To incorporate the concrete structure, it is assumed that the Stefan effect is valid for cylindrical pores. The Stefan effect in concrete with a pore system consisting of assumed cylindrical pores is reasonably well described with the following equation:

$$\Delta_\sigma = \Delta_F \cdot n_{filled,cap} = c_2 \cdot \frac{\eta}{\pi^2} \cdot \frac{L_p}{\emptyset_p{}^3} \cdot L_{FZ}{}^2 \cdot \beta_{cap} \cdot \dot{\varepsilon} \tag{5.21}$$

– The Stefan effect and tensile strength increase are dependent on pore structure, saturation degree and length of the fracture zone. It was found that (part of) the increase of the tensile strength can be ascribed to the moisture in the capillary pores, not the moisture in the gel pores. Since the pore structure of Blast Furnace Slag cement concrete has less (filled) capillary pores, BFS cement concrete exhibits less rate effects than Portland cement concrete.
– For the high loading rate regime, the tensile strength increase is caused by the resistance of the moisture in the capillary pores as well as micro inertia effects due to limitations on crack velocity. From presented analysis it can be concluded that beyond loading rates in the range of 10 – 40 GPa/s, rate effects due to limitations on the crack velocity and, therefore, limitations on crack propagation, contribute to the observed strength increase for all moisture contents and concrete types.
– Structural inertia of the fracture zone does not contribute to the increase in tensile strength for the moderate as well as the high loading rate regime. This holds for all moisture contents and concrete types.

The effect of the moisture content on the dynamic softening post-peak response was also studied. The stress-deformation curves and fracture characteristics were used to quantify the fracture energy and characterise the dynamic response. The following conclusions are drawn on the influence of moisture on the post-peak failure behaviour;

- The increase in fracture energy is not linearly proportional to the total length of the additional (micro) cracks. In the moderate regime only a mild increase in the total fracture lengths is observed. In the high loading rate regime, the increase in fracture lengths is somewhat higher, but is still insufficient to explain the high fracture energy increase.
- For normal and dry concrete and loading rates up to 50 GPa/s, the fracture energy, shape of the stress-deformation curve, width of the fracture zone and the amount of micro cracking are hardly affected by the loading rate.
- For wet concrete and loading rates up to 50 GPa/s, the enhanced resistance in the post peak behaviour is due to the viscous behaviour of concrete, i.e. the moisture in the pores causing the Stefan effect.
- For the high loading rate regime, loading rates exceeding 50 GPa/s, the enhanced resistance in the post-peak behaviour is partly caused by the viscous behaviour of concrete (wet concrete), partly by the increase in fracture lengths and also by micro inertia effects due to limitations on the crack velocity.
- Structural inertia of the fracture zone hardly affects the post peak behaviour as recorded in the experiments.

Now that the dominant mechanisms behind the rate dependency of concrete properties have been identified and important parameters have been determined, the tensile strength and fracture energy under dynamic loading conditions can be manipulated by selecting a concrete composition which has the right set of parameters, like pore size etc.

An extensive data set on the rate dependency of concrete fracture properties was generated. The dominant mechanisms found in the presented research can be implemented in dynamic models and the data set can be used to validate the developed models. With the acquired knowledge on the rate dependency of the concrete tensile strength and fracture behaviour, the response of concrete materials under dynamic loading can be better understood and predicted more accurately.

CHAPTER 6: CONCLUSIONS AND RECOMMENDATIONS

6.1 Objective

The subject of the research program was the influence of the loading rate on the fracture behaviour of concrete. Besides gathering experimental data on the rate dependency of concrete fracture properties, it is important to understand the physical mechanisms behind the rate effect in order to interpret and apply the data generated in this study.

One of the main objectives was to quantify the rate effects on tensile strength, stiffness as well as the fracture energy. The influence of the loading rate on fracture behaviour has been studied by determining the stress-deformation curves at different loading rates and quantifying the rate effect on fracture parameters, like cracks lengths and widths of the fracture zone.

With the experimental data presented in this thesis and the analysis of the data, the dominant mechanisms behind the rate dependency of concrete properties have been identified and an extensive data set with experimental results was generated. With the data on the rate effects on concretes with different moisture contents and a simplified analytical model based on the Stefan effect, the failure processes have been reconstructed and the mechanisms governing the rate dependent concrete response are explained and quantified.

6.2 Conclusions

In chapter 2, were theory on concrete properties, fracture characteristics and rate dependency from literature has been given and the results of some additional experiments

have been presented, the focus was on the failure processes and the relation between the conditioning (curing) of the specimens and the observed damage. The effect of conditioning under different relative humidity and drying temperatures has been considered. With a 50 degrees drying temperature, we are able to get an almost dry sample with negligible damage caused by the drying process.

The different experimental set-ups are presented in chapter 3. The three described set-ups for static testing and dynamic testing (Split Hopkinson Bar and Modified Split Hopkinson Bar) enable us to test concrete at three different loading rates; static ($1 \cdot 10^{-4}$ GPa/s), moderate (50 GPa/s) and high loading rate regime (>1000 GPa/s).
The direct measurement method used in the Split Hopkinson Bar and Modified Split Hopkinson Bar set-ups generates information on real-time strains and deformations. This makes it possible to reconstruct failure behaviour and gives insight in the different causes of the observed rate effects.

From literature (chapter 2) it was concluded that the moisture in the pores plays an important role in the rate dependency of concrete properties, especially in the moderate loading rate regime (up to 50 GPa/s). Therefore, the influence of moisture on the rate dependency of the tensile fracture properties has been studied by varying the loading rate, moisture content and microstructure. To study the influence of the microstructure, two types of concretes have been used; Portland cement concrete and Blast Furnace Slag (BFS) cement concrete.

To study the influence of moisture in the pore system on the rate effects on concrete tensile properties, the concrete specimens have been subjected to four different moisture conditions for approximately 21 days.
The four different moisture conditions are:

- "Normal" condition: specimens are stored under controlled conditions of 20°C and 50% RH;
- "Wet" condition: specimens are immersed in water;
- "Dry-50" condition: specimens are dried in an oven of 50°C and 15% RH;
- "Dry-105" condition: specimens are dried in an oven of 105°C and 2% RH.

Experimental results

For normally cured Portland cement concrete, the experimental data on tensile strength, Young's modulus, fracture energy and fracture characteristics for the three different loading rates have been presented in chapter 4. In chapter 5, the influence of moisture in the pore system on the fracture properties has been investigated by conducting dynamic experiments on concretes with the different moisture contents (normal, dry50, dry105 and wet) and different concrete compositions (Portland cement concrete and BFS cement concrete) at the three defined loading rates.

The results on tensile strength show that for the moderate loading rates (50 GPa/s) an increase of the tensile strength of approximately 2 MPa is found for dry and normally cured concrete compared to the static tests. For wet concrete, the increase in tensile strength was found to be more pronounced, approximately 4 MPa for Portland cement concrete and 3 MPa for Blast Furnace Slag cement concrete.
At high loading rates (1700 – 2450 GPa/s), the tensile strength results have shown an increase of approximately 5-7 MPa for normal and dry concrete and 12-15 MPa for wet concrete.

The fracture characteristics, i.e. fracture lengths and fracture widths, and the failure behaviour have been quantified by measuring the individual and summarized crack lengths and determining the stress-deformation curves. From the results it was concluded that the width and length of the macro fracture are not influenced by the loading rate. For normally cured and dry concrete and loading rates up to 50 GPa/s, the fracture energy, shape of the stress-deformation curve, width of the fracture zone and the number of micro cracks are hardly affected by the loading rate. Wet concrete shows enhanced resistance in the post-peak phase of the stress-deformation curve. For the high loading rate regime (> 50 GPa/s) the total summarized length of the micro cracks and the width of the fracture zone increase considerably, as well as the resistance in the post-peak phase of the stress-deformation curve and the fracture energy.

With the available experimental data on tensile strength, fracture characteristics and post-peak failure behaviour, the failure mechanisms have been reconstructed and the main causes for rate dependency of the tensile strength and fracture resistance have been identified. The most important possible causes are (1) structural inertia of the fracture

zone, (2) influence of inertia at micro level which can delay crack initiation and propagation, (3) additional micro cracking and (4) enhanced fracture resistance caused by moisture in the pores (Stefan effect).
By using basic principles of fracture mechanics and a simple model based on the Stefan effect, the different mechanisms and the loading rates at which these mechanisms have significant effect have been identified. NMR and MIP results provide necessary data on moisture in the pore system.

Structural inertia

One of the probable causes for the enhanced strength and failure resistance suggested in the past is structural inertia of the fracture zone. The experimental data generated in this study obtained by recording the transmitted stress wave directly beyond the fracture zone, was analysed to verify whether structural inertia in the axial direction plays a substantial role or not. For this experimental data and the method used to measure and analyse the data (1D approach), it was shown that structural inertia of the fracture zone does not contribute to the obtained enhanced tensile strength for the moderate as well as the high loading rate regime. Also, structural inertia of the fracture zone hardly affects the post peak behaviour of concrete. This holds for all concrete types and moisture contents studied.

Dominant mechanisms

It was concluded from the experimental data that the moisture content of concrete highly influences the tensile strength rate dependency, for the moderate as well as the high loading rate regime. The dominant mechanism in the moderate loading rate regime (<50 GPa/s) causing the strength increase due to moisture in the pores is called the Stefan effect. In the high loading rate regime, both the Stefan effect and the (pre peak) micro inertia effects on crack propagation due to the limitation on crack velocity contribute to the increase in *tensile strength*.

The enhanced *fracture resistance* in the post peak behavior for wet concrete and loading rates up to 50 GPa/s has been ascribed to the viscous effects of moisture in the concrete pores (Stefan effect). For the high loading rate regime, loading rates exceeding 50 GPa/s, the enhanced resistance in the post-peak behaviour is partly caused by the formation of additional (micro) cracks. However, the increase in (micro) crack length is insufficient to

explain the observed high fracture energy increase for the high loading rate regime. Therefore, the increased fracture toughness in the post-peak behaviour in the high loading rate regime has been explained by the formation of additional (micro) cracks as well as the viscous behaviour of concrete (wet concrete) and by the micro inertia effects due to material inherent limitation of the crack velocity.

Moisture model based on Stefan effect

Why the Stefan effect can be considered as a contributing factor explaining rate effects has been discussed in chapter 5. Based on the Stefan effect a simple model was proposed with which trends in experimental data could be explained and the sensitivity of the dynamic response to different parameters (i.e. moisture content, pore structure, width of fracture zone) can be evaluated. The Stefan effect model and the NMR data on pore structure and saturation of the pores have shown that the tensile strength increase due to the Stefan effect and the contribution of the Stefan effect to the enhanced resistance in the post-peak behaviour depend on the loading rate, pore structure, saturation degree and width of the fracture zone.

From the NMR data combined with the experimental data on strength and fracture energy and the equation from the Stefan effect model, it was concluded that only the moisture in the *capillary* pores contributes to the enhanced tensile strength and post-peak resistance.

Future application of data

The acquired knowledge on the mechanisms behind the rate dependency of concrete fracture properties can be used to improve numerical models. One of the most commonly used approaches to model concrete fracture is the application of continuum models. The properties and behaviour of the elements in a continuum model are defined by a constitutive law, which also determines the change in properties when fracture takes place. For modelling failure under dynamic loading conditions, the mechanisms behind the rate effects on concrete tensile properties, i.e. moisture in the capillary pores, additional micro cracking and micro inertia effects due to limitations on crack velocity, should be incorporated into the constitutive material model. Which mechanisms should be incorporated into the material model depends on the scale at which modelling takes place. For instance, when modelling the dynamic behaviour of mortar with (large) aggregate particles, the so called meso scale, only the mechanisms that are ascribed to the materials itself should be explicitly included into the material model. For this meso scale, the Stefan

effect and the micro inertia effects should be included in the material model. When sufficient level of detail is represented in the meso model, the structural inertia effects should be covered by the numerical calculations itself. Else, the structural inertia effects should also be included into the constitutive material model. An accurate prediction is only possible if the different elements and their material properties are properly taken into account.

The presented research has also shown that for modelling dynamic experiments the internal material length scale, an important parameter to model fracture processes, should be based on the width of the macro fracture zone and connected micro cracks. This zone contains the macro crack, which physically separates the specimen in two halves, as well as the micro cracks that are attached/connected to the macro crack. The width of the macro fracture zone with connected micro cracks does not significantly change with increasing loading rate. Subsequently, the internal length scale as defined for a specific model also does not significantly change with increasing loading rate (see paragraph 5.8.4).

The dominant mechanisms found in the presented research can be implemented in dynamic models and the acquired data set[1] can be used to validate the developed models. With the suggested dominant mechanisms and knowledge on the rate dependency of the concrete tensile strength and fracture behaviour, the response of concrete materials under dynamic loading can now be better understood and predicted more accurately.

6.3 Recommendations

Although the presented research has provided us with an extensive set of experimental data on dynamic tensile strength and fracture behaviour and with knowledge on the dominant mechanisms behind the rate dependency of the fracture properties of concrete, some recommendations are proposed to improve the results:

– The experimental methods presented in this thesis are adequate to experimentally determine the main contributions to the enhanced tensile strength and fracture resistance. However, the methods can be improved to

[1] *Available at the TUDelft, for information contact dr.ir. J. Weerheijm*

increase the accuracy of the data on the individual aspects. For instance, when the acceleration of the fracture zone could be properly determined by Digital Image correlation, the deformation distribution within the fracture zone can be obtained and the structural inertia effects can be more accurately calculated.

- In the presented research it is shown that only the moisture in the *capillary* pores contributes to the enhanced tensile strength and post-peak resistance. However, other researchers who tested concretes made with different water-cement ratio's [Toutlemonde 1995, Rossi 1997] concluded that the moisture causing the rate effect of concrete are not found in the *capillary* pores but in the *gel* pores. Therefore, it is recommended to perform dynamic tests in the future with concrete specimen using different water-cement ratio's and then also define the pore structures with NMR. From such a test program, further insight can be acquired about the type of pores which cause the rate effect.
- It is known from literature that the (nominal) strength decreases with increasing size of specimen [Burtscher 2004, Bazant 1984, Bazant 1997, Elfahal 2005]. Therefore, it is recommended to test different specimen sizes, bigger than the diameter of 74 mm used, with the same concrete composition to determine the influence of specimen size on the rate dependency of concrete fracture properties. Also, different types of concrete with larger aggregate particles should be tested to determine the influence of the aggregate grading on the rate dependency of concrete tensile strength and fracture behaviour. A grain size of approximately 16 - 32 mm is recommended to match standard concrete used in practice. These tests on size effects require a larger test set-up.
- The scatter in experimental results found in literature is large. The high scatter is caused by the difference in concrete mixture, testing techniques, size of specimens and moisture content. To be able to properly compare the experimental data on rate dependency, it is essential to standardize the test methods, including sample preparation and sample conditioning prior to testing, and start international cooperation for dynamic experiments.
- For experimental research, the data is collected with measurement devices due to diagnostics attached at the outside surface of the concrete specimens, while the fracture process and the transmitting of waves take place inside the specimen. It is not readily possible to monitor the fracture process inside a specimen. Therefore, to be able to reconstruct the fracture process inside the

specimen and accurately quantify the effects of the fracture process on the wave transmission, it is recommended to combine experimental research with numerical modelling.

– The analysis of the dynamic tests presented in this thesis is based on 1D wave propagation, assuming that the process is most dominant in the axial direction. For this 1D analysis it is assumed that the stress distribution is approximately homogeneous in the radial direction and that the notches have a negligible effect on the average stress distribution measured outside the fracture zone. To verify the legitimacy of this assumption, numerical modelling of the dynamic tests is recommended.

REFERENCES

Aligizaki, K.K. (2006) *Pore structure of cement based materials- testing, interpretation and requirements*, Taylor & Francis, p 60-107.

Bazant, Z.P. et al. (1982) *Creep and shrinkage in concrete structures*. John Wiley & Sons.

Bazant, Z.P. and Oh, B.H. (1983) 'Crack band theory for fracture of concrete' *RILEM Materials and Structures*, 16 (93): pp 155-177.

Bazant, Z.P. (1984) 'Size effect in blunt fracture: Concrete, rock, metal.' *Journal of Engineering mechanics* 110(4) pp 518-535.

Bazant, Z.P. and Xiang, Y. 'Size effect in compression fracture: splitting crack band propagation.' *Journal of Engineering mechanics* ASCE 123(2) pp 162-172.

Bentz, D.P., Garboczi, E.J., Quenard, D.A. (1998) 'Modelling Drying Shrinkage in Reconstructed Porous Materials: Application to Porous Vycor Glass', Modelling and Simulation in Materials Science and Engineering 6 (3), 211-236.

Bisschop, J. (2002) *Drying shrinkage microcracking in cement-based materials*, Ph.D thesis, Delft University of Technology.

Brara, A. and Klepaczko, J.R. (2006) 'Experimental characterization of concrete in dynamic tension', *Mechanics of Materials* 38: 253-267.

Brara, A. and Klepaczko, J.R. (2007) 'Fracture energy of concrete at high loading rates in tension', *Int. J. of Impact Engineering* 34: 424-435.

Breugel van, K. (1997) *Simulation of hydration and formation of structure in hardening cement-based materials.* Revised version of PhD, Delft University Press, Delft.

Burtscher, S.L. and Kollegger, (2004) J. 'Size effect experiments on granular materials in compression' *Proceedings of FraMCos 2004*, ISBN 0870311352.

Cadoni, E., Labibes, K., Albertini, C., Berra, M. and Gian-grasso, M. (2001a) 'Strain rate effect on the tensile behaviour of concrete at different relative humidity levels', *Materials and Structures* 34: 21-26.

Cadoni, E., Albertini, C., Labibes, K. and Solomos, G. (2001b) 'Behavior of plain concrete subjected to tensile loading at high strain rate', *Fracture Mechanics of Concrete Structures*: 341-347. Lisse: Swets&Zeitlinger.

Carpinteri, A. (1984) 'Stability of fracture process in RC beams' *J. Structural engineering* 110: pp 2073-2084.

CEB-FIP bulletin d'information no. 187 (1988), Synthesis Report *Concrete structures under impact and impulsive loading*.

Chen, W.W. and Sony, B. (2011) *Split Hopkinson (Kolsky) Bar: Design, Testing and Application*, Springer Science + Business Media.

Chen, E.P. and Sih, G.C. (1977) 'Transient response of cracks to impact loads', *Mechanics of fracture 4, Elastodynamic crack problems*. Edited by Sih, G.C., Noordhoff Int. Publishing, Leyden, the Netherlands.

Çopuroğlu, O. (2006) *The characterisation, improvement and modelling aspects of Frost salt scaling of cement based materials with a high slag content*, Ph.D thesis, Delft University of Technology.

Cotsovos, D.M. and Pavlovic, M.N. (2008a) 'Numerical investigation of concrete subjected to high rates of uniaxial tensile loading' *Intern. Journal of Impact Engineering* 35: p319-335.

Cotsovos, D.M. and Pavlovic, M.N. (2008b) 'Numerical investigation of concrete subjected to compressive impact loading. Part 1: A fundamental explanation for the apparent strength gain at high loading rates' *Computers and Structures* 86: p145-163.

Cotsovos, D.M. and Pavlovic, M.N. (2008c) 'Numerical investigation of concrete subjected to compressive impact loading. Part 2: Parametric investigation of factors affecting behaviour at high loading rates.' *Computers and Structures* 86: p164-180.

Curbach, M. and Eibl, J. (1990) 'Crack velocity in concrete' *Engineering Fracture mechanics* Vol 35: pp 321-326.

Elfahal, M.M., Krauthammer, T., Ohno, T., Beppu, M. and Mindess S. (2005) 'Size effect for normal strength concrete cylinders subjected to axial impact' *International Journal of Impact Engineering* 31 pp 461-481

Erzar, B. and Forquin, P. (2010a) An experimental method to determine the tensile strength of concrete at high rates of strain, *Experimental Mechanics* 50(7): 941-955.

Erzar, B. *Ecaillage, craterisation et comportement en traction dynamique de betons sous impact: approches experimentales et modelisation*. (2010b) PhD-thesis, University of Metz, France.

Graf, O., Albrecht, W, and Schäffler, H. (1960) The properties of concrete. Second edition, Berlin.

Grasley, Z.C. (2003) *Internal Relative Humidity, Drying Stress Gradients, and Hygrothermal Dilation of Concrete*, PhD thesis, University of Illinois.

Grote, D.L., Park, S.W. and Zhou, M. (2001) 'Dynamic behaviour of concrete at high strain rates and pressures: I Experimental characterization', *International Journal of Impact Engineering* 25: 869-886.

Hillerborg, A. Modeer, M and Petersson, P.E. (1976) Analysis of crack formation and crack growth in concrete by means of fracture mechanics and finite elements. *Cement and Concrete Research* 6: pp 773-782.

Hillerborg, A. (1985) The theoretical basis of a method to determine the fracture energy Gf of concrete. RILEM Materials and Structures, 18 (106), pp 291-296.

Hordijk, D.A. and Reinhardt, H.W. (1990) 'Fracture of concrete in uniaxial tensile experiments as influenced by curing conditions', *Engineering Fracture Mechanics* 35(3/4): 819-826.

Hordijk, D.A. (1991) *Local approach to fatigue of concrete*, Ph.D thesis, Delft University of Technology.

Isenberg, J., Bazant, Z.P., Mindess, S., Suaris, W. and Reinhardt, W. (1992) 'Dynamic Fracture', in '*Fracture Mechanics of Concrete and Concrete Structures'*, proceedings of FraMCoS-1, 1992 in Colorado USA.

Klepaczko, J.R. and Brara, A. (2001) 'An experimental method for dynamic testing of concrete by spalling', *Int. J. Impact Engineering* 25:387-409.

Körmeling, H.A., Zielinski, A.J. and Reinhardt, H.W. (1980) *Experiments on concrete under single and repeated uniaxial impact tensile loading*, report 5-80-3, Delft University of Technology.

Körmeling, H.A. (1984) *Impact of steel fibre concrete at -170°C*, report 5-84-13, Delft University of Technology.

Lee, O.S. and Kim, M.S. (2003) *Nuclear Engineering and Design* 226: 119-125.

Mackenzie, J.K. (1950) *The Elastic Constants of a Solid Containing Spherical Holes,* Proc Phys Soc B 683, 2-11.

Metha, P.K. (1986) *Concrete structure properties and materials*, Prentice Hall, Engelwood cliffs, NJ.

Metrikine, A.V. and Vrouwenvelder, A.C.W.M. (2004) *Dynamics of structure, part 2: Wave dynamics.* Lecture notes CT4140, Delft University of Technology.

Meyers, M.A. (1994) *Dynamic behaviour of materials*, John Wiley & Sons.

Mier van, J. (1997) *Fracture processes of concrete*, CRC Press, Delft.

Mindess, S., Young, J.F. and Darwin, D. (2002) *Concrete,* 2nd edition, Prentice hall, Englewood Cliffs, NJ.

Nguyen, A.V. (2000) 'Historical note on the Stefan-Reynolds equations', *Journal of Colloid and Interface Science:* 231, 195.

Nguyen, A.V. and Schulze, H.J. (2003) *Colloidal Science of Flotation* Publication CRC Press 2003

Novikov, S.A., Divnov, I.I. and Ivanov, A.G. (1966) The study of fracture of steel, aluminium and copper under explosive loading, *Fiz. Met. Metalloved* 21(4): 608-615.

Ozbolt, J., Weerheijm, J. and Sharma, A. (2013) Dynamic tensile resistance of concrete-Split Hopkinson Bar tests, *Proceedings of FRAMCOS 8*, 2013 in Toledo, Spain.

Pedersen, R.R. (2010a) *Computational modelling of dynamic failure of cementitious materials,* Ph.D thesis, Delft University of Technology.

Pedersen, R.R., Simone, A. and Sluys, L.J. (2010b) 'An analysis of dynamic fracture in concrete with a continuum visco-elastic visco-plastic damage model', *Engineering Fracture Mechanics*, In press.

Pedersen, R.R., Simone, A., Stroeven, M. and Sluys, L.J. (2007) 'Mesoscopic Modelling of Concrete under Impact', In '*Fracture Mechanics of Concrete and Concrete Structures'*, proceedings of FraMCoS-6, June 2007 in Catania, Italy (Taylor & Francis, London), 571-578.

Pedersen, R.R. & Simone, A. & Sluys, L.J. (2006) Modelling of dynamic failure of concrete using a viscoelastic viscoplastic damage continuum model. Subjected to Euro-C conference march 2006.

Reinhardt, H.W. (1984) 'Fracture mechanics of an elastic softening material like concrete' *HERON,* 29 (2): p 42.

Reinhardt, H.W. (1985) *Beton als constructiemateriaal- eigenschappen en duurzaamheid* (Concrete as construction material- properties and durability), Delft: University Press Delft.

Reinhardt, H.W., Rossi, P., Mier van, J.G.M. (1990) 'Joint investigation of concrete at high rates of loading' *Materials and structures* 23: 213-216.

Ross, A.C. and Kuennen, S.T. (1989) 'Fracture of concrete at high strain-rates' In *Fracture of Concrete and Rock: Recent Developments*. Editors Shah, S.P. et al. 152-161.

Ross, A.C., Jerome, D.M., Tedesco, J.W. and Hughes, M.L. (1996) 'Moisture and strain rate effects on concrete strength', *ACI Materials Journal* 93(3): 293-300.

Rossi, P. and Boulay, C. (1990a) 'Influence of free water in concrete on the cracking process' *Magazine of concrete research* 152: 143-146.

Rossi, P. (1990b) 'Coupling between the cracking process and viscous phenomena in concrete' *Engineering fracture mechanics* 35: 79-86.

Rossi, P. (1991) 'A physical phenomenon which can explain the mechanical behaviour of concrete under high strain rates' *Material and structures* 24: 422-424.

Rossi, P., van Mier, J.G.M., Boulay, C. and le Maou, F. (1992) 'The dynamic behaviour of concrete: influence of free water', *Materials and Structures* 25: 509-514.

Rossi, P. (1997) 'Strain rate effects in concrete structures: the LCPC experience', *Materials and Structures* Supplement March: 54-62.

Schuler, H. (2004) *Experimentelle und numerisch Untersuchungen zur Schädigung von Stoßbeanspruchtem Beton*, Ph.D thesis, Institut Kurzzeitdynamik Ernst-Mach-Institut.

Schuler, H., Mayrhofer, C. and Thoma, K. (2006) 'Spall experiments for the measurement of the tensile strength and fracture energy of concrete at high strain rates', *Int. J. of Impact Engineering* 32: 1635-1650.

Shah, S.P., Swartz, S.E. and Ouyang, C. (1995) *Fracture mechanics of concrete: Applications of fracture Mechanics to Concrete, Rock and other Quasi-Brittle Materials*. John Wiley & Sons, New York.

Souwerbren, C. (1998) *Beton Technologie*, BetonPrisma 's Hertogenbosch

Toutlemonde, F. (1995a) 'Resistance au choc des structures en beton' Du comportement du materiau au calcul des ouvrages, Ph.D thesis, l'ecole Nationale des Ponts et Chaussées.

Toutlemonde, F. (1995b) 'Major parameters governing concrete dynamic behaviour and dynamic failure of concrete structures' *Dymat journal* 2: 96-77.

Toutlemonde, F., Boulay, C. and Rossi, P. (1995c) 'High strain rate tensile behaviour of concrete: significant parameters' *Proceedings of FRAMCOS 2*, p. 709-718.

Toutlemonde, F. and Rossi, P. (1998) 'Free water in concrete pores: an Attempt of physical explanation of concrete behaviour' *Concrete and Blast effects*, ed W. Bounds, American concrete institute, Michigan.

Valckenborg, R.M.E., Pel, L., Hazrati, K., Kopinga, K. and Marchand J. (2001a) 'Pore water distribution in mortar during drying as determined by NMR', *Materials and Structures* 34: 599-604.

Valckenborg, R.M.E. (2001b) *NMR on technological porous materials*, Ph.D. thesis, Eindhoven University of Technology, the Netherlands.

Vegt, I., Weerheijm, J., Pedersen, R.R. and Sluys, L.J. (2006a) 'Modelling of impact behaviour of concrete- an experimental approach'. *In 'Computational modelling of Concrete Structures', proceedings of conference EURO-C 2006*, Mayerhofen, (Taylor & Francis, London), p 451-458.

Vegt, I., Weerheijm, J. and Schlangen, E. (2006b) 'Influence of moisture content on the dynamic behaviour of concrete', *Proceedings of the 16th European Conference of Fracture*, Alexandroupolis, Greece, July 3-7.

Vegt, I. and Weerheijm, J. (2006c) 'Dynamic response of concrete at high loading rates – A new Hopkinson Bar device', *Proceedings of the Int. Conf. Brittle Matrix Composites (BMC8)*, Warsaw, Poland, October 2006.

Vegt, I., Weerheijm, J. and Van Breugel, K. (2006d) 'Moisture content and the effect on dynamic concrete behaviour', *Proceedings of the 2nd Int. Conf. on Design and Analysis of Protective Structures*, Singapore, 13-15 November 2006.

Vegt, I., Weerheijm, J. and Van Breugel, K. (2007a) 'The fracture energy of concrete under impact tensile loading- a new experimental technique', *Proceedings of the CONSEC Conference*, Tours, France, June 2007.

Vegt, I., Weerheijm, J. and Van Breugel, K. (2007b) 'Failure mechanisms of concrete under impact loading', *Proceedings of the Framcos Conference*, Catania, Italy, June 2007.

Vegt, I., Weerheijm, J., Mediavilla Varas, J. and Breugel, K. van (2007c) 'Failure of concrete under impact loading', *Proceedings of 9th International Symposium on Plasticity and Impact Mechanics, IMPLAST 2007*, Bochum (Germany), 21-24 August, 2007, p. 247-254.

Vegt, I., Weerheijm, J. and Breugel, K. van (2007d) 'Concrete response under moderate and high dynamic tensile loading', *Proceedings of the Third International Conference on Structural Engineering, Mechanics and Computation "Recent Developments in Structural Engineering: Mechanics and Computation"*, 10-12 September, Cape Town, South Africa

Weerheijm, J. (1987) *Kontroleproeven aan en met de Split-Hopkinson bar*, report 25-87-9, Delft University of Technology.

Weerheijm, J. (1988) *Dynamische eigenschappen van beton I. Het experimentele onderzoek*, report PML 1988-61, Prins Maurits Laboratorium TNO.

Weerheijm, J. (1989) *Properties of concrete under dynamic loading 2. Biaxial loading device*, report PML 1989-59, Prins Maurits Laboratorium TNO.

Weerheijm, J. (1992) *Concrete under impact tensile loading and lateral compression*, Ph.D thesis, TNO Rijswijk.

Weerheijm, J., Doormaal, van, J.C.A.M. and Kasteele, van de, R.M. (2001) *Development of a new test set-up for dynamic tensile tests on concrete under high loading rates; Part 1: Results of test series A*, TNO Rijswijk.

Weerheijm, J., Doormaal, van, J.C.A.M. and Kasteele, van de, R.M. (2003) *Development of a new test set-up for dynamic tensile tests on concrete under high loading rates; Part 2: Results and evaluation of test series B and C on concrete*, TNO Rijswijk.

Weerheijm, J. and Van Doormaal J.C.A.M. (2004) 'Tensile failure at high loading rates; Instrumented spalling tests', *Proceedings of the International Conference FramCoS 5*, April 2004.

Weerheijm, J. (2006) 'Axial Dynamic Tensile strength of Concrete under Static Lateral Compression', *Key Engineering Materials* Vols. 324-325, p. 991-994.

Weerheijm, J. and Van Doormaal, J.C.A.M. (2007) 'Tensile failure of concrete at high loading rates: New test data on strength and fracture energy from instrumented spalling tests', *Int. J. of Impact Engineering* 34: 609-626.

Weerheijm, J. and Vegt, I. (2009a) 'The dynamic fracture energy of concrete, review of test methods and data comparison', *Proceedings of the int. conf. FRAMCOS-7*, Korea, 2009.

Weerheijm, J., Vegt, I. and Van Breugel, K. (2009b) 'The rate dependency of concrete in tension- New data for wet, normal and dry conditions', *Proceedings of the int. conf. DYMAT 9*, Brussels, 2009.

Weerheijm, J. and Vegt, I. (2010) 'The dynamic fracture energy of concrete - Review of test methods and data comparison'. In *Fracture Mechanics of Concrete Structures - FraMCOS-7:* pp. 419-427.

Weerheijm, J. and Vegt, I. (2011) 'How to determine the dynamic fracture energy of concrete. Theoretical considerations and experimental evidence', *Applied Mechanics and Materials* Vol 82: 51-56.

Weerheijm et al. (2013) *Understanding the tensile properties of concrete*, Edited by Weerheijm, J., Woodhead Publishing Limited.

Wittmann, F.H. (1972) 'Interaction of Hardened Cement Paste and Water', *Journal of the American Ceramic Society*, Vol 56, no 8, pp 409-415.

Wittmann, F.H. (1977) *Grundlagen eines Models zur Beschreibung charakteristischer Eigenschaften des Betons*, Deutscher Ausschuss fur Stahlbeton, Vol. 290, 45.

Wu, H., Zhang, Q., Huang, F. and Jin, Q. (2005) *International Journal of Impact Engineering* 32: 605-617

Ye, G. (2003) *The microstructure and permeability of cementitious materials*, Ph.D thesis, Delft University of Technology.

Zhang, X.X., Ruiz, G., Yu, R.C. and Tarifa, M. (2009) 'Fracture behaviour of high-strength concrete at a wide range of loading rates' *Int. J. of Impact Engineering* 36: pp 1204-1209.

Zheng, D. and Li, Q. (2004a) 'An explanation for rate effect of concrete strength based on fracture toughness including free water viscosity' *Engineering fracture mechanics* 71: 2319-2327.

Zheng, D. and Li, Q. (2004b) 'Rate effect of concrete with a simplification of crack interaction', *Proceedings of the Framcos Conference,* Colorado USA 2004. ISBN 0870311352.

Zhou, X.Q. and Hao, H. (2008) 'Mesoscale modelling of concrete tensile failure mechanisms at high strain rates' *Computers and Structures* 86: pp 2013-2026.

Zielinski, A.J. (1981) *Experiments on mortar under single and repeated uniaxial impact tensile loading*, report 5-81-3, Delft University of Technology.

Zielinski, A.J. (1984) *Concrete structures under impact loading- Rate effects*, report 5-84-14, Delft University of Technology.

APPENDIX A. INFLUENCE NOTCHDEPTH ON TENSILE STATIC STRENGTH

This appendix describes the influence of the notch depth on the measured strength of the concrete. Since the notch depth has varied in the different test conditions (see chapter 5), it is important to understand the influence of the notch depth on the results. In this appendix, static experiments with different notch depth will be described and the experimental results on tensile strength, fracture energy and stress-displacement curves presented.

Static experiments

To determine the influence of the notch depth on the static test results, static tests are conducted using different notch depths. The concrete used in these experiments has been subjected to normal conditions as described in chapter 3. The experimental data on strength and fracture energy are presented in Table A.1 and do not show a significant influence of the notch depth on the test results. The strength of the concrete with a notch depth of 4 mm seems to be lower, but the standard deviation is much higher. The actual strength could therefore easily be the same. The fracture energy of the concrete seems not to be influenced by the notch depth, although the standard deviation increases dramatically for the concrete with a notch depth of 6 mm.

Table A.1. Strength and fracture energy for static tests with different notch depths.

Notch depth [mm]	$f_{t,stat}$ [MPa]	Stand. dev. [MPa]	$G_{f,stat}$ [N/m]	Stand. dev. [N/m]
Normal 2mm	2.61	0.06	88.3	8.9
Normal 4mm	2.22	0.32	94.6	8.8
Normal 6mm	2.49	0.17	91.6	22.8

Unfortunately, during the period of storage in the climate chamber (20°C and 50% RH), the climate in the chamber was disturbed and the temperature and relative humidity were elevated. Therefore, the results from these static tests cannot be compared to earlier tests on concrete kept under normal conditions.

The representative stress-displacement curves of the concrete with different notch depth are shown in Figure A.1. The maximum value is different for the different notch depths, as already mentioned when discussing the strength, but the shape of the curves is very similar.

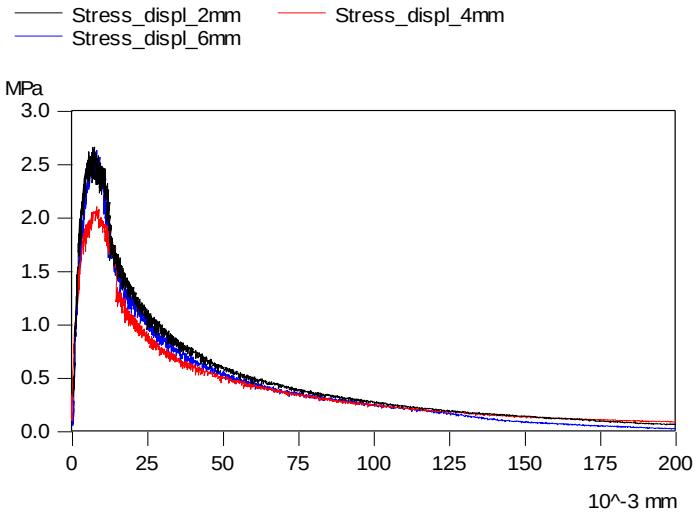

Figure A.1. Static stress-displacement curves for different notch depths.

The behaviour of the concrete up to the maximum value is the same. The different curves show the same elastic stiffness and amount of pre-peak non-linearity in the ascending branch. Also the behaviour after the macro crack has been formed, the descending branch of the curves, is alike.

From the experiments on different notch depths can be concluded that in case of the static tests, the influence of the notch depth on the results is not significant.

APPENDIX B. COMPARISON METZ AND TNO SET-UP

Comparison with Metz set-up and measuring method

The Hopkinson Bar method is used by many researchers to determine dynamic strength. It has been adapted over the last decade to expand the strain rate up to 100 /s. In Metz a new dynamic testing facility has been developed in LEM3 laboratory (Metz University) to test concrete specimens by means of spalling, reaching strain rates ranging from 30 /s to 200 /s [Erzar and Forquin 2010, Erzar 2010]. The device includes a gas gun, which launches a cylindrical projectile of 70 or 80 mm in length. The projectile strikes a Hopkinson bar with a diameter of 45 mm and a length of 120 mm. Both the projectile and the Hopkinson Bar are made out of high strength aluminium alloy. The instrumentation includes three strain gauges and two laser interferometers, used to determine wave speed, dynamic Young's modulus as well as strength [Erzar and Forquin 2010]. The method used to determine the strength is developed by Novikov [Novikov et al., 1966] and is based on the particle velocity and pull back velocity, measured on the rear free face of the specimen, using the laser equipment (see equation B.1).

$$f_{t,dyn} = \frac{1}{2}\rho c_0 \Delta v_{pb} \qquad (B.1)$$

Tests have been conducted in Metz with wet concrete specimens made in Delft, using the same concrete composition as used for the tests conducted in Delft and at TNO (see paragraph 3.3.1). Only Portland concrete was used and the specimens were all submersed in water, like was the case for the wet specimens in Delft. The diameter of the Metz specimens was 46 mm and the length 140 mm, which is much smaller than used for the Delft and TNO tests. Notched as well as unnotched specimens were tested.

The average strength found with the Metz set-up for the notched specimens is 12.6 MPa and for the unnotched specimens 11.2 MPa. The average strength from the MSHB tests performed at TNO for wet specimens is 17.1 MPa (see Table 5.9).

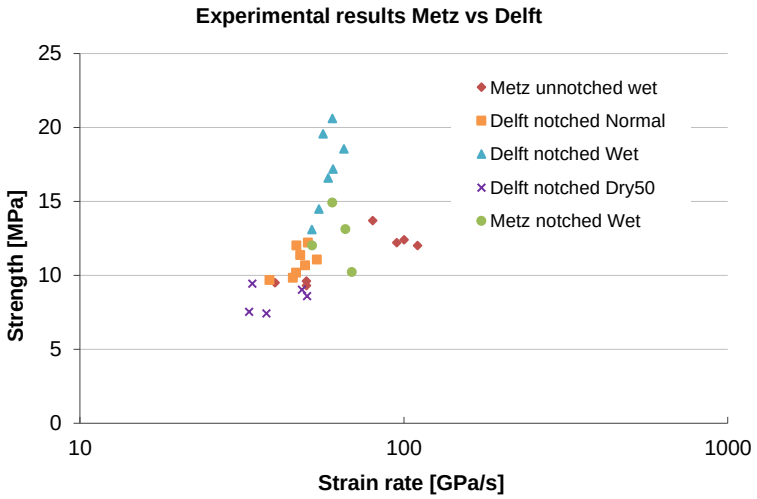

Figure B.1 Experimental data Metz, notched and unnotched, compared to data Delft (Portland concrete).

The average strength results for the TNO and Metz set-ups are similar, although the results for TNO are slightly higher (see Figure B.1). This is due to the concrete composition; the largest aggregate particle in the concrete is 8 mm, which is probably too large to get a homogeneous material for a specimen with a diameter of 46 mm, which is the diameter needed in the Metz set-up. However, in order to compare the test facilities, the concrete composition was kept the same for both set ups.

The advantages of the TNO set-up, compared to the Metz set-up, is the possibility to directly determine the fracture energy and also to measure the deformation and strains in time. These measurements provide insight in the behaviour of concrete during failure, which cannot be deduced from the experimental signals in Metz. In Metz, the experimental results are combined with numerical simulations, to determine fracture energy or to reconstruct failure behaviour.

The advantage of the Metz set-up is the easy determination of the strength. No costly strain gauges are needed and the method to determine the strength from the experimental results is short and simple.

CURRICULUM VITAE

Name	Ilse Vegt
Date of birth	July 14 1980
Place of birth	Den Helder, the Netherlands

1992 – 1998	High school, Gymnasium, CSG Jan Arentsz, Alkmaar, the Netherlands.
1998 – 2003	Civil Engineering, Delft University of Technology, the Netherlands. Thesis on Concrete with glass aggregate particles. Diploma Master of Science, 2003, with Honours.
2003 – 2004	Civil Engineer junior, Ingenieursbureau Temid, Heerhugowaard, the Netherlands.
2008 – 2010	Junior scientist at TNO Defence, Safety & Security, department of Physical Protection and Survivability, Rijswijk, the Netherlands.
2010 – present	Civil Engineer at the local government of Bergen, the Netherlands.
2004 – 2016	Faculty of Civil Engineering and Geosciences, Materials and Environment, Delft University of Technology, The Netherlands. PhD-study on the behaviour of concrete under dynamic tensile loading.

Publications

Vegt, I. and Weerheijm, J. (2016)

Influence of moisture on the fracture behaviour of concrete loaded in dynamic tension.

9th Int. Conference on Fracture Mechanics of Concrete and Concrete Structures, June, 2016, Berkeley USA.

Vegt, I. and Weerheijm, J. (2015)
The post peak response of concrete for dynamic tensile loading.
3rd International Conference on Protective Structures (ICPS3), Newcastle, Australia, 3-6 February 2015, M.G. Stewart & M.D. Netherton (Eds.)

Weerheijm, J. and Vegt, I. (2011)
How to determine the dynamic fracture energy of concrete. Theoretical considerations and experimental evidence.
Applied Mechanics and Materials Vol. 82 (2011) pp 51-56.

Vegt, I, Weerheijm, J. and Van Breugel, K. (2009)
The rate dependency of concrete under tensile impact loading: Fracture energy and fracture characteristics.
Proc. 13th International Symposium on the Interaction of the Effects of Munitions with Structures, 13th ISIEMS, May 2009.

Vegt, I., Weerheijm, J. and Breugel, K. van (2007)
Concrete response under moderate and high dynamic tensile loading.
A. Zingoni (ed.), in: Proceedings of the Third International Conference on Structural Engineering, Mechanics and Computation "Recent Developments in Structural Engineering: Mechanics and Computation", 10-12 September, Cape Town, South Africa
ISBN 9789059660540, Millpress, short version p. 199-200, long version on cd-rom p. 533-538

Vegt, I., Weerheijm, J., Mediavilla Varas, J. and Breugel, K. van (2007)
Failure of concrete under impact loading.
Editors: Prof. O.T.Bruhns; Dr. A. Meyers. Proceedings of 9th International Symposium on Plasticity and Impact Mechanics, IMPLAST 2007, Bochum (Germany), 21-24 August, 2007., p. 247-254

Vegt, I., Breugel, K., van and Weerheijm, J. (2007)
Failure mechanisms of concrete under impact loading.
A.Carpinteri, P. Gambarova, G. Ferro and G. Plizzari (eds.), in: Proceedings of the 6th Int. Conference on Fracture Mechanics of Concrete and Concrete Structures, June, 2007, Catania, Italy, ISBN 13 - Vol-1: 978 0 415 44065 3 ; Taylor & Francis Group, p. 579–587.

Vegt, I., Weerheijm, J. and Breugel, K. van (2007)
The fracture energy of concrete under impact tensile loading- A new experimental technique.
F. Toutlemonde (eds.), in: Proceedings of 5th International Conference on Concrete Under Severe Conditions environment and Loading, 4-6 June 2007, p. 1235-1242

Weerheijm, J., Vegt, I. and Breugel, K. van (2007)
Research developments and experimental data on dynamic concrete behaviour.
C.U. Grosse (ed.), in: Advances in construction materials 2007; Berlin: springer, p. 765-773

Vegt, I., Pedersen, R.R. and Sluys, L.J. and Weerheijm, J. (2006)
Modelling of impact behaviour of concrete - an experimental approach.
G. Meschke, R. de Borst, H. Mang and N. Bicanic (eds.), in: Proceedings of EURO-C 2006:"Computer Modelling of Concrete Structures", March 2006, Mayrhofen, Tirol, Austria, p. 451 - 458, Published by Taylor & Francis/Balkema, The Netherlands. ISBN 10: 0 415 39749 9 and ISBN 13: 978 0 415 39749 0.

Vegt, I. and Weerheijm, J. (2006)
Dynamic response of concrete at high loading rates - A new Hopkinson Bar Device.
A.M. Brandt, V.C. Li and I.H. Marshall (Eds.), In: Proceedings of the Eighth International Symposium on Brittle matrix composites 8, October, 2006, p. 559 – 569, ISBN 1 84569 031 1, Woodhead Publishing Limited, Cambridge and Warsaw 2006

Vegt, I. , Weerheijm, J. and Schlangen, E. (2006)
Influence of moisture content on the dynamic behaviour of concrete.
E.E. Gdoutos (ed.), in: Proceedings of the 16th European Conference of Fracture, "Fracture of Nano and Engineering Materials", Alexandroupolis, Greece, July 3 - 7, 2006,11 pages, on a CD rom, ISBN 13 978-1-4020-4971-2

Vegt, I., Weerheijm, J. and van Breugel K. (2006)
Moisture content and the effect on dynamic concrete behaviour.
2nd. International Conference on Design and Analysis of Protective Structures, Singapore, November 2006